University of Alberta
Department of Civil Engineering

Structural Engineering Report No. 179

FINITE ELEMENT ANALYSIS OF DISTRIBUTED DISCRETE CONCRETE CRACKING

by

Budan Yao

and

David W. Murray

May 1992

Structural Engineering Report No. 179

FINITE ELEMENT ANALYSIS OF DISTRIBUTED DISCRETE CONCRETE CRACKING

BY

Budan Yao
and
David W. Murray

Department of Civil Engineering
University of Alberta
Edmonton, Alberta
Canada
T6G 2G7

May 1992

ABSTRACT

In finite element analyses of concrete, the application of discrete cracking models has not been explored as much as that of smeared cracking models, due to the complication involved in the modeling. However, the increased interest in detailed local behavior of reinforced concrete at different loading stages, the need for investigation of dominant cracks and the inadequacies of smeared models, are stimulants to the development of discrete cracking models.

This thesis proposes and implements a systemic and automated finite element approach for distributed discrete concrete cracking. A vertex based topological data base is formed to represent explicitly all the adjacency relations included in the input finite element mesh, by the technique of "exhaustive nodal splitting". Crack initiation and propagation along element boundaries are simulated automatically by activating and deactivating the associated "nodal splitting numbers" in the data base.

The crack face behavior, crack widening, crack unloading and crack closing, are modelled on the basis of the softening response of cracked concrete associated with tensile fracture energy. The fracture energy criterion is introduced to the solution strategy in order to control crack instability. Concrete compressive yielding is modelled by classical plasticity theory for a continuum.

Several well-known "tension-pull" tests were simulated by the approach developed herein. The two main components of bond for deformed bars, the mechanical interlock and chemical adhesion, are modelled by explicitly representing the lugs on the reinforcing bars as steel elements and specifying a adhesive tensile strength for separation of the concrete-steel interface. Longitudinal splitting cracking is modelled by modifying the axisymmetrical formulation to a plane stress formulation.

In these simulations, distributed discrete cracking, longitudinal splitting cracking, and compressive yielding at the front faces of lugs, are identified. Bond stresses and bond slips are evaluated at the concrete-steel interface. The progression of dominant cracks,

compressive yielding and bond variables are traced through the loading histories.

By optimal fit of the global bond behavior of these "tension-pull" tests, patterns of dominant crack progression, of bond deterioration, and their correlation are identified. The comparison between these patterns provides some insight into global bond behavior.

ACKNOWLEDGEMENTS

The author wishes to express his deepest appreciation and gratitude to the thesis supervisor, Professor David W. Murray, for his patient guidance and constant support during the course of present research. The author wishes to thank Professor Alaa E. Elwi and Professor James G. MacGregor for valuable discussions.

The funding of this project was provided by NSERC (Natural Science and Engineering Research Council) through the operating grant 46307. The author withes to express his deep gratitude to NSERC for this support.

TABLE OF CONTENTS

Contents:

Chapter 3 : Formation of Topological Database from Finite Element Input

Chapter 4 : Simulation of Crack Propagation

Chapter 5 : Constitutive Relations at Crack Faces

Chapter 6 : Solution Strategy

Chapter 7 : Applications

Chapter 8 : Summary and Conclusions

LIST OF TABLES

Table:

LIST OF FIGURES

Figure:

NOMENCLATURE

Acronyms for the Topological Data Base:

CBEN	Crack back element number
CBNSN	Crack back nodal splitting number
CCBNN	Current crack back nodal number
CCFNN	Current crack front nodal number
CFEN	Crack front element number
CFNSN	Crack front nodal splitting number
DOF	Degree of freedom
ALSDI	Accumulated load step displacement increment
NE	Total number of distinct edges
NMELM	Total number of elements
NMNOD	Total number of input nodes
NS	Exhaustive nodal splitting number for the previous input node
NV	Total number of vertices
TCW	Total crack width
WS	Exhaustive nodal splitting number for the previous patch of element mesh

Names of Arrays for the Topological Data Base:

ANG(8)	Orientation array for edges emanating from a vertex
ID(2,NMNOD)	Nodal DOF status array
KEMT(NMNOD,17)	Nodal-element incidence array
KEMT2(NMNOD)	Array of initial nodal numbers corresponding to input nodal numbers
KSID1(4,3)	Array of edges of an element, defined by local nodal numbers
KSID(4,3)	Array of edges of an element, defined by global nodal numbers

MART(8,5,4)	Adjacency array for edges emanating from a vertex
NCRLC(NE,20,3)	Array of topological information for all edges
NCRNN(NV,6,8)	Array of vertex-edge adjacencies for all vertices
NCRNM(NV)	Array of total number of edges emanating from a vertex NV
NAEM1(8)	Array of back element numbers for edges emanating from a vertex
NPELM(12,NMELM)	Element-node incidence array

Scalars:

A_c	Area of crack face
C	Crack width for overlapping crack
d	Displacement at a point
d_e	Elastic component of d
d_w	Component of d due to cracking
d_{em}	Maximum value of d_e
d_m	The measure to select root in the "cylindrical arc-length" method
f'_c	Compressive strength of concrete
f'_{co}	Compressive strength for overlapping crack faces
f'_{sc}	Adhesive tensile strength between concrete and steel
f'_t	Tensile strength of concrete
f'_{th}	Tensile strength of Concrete in the hoop direction
F_{Wi-1}	Nodal force on the crack face for iteration i-1
f_{ys}	Yield strength of steel
h	Thickness
H	Height of a prism
k_{ci}	Stiffness for link element at iteration i when the crack is overlapped

k_{Wi}	Stiffness for link element at iteration i when the crack is open
L	Length of a "tension-pull" specimen, or crack spacing
L_c	Critical length of concrete prism under tension for occurrence of snap back behavior after cracking
L_{max}	Maximum crack spacing
L_{min}	Minimum crack spacing
$\Delta \ell$	Specified increment of arc-length
R_{nmax}	Maximum end forces recorded for a link element during the propagation of a crack
R_{cn1}, R_{cn2}	Forces applied at the two ends of an link element when the crack is overlapped
R_{n1}, R_{n2}	Forces applied at the two ends of an link element when the crack is open
s	Distributed normal stresses on edge **L**
s_{IALB}	Interval averaged Longitudinal bond slip
s_{IARB}	Interval averaged radial bond slip
s_{SALB}	Specimen averaged Longitudinal bond slip
s_{SARB}	Specimen averaged radial bond slip
$\lvert s_{LB} \rvert$	Absolute value of longitudinal slip at the front face of a lug
$\lvert s_{RB} \rvert$	Absolute value of radial slip at the front face of a lug
U_{IALS}	Interval averaged Longitudinal displacements of steel
U_{IARS}	Interval averaged radial displacements of steel
U_{IALC}	Interval averaged Longitudinal displacements of concrete
U_{IARC}	Interval averaged radial displacements of concrete
Δu	Displacement increment at the point of applied load
$\Delta \mathscr{u}$	Increment of strain energy
$\Delta \mathscr{u}_i$	Increment of strain energy at iteration i
W	Crack width
W_c	Ultimate crack width

W_{i-1}	Crack width at iteration i-1
W_{max}	Maximum crack width recorded during the propagation of a crack
Δw	Increment of work done by the external load
Δw_c	Increment of fracture energy required for crack growth
Δw_{ci}	Increment of fracture energy required for crack growth at iteration i
Δw_i	Increment work done by the external load at iteration i
β_t	Tolerance of angle between **n** and **p** to split an edge
η	Load convergence ratio
η_s	Critical η to switch to fracture energy control
γ	Angle of inclination of the front face of a lug to the axis of reinforced bar
λ	Load factor
λ_i	Load factor at iteration i
$\Delta\lambda_i$	Incremental load factor at iteration i
λ_{i-1}^{t}	Load factor at iteration i-1 of load step t
μ_1	$k_{ci}/\lvert kW_i \rvert$
σ_{IALB}	Interval averaged Longitudinal bond stress
σ_{IARB}	Interval averaged radial bond stress
σ_{SALB}	Specimen averaged Longitudinal bond stress
σ_{SARB}	Specimen averaged radial bond stress
σ_{tw}	Tensile stress across two faces of a crack with width W
θ	Local orientation of an edge
ζ	Nondimensional edge coordinate

Vectors:

F	External reference loads
$[F_a F_b F_c]$	Nodal forces equivalent to σ_{tw} at nodes a, b and c on edge L
L	Element edge

$\mathbf{n}$	Normal vector of an edge
$[\ N_a \quad N_b \quad N_c\ ]$	Shape functions in the nondimensional edge coordinate ζ at nodes a, b and c on edge L
$\mathbf{p}$	Principle stress
$\mathbf{Q}_{i-1}$	Unbalanced nodal forces
$\mathbf{R}$	Nodal forces equilibrating the internal stresses
$\mathbf{R}_{i-1}$	Nodal forces equilibrating the internal stresses obtained at iteration i-1
$\mathbf{R}^t_{i-1}$	Nodal forces equilibrating the internal stresses obtained at iteration i-1 for load step t
$\mathbf{R}^t_{i-1_e}$	The equivalent nodal forces required to equilibrate the internal stress of the solid elements at iteration i-1 for load step t
$\mathbf{R}^t_{i-1_{oc}}$	The nodal forces to which link elements are subject when the associated cracks are open at iteration i-1 of load step t
$\mathbf{R}^t_{i-1_c}$	The nodal forces to which link elements are subject when the cracks are overlapped at iteration i-1 of load step t
$\Delta \mathbf{R}^t_{i_c}$	Increment of the nodal forces to which link elements are subject when the cracks are overlapped from iteration i-1 to iteration i of load step t
$\Delta \mathbf{R}^t_{i_e}$	Increment of the equivalent nodal forces required to equilibrate the internal stress of the solid elements from iteration i-1 to iteration i of load step t
$[S_a S_b S_c]$	Tensile stresses at node a, b and c on edge L
$\mathbf{t}$	Orientation vector of an edge
U_1, U_2	Displacements for splitting nodes 1 and 2

U_{12}	Relative displacement for splitting nodes 1 and 2
U_e	An estimation of elastic displacement vector under the external reference load
$\mathbf{U_n}$	Distributed normal displacements on edge **L**
$\Delta \mathbf{U}$	Increment of nodal displacements
$\Delta \mathbf{U}_i$	Increment of nodal displacements in iteration i
$\Delta \mathbf{U}_i^I$	Incremental nodal displacements solved from external reference load
$\Delta \mathbf{U}_i^{II}$	Incremental nodal displacements solved from unbalanced nodal forces
$\mathbf{U}_{i-1}^t$	Total nodal displacements at iteration i-1 of load step t
$\mathbf{U}^{t-1}$	Total nodal displacements at the end of load step t-1
$\Delta \mathbf{U_n}$	Projection of U_{12} on vector **n**
$\Delta \mathbf{U_t}$	Projection of U_{12} on vector **t**
$[\mathbf{U_{na}}\ \mathbf{U_{nb}}\ \mathbf{U_{nc}}]$	Nodal displacements at node a, b and c on edge **L**

Matrices:

$[B]$	Transformation matrix
$\mathbf{K}$	Tangent stiffness matrix
$\mathbf{K}_i$	Tangent stiffness matrix at iteration i
$\mathbf{K}_i^t$	Tangent stiffness matrix at iteration i of load step t
$[K_{s_i}]$	Stiffness matrix for the link element in the local coordinate system
$[K_{W_i}]$	Stiffness matrix for the link element in the global coordinate system

CHAPTER 1

INTRODUCTION

1.1 Behavior of Reinforced Concrete Structures

In the last three decades, the emergence of high speed electronic computation has led to a revolution in the ability of engineers to predict internal forces in structures. Coincidentally, the development of the finite element method has extended these capabilities to two and three dimensional solid structures of arbitrary shape so that solution for internal stresses is now routine for problems which were intractable a few years ago.

In spite of the above developments the analyst's ability to predict behavior of reinforced concrete structures over their full range of response, up to the point of failure and into the post-failure region, is still far from satisfactory. In this respect the only way of checking the reliability of a numerical simulation of a structure is to verify the prediction against reliable experimental results. Such results, that are sufficiently well-documented for this purpose, are rare. In addition, if a general purpose program is desired, it is necessary that the analytical program yield reliable results for all of the different types failure mechanisms which have the potential to occur. The program should then be checked against experimental results which span the spectrum of all relevant failure mechanisms.

Reinforced concrete structures can fail in a large number of modes. Some of these are ductile, such as, flexural failure for under-reinforced beams and slabs. Others are 'brittle', such as, flexural failures for over-reinforced beams, punching shear failures of slabs, and shear failure of beams without web reinforcement. The type of failure, and consequently its characteristics, may be changed by altering the nature and distribution of the reinforcement, such as, placing web reinforcement in, or increasing the flexural reinforcement of, a beam. By including the effect of cracking, incorporating the reinforcement into the model, and modifying the continuum properties of the concrete depending upon the nature of the confinement, current analytical techniques are sufficient to predict some of these transitions between failure modes (Balakrishnan and Murray, 1989). Yet a rational method for including the complexities of concrete stress-strain response, cracking, steel-concrete interface behavior, and confinement, for the prediction of macroscopic behavior, in such a way that reliable results can be achieved, is lacking.

1.2 Cracking and Failure

A macroscopic failure mechanism in a reinforced concrete structure is developed as a result of concrete cracking or crushing, or some combination of these effects, usually involving progressive deterioration and often complex interaction between the reinforcement and the concrete. Final failure often involves rupture of the reinforcement. Since effective development of stress in the reinforcement cannot occur until after concrete cracking, cracking is an important factor in most failure mechanisms.

In structures of plain concrete, or for which the reinforcement is widely spaced, a single 'dominant crack' may be the primary cause of failure (e.g.- for structures of mass concrete, beams without web reinforcement or punching shear failures in slabs). In such cases a 'discrete' crack approach, which models the fracture of concrete in association with the dominant crack may capture the essential aspects of behavior. Techniques of discrete crack analysis to model such behavior have been developed based on fracture mechanics (Ingraffea and Saouma, 1985) and tested for a limited range of applications.

However, for structures with closely spaced (i.e. distributed) reinforcement a multitude of cracks may occur and cracking is often distributed over a significant portion of the structure prior to collapse. For such a structure it is generally undesirable and not feasible to attempt to trace the progress of each crack as a discrete crack and the general approach has been to modify the continuum constitutive properties for the concrete in an attempt to reflect the influence of cracking on 'averaged' stress-strain response. This 'smeared' cracking approach has been widely used, but the constitutive properties have often been determined in an ad-hoc manner which has led to considerable criticism of the overall approach.

If the smeared cracking approach is to be placed on a firm foundation, rational methods of determining the effective continuum properties must be found. Furthermore, a proper smeared simulation should be able to adequately represent behavior incorporating the spacing of cracks, the interface behavior between steel and concrete, and the effect of confinement produced by the reinforcement. No method currently exists which does this.

1.3 Levels of Analysis

If the heterogeneous nature of concrete is considered it is apparent that a model which adequately simulates local behavior is impractical for the analysis of a major structure. It, therefore, appears that a useful approach would be to adopt the concept of a system of hierarchical structural levels, from the concrete materials disciplines (Whittmann, 1983), to the problem of analytical modeling. This is particularly appropriate in view of the fact that all analyses to determine failure and failure mechanisms are nonlinear in nature.

One such classification of hierarchical levels for analytical purposes is illustrated in Fig. 1.1. To determine the proper response of a mesolevel element as input, to a macrolevel analysis, the element can be modeled on the microlevel. If cracking, interface behavior, and local crushing can be determined for the microlevel model, and properly assimilated to produce smeared properties which are appropriate for the mesolevel element, a reliable mesolevel analysis might be carried out without following in detail the events occurring at the microlevel. This study is an attempt to contribute to such approach.

1.4 Objectives and Scopes

The objectives of this study are:

1. To develop a systematic and automated approach for the finite element analysis of distributed discrete concrete cracking.

This approach includes the following features:

- Production, in a 'data preparation phase', of a topological data base which can represent explicitly and exhaustively the adjacency of the topological entities (vertices, edges, etc.) abstracted from the finite element mesh as input.

- Discrete crack automatic initiation and propagation along element boundaries created by referring to and modifying the topological data base.
- Constitutive relationships at discrete crack faces which are built on the softening response of cracked concrete associated with the tensile fracture energy.
- Solution strategy which switches from displacement control to fracture energy control as crack instability arises.

2. To apply the approach to the numerical simulation of "tension-pull" tests. By explicitly modeling the lugs on the surface of reinforcing bars in the finite element analyses, at the microlevel described in Sect. 1.3, discrete concrete cracking, longitudinal splitting concrete cracking, interface behavior and local crushing are identified and investigated through the complete loading history.

3. To evaluate bond stresses and bond slip on the surface of reinforcing bars of "tension-pull" tests.

Finite element solution of the above problem types is achieved by considering inelastic behavior caused by the progressive propagation of cracks and plastic yielding of concrete and steel. An incremental iterative formulation of equilibrium is adopted. Time-dependent, dynamic and bifurcation behavior are not considered.

Displacements are assumed to be small. The undeformed state is considered to be the initial configuration for the following equilibrium configurations. That is, geometry is not updated.

1.5 Outline of Report

A brief review of approaches to simulate concrete cracks in finite element analysis is presented in Chapter 2. A review of selected references on the investigation of bond is also included in the chapter.

In Chapter 3, the strategy for the formation of a new topological database, from finite element input, is described and illustrated by its application to a sample patch of a finite element mesh.

Chapter 4 presents discrete crack initiation criteria for concrete, and concrete-steel interfaces, and the procedure to trace crack growth. Systematic activation and deactivation of "nodal splitting numbers" simulates crack propagation by referring to and modifying the topological database.

The constitutive relations at crack faces are expressed in terms of the relative displacement of the coupled crack faces, called the crack width, and the associated nodal forces on the crack faces. The signs and magnitudes of the stiffness of these relations depend on the crack situation (open or closed cracks), the crack width, and the length of element adjacent to the crack faces. The approach to estimate this stiffness from known crack width-tensile stress curves forms the content of Chapter 5.

The solution strategies, which include displacement control, crack width control and control based on the criterion of fracture energy, are presented in Chapter 6.

In Chapter 7, the approaches described in the previous chapters are applied to four examples, with emphasis on the simulation of "tension-pull" tests. The finite element model explicitly includes the lugs as solid elements and identifies cracking, interface behavior and local crushing. Bond stresses and bond slip are evaluated at intervals referenced to lugs on the surface of the reinforcing bar.

Levels of Analysis **Characteristics**

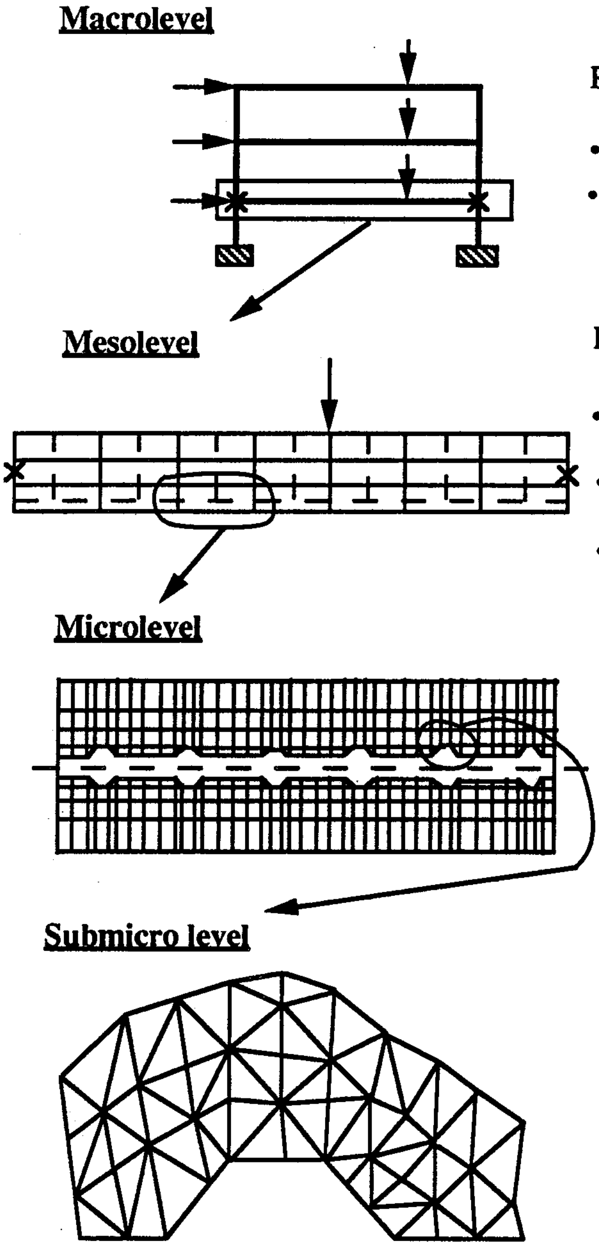

Macrolevel

Region = an assemblage of members
- one dimensional elements
- deformation described in terms of joint displacements

Mesolevel

Region = a member or joint assemblage
- two or three dimensional concrete elements
- discrete or smeared modeling of reinforcement
- smeared modeling of cracking

Microlevel

Region = an element used in a mesolevel model
- concrete and steel separated into subregions
- discrete crack and interface behavior included

Submicro level

Region = a subregion of a microlevel model
- concrete and steel separated into subregions
- discrete cracks, stress concentrations and fracture propagations included
- inhomogeneity may be included

Figure 1.1: Possible Hierarchy of Analytical Models

CHAPTER 2

LITERATURE REVIEW

2.1 Introduction

Knowledge of the fundamental mechanics of reinforced concrete, such as concrete cracking and bond, is essential if the development and application of nonlinear finite element analysis of reinforced concrete is to progress. This knowledge is obtained by thoroughly searching previous studies, or by carrying out tests if the information required is not available.

When the physical nature of the mechanics is basically understood, the next step is to find approaches which model this mechanics in finite element analyses. In this modelling process, compromise must be made between the capture of the detailed nature of the mechanisms and the mathematical model implemented in the finite element coding.

In this chapter, selective review of concrete cracking and bond are presented in Sect. 2.2 and 2.3 respectively. Each is reviewed by discussing its essential nature first, followed by its finite element modeling.

2.2 Concrete Cracks

2.2.1 Characteristics of Concrete Cracks

There are three characteristics of concrete cracks which distinguish them from cracks which occur in the other types of materials (Hillerborg, 1985).

The first characteristics is the long and narrow fracture process zone which exists for concrete cracks. The term 'fracture process zone' was defined originally in fracture mechanics as "a small region surrounding the crack where fracture develops through the successive stages of inhomogeneous slip, void growth and coalescence, and bond breaking on the atomic scale" (Kåre Hellan, 1984). The concrete fracture process zone is found "in front of a growing crack to be of the order of 100-200 mm or even longer" (Hillerborg, 1985). This concrete fracture process zone has a width about the aggregate size and consists of discontinuous microcracks (Mindess and Diamond, 1980; Cedolin et al., 1983). The damage due to microcracks along the concrete fracture process zones does not cause appreciable lateral deformation, as in the case of ductile fracture of metal where yielding produces a necking zone whose size depends on the the geometry of the specimen (Hillerborg,1985).

The linear fracture mechanics, or the K_{Ic} approach in which K_{Ic} is the fracture toughness (Broek, 1986), is "valid if the size of the process zone is small compared to the size of the area in which the singular term in the theoretical stress distribution is the dominant contribution to the stress field" (Ingraffea and Saouma, 1985).

The second characteristic for concrete cracks is that linear fracture mechanics is assumed not to be applicable to concrete because of the large size of its process zone, except for massive concrete structures such as dams, where the size of the fracture process zone is negligible compared to the size of the structure. (Ingraffea and Saouma, 1985; Hillerborg,1985).

The third characteristic of a concrete crack is its post-cracking softening. Tests (Evans and Marathe, 1968; Cantalano and Ingraffea, 1981; Petersson, 1981) show that "cracked concrete does indeed resist tension. The extent of resistance depends inversely on the average crack width" (Gopalaratnam and Shah, 1985). The σ-W curve, representing the relationship between the tensile stresses carried over a crack and the associated crack width, is claimed to be a material property (Hillerborg, 1985).

Ingreffea and Saouma (1985) have discussed the reasons why stress singularity terms are not required for the solution of crack propagation problem in concrete materials. Because "the singular stress term has little to do with stress at the tip of the crack" (Ingreffea and Saouma, 1985), singular elements or fine mesh layouts at crack tip are not necessary for modelling of concrete cracking. The modelling of post-cracking softening, however, becomes essential. The mechanism for tensile stress across a 'crack' is not yet fully understood. Gopalaratnam and Shah(1985) state:

> "The observed post-cracking resistance of concrete in direct tension may be due to discontinuities in cracking at the submicroscopic level and to bridging of cracked surfaces by aggregates and fibrous crystals."

2.2.2 Discussions of the Results of the Tests of Gopalaratnam and Shah (1985)

Some details and the results of the tests conducted by Gopalaratnam and Shah (1985) are given in Table 2.1. The terms marked σ_p in the table represent the peak tensile stresses recorded in the tests, and the terms marked G_F represent the fracture energy densities which were "calculated from the area under the net stress versus average displacement relationship" (Gopalaratnam and Shah, 1985) as shown in Fig. 2.1.

The coefficients of variation of G_F and σ_p for the four mixes of concretes listed in Table 2.1 are calculated in this study to be 16.2% and 19% respectively. For every mix, the quotient of G_F and σ_p, $W_c = 2G_F/\sigma_p$, is also calculated as shown in Table 2.1. The coefficient of variation for W_c of these concrete materials is only 4.16% which represents the ratio of the spread in the W_c's to their mean of 0.001286 in..

It seems to be indicated from the analysis of these test results that W_c can be estimated to be a constant of 0.001286 in. for different concrete materials with much less error than for fracture energy densities of the different concrete materials. Therefore, the fracture energy density of concrete can be calculated from the product of a constant W_c and the given tensile strength f_t'. Or f_t' can be calculated from the quotient of the given G_F and constant W_c.

This tendency of constant W_c is more apparent in the test results obtained from the three mixes of mortar shown in Table 2.1. The coefficients of variation of G_F and σ_p are 10.46% and 11.67%, respectively, while that of W_c is only 1.22%. This represents the magnitude of the spread of the W_c values to their mean value of 0.00202 in..

The correlation between σ_p and G_F described in the previous paragraph, for test data of concrete and mortar shown in Table 2.1, is illustrated as shown in Fig. 2.2. The two straight lines which have slopes of $(2/W_c)$ for the W_c's of the concrete and mortar data, respectively, indicate an excellent fit with the test data.

2.2.3 Discrete and Smeared Cracking Models

2.2.3.1 Introduction

Concrete cracking has "a major influence on the basic behavior of the (concrete) member" (Cedolin et al.,1982). "Failure of reinforced and prestressed concrete structures is initiated in many instances by cracking of plain concrete" (Gopalaratnam and Shah, 1985). Over the past 24 years, a number of models have been developed to simulate concrete cracking in finite element analyses. Each model "is composed of a suitable combination of three basic components; an initiation determination, a method of crack representation, and a criterion for crack propagation" (Cedolin et al.,1982).

The crack representations fall into two basic approaches: discrete cracking and smeared cracking. A description in chronological order for the approaches to discrete cracking is given in Sect. 2.2.3.2. The comparison between the discrete crack and smeared crack approaches is presented in Sect. 2.2.3.3.

2.2.3.2 Discrete Cracks

The first finite element analysis for reinforced concrete structures to model the effect of cracking was carried out by the discrete crack approach (Ngo and Scordelis, 1967). In this analysis, a particular crack configuration was activated by the separation of nodal points along a predefined crack path which coincided with some element boundaries. Link elements, called lumped stiffness elements, were introduced across cracks to simulate aggregate interlock (Ngo et al., 1970). The analysis was linear elastic, and linear interpolation elements were used.

A modification of this approach was made (Nilson, 1968) to allow finite elements to generate the location of the crack by disconnecting two elements along their common edge. "After each crack forms, the structure is unloaded, and the newly defined structure is reloaded" (Cedolin, et. al., 1982). To allow path independence on reloading, the compression zone behavior must remain linear.

This modified version was further improved and partially automated (Mufti, et al., 1970 and 1972; Al-Mahaidi, 1979) by incorporating a predefined crack utilizing two nodes at one nodal point connected by a linkage element. "When the stress in the elements exceeds the cracking strength of the concrete, the linkage element is softened to allow the crack to open" (Cedolin, et al., 1982).

A novel approach was proposed by Ngo and Scordelis (1975) in which graph theory was applied to treat the adjacency of elements as networks. In this approach new nodes are added to the element mesh only when new cracks were initiated and detected as gaps in the 'dual graph' for the cracked element mesh. Compared with the approach in which all nodes located on the possible crack path are doubled and connected by linkage elements, this approach is economical. The Frontal Solution Method (Irons, 1970) was implemented in the approach, "thus alleviating the constraint in the node numbering normally required in most banded type of solution schemes" (Ngo and Scordelis,1975). Because compression failure was not considered in the approach, and linear elastic response is assumed throughout the whole analysis, post peak descending behavior of a simple modulus of rupture test was simulated by "scaling the stress intensity" (Ngo and Scordelis, 1975).

"An algorithm has been developed which automatically remeshes in the vicinity of a crack to accommodate arbitrary, predicted trajectory" (Ingraffea and Saouma, 1985). In this approach, fracture mechanics was extensively applied. Two fracture models, the linear and nonlinear models, were implemented in the approach.

The linear model is based on classical, linear elastic fracture mechanics (LEFM). In the model, quarter-point singular elements (Shih, et al., 1976) are automatically installed at a newly created crack-tip. The stress intensity factors for pure Mode I, K_I, and Mode II, K_{II}, derived from the displacements at crack-tip, are used to determine initiation, orientation and stability of new cracks. The formulations may also be based upon one of two mixed-mode fracture initiation theories, namely, the theory of maximum circumferential tensile stress near the crack tip, $(\sigma_\theta)_{max}$, or, the theory of strain energy density near crack tip (Erdogan and Sih, 1963; Sih, 1974).

In the solution strategy of Ingraffea and Saouma's approach, either the increment of load or increment of crack length can be specified as the control factor. When the length of a crack is selected as control factor, the load at step i+1, P_{i+1}, is obtained from the load at step i, P_i, is

$$P_{i+1}=\left(\frac{K_{Ic}}{K_{I_{i+1}}}\right) P_i \qquad (2.2.1)$$

in which $K_{I_{i+1}}$ is the stress intensity factor K_I calculated from load P_i, crack length a_i and specified crack length increment Δa at step i+1. Expression (2.2.1) may be explained by the strategy of keeping the stress intensity factor K_I equal to K_{Ic}, or keeping the fracture energy (in the sense of LEFM) equal to the critical energy of crack initiation, through adjusting the external load level. This expression seems applicable only to a single dominant crack.

The nonlinear model of Ingraffea and Saouma (1985) is an outgrowth of the linear model. Most features for the linear model are still maintained in the nonlinear model such as the automatic placement of quarter-point singular elements at the crack-tip and the determination of orientation of new cracks from stress intensity factors, K_I and K_{II}. In the nonlinear model, post-cracking tension softening is implemented at the crack faces through the use of interface elements. Similar to the Dugdale approach (Dugdale, 1960) shown in Fig. 2.3, the crack faces carry post-cracking tension, "tending to close the crack. The size of (the cracked faces) is chosen such that the stress singularity disappears: K_I should be zero." (Broek, 1986). In incremental iteration, a new crack is initiated when K_I and/or K_{II} become greater than zero. This crack initiation criteria is in contrast to that for the linear model in which a crack initiates when the crack toughness, K_{Ic}, which is usually much greater than zero, is exceeded. Expression (2.2.1) seems not to be applicable to the nonlinear model, and user's specification of both the increments of crack length and load seems to be required in a highly iterative manner.

2.2.3.3 Smeared versus Discrete Approach

The smeared cracking model, first introduced by Rashid (1968), represents cracked concrete as an orthotropic continuum. "It is sufficient to switch from initial isotropic stress-strain law to an orthotropic law upon crack formation, with the axes of orthotropy being determined according to a condition of crack initiation" (Rots and Blaauwendraad, 1989). The smeared approach has prevailed in finite element analysis of reinforced concrete since 1970's. The popular applications of the smeared model are attributed mainly to two computational conveniences: " (1) automatic generation of cracks without the redefinition of the finite element topology and (2) complete generality in possible crack direction" (Cedolin, et al., 1982). This approach is also claimed to be the "only rational approach" to "diffuse crack pattern in large-scale shear wall or panels due to the presence of densely distributed reinforcement" (Rots and Blaauwendraad, 1989).

In spite of all the conveniences and widespread use of the smeared approach, there is no consensus as to its superiority relative to the discrete approach. A concrete crack is considered to be a "geometrical discontinuity that separates the (concrete) material" (Rots and Blaauwendraad, 1989). The smeared crack concept, for which the cracked concrete is represented as a continuum, conflicts with the discontinuous nature of cracks. On the other hand, discrete cracks, which are represented as displacement discontinuities, coincide with the nature of cracks. This coincidence, as described in the following, provides advantages in the finite element analyses of reinforced concrete structures. "For those problems that involve a few dominant cracks, it offers a more realistic representation of those cracks ..." (Cedolin, et al., 1982). Aggregate interlock, dowel action, post cracking softening and bond effects can be represented naturally with the discrete model, through the use of associated linkage elements which connect two crack faces and control the behavior of the crack as its two faces undergo relative displacements.

2.2.4 Comments Relative to this Study

The discrete crack representation is chosen for the microlevel model developed in this study. This model shares some common features with the previous studies. These features include discrete cracks along predefined element boundaries (Ngo,1975), implementation of post-cracking softening (Hillerborg, 1985; Ingraffea and Saouma, 1985) and explicit topological data base (Ingraffea and Saouma, 1985).

The characteristics of this model are as follows. In terms of topology, the data structure developed by Wawrzynek and Ingraffea (1987) is edge-based as shown in Fig. 2.4. The comment made by

Wawrzynek and Ingraffea (1986) on the three types of topological data structures, edge-based, face-based and vertex-based, are quoted below:

> "The data structure is designed so that most adjacency queries are edge-based. This is because we know a priori the multiplicity of an edge's adjacent elements. An edge has two adjacent vertices, two adjacent faces, and four adjacent edges (Fig. 2.3). It would be more difficult to design a data structure which has vertex or face based queries because one cannot know a priori the multiplicity of the adjacent topological elements for a face or a vertex."

The data structure developed in this study is vertex-based as shown in Fig. 3.4.

Ingraffea and Saouma (1985) developed an incremental iterative approach in which a crack length control is used for the solution of one single discrete crack in the category of linear elastic fracture mechanics (LEFM) as described in Sect. 2.2.3.2. In this study, a fracture energy control is developed for the incremental iterative solution of multiple discrete cracks in the category of nonlinear fracture mechanics.

2.3 Bond Stress and Bond Slip

2.3.1 Introduction

The previous studies on bond and slip (Mains, 1951; Lutz and Gergely, 1967; Nilson, 1968; Mirza and Houde, 1979) were carried out mainly through tests. They can be classified into two categories: the investigation of fundamental mechanisms of bond and the formulation of the relationship between basic variables related to bond and slip. These two categories are selectively reviewed in Sect. 2.3.2 and 2.3.3, respectively. The review of finite element models for bond and slip is presented in Sect. 2.3.4.

2.3.2 Mechanics of Bond and Slip

Bond stress may be defined as the "unit shearing force parallel to the bar axis on the steel-concrete interface" (Houde, 1973). Bond is considered to be made up of three components, namely, chemical adhesion, friction and mechanical interaction between concrete and steel.

Bond on plain bars which have no deformations, or lugs, on their surfaces depends primarily on chemical adhesion and friction.

Bond on deformed bars depends primarily on mechanical interlocking. "Initially, chemical adhesion combined with mechanical interaction prevents slip. After adhesion is destroyed, and slip occurs, the ribs of a bar restrain this movement by bearing against the concrete between the ribs" (Lutz and Gergely, 1967). Houde (1973) stated that

> "The bearing pressure developed at the lug interface can be resolved into two components ... : one parallel to the bar tending to shear a cylinder of concrete, concentric with the bar deformation, and a radial component which tends to split the concrete. If the bearing pressure at the bar lugs is large, it can cause local crushing of the concrete. Experimental evidence to date indicates that in unrestrained pull-out test (without restraining steel in the form of ties or spiral), bond failures always occurred by splitting of concrete, and very rarely due to shearing or crushing of the surrounding concrete."

It has been suggested (Lutz and Gergely, 1967) that the chemical adhesive strength can be estimated from adhesion tests of nonreactive aggregates to mortar. Tensile bond tests (Hsu and Slate, 1963) yielded 150 to 300 psi of adhesive strength for 'saturated surfaced dry' specimens and about 50 psi for 'air dried' specimens. Shear tests (Taylor and Broms, 1964) yielded 280 to 600 psi of adhesive strength. "From these results it appears much more likely that adhesion will be lost in tension rather than in shear." (Lutz and Gergely, 1967)

2.3.3 Relationships between Variables Related to Bond

2.3.3.1 Crack Spacing

Broms (1965) showed that the measured average crack spacing S_{ave} obtained from the tests of tension members reinforced with a single bar was about twice the thickness of the concrete cover, t, as expressed by the equation:

$$S_{ave} = 2t \tag{2.3.1}$$

The scatter of crack spacings from S_{ave} is expected to be from 33% (Hognestad, 1963; Broms, 1965) to 50% (Houde, 1973).

2.3.3.2 Bond Slip and Bond Stress

Nilson (1968) fitted the following third degree polynomial to the data obtained from his tests:

$$u = 3.606 \times 10^6 d - 5.356 \times 10^9 d^2 + 1.986 \times 10^{12} d^3 \qquad (2.3.2)$$

in which u is the nominal bond stress in psi and d is the local bond slip in inches. Based on the test data obtained from an improved technique of measurement, Nilson (1971) proposed the following bond stress-slip relationship:

$$u = 3{,}100 \times (1.43c + 1.50) \times d \times f_c' \qquad (2.3.3)$$

in which the bond stress $u < (1.43c + 1.50) \times f_c'$, c is the distance in inches from the loaded end of the bar, f_c' is the concrete strength in psi, and d is the slip in inches.

Equation (2.3.3) indicates that the slope of u to d, increases as the distance from loaded end, c, increases.

The influence of the steel stress and the section geometry, represented by the reinforcing ratio A_s/A_c, in which A_s and A_c are the cross sectional areas of reinforcing bar and concrete, on the average slip at the loaded end of the bar have been evaluated through tests (Mirza and Houde, 1979) as shown in Fig. 2.5. The slip may be expressed by an equation of the form:

$$d = k_1 f_s^{k_2} (A_c/A_s)^{k_3} \qquad (2.3.4)$$

in which the value of the slip is in 10^{-4} in., and the steel stress f_s is expressed in ksi. The coefficients, k_2 and k_3 are 1.0 and 0.33, respectively. The value of k_1 ranges from 0.18 to 0.22 $\times 10^{-4}$ in/ksi as the steel stress levels vary.

The tendency that slip increases with an increase in the dimension of the cross section is only valid to a certain size. After the size is exceeded, the slip decreases as shown in Fig. 2.5.

2.3.4 Finite Element Implementation

"The link element was first published by Ngo and Scordelis (1967) to simulate the effect of bonding and bond slip.... The basic concept is to derive an element whose stiffness characteristic is independent of its physical dimensions such as cross-sectional area and length." (Ngo, 1975)

"Following the same basic concept of the link element, Goodman, Taylor and Brekke (1968) later developed a joint element which assumes the shape of a line instead of a point...." (Ngo, 1975). Ngo introduced a 'bond element' as a special kind of joint element into his approach of finite element analyses. The spring constant assigned to the 'bond element' is on the basis of the shear force per unit length.

The finite element approaches to bond have not changed much from the early approach (Ngo, 1975). The two types of element, link element (or lumped interface element) and joint element (or continuous interface element), are still used. However, the determination of the stiffness constants (lumped or continuous) has been updated by the experimental investigations of bond, such as that described in Sect. 2.3.3.

2.3.5 Comments Relative to this Study

As discussed in Sect. 2.2.3.3, the discrete crack model offers a more realistic representation for detailed local behavior of reinforced concrete, such as the bond effect. In this study, deformations on the surfaces of bars are explicitly modeled so that the behavior of deformed bars can be reflected on a rational basis. Strength and crack initiation criteria for concrete and concrete-steel interfaces are specified separately. Bond stress and bond slip are evaluated at the interface of concrete and steel.

Concrete cracking, in the plane which coincides with the axis of a reinforcing bar, is represented by discrete cracks. The longitudinal splitting cracking modelled by modifying the axisymmetrical formulation to a plane stress formulation.

To reflect the local crushing caused by the bearing pressure at lugs, Von Mises plastic model (Chen, 1982), has been used. Because local crushing, which occurs at concrete-steel interfaces where two different materials are in contact, is associated with in plane and longitudinal splitting cracking, the effects of hardening due to hydrostatic compression are assumed not to be important. This is the the reason for that the relatively simple Von Mises plastic model, rather than more complicated models, is selected.

Link elements are used to represent behavior of discrete concrete cracking (opening or closing) and cracking at the concrete-steel interface.

Table 2.1: Material Properties of the Test Mixes

Materials	Series *	Mix proportions (by weight) cement:sand: aggregate:water *	age, days *	σ_p psi *	$\bar{x}$ of σ_p psi	$\bar{\sigma}_x$ of σ_p %	G_F lb/in. *	$\bar{x}$ of G_F lb/in.	$\bar{\sigma}_x$ of G_F %	$W_c = 2G_F/\sigma_p$ 10^{-3}in.	$\bar{x}$ of W_c 10^{-3}in.	$\bar{\sigma}_x$ of W_c %
Concrete	C1	1:2:2:0.45	28	525	459.75	19	0.322	0.294	16.2	1.2267	1.286	4.16
	C2	1:2:2:0.60	28	439			0.297			1.3531		
	C3	1:2:2:0.60	3	326			0.216			1.3251		
	C4	1:2:2:0.45	28	549			0.341			1.2422		
Mortar	M1	1:2:0:0.40	28	540	472	11.67	0.537	0.476	10.46	1.9889	2.02	1.22
	M2	1:2:0:0.45	28	471			0.476			2.0212		
	M3	1:2:0:0.50	28	405			0.415			2.0493		
Paste	P1	1:0.5:0:0.35	28	471			0.404			1.7155		

* adapted from Gopalaratnam and Shah (1985)

$\bar{x}$, $\bar{\sigma}_X$: mean and coefficient of variation calculated in this study

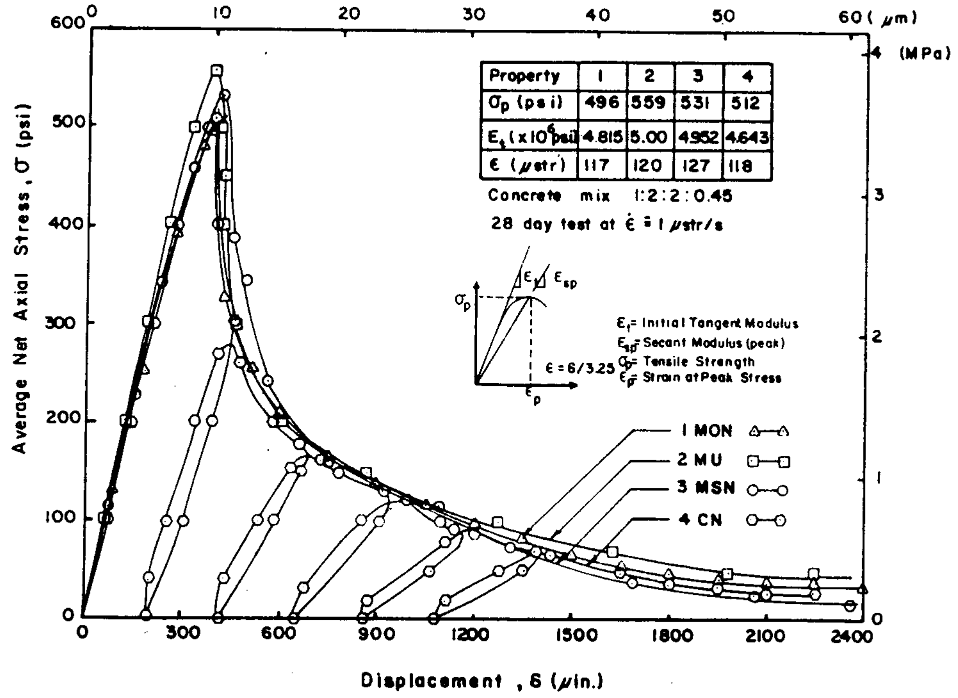

Figure 2.1: σ – δ Curves from Tests Performed on A Concrete Mix (Adapted from Gopalaratnam and Shah)

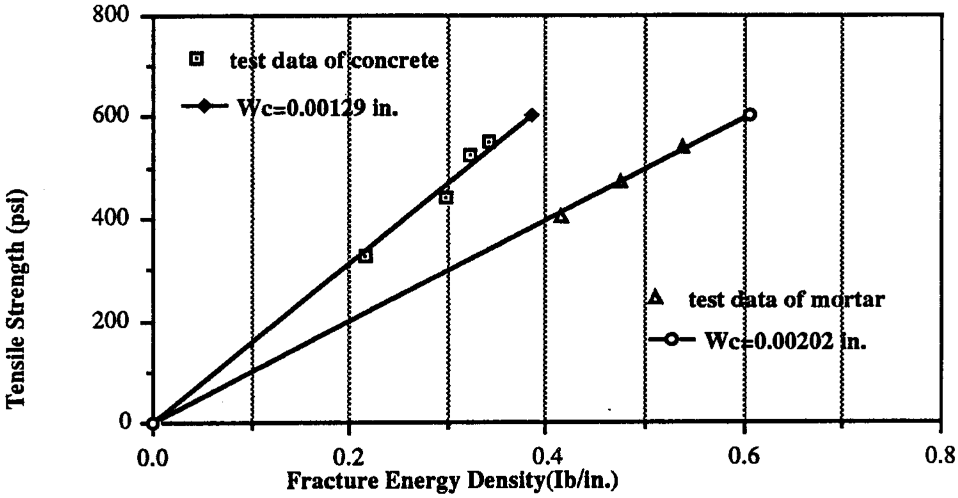

Figure 2.2 Correlation between Tensile Strength and Fracture Energy Density

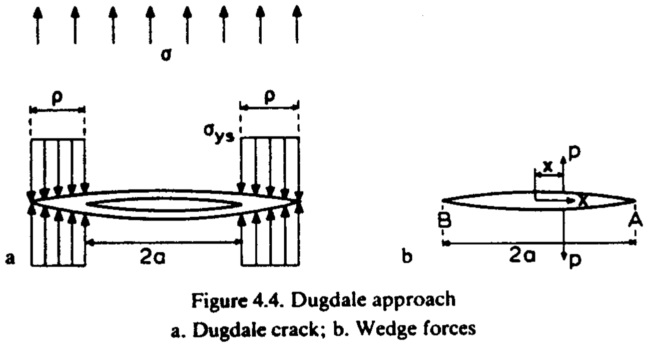

a. Dugdale crack b. Wedge forces

Fig. 2.3 Dugdal Approach (Adapted from Broek)

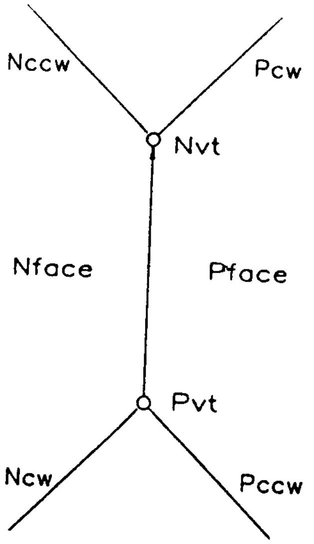

Figure 2.4 The Local Topology for An Edge Based Data Structure
(Adapted from Wawrzynek and Ingrafea)

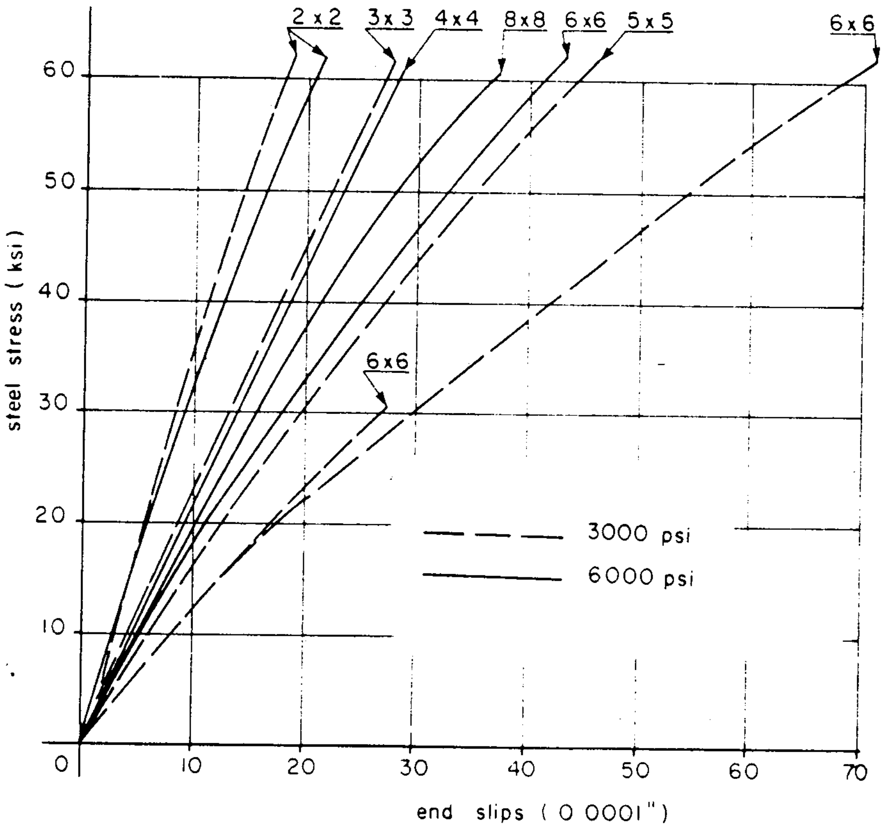

Figure 2.5: Effect of Cover and Concrete Strength on Slip
(Adapted from Mirza and Houde)

CHAPTER 3

FORMATION OF TOPOLOGICAL DATABASE FROM FINITE ELEMENT INPUT

3.1 Introduction

In the analysis of concrete for discrete cracking, the creation of a crack requires that the material points immediately adjacent to one side of the crack have different displacements than the material points immediately adjacent to the other side of the crack. In a finite element analysis, in which the displacements of material points are expressed by interpolating displacements occurring at a discrete set of 'nodal' points, this 'split' requires that additional nodes be introduced in order to represent the discontinuity of displacements across the crack.

The splitting phenomenon is illustrated in Fig. 3.1. In Fig. 3.1a, the displacements may be expressed as continuous functions over the entire region in terms of the displacements of the 9 nodes (A, B, M, C, D, E, N, F and K) by interpolation over the 8 'element' subregions (1-8). If a crack were to occur along line MKN, an additional node, L, must be introduced, as illustrated in Fig. 3.1b, in order to describe the displacements. The original node K will be said to be 'split' into two nodes, designated as L and K. The result is that the number of nodes defining the problem, and the nodal numbers defining the elements must be modified. To keep track of such information in a systematic way, such that it properly reflects the definition of the elements and the change in the stiffness characteristics of the structure, is a formidable task.

The rapid developments in computer graphics (Mäntylä,1988) have led to a definition of a number of different types of data structures for the efficient handling of such systems. Wawrzynek and Ingraffea (1987) and Martha and Ingraffea (1989) have devised advanced flexible data structures for efficient handling of the topology of discrete cracking for two and three dimensional problems respectively, in interactive graphical computer environments. However, one conclusion from that work is that, "Because this type of data management system is so central to a program architecture, programs that were not originally designed to use high-level calls to a data management system cannot be easily converted" (Wawrzynek and Ingraffea, 1987).

The strategy for handling discrete cracking developed herein was designed prior to a knowledge of these systems and to be incorporated into the existing nonlinear finite element program called NORCO (Balaknishnan and Murray, 1989). The primary motivation was to study the effect of cracking, with a view to determining appropriate properties for smeared cracking models, rather than to produce a program for efficient analysis of discrete cracking as a desirable general purpose approach to nonlinear analysis. Consequently, its efficiency may not be competitive with those strategies made possible by specially designed data structures.

Nevertheless, it appears appropriate to present the strategy developed herein using the terminology associated with recent developments in data structures. Section 3.2 introduces this terminology, which is then used throughout the remainder of the work.

One of the reasons that it was necessary to develop the radically different data structures, contained in the works cited above, was the desire to solve fracture mechanics problems. These problems are generally dominated by a single crack, as discussed in Sect. 1.2. For such problems the crack trajectory is unknown a priori, and 'remeshing', with the associated complexities of reorienting element boundaries and translating nodal points, arises. However, for the purposes of the work presented herein, associated with multiple small discrete cracks, it is assumed that the analyst has a priori knowledge of probable crack orientation and that he can incorporate this into his original mesh layout. Consequently, the strategy to be presented confines the topological treatment of the problem to cracking along predefined element boundaries.

3.2 Some Topological Terminology and Definitions

There are many definitions for topology. The one given is quoted from Weiler (Weiler,1986):

"Topology, by definition, is an abstraction, a coherent subset, of the information available from the geometry of a shape. More formally, it is a set of properties invariant under a specified set of geometric transformations. Invariance of these properties under transformation implies by definition that the properties represented by the topology do not include the set of information which is actually changed by such transformations." Topology "can theoretically be derived from the complete geometric specifications", and "support a meaningful view of the whole".

In two-dimensional finite element analysis, the input consists of three types of information, namely geometrical information, topological information and material information.

Geometrical information consists of the global coordinates of the nodes.

Topological information consists of the global nodal numbers of the individual elements. Usually these global nodal numbers are given in prescribed sequence of corresponding local nodal numbers. Thus a local-global node correspondence is indicated by the order in which the element global nodes are input.

Material information consists of the parameters describing the physical properties of the materials of the elements.

When automated initiation and propagation of discrete cracks are introduced in finite element analysis, frequent changes occur in the topology of the structure being analyzed. This requires a robust topological data structure which supplies explicit topological adjacency relationships between "topological elements". The seven topological elements that are related to this study are: vertex, edge, face, graph, loop, edgeuse and vertexuse.

The definitions of vertex, edge, face, graph and loop, as given by Wawrzynek and Ingraffea (1987), are as follows.

"A vertex is a point in space; in the planar case, a point in the plane in which the mesh construction will take place. In the discussion to follow, a vertex is isomorphic to a node in the finite element sense and the terms will be used interchangeably."

"An edge is a set of two vertices. The edges discussed here will be directed edges, edge points from one vertex to the other. The finite element analogy to the edge is a portion of an element boundary that connects two adjacent elements. In general, an edge will be shared by two elements, except along a structural boundary where the edges are adjacent to only one element."

As is illustrated in the following sections, the topological database developed in this work is 'vertex based.' So the definition of the direction of an edge depends on which of the two vertices of the edge is referenced. Whereas in the 'edge based' database, the direction of one edge is not changed once it is defined.

"A graph is a set of vertices and distinct edges that utilize the vertices. Distinct edges mean that at most one edge joins any two vertices."

For the purposes of this work, the term graph may be confined to refer to the set of all vertices and distinct edges in a mesh.

"If we embed a graph on a surface, a face is a polygon on the surface bounded on all sides by edges and vertices of the graph."

In the two dimensional finite element work herein, a face does not have internal vertices or edges. Hence a "face" is identical to a single solid element.

"A loop is a connected boundary of a single face."

Weiler (Weiler, 1986) gave the definitions of "edgeuse" and "vertexuse" for three dimensional modeling. Similar definitions for two dimensional finite element analysis are adopted in this study.

"An edgeuse is an oriented boundary curve segment on a loop ...."

"A vertexuse is a structure representing the adjacency use of a vertex by an edge as an edge point ...."

In the next section, a simple example is given to show the meaning of these definitions.

3.3 A Simple Example

Figure 3.2 shows a mesh with 9 solid elements and 16 nodes. The bold line 9-10-11-12 represents reinforcement elements. So the total number of elements is 12.

According to the definitions of topological elements given in Sect. 3.2, there are 16 vertices (or nodes), 9 faces (or elements) and 24 distinct edges.

Edge 6-7 has two edgeuses: one is on loop 2-3-7-6 and another one is on loop 6-7-11-10. As used by Weiler (1986) edge 6-7 is called the "owneredge" of its two edgeuses. Vertex 6 has one 'vertexuse' for each 'edgeuse' which is associated with an edge emanating from it. Because four edges are incident to vertex 6, and each edge has two edgeuses, there are eight vertexuses for vertex 6.

As edge 1-2 is located on the boundary of the mesh, it only has one edgeuse. Similarly vertex 2 only has four vertexuses instead of eight.

One special case is that the reinforcement is embedded in the boundaries of 2 elements. If truss element 9-10 is considered as a special case of a loop; that is an open loop, then edge 9-10 has three edgeuses: two from loops enclosing the solid elements and one from an open loop including the truss element. As a result, the total number of vertexuses of vertex 10 is ten.

Another special case is when an edge is located on a line of symmetry as shown by line 13-14-15-16 in Fig. 3.2. Though only one loop covers edge 13-14 in the mesh, it is considered that there are two edgeuses for edge 13-14 because another loop is implicit on the right side of line of symmetry.

3.4 Exhaustive Enumeration for Nodal Splitting

Figure 3.3a shows the mesh of Fig. 3.1a with all the discrete cracks which can emanate from node K along element boundaries. Exhaustive enumeration gives a system of nodal and crack numbering which will permit any or all of these cracks to develop during a stress analysis. The approach is based upon nodal 'splitting' in which node K is split into two nodes, as illustrated in Fig. 3.1b, when a crack passes through it. When such a split occurs it is desirable that the new node, node L of Fig. 3.1b, is numbered K+1 in order that the resulting bandwidth of the stiffness matrix be maintained, approximately, at a minimum. Therefore, an 'exhaustive enumeration' scheme is introduced, which permits the extreme case of all possible nodal splitting, and the set of sequential nodal numbers associated with node K are held in reserve to be activated or deactivated as required.

Continuing with the example of Figs 3.1 and 3.3, exhaustive enumeration produces another seven nodal numbers, K+i, in which i is in the range $1 \leq i \leq 7$, because eight edges emanate from the unsplit node K, as shown in Fig. 3.3a.

The 'split' nodal numbers increase by one each time an edge is crossed in executing a clockwise circuit around the node, commencing at $\theta = 180^{o}$, where θ is the counterclockwise angle measured from the positive X axis and $180^{o} \geq \theta \geq -180^{o}$. This results in the nodal numbering of Fig. 3.3a.

The nodal numbering for problem definition in the input file (hereinafter, called the 'input nodal number') is sequential with each node having a number one greater than the node preceding it in the input numbering sequence. During exhaustive enumeration, the 'initial nodal number' a node receives (i.e.- K in the example of Fig. 3.3) is one greater than the maximum split node number of the previous node in the input numbering sequence. That is, the initial node number for the node following node K, will be (K+7)+1=K+8. Consequently, the number of nodal numbers assigned during exhaustive enumeration is much greater than the number which is input. The newly produced list of exhaustive nodal numbers forms a basis on which all possible crack patterns can be represented.

Exhaustive nodal numbering is carried out in the 'data preparation phase' of problem solution. For the uncracked structure, only the initial nodal number (i.e.- the K number of Fig. 3.3a) at each node will be active. As an example of how the other nodal numbers are activated when a crack is formed, consider that the crack of 3.1b is introduced into the patch of Fig.3.1a. Using the exhaustive numbering of Fig. 3.3a, the resulting active nodal numbers at node K become K and K+4 as illustrated in Fig. 3.3 b. This is established by the following procedure.

When a counterclockwise circle is traced around a node, the crack edge that the circle first crosses is defined as the 'crack back' and the second edge crossed is defined as 'crack front'. In Fig. 3.3b two cracks are encountered by the counterclockwise circle b around the center node. Crack 1 initiates at the center node and terminates at node M while crack 2 initiate at the center node and terminates at node N. Starting from a crack front all the elements encountered by a counterclockwise rotation about the node are given the same nodal number until the next crack is encountered. Thus, in Fig. 3.3 the nodal number which is on the front edge of crack 1, and is associated with element 1, is assigned to elements 1, 8, 7 and 6. Similarly, the nodal number K+4, which is the number on the front edge of crack 2, associated with element 5, is assigned to elements 5, 4, 3 and 2.

Only two of the eight nodal numbers associated with initial node K become active for assembly into the stiffness matrix by this process. The other six nodal numbers remain inactive. The normal finite element program assigns degrees of freedom based on an array ID(2,NMNOD) where NMNOD equals total number of input nodes and 2 indicates that there are two degrees of freedom for every node. Degrees of freedom are assigned to a node depending upon a boundary condition code, input to the ID array, which indicates whether the degree of freedom is 'active' or 'inactive'. Similarly, after exhaustive enumeration, the degrees of freedom for the inactive nodes remain at zero and consequently are not assembled into the stiffness matrix. Therefore, no penalty in the solution is incurred by the exhaustive enumeration of nodal numbers. For the 'unsplit' node, only the initial nodal number is active and the other seven nodal numbers remain inactive.

The algorithmic procedure for carrying out systematic exhaustive enumeration is presented in Sect. 3.6.

3.5 Topological Basis for Exhaustive Enumeration

The basic ideas and application of exhaustive enumeration for nodal splitting and crack identification can be expressed in terms of the topological terminology and definitions of Sect. 3.3. In this respect every "corner" node of a finite element is considered to be a topological 'vertex'. Every element 'edge' emanating from a vertex may be identified since it is part of a loop. The 'edgeuses' for each edge may be enumerated and the sum of all 'edgeuses' for all edges emanating from the vertex gives the number of 'vertexuses' for the vertex. In the data preparation phase of the solution a topological data base is constructed to exhaustively enumerate these features.

As an example, the 'edgeuses' and 'vertexuses' associated with the center node of Fig. 3.1a, with 'initial' node number K, are illustrated in Fig. 3.4. The edgeuses of the edges emanating from node K are associated with the elements incident to node K. The boundary of each of these elements forms a 'loop', and the boundary between two elements has two edgeuses, one associated with each loop. Consequently, vertex K has 16 vertexuses, one associated with each edgeuse of each of the edges emanating from K.

In Fig. 3.4 the edgeuses for the edges emanating from node K are identified in sequence in a clockwise direction, and are drawn separately from their owneredges for the purpose of illustration. Two cases arise according to the topological relation between two edgeuses in sequence:

Case A. The current edgeuse and the previous edgeuse in the sequence do not belong to same loop. A new nodal splitting number is then introduced, and this number is assigned to the vertexuse associated with the current edgeuse. This case occurs at edgeuses with local edgeuse number 2, 4, 6, 8, 10, 12, 14 and 16. Their associated vertexuse are assigned nodal splitting number K, K+1, K+2, K+3, K+4, K+5, K+6 and K+7 respectively.

Case B. The current edgeuse and the previous edgeuse in sequence belong to same loop. No new nodal splitting number is introduced, and the vertexuse associated with the current edgeuse has the nodal splitting number of the vertexuse associated with previous edgeuse. This case occurs at edgeuses with local edgeuse number 1, 3, 5, 7, 9, 11, 13 and 15, and their associated vertexuses have nodal splitting number K+7, K, K+1, K+2, K+3, K+4, K+5 and K+6 respectively.

Based on the assumption that cracks can only form along element boundaries, Case A corresponds to a pair of splitting nodes, one on each side of a possible crack, while Case B corresponds to the corner node of a element where interior cracking is not permitted.

3.6 Procedure for Formation of Topological Data Base

3.6.1 Introduction

The description of the procedure for the formation of a topological data base to facilitate the analysis of cracking along interelement boundaries can now be undertaken. In this chapter the description is confined to the construction of the data base in the 'data preparation' phase of the problem. Modifications to this data base during the 'problem run phase' will be discussed in Chapter 4. Note that names of arrays are summarized in the section on Nomenclature, pg. xviii.

To assist in the description of the procedure, the patch shown in Fig. 3.5 will be used as an example throughout. The nodal and element numbers in Fig. 3.5a are assumed to be those from the input data, implying that numbers not shown in the patch exist elsewhere in the discretization. However, the system of sequential identification of vertex and edge numbers will be explained as if the patch were being processed independently from the remainder of the mesh.

3.6.2 Vertex Based Identification of Edges and Edgeuses

The process of identification of edges and exhaustive enumeration of nodes proceeds by sequentially processing the nodes in the sequence of their input numbering. In preparation for this the element-nodal incidence array NPELM(12,NMELM), where NMELM equals the total number of elements and 12 indicates a maximum of 12 nodes for every element, are input as given in Table 3.1 for the patch of Fig. 3.5a and processed to form the nodal-element incidences. Concentrating on node 309, which is the central node of the patch, all element-node incidences are searched to find those elements which have node 309 in their definition. When this is done, the elements in Table 3.1 are identified as incident to this node and their identities stored in a array KEMT(J,M), where J is the input nodal number. The row of nodal-element incidence, for node 309, is shown in Table 3.2. The total number of elements incident to node 309 are accumulated and stored in the array element KEMT(309,1). In this study, the maximum number of incident elements permitted is 8, as illustrated in Fig. 3.4.

In the procedure developed, herein, only 'corner' nodes will be considered as 'vertices' and the 'edges' emanating from the vertex at input node 309 will now be identified. For this purpose the parent element in nondimensional coordinates, shown in Fig. 3.6 is used to identify the local numbering pattern for the input nodes and the sides of the element. The definition of the parent element edges in terms of local nodes is shown in column (a) of Table 3.3, as the array KSID1. These local nodal numbers, which form the pattern for element-nodal incident input, permit the global nodal number of the element edges to be picked from the element-nodal incident array NMELM (Table 3.1) to form the edge array KSID for element 9 as shown in column(b) of Table 3.3. Since the process is to identify edges for element 9 which emanate from node 309, the rows of KSID are examined and if node 309 is present as the third entry rather than the first entry of a row in KSID (because 309 is a "corner" node, and element 9 has 3 nodes on its sides, node 309 cannot be present as the second entry), the nodal numbers in position 1 and 3 are interchanged to result in the KSID array shown in column (c) of Table 3.3.

The temporary array MART(I,J,K) is now constructed from KSID to contain edges emanating from node 309. The above process has identified two of these (the last two rows in column (c) of Table 3.3). However, in the exhaustive enumeration process, node 309 will be assigned a set of different nodal numbers to permit the node to be split along each edge. Therefore, a common edge between, say elements 9 and 10, must be treated as a separate edge in each element, i.e.- for each edgeuse as defined in Sect. 3.3. In a manner consistent with Weiler (1986), the edge identified in terms of input nodes may be called the 'owneredge' of its edgeuses.

Since element 9 is the first element processed in association with node 309 (see Table 3.2), the edges identified above are assigned local owneredge numbers 1 and 2, and their nodal definitions are stored in array MART, together with the element number from which they arise, as shown in the upper partition of Table 3.4. Processing the elements 10, 18 and 19, of Table 3.2, as discussed above, identifies the other edges emanating from 309 associated with all other incident elements. They are entered sequentially into MART as shown in the second, third and fourth partitions of Table 3.4. If the edges arising from these latter elements have nodes identical to those of a previously assigned owneredges, the edge is not given a new owneredge number, but this second edgeuse of a previously identified owneredge is entered, together with its element number, into the first empty column for the owneredge number. This process is made possible because the fourth column for the owneredge is assigned an element number of zero and the input nodal numbers are stored in this column to serve as an identification array for the edge. Nodal numbers in the other columns will be reassigned for nodal splitting as is described in the following but the input nodal numbers are always retained in column 4. At most, three edgeuses of an owneredge are possible: two from adjacent solid elements and one for reinforcement inserted along the edge.

Each owneredge emanating from the vertex has its local orientation, θ, defined as the angle between the emanating directions of the edge and the X axis of the global coordinates. These are computed, in the range $-180° \leq \theta \leq 180°$, and stored in the ANG (8) as shown in the bottom row of Table 3.4.

3.6.3 Ordering Edgeuses and Exhaustive Nodal Numbering

The owneredges and edgeuses for edges emanating from nodal 309 have now been identified and appear in the temporary array MART as shown in the bottom partition of Table 3.4. This array is now rearranged so that the owneredges are placed in descending order of the angle θ. MART then becomes as shown in Table 3.5a. Next, edgeuses which have a common element number in successive owneredges (i.e. N and N+1) are found. These element numbers are in the first row(K=1) of the array MART shown in Table 3.5a. The element number for the first edgeuse of owneredge N+1 is made to be the same as that for the second edgeuse of owneredge N. After these interchanges MART appears as show in Table 3.5b. The second element number appearing in the edgeuse for each owneredge is called the "back element" number, because in a counterclockwise circuit around the node it would be the element behind the crack on an owneredge. These back element numbers are stored in the temporary array NEAM1, as shown in the bottom line of Table 3.5c.

Exhaustive enumeration for this node (309) may now be carried out. If the last nodal splitting number for the previous node was NS, then nodal number 309 for the second edgeuse of the first owneredge is changed to NS+1 and, at the same time, NS+1 is inserted for node 309 in the first edgeuse of the second owneredge. This process continues through all the edgeuses at the node to produce the nodal numbers shown on Table 3.5c.

The result of this is to produce the local owneredge number and the nodal splitting numbers for node 309, shown in Fig 3.5b for each element. The back and front of each potential crack for each owneredge emanating from node 309 are indicated by 'b' and 'f' adjacent to the edge.

3.6.4 Construction of Exhaustive Enumeration Database

The information contained in the temporary array MART, shown in Table 3.5, is fundamental to a global database which it is necessary to construct in order to provide the flexibility to deal with all possible potential crack patterns along element boundaries. However, prior to discussing the assembly of this database from the MART array, the method of global numbering of vertices and owneredges must be introduced.

For the purpose of illustration it is again assumed that the patch of Fig. 3.5a constitutes the entire mesh. Processing the vertices in ascending order of their input nodal numbers, the vertices and owneredges are numbered sequentially as they arise in the process described in Sect. 3.6.1 and 3.6.3. For the patch of Fig. 3.5a the global vertex and owneredge numbering would be as shown in Fig. 3.5c. As each "corner" node is processed, in turn, it is given a vertex number. For the patch of Fig. 3.5a, two new owneredges arise with each of the vertices 1 and 2, 4 and 5, while one arises at vertex 3. These are consecutively numbered in the order in which they appear in the temporary array MART by the process of Sect. 3.6.3.

3.6.4.1 Database Edge Array NCRLC

Progressing through the patch of Fig. 3.5 as discussed in Sect. 3.4, the owneredges which sequentially arise by the process are assembled into a global array with identifications as shown in Table 3.6, as each vertex node is processed. They are given the global identification numbers designated by NE in the table. Owneredge NE=8 and NE=9 arise from the processing of node 309, through the MART array of Table 3.5c. Note that two of the owneredges in Table 3.5c appear in Table 3.6 prior to processing node 309: owneredge NE=3 first appears for vertex 2; while, owneredge NE=7 first appears for vertex 4. Therefore, the local owneredges presented in MART must first be compared with previously saved global owneredges to ensure that they will not be duplicated, prior to being given a global identity number.

In the illustrative example for the MART array of Table 3.5c, the local owneredges 1 and 2 are given the global owneredge numbers of 8 and 9, respectively, but local owneredges 3 and 4 are not assigned new global numbers since these edges already have global numbers 3 and 7.

A three dimensional database array NCRLC(NE,ND,NN) is designed to be the assemblage of topological information for all owneredges. NE is the global identification number for owneredge; NN, ranging from 1 to 3, represents a local ordering of the nodes on the edge; and ND ranging from 1 to 20 represents a maximum of 20 information parameters (i,e, - attributes) associated with each node on the edge.

For owneredges which have not appeared in NCRLC prior to processing node 309 (i.e- global owneredges NE=8 and NE=9), their nodal identification as shown in Table 3.6 is stored in NCRLC(NE,20,1), NCRLC(NE,20,2) and NCRLC(NE,20,3), as shown in Table 3.7. These three numbers are used as an identification array for the owneredge, so that if they arise again during the processing of nodes other than node 309, they will not be duplicated. The other information stored for these new owneredges (8 and 9) consists of their crack front nodal number (ND=1), their crack back nodal number (ND=2), the edge local orientation (ND=5) and the back element number (ND=6). This information is all available from array MART, and its associated arrays ANG and NEAM1, as shown in Tables 3.5 and 3.6. The quantities stored in NCRLC are defined in the Notes to Table 3.7.

For the new owneredges identified at node 309 (i,e.- NE=8 and 9), the information is stored in NCRLC using local nodal number NN=1, and subscripts ND=1, 2, 5, 6 and 10 respectively, as shown in Table 3.7.

For owneredges which appeared in NCRLC prior to processing node 309 (i.e.- owneredges NE=3 and NE=7), their nodal identifications have already been stored in association with the processing of a previous node. Their identities may be established by checking the nodal numbers of the fourth columns of Table 3.5c with those in Table 3.6.

The same kind of information as for the new owneredges is now stored for the old owneredges 3 and 7 at the location of node 309 for these edges. This data is available from arrays MART, ANG and NEAM1, under local owneredges 3 and 4, as shown in Table 3.5c. However, this new information is stored in NCRLC using local nodal number NN=3 instead of NN=1, as shown in Table 3.7, because position NN=1 is already occupied by the information associated with the first edgeuse of the owneredge when it was first identified.

Examination of Table 3.7 for owneredges NE=3 and NE=7 indicates that the orientation and crack back element number of an owneredge are different for the two vertices of an edge. This is due to the vertex based approach adopted in this study where all owneredges are oriented away from the vertex to which they are referred. This does not cause any confusion because a vertex based approach deals with edges through their common end vertices, for which a uniform clockwise ordering of emanating owneredges is implemented.

The information from Table 3.7 can be identified in its position in the three dimensional NCRLC array that is shown in Table 3.8, which is assembled in the order of the global owneredge identification identified in Fig. 3.5c, as the first rows for NE=3 and 7, and the the last rows for NE=8 and 9.

3.6.4.2 Database Vertex Array NCRNN

The processing to determine owneredges and edgeuses, leading to the contribution of the MART arrays of Sect. 3.6.3 to NCRLC of Sect. 3.6.4.1. is vertex based, and the nodes are processed in sequential order of their input numbers. The corner nodes are defined as vertices as described in Sect. 3.6.4 and given a global vertex number. For the patch of Fig. 3.5a, these global vertex members are shown in Fig. 3.5c.

The MART array of Sect. 3.6.3 also contains information for input node 309, which is stored in a vertex database designated as NCRNN. As for NCRLC, NCRNN is a three dimensional array as indicated in Table 3.10.

However, for each vertex, the information stored may be represented as a two dimensional array and is easier to described in this context. The information for vertex 5 of Fig. 3.5c (input node 309) is shown in Table 3.9a where it is identified by the local owneredge number NM. The information originally stored from MART for each edge consists, in part, of the crack front element number (NT=6), the crack back element number (NT=7), the nodal splitting number for the crack front (NT=1 and 10), the nodal splitting number for the crack back (NT=2 and 11), the corresponding global owneredge number (NT=16) and the position NN in NCRLC(NE, ND, NN) in which the input nodal number of this vertex appears in the edge identifier (NT=17).

Table 3.9a contains the nodal numbers in lines 1 and 2 as if all edges were cracked at input node 309, and also in lines 10 and 11. If there are no cracks passing through the vertex only one nodal number should be associated with the node. The number assigned is the lowest splitting number that arises at the node. Consequently, for an uncracked condition, all nodal numbers in line 1 and 2 are set to NS+1, so that the entries for vertex 5 appear as shown in Table 3.9b. Nodal numbers from the exhaustive nodal numbering are retained in lines 10 and 11 and can be activated at any time by assigning them to line 1 and 2 in such a way as to produce any combination of cracks that can appear at vertex 5.

The complete three dimensional array for NCRNN, for the patch of Fig. 3.5a is shown in Table 3.10. In Table 3.10, NV represents global vertex number for the corner nodes. Therefore, input node 309 is assigned a global vertex number 5 (NV=5), and its topological information given in Table 3.9 is stored in the 5th row of Table 3.10, such that the last row of Table 3.10 is composed of the first column of Table 3.9b. If NS represents the last nodal splitting number for the previous node to node 309 (NV=5), and WS represents the last splitting number for previous node to node 105 (NV=1), then NS of Table 3.9 equals WS+14 resulting in the global splitting numbers shown in columns 10 and 11 of Table 3.10.

A one dimensional array NCRNM is used to record the total number of edges emanating from a vertex (corner node), so NCRNM(I) gives total number of edges emanating from the corner node which has a sequential number I. On the left side of Table 3.10, the value of NCRNM corresponding to the vertices NV are listed.

The presence or absence of cracking is indicated by a flag in the array NCRLC. This indicator, using 1 for uncracked conditions, and 0 or negative values for various cracking conditions, is stored for each owneredge at each nodal point under ND=3 in Table 3.7. The interface indicator of an owneredge, using 0 for being continuous concrete material, 1 for being a boundary between concrete and steel materials and 2 for being continuous steel material, is stored for ND=4. The criterion for whether or not a crack is considered to occur along an owneredge, and how this is incorporated into the database arrays is discussed in Chapter 4.

3.6.4.3 Summary of Usages for Some Entries in Array NCRNN

Some key entries in array NCRNN which will be repeatedly used in Chapter 4 are summarized as follows (see Table 3.9).

1) The information stored in NCRNN(NV, 6, NM) and NCRNN(NV, 7, NM) gives respectively the crack front element number (CFEN) and crack back element number (CBEN) for the edge with local owneredge number NM emanating from the vertex with global vertex number NV.

2) Stored in NCRNN(NV,1,NM), NCRNN(NV,2,NM) are the global nodal numbers currently activated for the elements in NCRNN(NV,6,NM) and NCRNN(NV,7,NM). These global numbers correspond to the vertexuses of the vertex NV in the loops of these two elements. The two numbers reflect the current crack condition of vertex NV along edge NM. This pair of entries, NCRNN(NV,1,NM) and NCRNN(NV,2,NM), are called the current crack front nodal number (CCFNN) and current crack back nodal number (CCBNN) respectively.

3) Stored in NCRNN(NV,10,NM) and NCRNN(NV,11,NM) are the nodal numbers associated with the elements in NCRNN(NV,6,NM) and NCRNN(NV,7,NM) if all the potential nodal splittings occur at vertex NV. All these pairs of numbers for the local owner edge NM=1 to NM=NMM, where NMM is the total number of edges emanating from vertex NV, reflect the extreme or "worst" cracking condition at the vertex. This pair of entries, NCRNN(NV,10,NM) and NCRNN(NV,11,NM) are called crack front nodal splitting number (CFNSN) and crack back nodal splitting number (CBNSN) respectively.

4) Stored in NCRNN(NV,3,NM), and not shown in Table 3.9, is a flag for the cracking status at vertex NV along edge NM. Its values are assigned as follows:

1 = uncracked;
0 = incipient cracking;
-1 = cracked, with tensile stress exists between two crack faces at vertex NV along edge NM;
-2 = cracked and no tensile stress existing between the two crack faces;
-3 = free edge.

5) Stored in NCRNN(NV,4,NM), and also not shown in Table 3.9, is a flag for material adjacency along edge NM at vertex NV. Its values are assigned as follows:

0 = elements on both sides of edge NM at vertex NV are concrete.
1 = element on one side is concrete, and the one on other side is steel.
2 = elements on both sides are steel.

3.6.5 Variations in Database Procedures

3.6.5.1 Treatment of Boundary and Corner Nodes

The procedure described in Sect. 3.6.2 and Sect. 3.6.3 is able to deal with boundary nodes as well as interior nodes. Node 107 in Fig. 3.5a is a boundary node, and processing of its temporary array MART is shown in Table 3.11. Two of three owneredge emanating from the node, owneredge 107-106-105 and 107-108-109, only have one edgeuse stored as shown in Table 3.11a.

In the processing of array MART to order the owneredges according to decreasing values of orientation ANG, owneredge 107-108-109 has no back element edgeuse and another owneredge 107-106-105 has no front element edgeuse, as shown in Table 3.11b. Fig. 3.5e depicts the topological meaning of temporary array MART. As a counterclockwise circle is drawn around node 107, the circle "enters" the structure at owneredge 107-108-109, and the "entrance" is represented by the existence of a crack front (first column) and absence of a crack back (second column). On the contrary, the circle "exits" the structure at owneredge 107-106-105, and this "exit" is represented by the absence of a crack front and existence of a crack back. Exhaustive nodal numbering, Table 3.11c, progresses the same way as in Table 3.5 but zero nodes are not assigned splitting numbers.

The procedure of storing MART to the topological database is the same as described in Sect. 3.6.4.1 and Sect. 3.6.4.2. A point of particular interest is the determination of the cracking flag, ND=3 in array NCRNN(NT,ND,NN), described in Sect. 3.6.4.2. A boundary owneredge can be a free boundary of a structure or a line of symmetry of a structure. This can be identified by inspection of the 'ID array' for the degree of freedom. If both D.O.F of the boundary node are nonzero (active), a free boundary node is detected. Otherwise, it is a node on a line of symmetry, or a constrained node. In the case of a free boundary, the crack flag (ND=3 in Table 3.7) is set to -3 so that no crack evaluation will be executed (see Chapter 4). In the second case the crack flag is set to 1 to indicate an uncracked state for a potential crack.

3.6.5.2 Treatment of Midside Node

A vector in the vicinity of a vertex drawn from the back element or (crack back) to the front element across owneredge i and perpendicular to the edge, will be called the normal of the owneredge, and designated as **ni**. These owneredge normals are shown for node 309 in Fig. 3.5d, and for node 107 in Fig. 3.5e. If the orientation vector for owneredge i, denoted by **ti**, is rotated 90^{o} counterclockwise, it will coincide with **ni**. This is an equivalent representation of the adjacency relation, and is used frequently in the crack evaluation which will be discussed in Chapter 4.

Node 308 in Fig. 3.5a is taken as an example of the treatment of a midside node. The processed array MART at this node is shown in Table 3.12. For an interior node three steps, denoted by (a), (b) and (c) respectively, have been shown in Table 3.3. Two of these steps, (a) and (b), are applicable to midside nodes, but step (c), which exchanges the two nodes in position 1 and 3 if the vertex being processed is not at position 1, is eliminated. The ordering of edges by decreasing values of ANG, as shown in Table 3.5a, is also eliminated because there is only one owneredge incident to a midside node. As shown by Table 3.12a and Fig. 3.5e, the orientations of the two edgeuses of the owneredge differ by 180^{o}. For consistency with the coincidence of the owneredge orientation vector **t** after the counterclockwise 90^{o} rotation and the normal vector **n**, as described at the beginning of this section, the orientation of the first edgeuse at a midside node is defined as the owneredge orientation, and the element which brings the second edgeuse is defined as the back element. As shown by Table 3.12a and Fig. 3.5e, the orientation of the owneredge at node 308 is -90, and the back element is 18. Exhaustive enumeration of nodal splitting proceeds as shown in Table 3.12b.

As the array MART is stored into the topological database, only array NCRLC is updated. Array NCRNN is for vertices only, and no midside node information is required. The same kind of information as described in Sect. 3.6.4.1 for vertices is saved for the midside nodes. Recalling that data for vertices are stored at the local position number NN=1 or NN=3 in NCRLC(NE,ND,NN), data for midside nodes is stored for NN=2. Midside node 308 appears in Table 3.7 and Table 3.8 under the subscripts NE=7 and NN=2 in which the nodal splitting number have been made consistent with the other nodes in this tables.

3.6.5.3 Treatment of Reinforcing Element and Interfaces

To illustrate the treatment of reinforcing elements, a line of reinforcement along line 311-310-309-308-307 in the mesh shown in Fig. 3.5a is inserted in Fig. 3.5f. These reinforcing elements are 3-node truss elements and designated as element 13 and 14, as shown in Fig. 3.5f. Sequential construction of array MART for node 309 is illustrated in Table 3.13. It is similar to the result in Table 3.4 for the mesh in Fig. 3.5a except that the reinforcing elements add a third edgeuse to two of the local owneredges. By comparing the last partition of Table 3.13 and Table 3.5, it is found that, in Table 3.13, for edges 309-308-307 and 309-310-311 the number of edgeuses is increased from 2 to 3, and the newly added edgeuses associated with the reinforcing elements appear in the second edgeuse position.

Every edgeuse of the owneredge emanating from node 309 is examined. If one edgeuse is associated with a reinforcing element which is identified by its type of flag, and is not at the third edgeuse position, its position is exchanged with third edgeuse. The result is shown in Table 3.14a. The procedure then followed is exactly the same as that for no reinforcing element: reordering edges in order of decreasing magnitude of ANG, reordering the first two edgeuses so the same element numbers are in paired in sequential owneredges. After the exhaustive enumeration is finished for all splitting nodes of the solid elements, the maximum nodal splitting number is increased by 1 to get additional nodal splitting numbers for reinforcing nodes as extreme cracking occurs. This is illustrated in Table 3.14b and Fig. 3.5h.

As owneredge 309-310-311 and 309-308-307 are stored into the topological database NCRLC(NE,ND,NN), NCRLC(NE,12,NN) is used as a flag to denote insertion of reinforcement, and is set to one if reinforcement is present (otherwise it is zero). The exhaustive enumeration nodal number for the reinforcement, and the two numbers of the reinforcing elements incident to the node, 13 and 14, follow in ND=13 to 15.

3.6.5.4 Variation of Element Type

3.6.5.4.1 Quadratic Triangle Element

The procedures for quadratic triangle elements are almost the same as for quadratic rectangular elements. The only difference is in the formation of array KSID1, the parent element edge definition in terms of local nodal numbers, as described in Sect. 3.6.2. Array KSID1 for quadratic triangles is shown in Fig. 3.6b, and can be written in the order of a counterclockwise sequence as illustrated by the labels in Fig. 3.6.

3.6.5.4.2 Linear Element

The procedures for linear elements are almost the same as for quadratic elements. The only difference is that no midside node is dealt with. As a result, only two nodes exist on any edge instead of three. Then, only the first two of three positions for local nodes on an owneredge are used in arrays such as KSID1, KSID, MART and NCRLC.

3.7 Transformation of Problem from Input Numbering to Exhaustive Enumeration

As the exhaustive enumeration at a node with input nodal number I is completed, the lowest splitting number that arises at the node, namely, NS+1, is saved to an array designated as KEMT2 at position I, that is, KEMT2(I)= NS+1.

For the example shown in Fig. 3.5a, if it is assumed that the new nodal number for node 105 is WS+1, the corresponding value of KEMT2 is given in parenthesis besides the input nodal number in Fig. 3.5h. Array KEMT2 represents a correspondence in an uncracked structure between the input nodal number and the lowest nodal splitting number for this node arising from exhaustive enumeration. The KEMT2 array for the example of Fig. 3.5h is as shown in Table 3.15.

The last procedure in the "data preparation phase" is to transform the problem input numbering system to that obtained from exhaustive enumeration, and array KEMT2 is used for this transformation. The transformation includes two parts:

1) The global node number is replaced in the element-nodal incidence array NPELM by new numbering. This is shown by Table 3.16 for the example shown in Fig. 3.5a. This new numbering recorded in array KEMT2, is used to represent the initial uncracked structure, and was denoted to be the 'initial nodal number' in Sect. 3.4.

Initial nodal numbers are also introduced into the global array NCRNN to replace the numbers at positions NT=1 and NT=2 as shown in Tables 3.9b and 3.10. As the numbers in these two positions are designed to represent current crack front and crack back nodal numbers, they are both identical to the initial nodal number for an uncracked state. Noticing the exhaustive splitting numbers are also stored in NT=10 and NT=11 for array NCRNN, the exhaustive splitting numbers are not lost by altering the values in positions NT=1 and NT=2.

2) The arrays which were originally defined having length equal to the total number of input nodes (NMNOD), must be expanded to encompass the maximum nodal number obtained by exhaustive enumeration. For the example in Fig. 3.5a, the total number of input nodes is 21, and the maximum number of nodes after exhaustive enumeration is 32. How an array is expanded depends on its function. The array which contains the nodal geometry is expanded by assigning the geometry of the input node to all nodes, in the group produced by exhaustive enumeration, for this input node. As shown in Table 3.15, input node 309 correspond to 4 nodes, namely, nodes WS+15 to WS+18. This can be determined by the difference in the first nodal splitting number for nodes 310 and 309. These four split nodes will be assigned the same initial position as input node 309.

The ID array which contains the 'activity status' (or boundary condition code) for the degrees of freedom (DOF) of the nodes, is expanded by assigning the activity status of the input node to the first node in the group produced by exhaustive enumeration (i.e.- initial nodal number). The DOF's of the other nodes in the group are assigned an activity code of one indicating they are inactive in the initial uncracked state. These procedures are discussed in detail in Chapter 4.

Table 3.1 Element-Nodal Incidence Array NPELM for Fig. 3.5

Element No. I	Element-Nodal Incidence Array NPELM (K,I) K=1, 8
-	
9	307, 105, 107, 309, 210, 106, 211, 308
10	309, 107, 109, 311, 211, 108, 212, 310
-	
18	509, 307, 309, 511, 405, 308, 406, 510
19	511, 309, 311, 513, 406, 310, 407, 512

Table 3.2 Nodal-Element Incidence Array KEMT(J,M) for Node 309 of Fig. 3.5

Input Node J	KEMT (J,M)				
	M=1	M=2	M=3	M=4	M=5
	Number of Element Incidences	Incident Element			
309	4	9	10	18	19

Table 3.3 Processing of Edge Identification Array KSID for Node 309 in Element 9 of Fig. 3.5

Parent Element Side No.	a) Local Nodal Definition: KSID1 in Parent Element	b) Global Nodal Definition: KSID in Real Element	c) Vertex Focused Global Definition: KSID in Real Element
1	1 5 2	307 210 105	307 210 105
2	2 6 3	105 106 107	105 106 107
3	3 7 4	107 211 309	309 211 107
4	4 8 1	309 308 307	309 308 307

Table 3.4 Processing of Edgeuse Array MART(N,K,J) for Edges Emanating from Node 309 in Fig. 3.5

LOCAL OWNEREDGE No. N		1				2				3				4			
LAST ELEMENT PROCESSED	K	MART(1,K,J)				MART(2,K,J)				MART(3,K,J)				MART(4,K,J)			
		J				J				J				J			
		1	2	3	4	1	2	3	4	1	2	3	4	1	2	3	4
9	1	9			0	9			0								
	2	309			309	309			309								
	3	211			211	308			308								
	4	107			107	307			307								
	5	0			0	0			0								
10	1	9	10		0	9			0	10			0				
	2	309	309		309	309			309	309			309				
	3	211	211		211	308			308	310			310				
	4	107	107		107	307			307	311			311				
	5	0			0	0			0	0			0				
18	1	9	10		0	9	18		0	10			0	18			0
	2	309	309		309	309	309		309	309			309	309			309
	3	211	211		211	308	308		308	310			310	406			406
	4	107	107		107	307	307		307	311			311	511			511
	5	0	0		0	0	0		0	0			0	0			
19	1	9	10		0	9	18		0	10	19		0	18	19		0
	2	309	309		309	309	309		309	309	309		309	309	309		309
	3	211	211		211	308	308		308	310	310		310	406	406		406
	4	107	107		107	307	307		307	311	311		311	511	511		511
	5	0	0		0	0	0		0	0	0		0	0	0		0
ANG (θ)		0				-90				90				180			

Table 3.5 Processing the MART(N,K,J) ARRAY for Exhaustive Enumeration

a) Reorder Distinct Edges Emanating from Node 309 in Order of Descreasing Magnitude of ANG

ANG(θ)		180 >				90 >				0 >				-90			
Local Owneredge No. N		1				2				3				4			
		MART(1,K,J)				MART(2,K,J)				MART(3,K,J)				MART(4,K,J)			
	K	J				J				J				J			
		1	2	3	4	1	2	3	4	1	2	3	4	1	2	3	4
	1	18	19		0	10	19		0	9	10		0	9	18		0
	2	309	309		309	309	309		309	309	309		309	309	309		309
	3	406	406		406	310	310		310	211	211		211	308	308		308
	4	511	501		501	311	311		311	107	107		107	307	307		307
	5	0	0		0	0	0		0	0	0		0	0	0		0

b) Record Elements to Pair Element Numbers in Sequential Edgeuses

	1	18	19	—	— →	19	10	—	— →	10	9	—	— →	9	18		
	2	309	309			309	309			309	309			309	309		
	3	406	406			310	310			211	211			308	308		
	4	511	511			311	311			107	107			307	307		
	5	0	0			0	0			0	0			0	0		

c) Renumber Node 309 for Exhaustive Enumeration

	1	18	19		0	19	10		0	10	9		0	9	18		0
	2	NS+4	NS+1		309	NS+1	NS+2		309	NS+2	NS+3		309	NS+3	NS+4		309
	3	406	406		406	310	310		310	211	211		211	308	308		308
	4	511	511		511	311	311		311	107	107		107	307	307		307
	5	0	0		0	0	0			0	0			0	0		
NEAM1		19				10				9				18			

Table 3.6
Processing Global Identification of Sequential Owneredges in NCRLC(NE,20,NN)

Last Node Pro-cessed	NN	Global Owneredge Number NE								
	Edge Local Nodal No.	1	2	3	4	5	6	7	8	9
105	1	105	105							
	2	210	106							
	3	307	107							
107	1	105	105	107	107					
	2	210	106	211	108					
	3	307	107	309	109					
109	1	105	105	107	107	109				
	2	210	106	211	108	212				
	3	307	107	309	109	311				
307	1	105	105	107	107	109	307	307		
	2	210	106	211	108	212	405	308		
	3	307	107	309	109	311	509	309		
309	1	105	105	107	107	109	307	307	309	309
	2	210	106	211	108	212	405	308	406	310
	3	307	107	309	109	311	509	309	511	311

Table 3.7 Entries in NCRLC for Node 309

NE	8			9			3			7		
NN / ND	1	2	3	1	2	3	1	2	3	1	2	3
1	NS+4			NS+1			(*)	(*)	NS+2	(*)	NS-1	NS+3
2	NS+1			NS+2			(*)	(*)	NS+3	(*)	NS	NS+4
3												
4												
5	180			90			(180)		0	(90)	-90	-90
6	19			10			(10)		9	(9)	18	18
10												
20	309	406	511	309	310	311	(107)	(211)	(309)	(307)	(308)	(309)

Data Description:

NE= Global owneredge number

NN= Edge Local Nodal Number

ND= 1= Nodal splitting number on back of owneredge
2= Nodal splitting number on front of owneredge
3= Crack status indicater; for exampe, 1 for uncracked state and -1 for cracked state
4= Interface indicator of the edge; for example 0 for concrete element on both sides and 1 for one concrete element on one side with steel element on the other side
5= Orientation of the owneredge when emanating from node for NN=1
6= Crack back element number
10=

20= Input node Identification

Notation:

( )= Indicates information stored from MART arrays previous to that for input node 309

(*)= Proviously evaluated but unspecified for this example

Table 3.8 Processing of Global Array NCRLC(NE,ND,NN) for Fig. 3.5

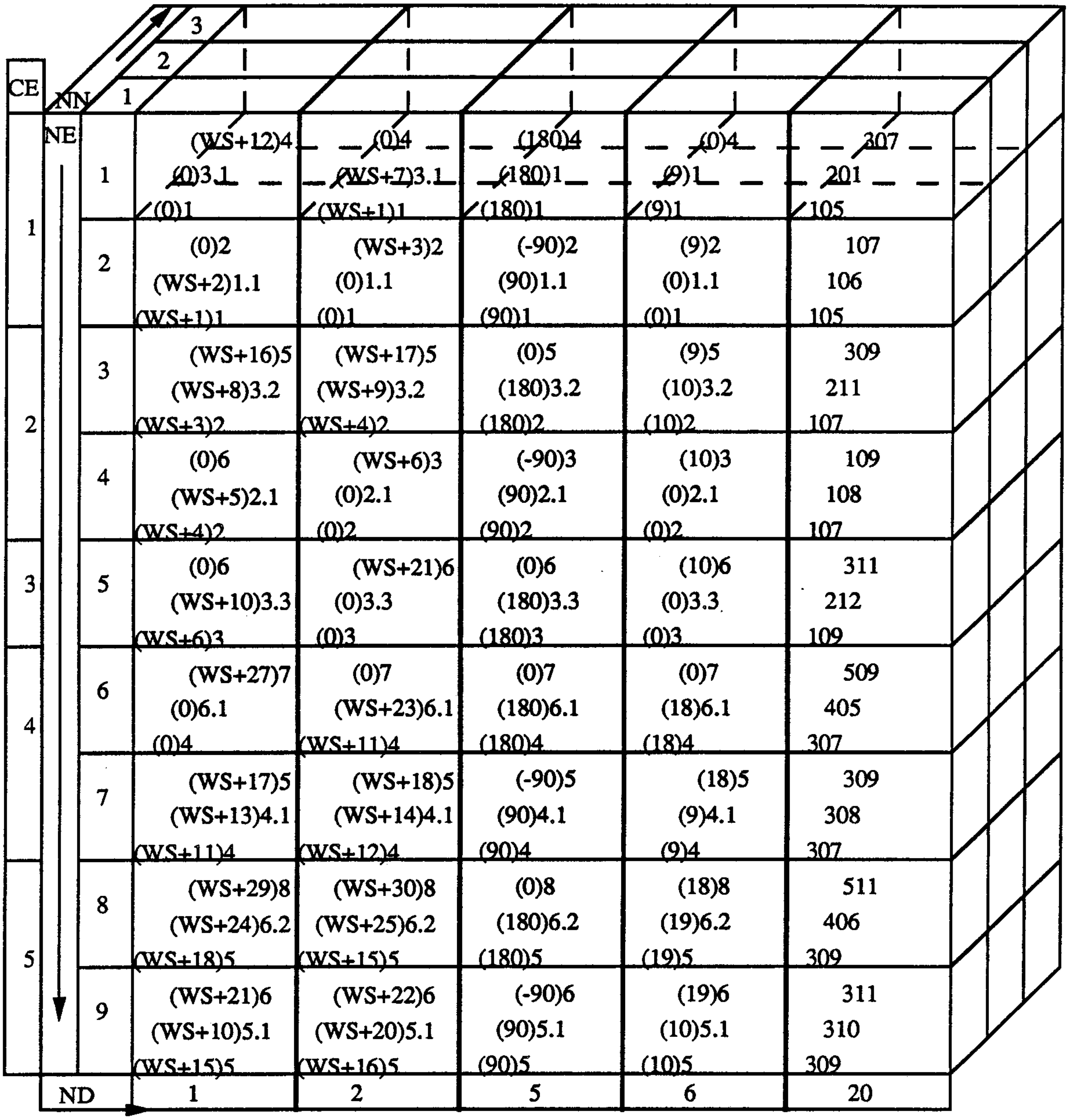

CE	NE	NN	ND 1	ND 2	ND 5	ND 6	ND 20
1	1	3	(WS+12)4	(0)4	(180)4	(0)4	307
		2	(0)3.1	(WS+7)3.1	(180)1	(9)1	201
		1	(0)1	(WS+1)1	(180)1	(9)1	105
	2	3	(0)2	(WS+3)2	(-90)2	(9)2	107
		2	(WS+2)1.1	(0)1.1	(90)1.1	(0)1.1	106
		1	(WS+1)1	(0)1	(90)1	(0)1	105
2	3	3	(WS+16)5	(WS+17)5	(0)5	(9)5	309
		2	(WS+8)3.2	(WS+9)3.2	(180)3.2	(10)3.2	211
		1	(WS+3)2	(WS+4)2	(180)2	(10)2	107
	4	3	(0)6	(WS+6)3	(-90)3	(10)3	109
		2	(WS+5)2.1	(0)2.1	(90)2.1	(0)2.1	108
		1	(WS+4)2	(0)2	(90)2	(0)2	107
3	5	3	(0)6	(WS+21)6	(0)6	(10)6	311
		2	(WS+10)3.3	(0)3.3	(180)3.3	(0)3.3	212
		1	(WS+6)3	(0)3	(180)3	(0)3	109
4	6	3	(WS+27)7	(0)7	(0)7	(0)7	509
		2	(0)6.1	(WS+23)6.1	(180)6.1	(18)6.1	405
		1	(0)4	(WS+11)4	(180)4	(18)4	307
	7	3	(WS+17)5	(WS+18)5	(-90)5	(18)5	309
		2	(WS+13)4.1	(WS+14)4.1	(90)4.1	(9)4.1	308
		1	(WS+11)4	(WS+12)4	(90)4	(9)4	307
5	8	3	(WS+29)8	(WS+30)8	(0)8	(18)8	511
		2	(WS+24)6.2	(WS+25)6.2	(180)6.2	(19)6.2	406
		1	(WS+18)5	(WS+15)5	(180)5	(19)5	309
	9	3	(WS+21)6	(WS+22)6	(-90)6	(19)6	311
		2	(WS+10)5.1	(WS+20)5.1	(90)5.1	(10)5.1	310
		1	(WS+15)5	(WS+16)5	(90)5	(10)5	309

Notation:	
CE	sequential corner node (vertex) number
(WS+11)4	exhaustive splitting number WS+11 which is produced at the 4th corner node
(WS+13)4.1	exhaustive splitting number WS+13 which is produced at the 1st mideside node after the 4th corner node

Table 3.9 Entries into NCRNN (NV,NT,NM) for Vertex 5 of Fig. 3.5

(a)

NV	5			
NM NT	1	2	3	4
1	NS+4	NS+1	NS+2	NS+3
2	NS+1	NS+2	NS+3	NS+4
6	18	19	10	9
7	19	10	9	18
10	NS+4	NS+1	NS+2	NS+3
11	NS+1	NS+2	NS+3	NS+4
16	8	9	3	7
17	1	1	3	3

NS+1=WS+15
NS+2=WS+16
NS+3=WS+17
NS+4=WS+18

(b)

NM NT	1	2	3	4
1	NS+1	NS+1	NS+1	NS+1
2	NS+1	NS+1	NS+1	NS+1
6	18	19	10	9
7	19	10	9	18
10	NS+4	NS+1	NS+2	NS+3
11	NS+1	NS+2	NS+3	NS+4
16	8	9	3	7
17	1	1	3	3

Data Descriptors:

NV= Global Vertex Number
NM= Local Owneredge Number of Edges Emanating from this Vertex
NT= 1= Current Crack Front Nodal Number (CCFNN)
2= Current Crack Back Nodal Number (CCBNN)
6= Crack Front Element Number (CFEN)
7= Crack Back Element Number (CBEN)
10= Crack Front Nodal Splitting Number (CFNSN)
11= Crack Back Nodal Splitting Number (CBNSN)
16= Global owneredge number
17= Position of input nodal number for this vertex, in crack nodal identification in NCRLC.

Table 3.10 Processing of Global Array NCRNN(NV,NT,NM) for Fig. 3.5h

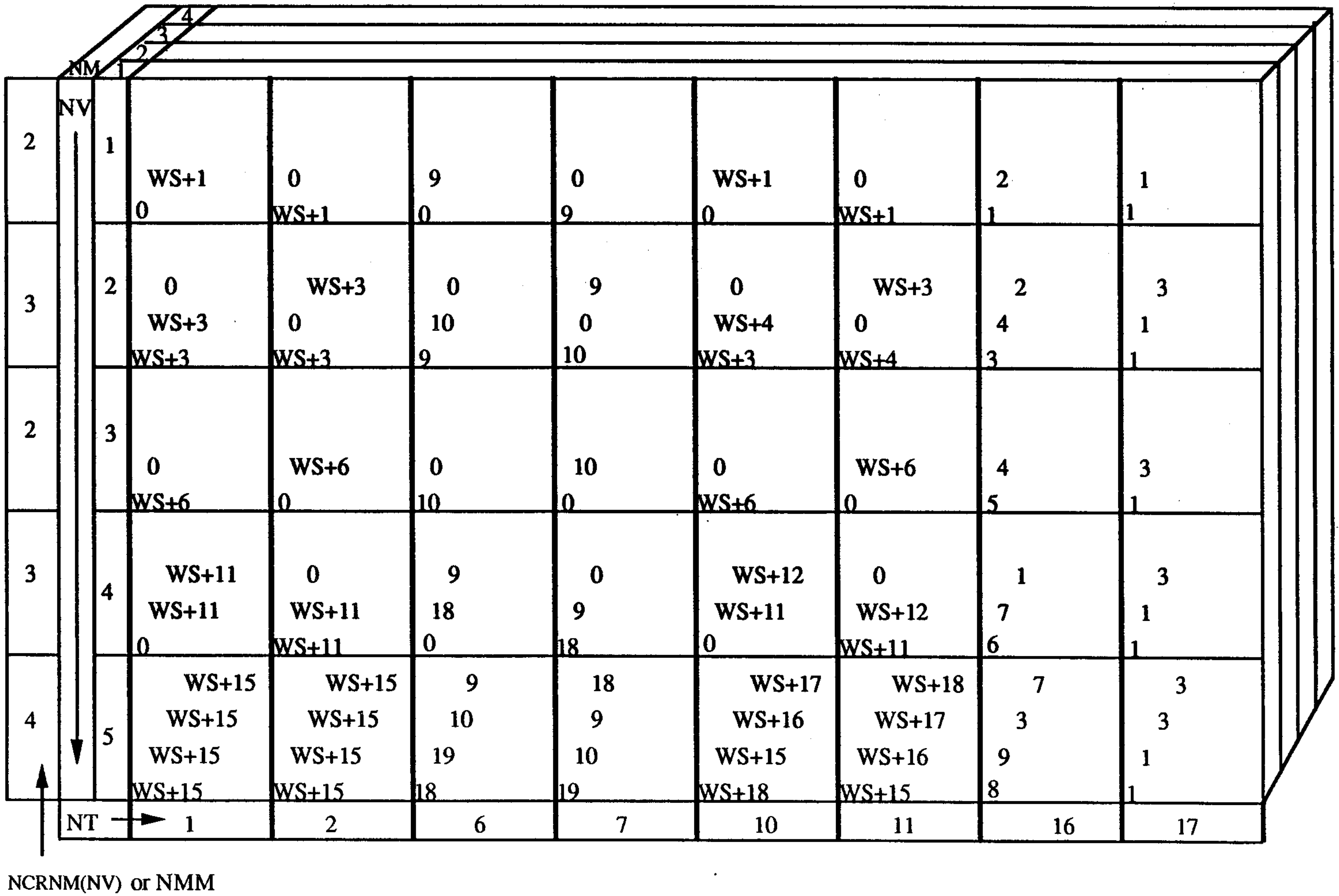

NCRNM(NV) or NMM	NV \ NT	1	2	6	7	10	11	16	17
2	1	WS+1 0	0 WS+1	9 0	0 9	WS+1 0	0 WS+1	2 1	1 1
3	2	0 WS+3 WS+3	WS+3 0 WS+3	0 10 9	9 0 10	0 WS+4 WS+3	WS+3 0 WS+4	2 4 3	3 1 1
2	3	0 WS+6	WS+6 0	0 10	10 0	0 WS+6	WS+6 0	4 5	3 1
3	4	WS+11 WS+11 0	0 WS+11 WS+11	9 18 0	0 9 18	WS+12 WS+11 0	0 WS+12 WS+11	1 7 6	3 1 1
4	5	WS+15 WS+15 WS+15 WS+15	WS+15 WS+15 WS+15 WS+15	9 10 19 18	18 9 10 19	WS+17 WS+16 WS+15 WS+18	WS+18 WS+17 WS+16 WS+15	7 3 9 8	3 3 1 1

Table 3.11 Processing of Array MART at Boundary Node 107 of Fig. 3.5

a) Sequential Construction of Array MART at Boundary Node 107

Last Element Processed	K	MART(1,K,J)				MART(2,K, J)				MART(3,K,J)			
		J				J				J			
		1	2	3	4	1	2	3	4	1	2	3	4
9	1	9				9							
	2	107			107	107			107				
	3	106			106	211			211				
	4	105			105	309			309				
10	1	9				9	10			10			
	2	107			107	107	107		107	107			107
	3	106			106	211	211		211	108			108
	4	105			105	309	309		309	109			109
ANG		-90				180				90			

b) Reorder Distinct Edges in Order of Decreasing Magnitude of ANG and Reorder Elements to Pair Element Number in Sequential Edgeuses

	1	9	10			10	0			0	9		
	2	107	107		107	107	0		107	0	107		107
	3	211	211		211	108	0		108	0	106		106
	4	309	309		309	109	0		109	0	105		105
ANG		180				90				-90			
NEAM1		10				0				9			

c) Renumber Node 107 by Exhaustive Enumberation

	1	9	10			10	0			0	9		
	2	NS+2	NS+1		107	NS+1	0		107	0	NS+2		107
	3	211	211		211	108	0		108	0	106		106
	4	309	309		309	109	0		109	0	105		105

Table 3.12 Processing of Array MART at Midside Node 308 of Fig. 3.5

a) Sequential Construction of Array MART at Node 308 in Fig.3.5

Local Owneredge No.		1			
Element Processed	K	MART (I,K,J)			
		J			
		1	2	3	4
9	1	9			
	2	309			
	3	308			
	4	307			
	5				
18	1	9	18		
	2	309	307		
	3	308	308		
	4	307	309		
	5				
ANG		-90	90		

b) Renumber Node 308 for Exhaustive Enumeration

	1	9	18		
	2	309	307		
	3	NS-1	NS		
	4	307	309		

Table 3.13 Processing of Array MART for Embedded Reinforcement in Fig. 3.5f

Local Owneredge No.		1				2				3				4			
Last Element Processed		MART(1,K,J)				MART(2,K,J)				MART(3,K,J)				MART(4,K,J)			
		J				J				J				J			
		1	2	3	4	1	2	3	4	1	2	3	4	1	2	3	4
9	1	9				9											
	2	309			309	309			309								
	3	211			211	308			308								
	4	107			107	307			307								
	5																
10	1	9	10			9				10							
	2	309	309		309	309			309	309			309				
	3	211	211		211	308			308	310			310				
	4	107	107		107	307			307	311			311				
	5																
13	1	9	10			9	13			10							
	2	309	309		309	309	309		309	309			309				
	3	211	211		211	308	308		308	310			310				
	4	107	107		107	307	307		307	311			311				
	5																
14	1	9	10			9	13			10	14						
	2	309	309		309	309	309		309	309	309		309				
	3	211	211		211	308	308		308	310	310		310				
	4	107	107		107	307	307		307	311	311		311				
	5																
18	1	9	10			9	13	18		10	14			18			
	2	309	309		309	309	309	309	309	309	309		309	309			309
	3	211	211		211	308	308	308	308	310	310		310	406			406
	4	107	107		107	307	307	307	307	311	311		311	511			511
	5																
19	1	9	10			9	13	18		10	14	19		18	19		
	2	309	309		309	309	309	309	309	309	309	309	309	309	309		309
	3	211	211		211	308	308	308	308	310	310	310	310	406	406		406
	4	107	107		107	307	307	307	307	311	311	311	311	511	511		511
	5																
		0				-90				90				180			

Table 3.14 Processing of Array MART for Reinforcement shown by Fig. 3.5g

a) Exchange Edgeuse Brought by Reinforcing Element to 3rd column in Array MART

Local Owneredge No.	1				2				3				4			
	MART(1,K,J)				MART(2,K,J)				MART(3,K,J)				MART(4,K,J)			
	J				J				J				J			
	1	2	3	4	1	2	3	4	1	2	3	4	1	2	3	4
1	9	10		0	9	18	13		10	19	14		18	19		
2	309	309		309	309	309	309	309	309	309	309	309	309	309		309
3	211	211		211	308	308	308	308	310	310	310	310	406	406		406
4	107	107		107	307	307	307	307	311	311	311	311	511	511		511
5																
ANG	0				-90				90				180			

b) Renumber Node 309 for Exhaustive Enumeration

1	18	19			19	10	14		10	9			9	18	13	
2	NS+4	NS+1		309	NS+1	NS+2	NS+5	309	NS+2	NS+3		309	NS+3	NS+4	NS+5	309
3	406	406		406	310	310	310	310	211	211		211	308	308	308	308
4	511	511		511	311	311	311	311	107	107		107	307	307	307	307
5																
ANG	180				90				0				-90			

Table 3.15: Array KEMT(I) for Fig. 3.5

Node Sequential No.	1	2	3	4	5	6	7	8	9	10	11	12	13	14	15	16	17	18	19	20	21
Vertex Sequential No.	1		2		3				4		5		6				7		8		9
Input Nodal Number I	105	106	107	108	109	210	211	212	307	308	309	310	311	405	406	407	509	510	511	512	513
KEMT2(I) =WS+	1	2	3	5	6	7	8	10	11	13	15	19	21	23	24	26	27	28	29	31	32

Table 3.16: Correspondence between Input and Initial Nodal Numberin Array NPELM

NPELM(N,M)									
Element No. M	Local Nodal No. N	1	2	3	4	5	6	7	8
9	Input	307	105	107	309	210	106	211	308
	Initial=WS+	11	1	3	15	7	2	8	13
10	Input	309	107	109	311	211	108	212	310
	Initial=WS+	15	3	6	21	8	5	10	19
18	Input	509	307	309	511	405	308	406	510
	Initial=WS+	27	11	15	29	23	13	24	28
19	Input	511	309	311	513	406	310	407	512
	Initial=WS+	29	15	21	32	24	19	26	31

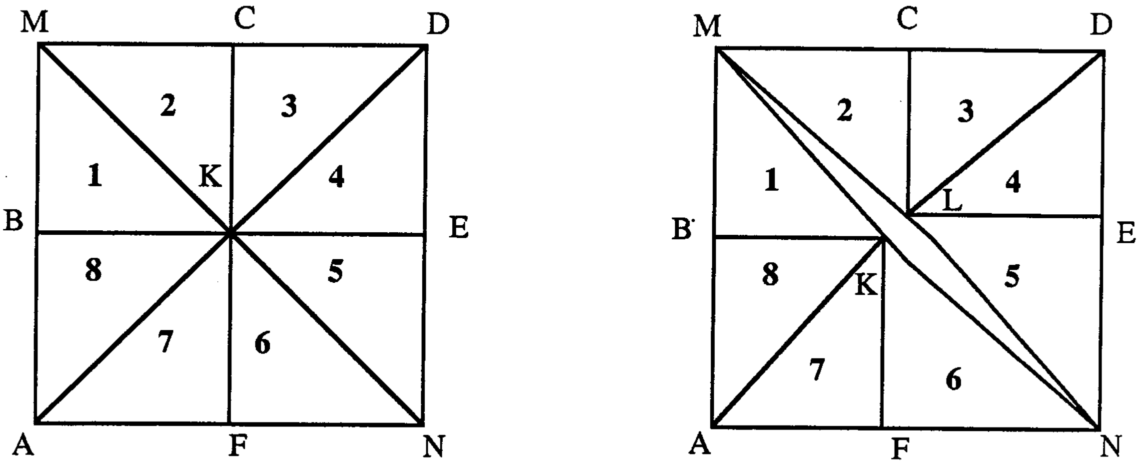

(a) Before cracking

(b) After cracking

Fig. 3.1 Discrete Crack Formation

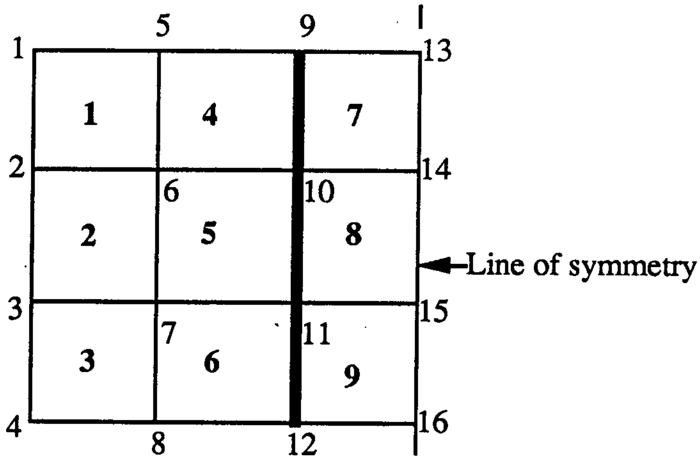

Fig. 3.2 A Mesh of Elements

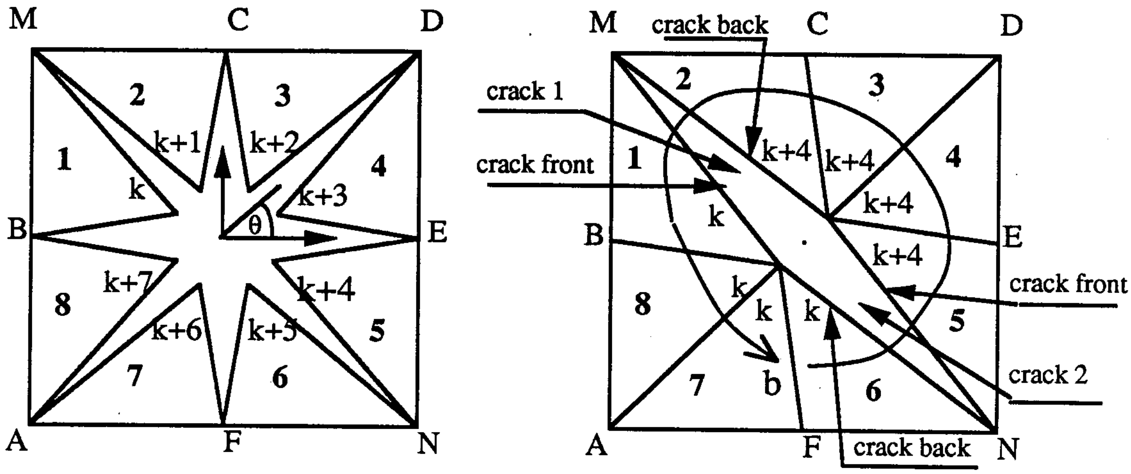

(a) Extreme of nodal splitting around node K

(b) Nodal splitting with 2 active nodal numbers

Fig. 3.3 Two Examples of Nodal Splitting

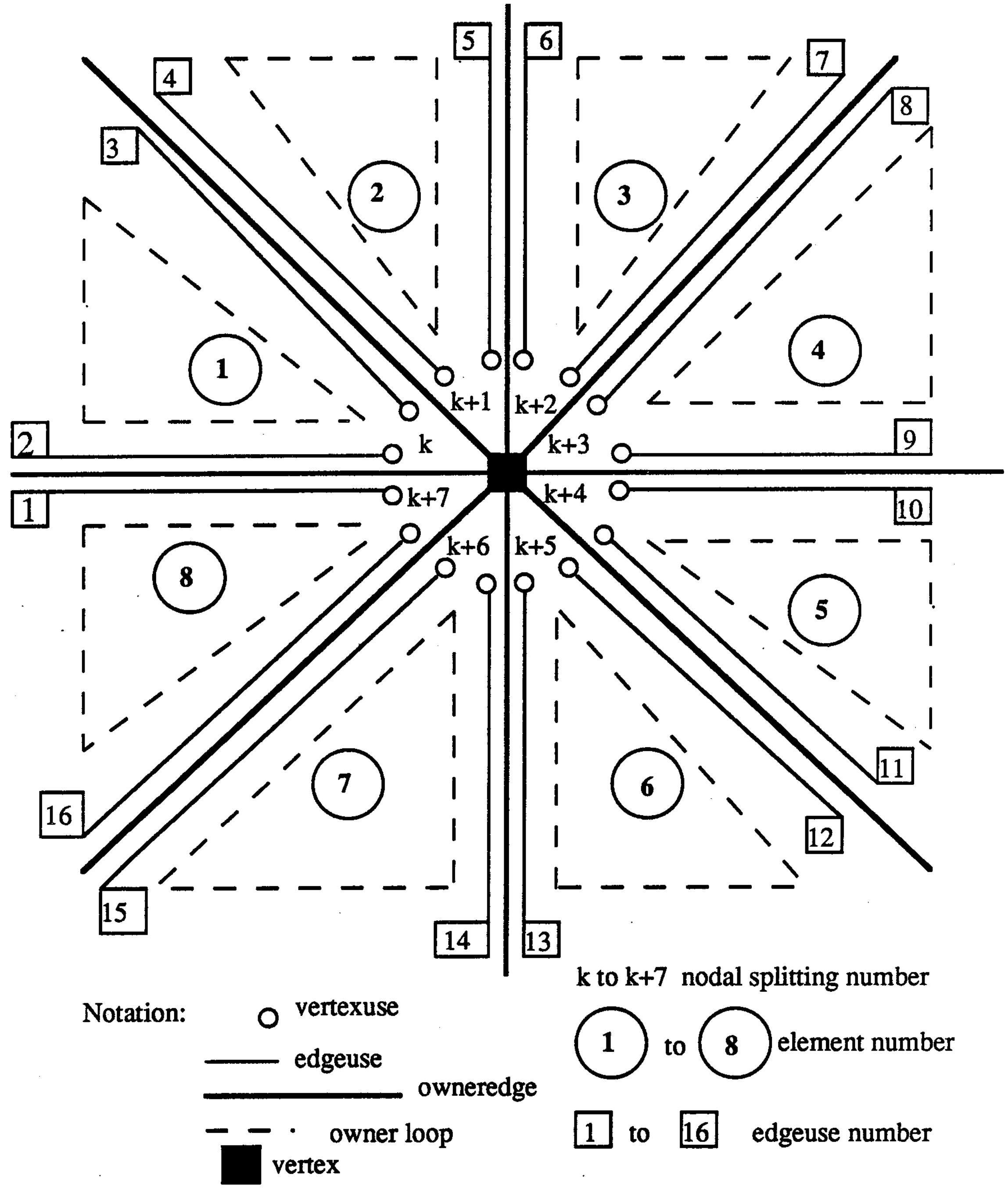

Fig. 3.4 Decomposition of Edges and Vertices

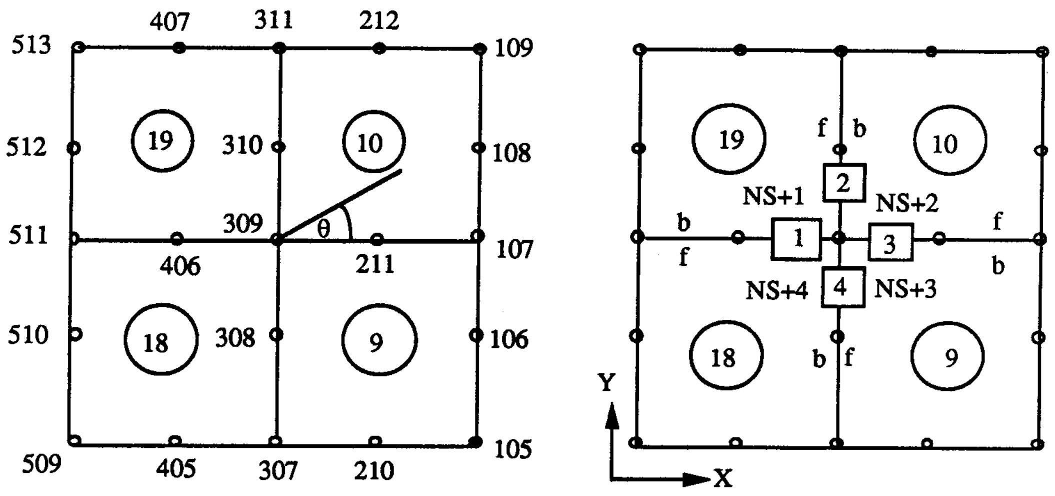

a) Input nodal and element numbers

b) Nodal splitting numbers for node 309

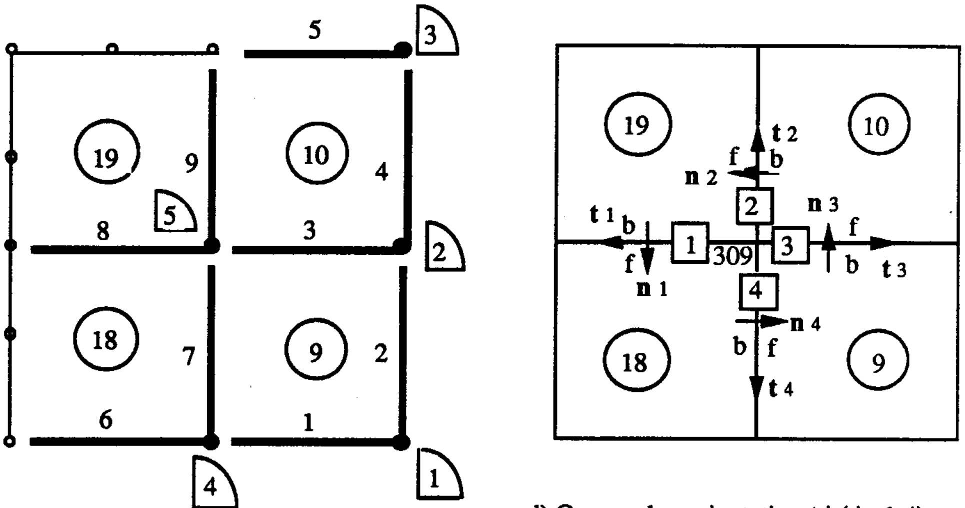

c) Global vertex and owneredge numbers

d) Owneredge orientation **t** i (i =1,4) and owneredge normal **n** i (i=1,4) for node 309

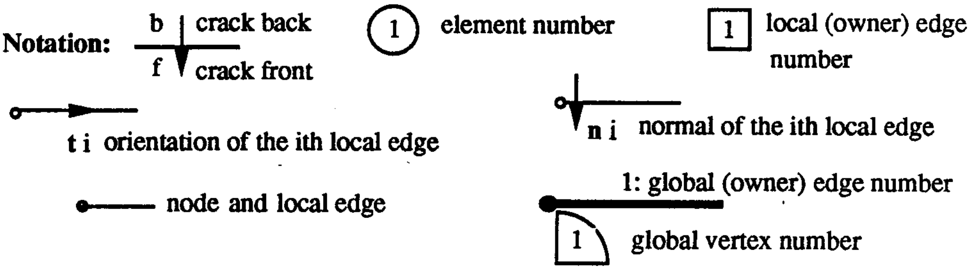

Fig. 3.5: Example of Exhaustive Enumeration (continued in the next page)

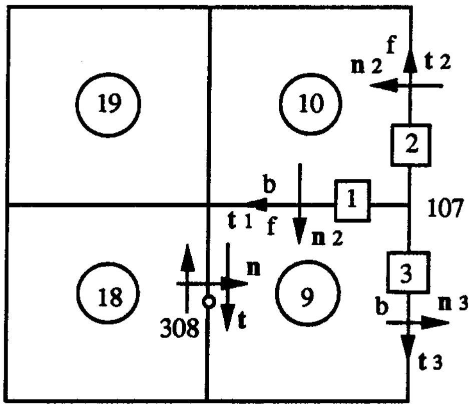

e) Orientation t i and normal n i for owneredges incident to corner node 107 and midside node 308

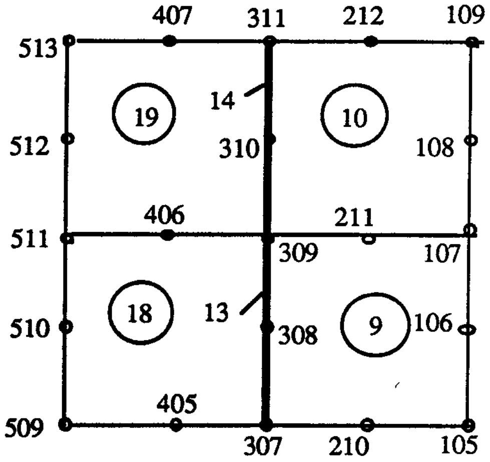

f) Inserted reinforcing element

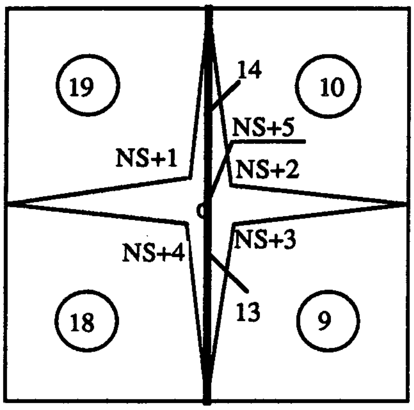

g)Exhaustive enumeration for the example in Fig. 3.5 f)

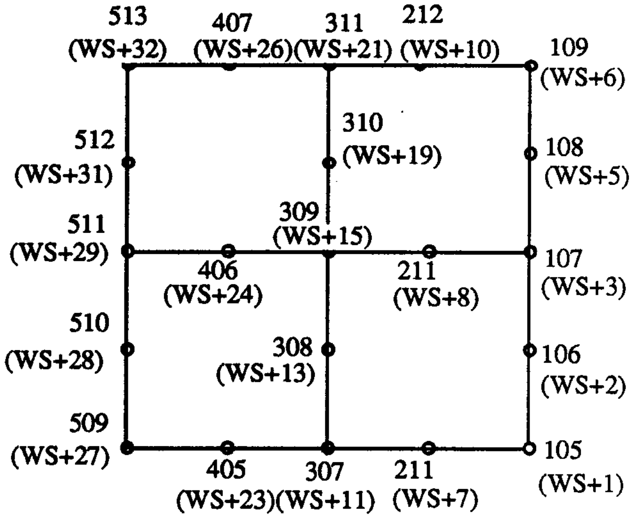

h) Correspondence between input nodal number and initial nodal number

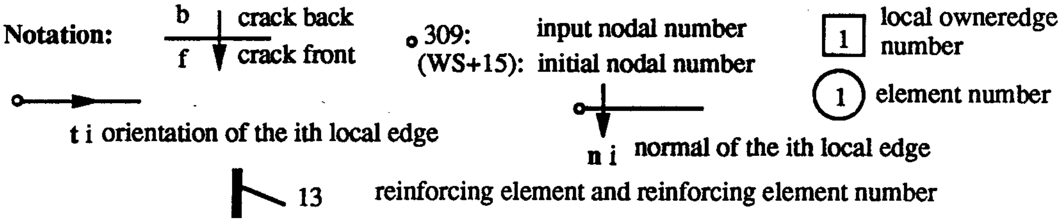

Fig. 3.5: Example for Exhaustive Enumeration

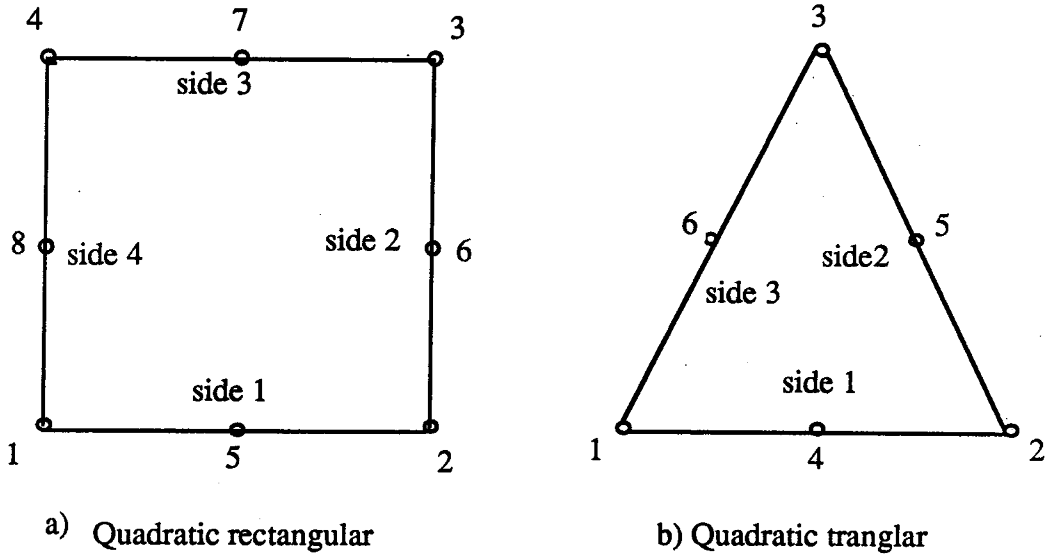

a) Quadratic rectangular

b) Quadratic tranglar

Fig. 3.6 Local Nodal and Side Numbering Schemes

CHAPTER 4

SIMULATION OF CRACK PROPOGATION

4.1 Introduction

In the section 3.4, the approach for simulation of crack propagation was briefly outlined. The detailed description of the procedures used is presented in this chapter.

The procedure for crack propagation includes three parts:

1) Initiate new cracks. At every input node, examine the satisfaction of crack initiation criteria for every uncracked edge emanating from it. If the criteria are met, change the crack flag accordingly.

2) Update the adjacency relations. For every newly introduced split node, activate the associated nodal splitting numbers, and introduce them into the element-nodal incidence array NPELM for the incidental elements. Update current crack front and back nodal numbers as well.

3) Find the relative normal and tangential displacements of a pair of split nodes on both faces of every crack and define the nodal stresses and nodal forces accordingly.

Procedures for the first two parts will be discussed in Sects. 4.2 and 4.3, respectively. For the third part, the procedure will be described in Chapter 5.

4.2 Determination of Element Nodal Stress

4.2.1 Scheme of Integration

Because the strategy is to introduce cracks at boundaries of elements according to the state of stress at the element node, determination of nodal stress becomes an unavoidable step in the procedure. In this study, the quadratic triangular element with the integration scheme (Zienkiewicz, 1971) shown in Fig. 4.4 is used because of the following considerations.

1) Triangle elements can provide more edges emanating from one vertex in a regular mesh, than quadrilateral elements.

2) The coincidence of integration points for the stiffness matrix and element node eliminates the requirement of extrapolating (from

integration points) or extra computing (through nodal strain) for nodal stresses. In the case where the constitutive relation between stress and strain for the element is nonlinear, it eliminates the requirement of extra memory for accumulated nodal stresses in an incremental approach.

4.2.2 Averaging Nodal Stresses at Vertices

The stresses at a vertex are obtained by averaging the corresponding nodal stresses from all elements incident to this vertex. The principal stresses at the vertex are then calculated.

Two cases should be considered here. First, is the case where one or more cracks run through a vertex in the concrete material and divide the neighborhood at this vertex into sectors. In the example shown in Fig. 3.3b, a diagonal crack runs through the center node K from corner M to opposite corner N. The possibility for further cracking is examined separately on the two sectors formed by the 'through crack'.

In the first sector composed by elements 2, 3, 4, and 5, the stresses at vertex K+4 are obtained by averaging nodal stresses from element 2, 3, 4 and 5, and then the principal stresses and their orientation at vertex K+4 are calculated. The principal tensile stress and its orientation is used to check the cracking possibilities along edges (K+4)-C, edge (K+4)-D, and edge (K+4)-E at vertex K+4. This process is repeated in the other sector composed of elements 1, 8, 7 and 6.

The second case is when the vertex is located on a boundary between steel and concrete elements. As illustrated in Fig. 4.2a, the principal stress for concrete at vertex K is derived from the concrete elements 1 and 2, and the incident steel elements 3 and 4 are excluded from the evaluation.

4.3 Evaluation of Crack Situation

4.3.1 Crack Initiation Criteria

Tensile strength is adopted as the crack initiation criterion. For a pair of unsplit vertexuses which are located on the two edgeuses of an owneredge, four different cases characterized by the material types of the solid elements, on both sides of the edge, are described below in Sects 4.3.1.1 to 4.3.1.4.

4.3.1.1 Case 1: Concrete Elements on Both Sides of the Edge

Because the unsplit pair of vertexuses are located on the two edgeuses of an edge located inside continuous concrete material, the orientation of the impending crack should be perpendicular to the orientation of the principal stress. Because the predefined edge is not likely to be exactly perpendicular to the orientation of principal stress, a tolerance $ß_t$, or a "threshold" value, is selected so that when the angle between the direction of the normal for the edge at the vertex and the orientation of the principal stress is smaller than this tolerance, a crack is deemed initiated at the vertex along the direction of the edge, provided that the principal stress is larger than tensile strength, denoted by f_t'.

Two examples are shown in Fig. 4.1. In Fig 4.1a, vector **p** represents the principal stress at vertex K, and the unit vector n represents the two possible normal directions for edge BF, one for edge KB and one for edge KF. Assume vector **p** falls into the the sectors bounded by the two lines separated by angle $2ß_t$ and centered about the normal. For this condition node K is split along both edges KB and KF, as shown in Fig. 4.1b. The criteria for cracking along an edge at vertex K inside the concrete material can be described mathematically as

$$P \geq f_t' \quad \text{and} \qquad (4.3.1a)$$

$$\cos(\mathbf{p}\wedge\mathbf{n}) \geq \cos(ß_t) \qquad (4.3.1b)$$

where P is the norm of vector **p** and **p**^**n** is the angle between vectors **p** and **n**. Fig. 4.1c and Fig. 4.1d show another example centered at node K from which eight edges emanate. The angle $ß_t$ is used to define the limit of "closeness" of an edge to the principal stress orientation to be split. Therefore, $ß_t$ is mesh dependent. For the mesh in Fig. 4.1a, $ß_t$ is set to be 45° so a crack will be initiated on one of the four edges emanating from vertex K wherever the principal stress exceed f_t'. For the mesh in Fig. 4.1c, $ß_t$ is set to be 22.5°.

A classical plastic stress-strain relation is adopted for concrete behavior. Because the yield strength for tension is specified equal to the yield strength for compression, which is much higher than the tensile strength for boundary cracking, f_t', discrete cracking along element boundaries dominates the behavior in tension.

4.3.1.2 Case 2: Interface between Concrete and Steel Elements

This case simulates the boundary between a solid steel reinforcing element (as opposed to a line element) and the surrounding concrete. Due to the material discontinuity at the edge and a lower adhesive strength, f'_{sc}, between concrete and steel than the concrete tensile strength, f'_t, only the concrete stress component perpendicular to the edge at the vertex is considered. If this stress component is larger than the adhesive strength f'_{sc}, a crack is deemed to be initiated at the vertex along the boundary of the two materials.

4.3.1.3 Case 3: Steel Elements on Both Sides of the Edge

Because the edge considered is located inside the steel material, the constitutive relations for steel will apply. In this study, classical plastic stress-strain relations are adopted for steel in both tension and compression. A yield stress f_{ys} is specified and, as it is reached, the steel will "flow" along the yield surface. Discrete cracking at the boundary of two solid steel elements, or rupture of steel, is eliminated by specifying a very high tensile strength for boundary cracking.

4.3.1.4 Case 4: Reinforcement Embedded between Two Concrete Elements

This is a special case of Case 1, and the criteria for nodal splitting is the same. However, after nodal splitting, three nodes will exist at the same initial geometrical position: two nodes for the pair of concrete faces of the crack, and one node for the reinforcement truss element which is no longer attached at the vertex to the incidental solid elements. Fig. 4.3 gives an example.

Although the crack pattern of Fig. 4.3b creates a mechanism which cannot sustain force in the lateral direction on the truss element, test runs for the condition have not exhibited numerical problems.

4.4 Updating Adjacency Relations for New Cracks

4.4.1 Updating NPELM and ID Arrays

4.4.1.1 Procedure for Assembly of Stiffness Matrix in NORCO

In the finite element procedure adopted herein, direct solution strategies using algorithms based on Gaussian elimination are used with the the upper triangle of the stiffness matrix in a skyline-like form as a one-dimensional array.

Before the element stiffness matrix is assembled into this one-dimensional array, the height of the skyline columns for the stiffness matrix are calculated and the accumulation of these heights is carried out so that the addresses of the diagonal elements of the stiffness matrix in the one-dimensional array are known.

To evaluate the height of the skyline columns, two arrays are needed. These two arrays in the finite element program NORCO (Balaknishnan and Murray, 1989), which is the program adopted as a point of departure for this study, are the element-nodal incidence array NPELM and array ID which have been defined in Sect. 3.6.2 and Sect. 3.4, respectively.

By processing elements one by one, the maximum equation number differences between a node and all nodes incident to it can be determined from array NPELM and ID, and the heights of the columns of the skyline for stiffness matrix can be calculated from these.

4.4.1.2 Procedure for Changing Topology of Structure

For problems where the topology of the structure is never changed, the assessment of total length of the one-dimensional stiffness matrix array, and the addresses of diagonal stiffness terms, is only done once in the "data preparation phase" and never altered in the "problem run phase".

But if the topology of structure changes during the analysis, as occurs in this study, the assessment of addresses for diagonal stiffness terms has to be repeated frequently in the "problem run phase".

The procedure of exhaustive enumeration for nodal splitting was described in detail in Chapter 3. Every vertex is associated with several vertexuses. If a nodal splitting number for one vertexuse is taken by any element, as its element global nodal number, the nodal splitting number is said to be active. Otherwise it is inactive. That is, active nodal splitting numbers are inserted into array NPELM(12, NPELM), whereas inactive nodal numbers are not. The array ID(2,NMNOD) is used as an activity code in the crack updating process: 0 for an active DOF and 1 for an inactive or restrained DOF. When all nodes are processed, the zero values of the ID array are replaced by the numbers of the active DOF's accumulated from the first node. This new value becomes the equation number for the DOF of the node. The unit values in the ID array, for inactive or restrained DOF's, are replaced by zero.

In other words, the equation number for a DOF of an active node, if the DOF is not one of predefined zero displacement, is set to a nonzero equation number. The equation number for each DOF of an inactive node is set to zero. An inactive node and an active node with 2 DOF of predefined zero displacement both have two zero equation numbers. The former is not included in any loop of element, so it is 'isolated' from the structure. The latter is included in the loop of at least one element, so its roll is indicated as such by the nodes it relates in the loops.

As new discrete cracks are introduced, which means vertices are being split and new vertexuse nodal splitting numbers are being activated, both the NPELM and ID array are updated. Based on these updated arrays, the total length of the one dimensional array for the stiffness matrix, and the addresses for the diagonal terms in the array, are recomputed. Then the element stiffness matrices are assembled to the global stiffness matrix using the newly produced addresses for the one-dimensional stiffness matrix array.

The external nodal forces equivalent to external load (distributed or concentrated) are assembled to the right hand side of the equilibrium equations according to the newly produced ID array. The value of equivalent nodal forces integrated from element stresses are also assembled with opposite sign accordingly. When the equilibrium equations are satisfied, the effect on displacements due to new cracks is determined.

4.4.2 Updating Adjacency Relations

The two global arrays of topological information, NCRLC and NCRNN, which were constructed in the "data preparation phase" (see Sect. 3.6.4) include all the information for crack pattern recognition, and are modified to record crack propagation.

4.4.2.1 General Processing at a Vertex

The strategy of crack simulation processing is:

a) find the first cracked edge NM1=NM emanating from a vertex NV in ascending order (or in a clockwise circle around the vertex, i.e- NM=1,2,...) by checking NCRNN(NV,3,NM);

b) record the local current cracked edge number NMZ=NM;

c) insert the crack front nodal splitting number (CFNSN) NCRNN(NV,10,NMZ) of the cracked edge NMZ into the element- nodal incidence array NPELM for the crack front element (CFEN) NCRNN(NV,6,NMZ); assign CFNSN to the current crack front nodal number (CCFNN) NCRNN(NV,1,NMZ); deactivate the old CCFNN and activate new CCFNN in the ID array;

d) insert CFNSN, NCRNN(NV,10,NMZ), into the element-nodal incidence array NPELM for the crack back element (CBEN) of the next edge NM in a counterclockwise circle around the vertex, (i.e.- NM=NMZ-i, i=1,2,...); assign CFNSN to the current crack back nodal number (CCBNN) of the next edge NM; deactivate the old CCBNN in the ID array;

e) if the next edge NM is an uncracked edge, repeat the procedure in step d) for CFEN and CCFNN of edge NM;

f) if the next edge NM is a cracked edge and NM does not equal NM1, that is, the counterclockwise circle starting from edge NM1 is not completed, repeat step b) to e);

g) if NM equals NM1, the updating processing at node NV is completed.

A flow chart of the general processing is given in Fig. 4.5. The example shown in Fig. 3.5 is illustrated in Fig. 4.6 to describe the processing. The following six steps give details of the processing at input node 309 of the example. Table 4.1a is produced to show the evolution of the numbers at vertex 309 in the example.

Step 1 : The crack situation at the vertex 309 is shown in Fig. 4.6a. The crack flags for edges emanating from node 309 contained in NCRNN(NV,3,NM) are checked in ascending order as shown by the clockwise circle a. As the first edge with a zero or negative valued crack flag is found, that is edge 2 (NM=2) in Fig. 4.6a, the checking of the edge crack flags is stopped. A counter KL2 is set to zero.

Step 2 : The counter NMZ which records the current crack edge number is set to 2. The CFNSN for edge 2, NCRNN(NV,10,2) which equals WS+15 as shown in Tables 3.10 and 4.1a, is brought into the element-nodal array NPELM of the crack front element, which is NCRNN(NV,6,2) or 19 in the example, to replace the CCFNN, NCRNN(NV,1,2) which is also WS+15, so the replacement update is trivial. The newly introduced CCFNN is stored in a temporary array KMEM at the vertex for later reference.

The activity code of the old CCFNN should be deactivated because the new CCFNN will be activated. But this deactivation is executed only after confirmation that none of the numbers in temporary array KMEM coincide with it. At edge 2, the current crack front number is the only number in array KMEM, so no deactivation is carried out.

The updating process at the crack front of edge 2 is trivial because the old CCFNN before updating is the same as the newly introduced CCFNN: both are WS+15. But this is not the case for the crack back of edge 1.

Step 3 : Beginning from crack front of edge 2, edges emanating from node 309 are processed in descending order as shown by the counterclockwise circle b in Fig. 4.6a. The first edge following is edge 1. Counter KL2 is increased from 0 to 1. As in Step 2, the crack back and crack front of edge 1, the CCFNN and CCBNN are equal the latest crack number, which is WS+15. So the updating process at edge 1 is trivial.

Step 4 : The next edge being processed in descending order is edge 4 (NM=4). The counter KL2 is increased from 1 to 2. Because the CCBNN is equal the latest crack number, the updating process for the crack back of edge 4 is also trivial. Since the crack flag for edge 4, NCRNN(NV,3,4) is zero which indicates edge 4 is an incipient crack, the procedure in Step 2 is repeated. That is, the crack front splitting number, NCRNN(NV,10,4), which is WS+17 (Tables 3.10 and 4.1) is different from CCFNN of edge 4, WS+15. The global nodal number WS+15 in the array NPELM for the crack front element 9 is replaced by WS+17, Node WS+17 is activated by setting the components of ID array for WS+17 to zero. But deactivation of DOF for the old CCFNN, WS+15, is not carried out, because it is stored in array KMEM. The newly introduced CCFNN WS+17 is added to temporary array KMEM.

Displacements of node WS+15 are assigned to WS+17, and then the CCFNN of edge 4, WS+15, is replaced by WS+17. The counter NMZ which records the latest crack in processing is renewed to 4 (NM=4).

Step 5 : The next edge in descending order is edge 3 (NM=3). Counter KL2 is increased from 2 to 3. As edge 3 is uncracked, the CCFNN and CCBNN which are both WS+15, are replaced by the crack front number of latest crack NMZ (edge 4), WS+17. Because WS+15 is in KMEM, deactivation of WS+15 is not carried out.

Step 6 : The next edge in descending order is edge 2, and counter KL2 is increased to 4. The current crack back number for edge 2, WS+15, is replaced by the crack front nodal number of latest crack NMZ, WS+17. Because the counter KL2 is equal to the total number of edges emanating from node 309, NMM, the updating processing at node 309 is completed.

It is emphasized that the first cracked edge, edge 2, obtains its crack front nodal number WS+15 from its nodal splitting number, NCRNN(NV,10,2), but its crack back number is determined at the end of the processing because this crack back number is decided by the crack front number of the latest crack NMZ(edge 4), not by edge 2 itself.

Figure 4.6b shows the result of the above processing at node 309.

4.4.2.2 Discussion of Updating Process

The trivial updating process which occurred in Steps 2 and 3 of the example illustrated in Sect. 4.4.2.1 disappears if the incipient crack passing vertex 309 is horizontal as shown in Fig. 4.7a. The updating of nodal numbers is represented in Table 4.1b. The first incipient crack is edge 1, and its crack front splitting number, WS+18 (Table 3.10), is different from its CCFNN which is WS+15 (also its initial nodal number in the case). Processing at the next edge in descending order, uncracked edge 4, is also not trivial. The CCFNN WS+15 is replaced by the latest crack front number WS+18. The second incipient crack, edge 3 brings its CFNSN, WS+16 to its crack front element 10 to replace WS+15. The processing at edge 2 is similar to that at edge 4 but WS+15 is replaced by WS+16 instead by WS+18.

The result of the complete updating is shown in Fig. 4.7b.

For one crack pattern (either vertical or horizontal, passing through node 309), there are 4 updating processings corresponding to the 4 edges emanating from the node. In the total of 8 updating processing associated with the two crack patterns there are 2 which are trivial (Fig. 4.6b). The probability of trivial processing is 1/4.

For the case where 8 edges emanate from a vertex, an example is given in Fig. 4.8.

The 4 possible crack patterns where cracks run straight through the patch involve a total of 4•8=32 updating processings at edges, and 4 of them are trivial as shown in Fig. 4.8c. So the probability of trivial processing is 1/8.

4.4.2.3 Non-Strength Crack Criterion

Cracks which change orientation at a vertex, such as that shown in Fig. 4.8f, need somewhat more discussion. For the treatment of the special cases, such as shown in Fig. 4.9, a non-strength crack criterion is added.

Assume a progressive crack propagates from vertex N to L of Fig. 4.9a, as shown in Fig. 4.9b. The nodes N and L are split because the crack strength criterion is met at these vertices. That is, the value of the principal stress is larger than tensile strength and the angle between the orientation of the principal stress and the normal of an edge **n** is smaller than the tolerance β_t (Sect. 4.2.2.1). But the cracking criterion is not met at vertex K along edge KLN which is local edge 6. Two possibilities arise: one is that the stress of the principal stress is smaller than the tensile strength, the other is that the value is larger than the tensile strength, but the orientation of the principal stress deviates from the edge normal **n** by more than the tolerance β_t.

If the principal stress at vertex K exceeds the tensile strength but the normal of edge 3 deviates from the orientation of the principal stress by less than the tolerance β_t, a crack is initiated at the vertex along edge 3. This is represented by setting the crack flag NCRNN(NV,3,3)=0. But if the crack criterion is not satisfied at edge 6 at vertex K, the updating process as described in Sect. 4.4.2.2 cannot make the crack run through vertex K with this change of orientation. Such a 'point pinned crack' shown in Fig. 4.9c is not a realistic phenomena, and a supplementary non-strength crack criterion is introduced to eliminate it. The criteria state that an edge is cracked (i.e. the node is split) at a vertex if:

1) For a quadratic element there are another two nodes along the edge which are already cracked or for which cracking is incipient (in the example of Fig. 4.9, these nodes are L and N on edge 6). For a linear element, only one other node needs be cracked or be in a state of incipient cracking; and

2) At least one edge emanating from the vertex is already cracked at the vertex (or cracking is incipient). In the example, these are edges 3 and 7.

The result of the application to the example is shown in Fig. 4.9d.

As a crack changes orientation at a vertex, the "point pinned crack" described in Fig. 4.9 is not always the case. Another situation is that the crack propagates from node N to L and then to K. Even if it then changes orientation to M no problems arise, because a "point pinned crack" does not occur, and the non-strength crack criteria is not required.

4.4.2.4 Variations in Crack Processing

4.4.2.4.1 Processing at a Midside Node

The examples shown in Figs. 4.10a and 4.10b are used to illustrate midside node processing. If a vertex with input node 308 is to be split, the back element 9 (NCRLC(7,6,2) shown in Table 3.8) will be assigned the crack back number WS+14 (NCRNN(7,2,2) in Table 3.8) to replace WS+13. The component of the ID array for WS+14 is activated and node WS+14 is assigned an initial displacement the same as that of node WS+13.

4.4.2.4.2 Processing at a Boundary Node

This situation is illustrated in Fig. 4.10a and Table 3.8. Assume a crack is initiated at edge 2 (307-308-309) and the edge is processed in a descending order, two free boundary edges with crack flag equal -3 are encountered. A rule is defined which states that: (a) a boundary edge with a zero crack front nodal number (edge 1, i.e. - 307-405-509) is processed as an uncracked edge; and; (b) a boundary edge with a nonzero crack front nodal number (edge 3, i.e. - 307-210-105) is processed as a cracked edge. This rule does not have any physical meaning but is just for convenience so an enclosed processing circle used at an inner vertex can be applied and, as shown in the example of Fig. 4.10a, processing edge 3 as a cracked edge brings nodal number WS+12 into element 9. Free edges are bypassed by crack updating processing because they are initially 'real' boundaries as designated by NCRNN(NV,3,NM)= -3. For a boundary representing a line of symmetry in a structure (crack flag assigned as inner edge with NCRNN(NV,3,NM)=1), cracking along the boundary is simulated by releasing the restraint by updating the ID array from 1 to zero, so that it becomes a cracked free edge.

The crack propagation for the example shown in Fig. 3.5h is given in Fig. 4.10 where a crack propagates from input node 307 to 309. The cracking or splitting at these three nodes can occur in different iterations if the crack is gradually propagating, or can occur in one iteration if the crack criteria is met at these three nodes simultaneously. The arrays NPELM and ID for the uncracked patch shown in Fig. 3.8 are listed in Table 3.16 and Table 4.2 respectively. The same arrays for the cracked patch in Fig. 4.10c are given in Table 4.3 and Table 4.4.

Table 4.1a Numbers in Updating Processing for Fig. 4.6

Step No		NM	KL2	NMZ	NCRNN (NV,3,NM)	NCRNN (NV,1,NM)	NCRNN (NV,2,NM)	NCRNN (NV,10,NM)	NCRNN (NV,6,NM)	ID for NCRNN (NV,1,NM) before updating	KMEM
1											
		2	0	0	0	WS+15	WS+15	WS+15	19	0	0
2	b	2	0	2	0	WS+15	WS+15	WS+15	19	0	WS+15
	a	2	0	2	1	WS+15	WS+15	WS+15	19		WS+15
3	b	1	0	2	1	WS+15	WS+15	WS+18	18	0	WS+15
	a	1	1	2	1	WS+15	WS+15	WS+18	18		WS+15
4	b	4	1	2	0	WS+15	WS+15	WS+17	9	0	WS+15
	a	4	2	4	0	WS+17	WS+15	WS+17	9		WS+15 WS+17
5	b	3	2	4	1	WS+15	WS+15	WS+16	10	0	WS+15 WS+17
	a	3	3	4	1	WS+17	WS+17	WS+16	10		WS+15 WS+17
6	b	2	3	4	0	WS+15	WS+15	WS+15	19	0	WS+15 WS+17
	a	2	4	4	0	WS+15	WS+17	WS+15	19		WS+15 WS+17

→ Completed Updating at Vertex 309 Due to KL2=NMM, Total Edge No. Emanating from vertex 309

Notation: b- Before Updating
a- After Updating

ID= 0 -deactivated
1 - activated

Table 4.1b Numbers in Updating Processing for Fig. 4.7

Step No		NM	KL2	NMZ	NCRNN (NV,3,NM)	NCRNN (NV,1,NM)	NCRNN (NV,2,NM)	NCRNN (NV,10,NM)	NELM NCRNN (NV,6,NM)	ID for NCRNN (NV,1,NM) before updating	KMEM
1		1	0	0	0	WS+15	WS+15	WS+18	18	0	0
2	b	1	0	1	0	WS+15	WS+15	WS+18	18	0	WS+18
	a	1	0	1	0	WS+18	WS+15	WS+18	18		WS+18
3	b	4	0	1	1	WS+15	WS+15	WS+17	9	1	WS+18
	a	4	1	1	1	WS+18	WS+18	WS+17	9		WS+18
4	b	3	1	1	0	WS+15	WS+15	WS+16	10	1	WS+18
	a	3	2	3	0	WS+16	WS+18	WS+16	10		WS+18 WS+16
5	b	2	2	3	1	WS+15	WS+15	WS+15	19	1	WS+18 WS+16
	a	2	3	3	1	WS+16	WS+16	WS+15	19		WS+18 WS+16
6	b	1	3	3	0	WS+18	WS+15	WS+18	18	0	WS+18 WS+16
	a	1	4	3	0	WS+18	WS+16	WS+18	18		WS+18 WS+16

→Completed Updating at Vertex 309 Due to KL2=NMM, Total Edge No. Emanating from 309

Notation: b- Before Updating
a- After Updating

ID=1 deactivated
0 activated

Table 4.2 ID Array for the Uncracked Patch in Fig.4.10

Nodal No. I = WS+	1	2	3	4	5	6	7	8	9	10	11	12	13	14	15	16	17	18	19	20	21
ID(1,I)	0	0	0	1	0	0	0	0	1	0	0	1	0	1	0	1	1	1	0	1	0
ID(2,I)	0	0	0	1	0	0	0	0	1	0	0	1	0	1	0	1	1	1	0	1	0

Notation: 0- activated, 1- deactivated

Table 4.3 Array NPELM(I,J) for Fig. 4.10

J = Elem. No.	Nodal No.	I= Local Nodal No							
		1	2	3	4	5	6	7	8
9	IP	307	105	107	309	210	106	211	308
	RI=WS+	11	1	3	15	7	2	8	13
	U =WS+	12	1	3	17	7	2	8	14
10	IP	309	107	109	311	211	108	212	310
	RI=WS+	15	3	6	21	8	5	10	19
	U= WS+	17	3	6	21	8	5	10	19
18	IP	509	307	309	511	405	308	406	510
	RI=WS+	27	11	15	29	23	13	24	28
	U= WS+	27	11	15	29	23	13	24	28
19	IP	511	309	311	513	406	310	407	512
	RI=WS+	29	15	21	32	24	19	26	31
	U =WS+	29	15	21	32	24	19	26	31

Notation: IP- Input Nodal Number, RI- Redefined Initial Number, U-Updated Nodal No.

Table 4.4 ID Array for the Cracked Patch in Fig.4.10

Nodal No. I = WS+	1	2	3	4	5	6	7	8	9	10	11	12	13	14	15	16	17	18	19	20	21
ID(1,I)	0	0	0	1	0	0	0	0	1	0	0	0	0	0	0	1	0	1	0	1	0
ID(2,I)	0	0	0	1	0	0	0	0	1	0	0	0	0	0	0	1	0	1	0	1	0

Notation: 0- activated, 1- deactivated

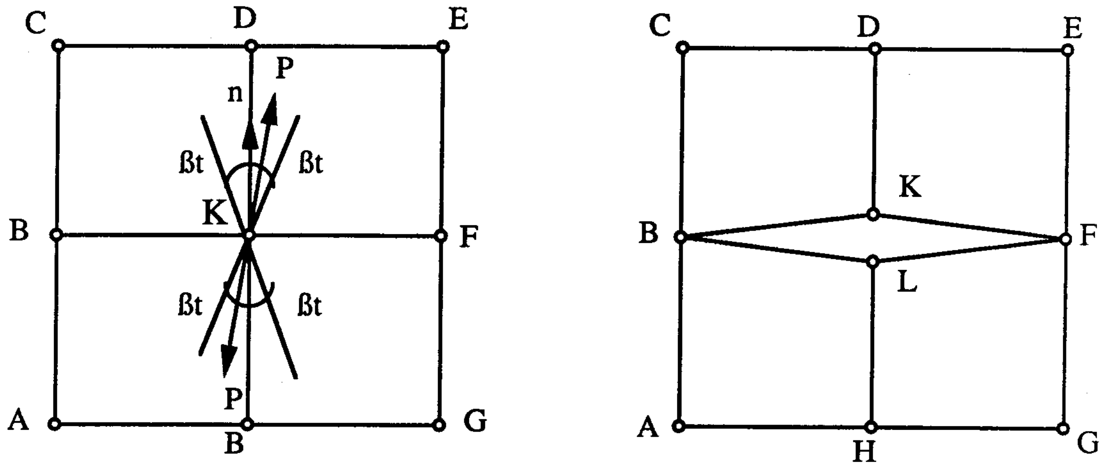

(a) 4 Edges Emanating from K, before Cracking

(b) 4 Edges Emanating from K, after Cracking

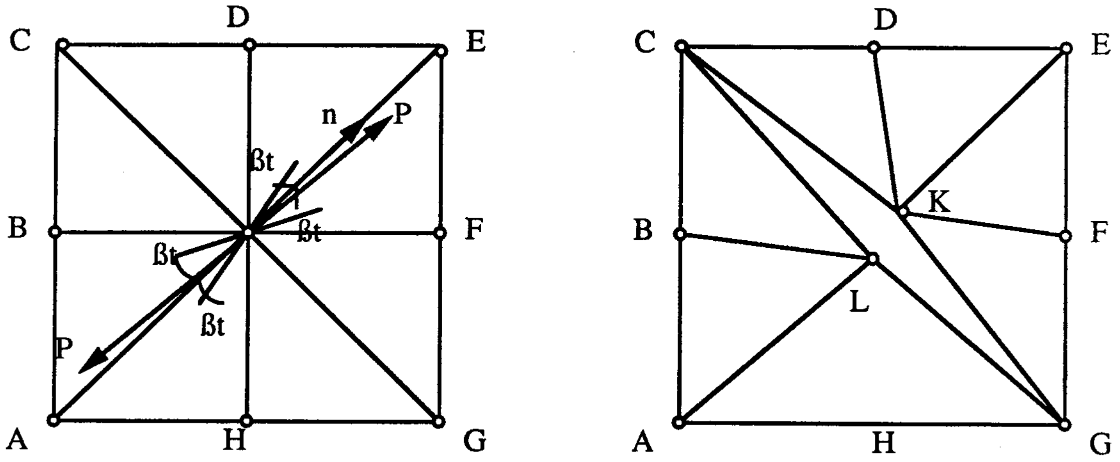

(c) 8 Edges Emanating from K, before Cracking

(d) 8 Edge Emanating from K, after Cracking

Fig. 4.1: Cracking Criterion for Interior Concrete Edge

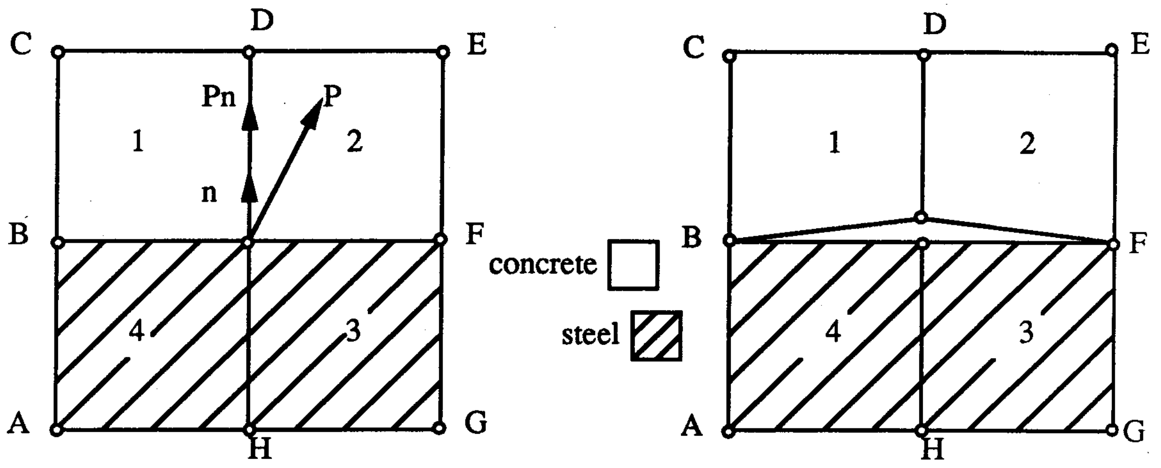

(a) Before Cracking

(b) After Cracking

Fig. 4.2 Cracking Criterion for Concrete-Steel Boundary

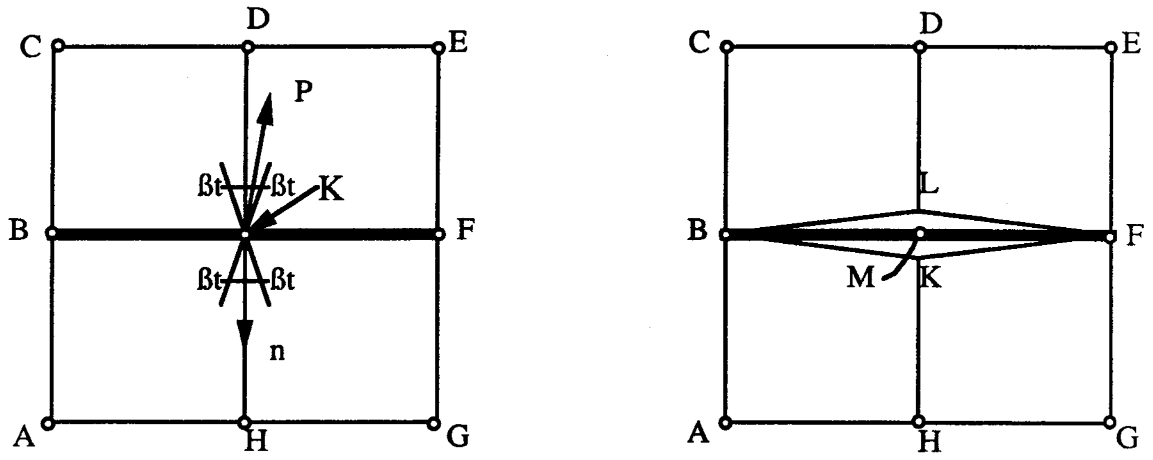

(a) Before Cracking

(b) After Cracking

Fig. 4.3 Cracking Criterion for Stirrup on Element Boundary

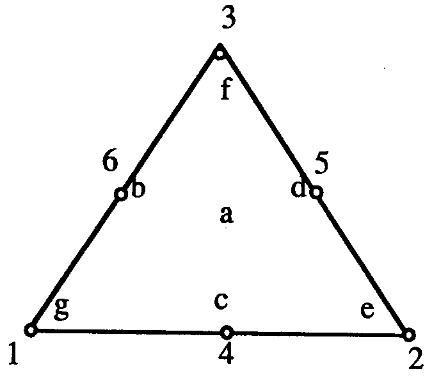

Local Nodal No		6	4	5	2	3	1
Integral Point No	a	b	c	d	e	f	g
Local Area Co-ordinates	1/3	1/2	0	1/2	1	0	0
	1/3	1/2	1/2	0	0	1	0
	1/3	0	1/2	1/2	0	0	1
Weight=1/120×	27	8	8	8	3	3	3

Fig. 4.4 Integration for Quadratic Triangular Element

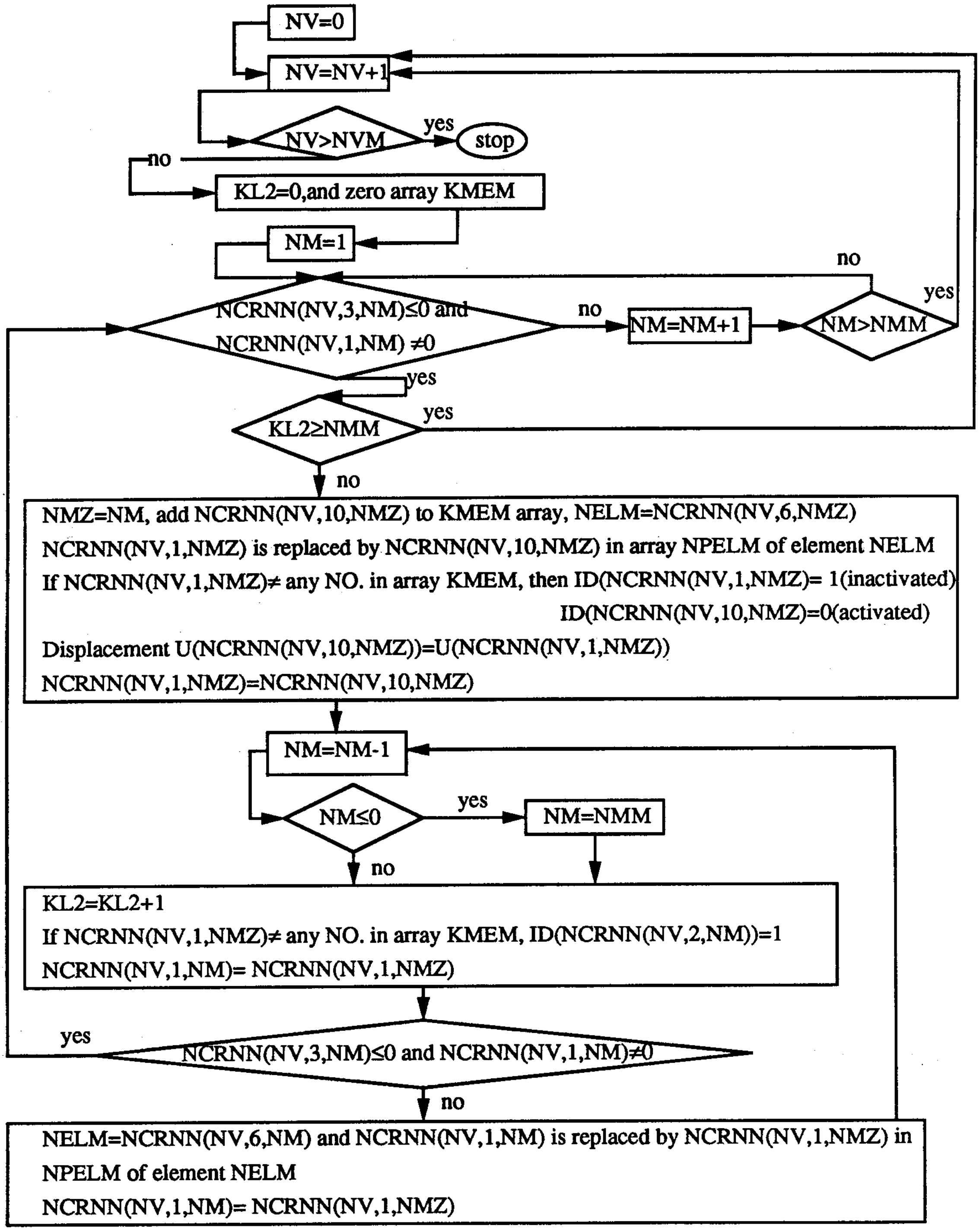

Fig. 4.5 Flowchart for Updating Adjacencies at A Vertex

(Subroutine PARC4)

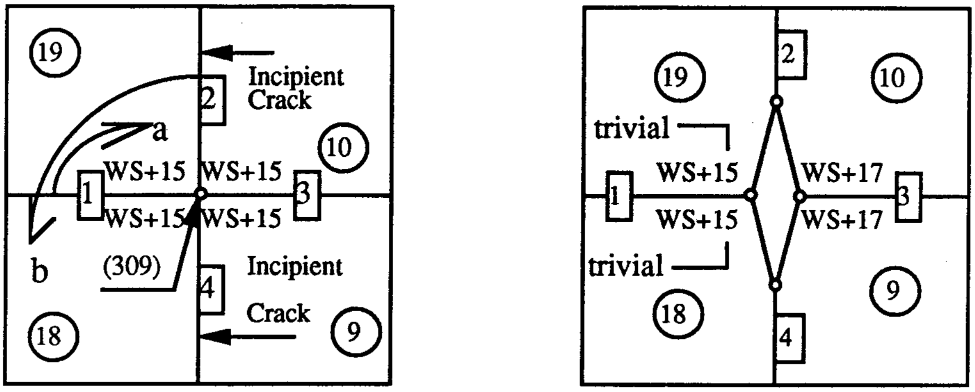

(a) Before Updating (b) After Updating

Fig. 4.6 Example for Vertical Crack Simulation

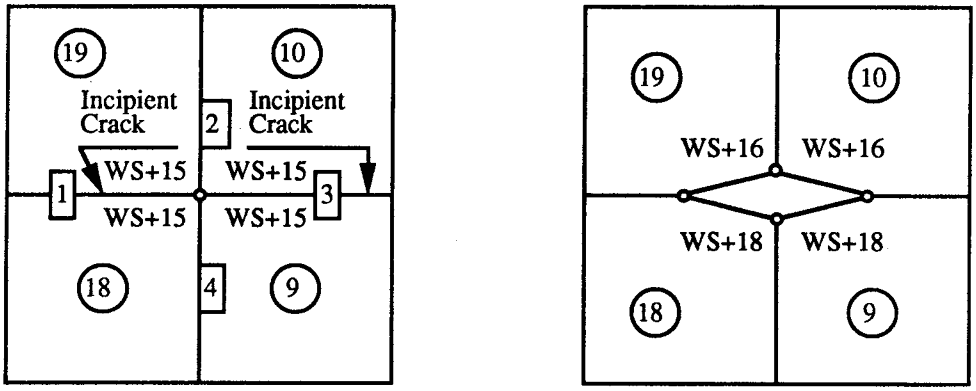

(a) Before Updating (b) After Updating

Fig. 4.7 Example for Horizonal Crack Simulation

Notation :

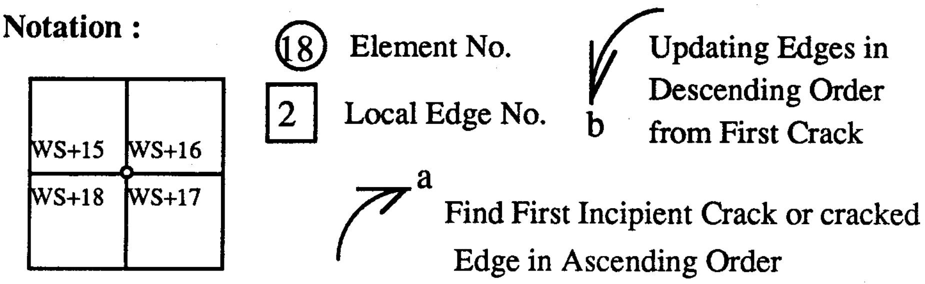

Exhaustive splitting No at 309

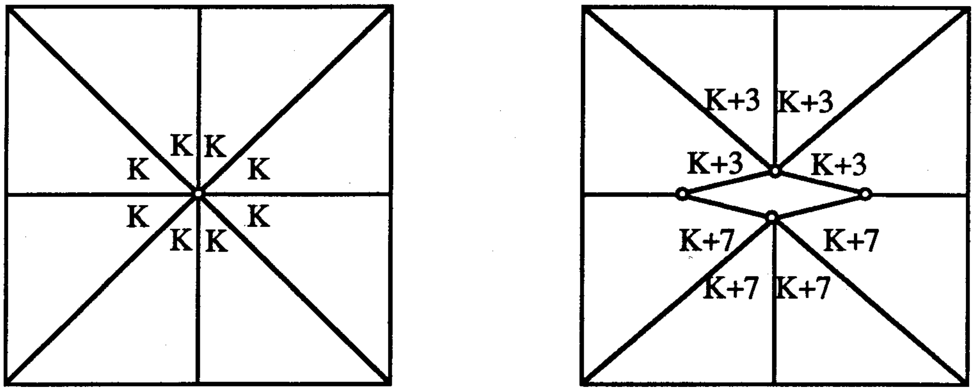

(a) Uncracked State

(b) Horizontal Crack

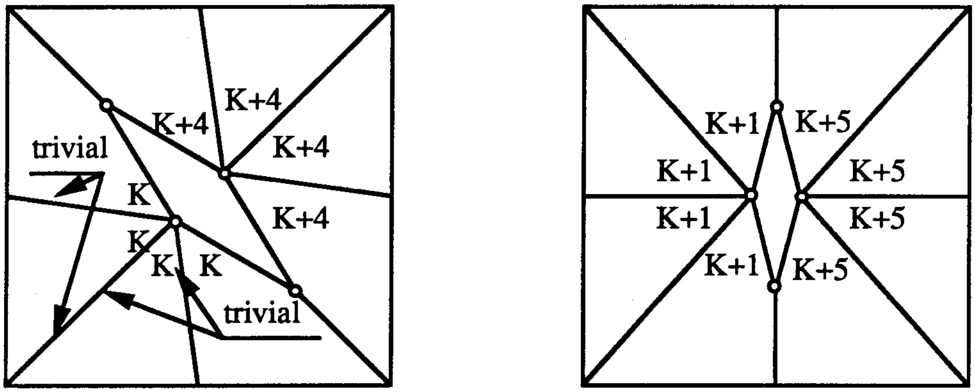

(c) 135° Inclined Crack

(d) Vertical Crack

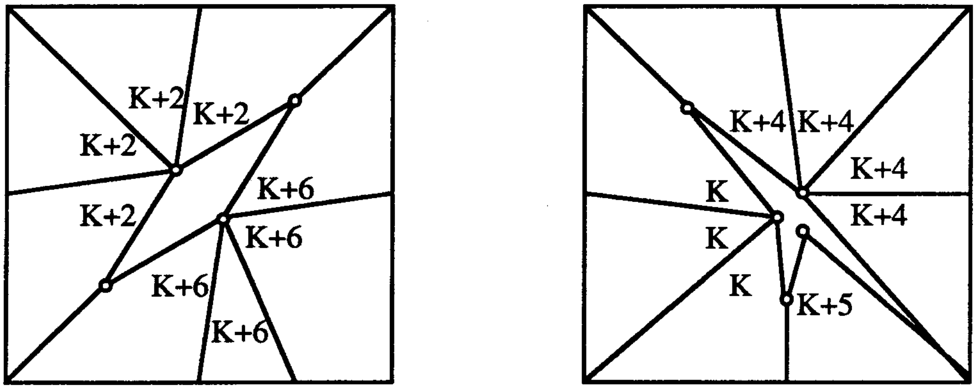

(e) 45° Inclined Crack

(f) Crack Changing Orientation
at A Vertex

Fig. 4.8 Example for 8 Edges Emanating from A Vertex

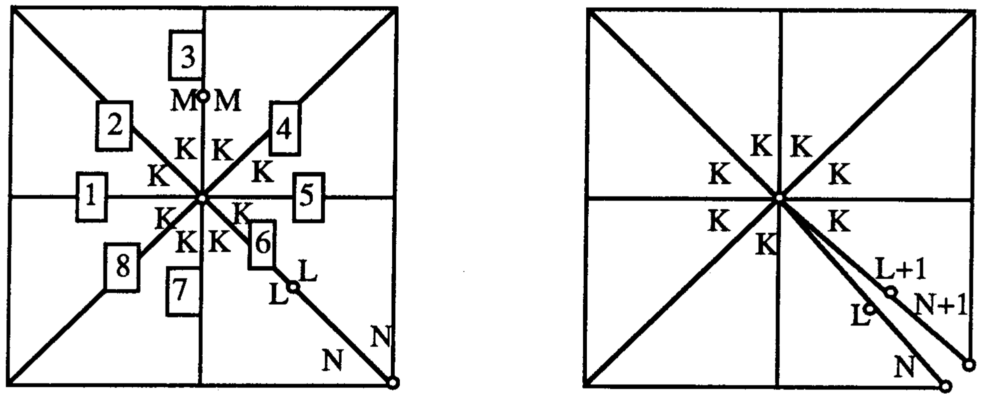

L = midside node

(a) Uncracked State

(b) Crack Propagates Passing Vertices N and L

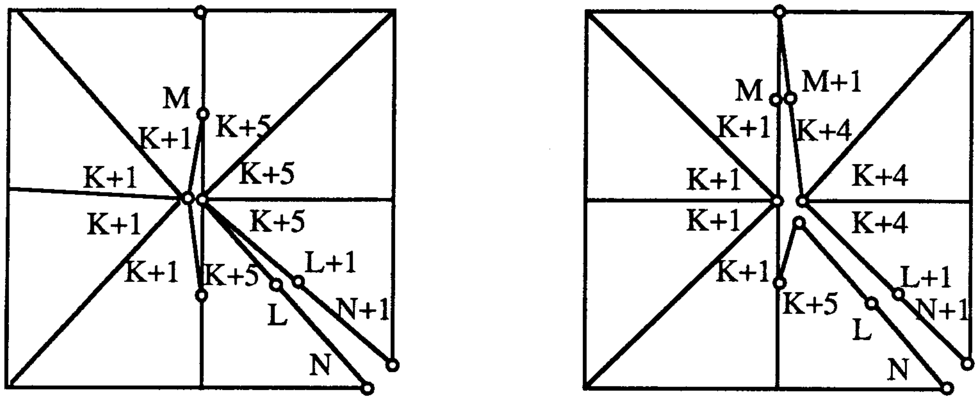

c) Crack Pined at Vertex K

d) Application of Nonstrength Crack Criteria

Fig. 4.9 Example Application of Non-Strength Crack Criterion

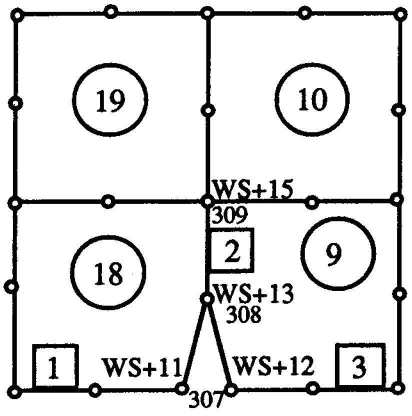

a) First Iteration

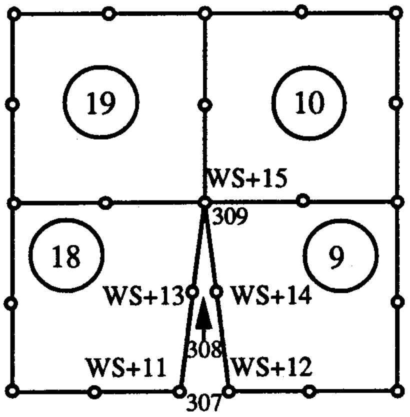

b) Second Iteration

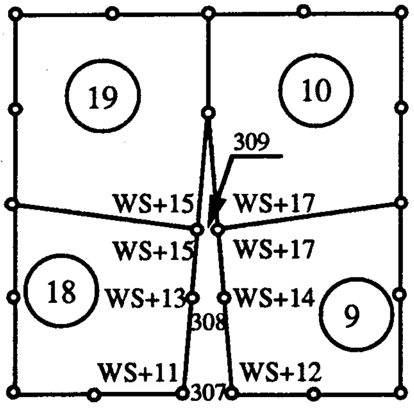

C) Third Iteration

Fig. 4.10 Example for Crack Propagation

CHAPTER 5

CONSTITUTIVE RELATIONS AT CRACK FACES

5.1 Introduction

As described in Chapter 2, a long crack fracture process zone and post-cracking softening are characteristics of concrete cracking. These characteristics also dominate the modeling methods for finite element analysis of concrete cracking. As a result, implementing the post-cracking softening relation into the analytical procedure becomes an essential part of finite element analysis of concrete structures.

In smeared crack analysis, this softening relation is realized through stress-strain relations at integration points inside solid elements. In the discrete crack approach, the crack is simulated by splitting nodes along a common boundary between two elements. In this study force-displacement relations at discrete crack faces are assigned based on concrete fracture mechanics. Normal stress across cracks is assumed to be related to crack width as discussed in Sects 5.2 and 5.3. Shear stresses, which might be transferred across crack interfaces, have been neglected.

5.2 A Normal Stress-Crack Width Relation

5.2.1 Determination of Crack Width

As described in Chapter 3, a pair of unsplit vertexuses represents a material point in a structure, with zero relative displacement between these two vertexuses. A pair of split vertexuses represents two different material points located on the two faces of a crack which runs through the vertex and is oriented along the owner edge associated with the two vertexuses. In the case of a pair of split vertexuses, the relative displacement between them is nonzero. This relative displacement can be projected in any direction to obtain its components in those directions. The components perpendicular and parallel to the owner edge are of most interest.

Two split nodes 1 and 2 located on opposite sides of a crack on owneredge **L** are shown in Fig. 5.1. Vector **n** is normal to edge **L** and vector **t** is defined perpendicular to vector **n** by rotating **n** 90° clockwise. According to the definition of "crack front" and "crack back", node 1 is on the "crack front" and node 2 on the "crack back" for the crack emanating from the split vertex in the direction **A** to **B**. The relative displacement between node 1 and node 2, $\mathbf{U}_{12}$, is written in terms of the displacement of node 1, $\mathbf{U}_1$, and the displacement of node 2, $\mathbf{U}_2$, as:

$$\mathbf{U}_{12}=\mathbf{U}_1-\mathbf{U}_2 \qquad (5.2.1.1)$$

where vectors are implied by the bold face symbols.

The projection of $\mathbf{U}_{12}$ on vector **n** is denoted by $\Delta\mathbf{U}_n$. Because $\Delta\mathbf{U}_n$ represents the distance between two crack faces along the direction normal to the crack, it is also called the "crack width" and denoted by W. The projection of $\mathbf{U}_{12}$ on vector **t** is denoted by $\Delta\mathbf{U}_t$, and it represents the relative displacement of the two crack faces along the direction tangential to the crack. The expression for the magnitudes of the components of $\Delta\mathbf{U}_n$ and $\Delta\mathbf{U}_t$ are as follows:

$$W=|\Delta\mathbf{U}_n|=\mathbf{U}_{12}\bullet\mathbf{n} \qquad (5.2.1.2a)$$

$$|\Delta\mathbf{U}_t|=\mathbf{U}_{12}\bullet\mathbf{t} \qquad (5.2.1.2b)$$

5.2.2 Relations between Tensile Stress and Crack Width

Post-cracking softening of concrete is a term used to describe the reduction in the average tensile stress transferred across the section where a crack is forming. The magnitude of the tensile stress decreases as the 'crack width' becomes greater. As discussed in Sect. 2.2, this concept has been established by a number of experimental investigations, and the tensile relationship of Gopalaratnam and Shah has been shown in Fig. 2.1.

Several linear and bilinear analytical relations between normal tensile stress and 'crack width' are widely used in finite element analysis of concrete cracking.

a) Linear Relation

As shown in Fig. 5.2, line AE divides the coordinate axis of deformation into two parts: the part on the right represents crack width, and the part on the left represents strain. The ultimate crack width at which tensile stress between two crack faces is assigned to decrease to zero is denoted as W_c. The two parameters, f_t' and f_c', represent the tensile strength and compressive strength of concrete respectively. If the crack width W is smaller than W_c, the tensile stress at W, σ_{tw}, is

$$\sigma_{tw}=f'_t(1-W/W_c). \qquad (5.2.2.1)$$

b) Bilinear Relation

To simulate the common feature exhibited in test curves, which show a steep drop after f'_t is reached, a bilinear relation is widely used in analysis (Gerstle, Ingraffea and Gergely, 1982, Petersson 1981). The bilinear relation proposed by Gerstle, Ingraffea and Gergely (1982), shown in Fig. 5.3 has been adopted in this study. If the area under the bilinear curve to the right of line AE in Fig. 5.3 is kept the same as that under the linear curve in Fig.5.2 (that is, the fracture energy density is kept the same), the ultimate crack width in the bilinear relation must be about 4 times the W_c defined in the linear relation of Fig. 5.2.

c) Discontinuous Linear Relation

The bilinear curve shown in Fig. 5.3 includes two segments: AB and BC. The line AB has a steep slope of negative stiffness of considerable magnitude. Because this negative stiffness when assembled into the stiffness matrix of a structure may lead to numerical instabilities, a 'discontinuous' linear relation, as shown in Fig. 5.4 is preferable. Extending line CB of Fig.5.3 to meet the vertical line AE at D, line DC may be used to approximate the relation between tensile stress and crack width. Then the tensile stress is not continuous when the crack just occurs. A simple calculation shows a 14 percent decrease of area under the 'discontinuous' line in comparison to that under the bilinear curve. The negative slope of softening still remains in the 'discontinuous' relation but the steep transient slope is eliminated.

5.3 Relation between Normal Tensile Force and Crack Width

5.3.1 Introduction

When a discrete crack approach is adopted to simulate concrete cracking, the application of the relation between normal tensile stress and crack width implies the normal stresses are distributed along the two faces of the crack. This situation is similar to that where external distributed surface traction is applied to the boundaries of a structure since the normal stress across cracks is similar to the surface traction normal to the boundaries of a structure.

Two characteristics for the crack face are:

1) The normal tensile stress is always applied equally to the two faces of a crack, which have the same geometrical position before initiation of cracking, and

2) The normal tensile stresses are introduced only after the crack is initiated by nodal splitting and subsequently the magnitude of the stress is a function of crack width.

5.3.2 Nodal Forces Equivalent to Distributed Normal Tensile Stress

The example shown in Fig. 5.5 is used to illustrate the procedure by which surface forces can be obtained from the relation between normal stress and crack width. This procedure includes four steps:

Step 1- Examine every vertex. If the vertex is split along an owneredge, find the two activated nodal numbers, and then the displacements for the two split nodes. This step was described in Sect. 4.4.

Step 2- For every pair of split nodes, find the crack width, or the relative normal displacement between the two split nodes as discussed in Sect. 5.2.1.

Step 3- Determine the normal tensile stress on the crack faces associated with the crack width, by application of the relations described in Sect. 5.2.2. The example in Fig. 5.5 illustrates the correspondence between crack width and normal tensile stress.

Step 4- Calculate the equivalent nodal forces at the crack faces from the distributed surface traction equal to the normal tensile stress obtained in Step 3.

Formulae for obtaining the work equivalent normal nodal forces along an element edge L, designated as F_a, F_b, F_c, to the normal tensile stress are derived from virtual work by integrating along the element edge, which yields

$$[F_aF_bF_c]\delta\begin{Bmatrix}U_{na}\\U_{nb}\\U_{nc}\end{Bmatrix}=\int_L s\delta u_n dL=\int_L [S_aS_bS_c]\begin{Bmatrix}N_a\\N_b\\N_c\end{Bmatrix}[\,N_a\quad N_b\quad N_c\,]\delta\begin{Bmatrix}U_{na}\\U_{nb}\\U_{nc}\end{Bmatrix}dL$$

(5.3.2.1)

in which the a,b,c subscripts identify with the three nodes along the edge, s is the normal stress on the edge, S is its value at a node, and N represents an edge shape function. The nodal forces are

$$F_a=\int_{-1}^{1}[S_aS_bS_c]\begin{Bmatrix}N_a\\N_b\\N_c\end{Bmatrix}N_a\sqrt{\left(\frac{\partial X}{\partial\zeta}\right)^2+\left(\frac{\partial Y}{\partial\zeta}\right)^2}\,d\zeta \qquad (5.3.2.2a)$$

$$F_b=\int_{-1}^{1}[S_aS_bS_c]\begin{Bmatrix}N_a\\N_b\\N_c\end{Bmatrix}N_b\sqrt{\left(\frac{\partial X}{\partial\zeta}\right)^2+\left(\frac{\partial Y}{\partial\zeta}\right)^2}\,d\zeta \qquad (5.3.2.2b)$$

$$F_c=\int_{-1}^{1}[S_aS_bS_c]\begin{Bmatrix}N_a\\N_b\\N_c\end{Bmatrix}N_c\sqrt{\left(\frac{\partial X}{\partial\zeta}\right)^2+\left(\frac{\partial Y}{\partial\zeta}\right)^2}\,d\zeta \qquad (5.3.2.2c)$$

in which the differential length dL along the edge has been expressed as

$$dL=\sqrt{\left(\frac{\partial X}{\partial\zeta}\right)^2+\left(\frac{\partial Y}{\partial\zeta}\right)^2}\,d\zeta$$

and ζ is the nondimensional edge coordinate.

5.3.3 Stiffness and Nodal Forces for Split Nodes

5.3.3.1 Introduction

The equilibrium equation for nonlinear finite element analysis can be formulated as (Bathe and Dvorkin, 1983):

$$\mathbf{K}_i\Delta\mathbf{U}_i=\lambda_i\mathbf{F}-\mathbf{R}_{i-1} \qquad (5.3.3.1)$$

in which i is an iteration number, **K** is the tangent stiffness matrix, λ is the load factor, **F** is the vector of external reference loads, Δ**U** is the unknown increment of nodal displacements, and **R** is the vector of external nodal forces which equilibrates the internal stresses.

When the distributed normal tension between two crack faces is simulated by spring elements connecting pairs of split nodes, similar to the 'link element' proposed by Ngo and Scordelis (1967) to simulate bond between reinforcing bars and concrete, these spring elements contribute to the terms $\mathbf{K}_i$ and $\mathbf{R}_{i-1}$ in Eq. 5.3.3.1 just as other elements do. These contributions can be evaluated in terms of the nodal forces equivalent to the normal stresses.

5.3.3.2 Contributions to Tangential Stiffness K and Nodal Force Vector R

The nodal force equivalent to the normal tensile stress at a node is denoted by $F_{W_{i-1}}$, where subscript W_{i-1} indicates the crack width and associated tensile stress and equivalent nodal force are calculated from the displacements determined for iteration i-1. When the crack width at the node reaches W_c, the ultimate crack width, the associated equivalent nodal force is zero. This is because the normal tensile stress at W_c is zero. If a linear relation between the equivalent nodal force and crack width is assumed, the force can be expressed as:

$$F_{W_{i-1}} = k_{W_i}(W_{i-1} - W_c) \qquad \text{for } 0 < W_{i-1} < W_c \qquad (5.3.3.2)$$

in which k_{W_i} is the slope of the curve for the relation between equivalent nodal force $F_{W_{i-1}}$ and crack width W_{i-1}. Equation (5.3.3.2) can be rearranged as:

$$k_{W_i} = F_{W_{i-1}}/(W_{i-1} - W_c) \qquad \text{for } 0 < W_{i-1} < W_c \qquad (5.3.3.3a)$$

and

$$k_{W_i} = 0 \qquad \text{for } W_{i-1} \geq W_c. \qquad (5.3.3.3b)$$

The nodal force $F_{W_{i-1}}$ is determined by integration of the normal stress acting on the crack, as described in Sect. 5.3.2. Because it is positive and W_{i-1} is smaller than W_c, k_{W_i} is negative indicating a descending slope of the curve of the relation between equivalent nodal force and crack width as shown in Fig. 5.6.

The link elements simulating distributed normal tension between two crack faces have stiffness k_{W_i} given by Eq.(5.3.3.3), and apply forces $F_{W_{i-1}}$ given by Eq.(5.3.2.2), to the two crack faces. Then, the springs are subject to forces, R_{n1} and R_{n2}, which have the same magnitudes as $F_{W i-1}$ but opposite directions.

The contribution to the tangential stiffness matrix for a pair of split nodes, such as nodes 1 and 2 as shown in Fig. 5.1, is assumed equal to $k_{W i}$. This assumption is accurate for uniform crack width. Substituting Eq.(5.2.1.2a) for W and differentiating Eq.(5.3.3.2) by assuming constant $k_{W i}$, results in the following equation:

$$dF_{W i-1}= k_{W i}(dU_{n1}-dU_{n2}) \qquad (5.3.3.4)$$

The equilibrium equations for one of these springs is similar to Eq. (5.3.3.4):

$$k_{W_i}\ (dU_{n1}-dU_{n2}) = dR_{n1} \qquad (5.3.3.5a)$$

$$k_{W_i}\ (dU_{n2}-dU_{n1}) = dR_{n2} \qquad (5.3.3.5b)$$

which can be written as

$$\begin{bmatrix} k_{W_i} & -k_{W_i} \\ -k_{W_i} & k_{W_i} \end{bmatrix} \begin{Bmatrix} dU_{n1} \\ dU_{n2} \end{Bmatrix} = [K_{W_i}] \begin{Bmatrix} dU_{n1} \\ dU_{n2} \end{Bmatrix} = \begin{Bmatrix} dR_{n1} \\ dR_{n2} \end{Bmatrix} \qquad (5.3.3.6)$$

in which R_{n1}, R_{n2} are the forces which the link element is subject to at node 1 and node 2 respectively.

The orientation of R_{n1} coincides with the normal of the cracked edge, **n**, and that of R_{n2} is opposite to **n** as shown in Fig. 5.7a.

Expressing force and displacement in Eq.(5.3.3.2.5) in terms of their components in X and Y directions yields the relations:

$$[K_{S_i}]\ d\begin{Bmatrix} U_{1x} \\ U_{1y} \\ U_{2x} \\ U_{2y} \end{Bmatrix} = d\begin{Bmatrix} R_{1x} \\ R_{1y} \\ R_{2x} \\ R_{2y} \end{Bmatrix} \qquad (5.3.3.7)$$

in which

$$[K_{S_i}] = [B]^T [K_{W_i}] [B]$$

where $[B]$ denotes the transformation matrix, $[K_{W_i}]$ is the matrix in Eq. (5.3.3.6) and the subscript $_s$ indicates of stiffness of the spring.

This stiffness matrix $[K_{S_i}]$ is the contribution of the spring linking the crack faces to the tangential stiffness matrix of the structure, K_i, and can be assembled into K_i by referencing the equation numbers of the global nodal numbers for nodes 1 and 2 (Sect. 4.4.1.1).

The terms shown in Eq.(5.3.3.7), R_{1x}, R_{1y}, R_{2x} and R_{2y}, are the negative of the components of the normal forces arising from the normal tensile stresses at crack faces. These forces are evaluated by Eq. 5.3.2.2 and can be assembled into R_{i-1} of Eq. 5.3.3.1 in the same way as $[K_{s_i}]$ is to K_i.

5.3.3.3 Treatment of Decrease of Crack Width

When two crack faces approach, instead of moving away from each other, the crack width decreases. The treatment adopted in this study for this case is based on the assumption that the tensile stress normal to two crack faces decreases proportionally to the decrease of crack width. When the crack width decreases to zero, the tensile stress is reduced to zero. The relation is shown in Fig. 5.8.

For every pair of split nodes a record of maximum crack width, W_{max}, is kept updated. If the current crack width is smaller than W_{max}, the tensile stress across the crack is defined by point B on line DF (crack unloading) instead of point A on line ED (tension softening) shown in Fig. 5.8. After the recorded maximum crack width is regained, the tensile stress across the crack is recovered (crack reloading). This procedure is shown by the arrows in Fig. 5.8.

5.3.4 Discussion

The procedure presented in this chapter develops the relation between nodal force and crack width at crack faces where tension softening exists. The key step in this procedure is the determination of the nodal forces equivalent to the tensile stress normal to crack faces.

The equivalent nodal forces, F_a, F_b and F_c, evaluated from Eq. (5.3.2.1) reflect a combination of cracking factors or cracking parameters. These cracking factors include crack width, which determines the magnitude of tensile stress denoted by s in Eq.(5.3.2.1), and the cracked edge length, denoted by L in Eq.(5.3.2.1).

The examples for uniform crack width shown in Fig. 5.9 are used for the purpose of illustration and discussion. When the crack width, denoted by W_{i-1} in Eq. (5.3.3.2), is uniform along crack faces the magnitude of the equivalent nodal force, $|F_{W\,i-1}|$, can be used to compare $k_{W\,i}$'s at different locations.

For the case shown in Fig. 5.9b where the crack has equally spaced nodes and linear elements, the magnitude of $k_{W\,i}$ is the same for each node along the crack faces. For the other cases shown in Fig. 5.9a, 5.9c and 5.9d where the elements are quadratic or different in size, $k_{W\,i}$ is nodal position dependent. But the signs of $k_{W\,i}$ for all cases are nonpositive indicating tension softening.

5.4 Relations for Overlap of Crack Faces

When the discrete cracks are distributed, an abrupt crack initiation or propagation may cause unloading or closing of an adjacent crack, and may further cause the two crack faces of the adjacent crack to interfere with or overlap each other. Gradual crack propagation can cause stress redistribution and, as a result, some locations previously in tension may shift to compression. Crack face overlapping, as shown in Fig. 5.7b may arise at the cracks in these previous tension locations. Compression will then be developed between the two crack faces to prevent the faces from overlapping. To simulate this phenomenon, a relation to inhibit overlap of crack faces, dependent on the relative displacement of two overlapped faces has been employed. If two crack faces overlap, the scalar $\mathbf{U}_{12} \cdot \mathbf{n}$ defining W in Eq.(5.2.1.2a) is nonpositive. To distinguish the condition from the crack width W which is nonnegative, the absolute value of the scalar $\mathbf{U}_{12} \cdot \mathbf{n}$ is denoted by C for an overlapping crack.

Similar to the procedure for tension softening, the contributions of the overlapping compression to the terms $\mathbf{K}_i$ and $\mathbf{R}_{i-1}$ in Eq.(5.3.3.1.1) are evaluated and assembled. These contributions can also be represented by a compressive spring connecting the split nodes associated with the overlapped crack faces. This spring (link element) has stiffness k_{ci} and is subject to forces R_{cn1} and R_{cn2} at its two ends. Stiffness k_{ci} is positive indicating a ascending curve for overlapped displacements vs. compressive nodal forces as shown in Fig. 5.6.

The terms k_{ci}, R_{cn1} and R_{cn2}, have their counterparts in the spring for tension softening, namely, $k_{W\,i}$, R_{n1} and R_{n2}. Replacing $k_{W\,i}$, R_{n1} and R_{n2} respectively by k_{ci}, R_{cn1} and R_{cn2} in equations from

Eq.(5.3.3.4) to Eq.(5.3.3.6), the equilibrium equations for the spring can be obtained.

The stiffness k_{ci} should depend on nodal spacing in the same manner as $k_{W\,i}$ (Fig.5.9). However, k_{ci} should have a magnitude considerably greater than $|k_{W\,i}|$. It is convenient to compute k_{ci} from the ratio of magnitudes, $\mu_1 = k_{ci}/|k_{W\,i}|$. Then k_{ci} can be calculated from $k_{W\,i}$ which was previously evaluated for the earlier crack propagation. The approach adopted is that for a pair of split nodes, the maximum nodal force equivalent to the normal tensile strength at the crack faces is stored and designated as R_{nmax}. From this an estimation of $|k_{W\,i}|$ is:

$$k_W = R_{nmax}/W_c$$

where W_c is the ultimate crack width.

Then k_{ci} is calculated as $k_{ci} = \mu_1 k_W$. One could argue that an infinite spring stiffness would be required to eliminate overlap and maintain nodal displacements the same on each side of the closed crack. However, infinite stiffnesses are not acceptable numerical values, and experience has shown that the solution is most stable if a value of μ_1 is chosen less than 20. Assembling k_{ci}, R_{cn1} and R_{cn2} are exactly the same as in the procedure for tension softening.

The parameter μ_1 can be selected to reduce, but not to eliminate, the overlap produced in the numerical simulation procedure.

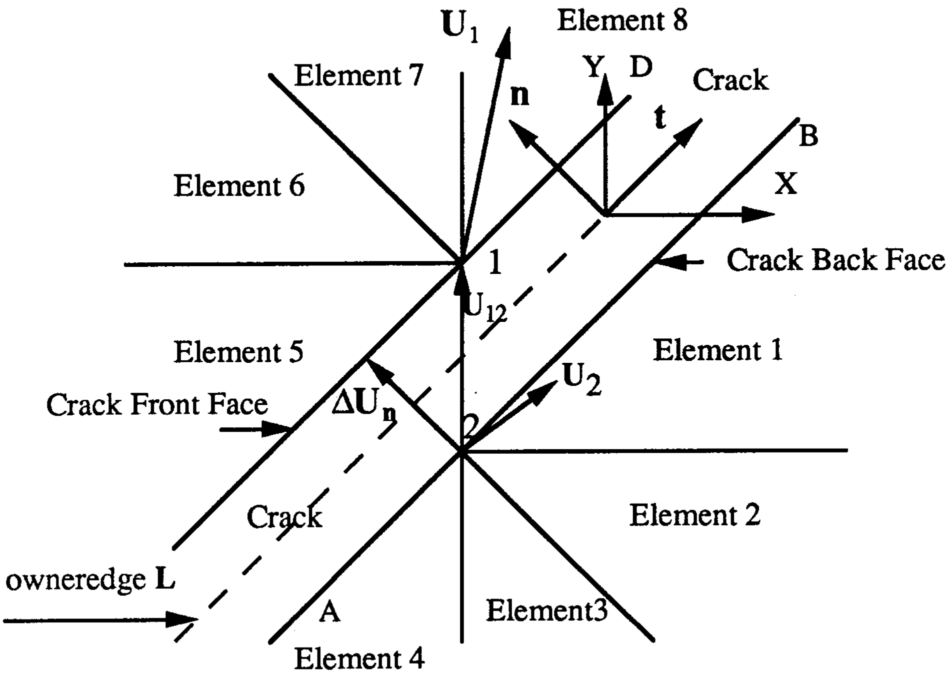

Fig. 5.1 Diagram for Relative Nodal Displacements

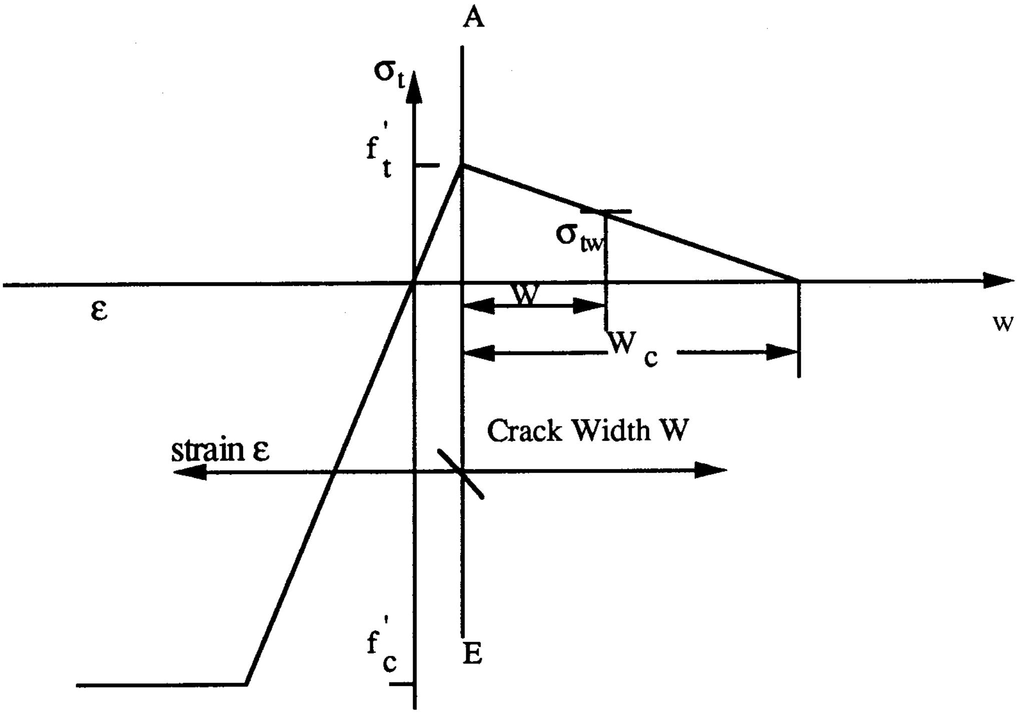

Fig. 5.2 : Normal Tensile Stress at Crack Faces: Linear Relation

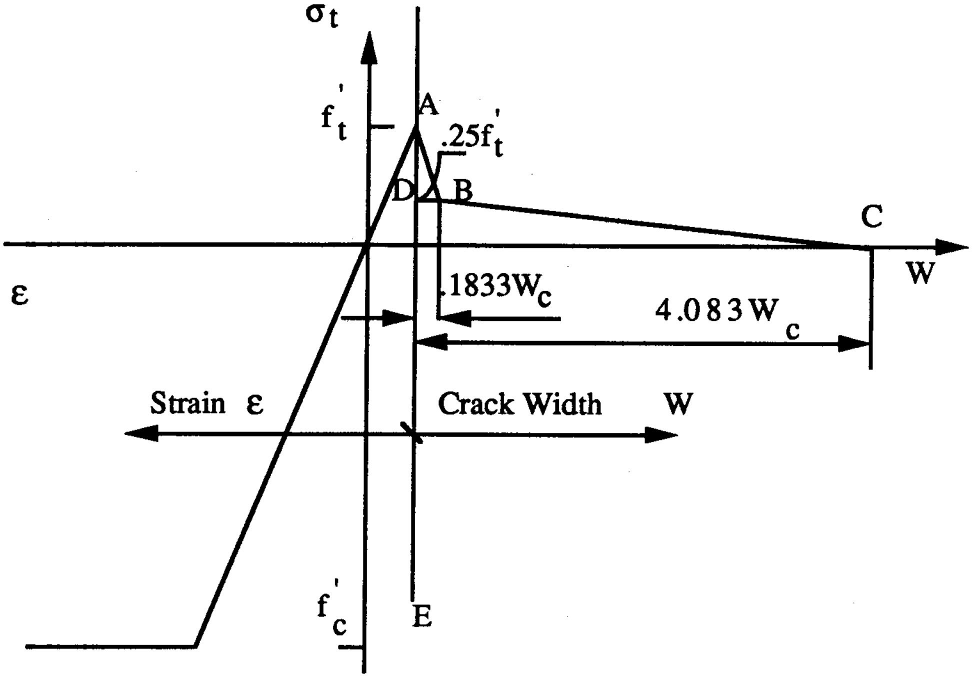

Fig. 5.3: Normal Tensile Stress at Crack Faces: Bilinear Relation

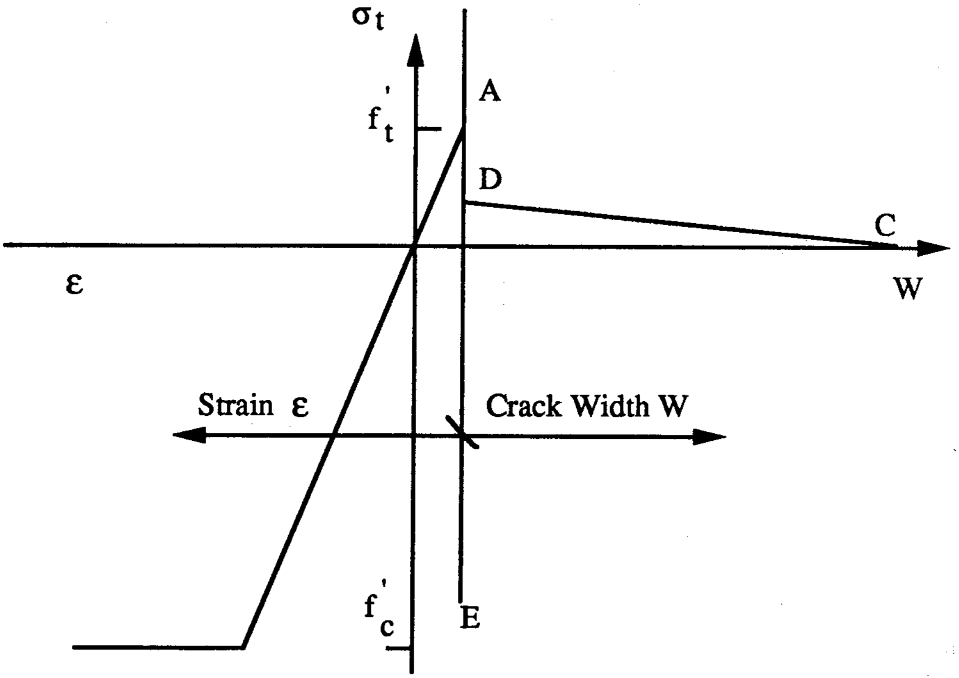

Fig. 5.4 : Normal Tensile Stress at Crack Faces: Discontinuous Relation

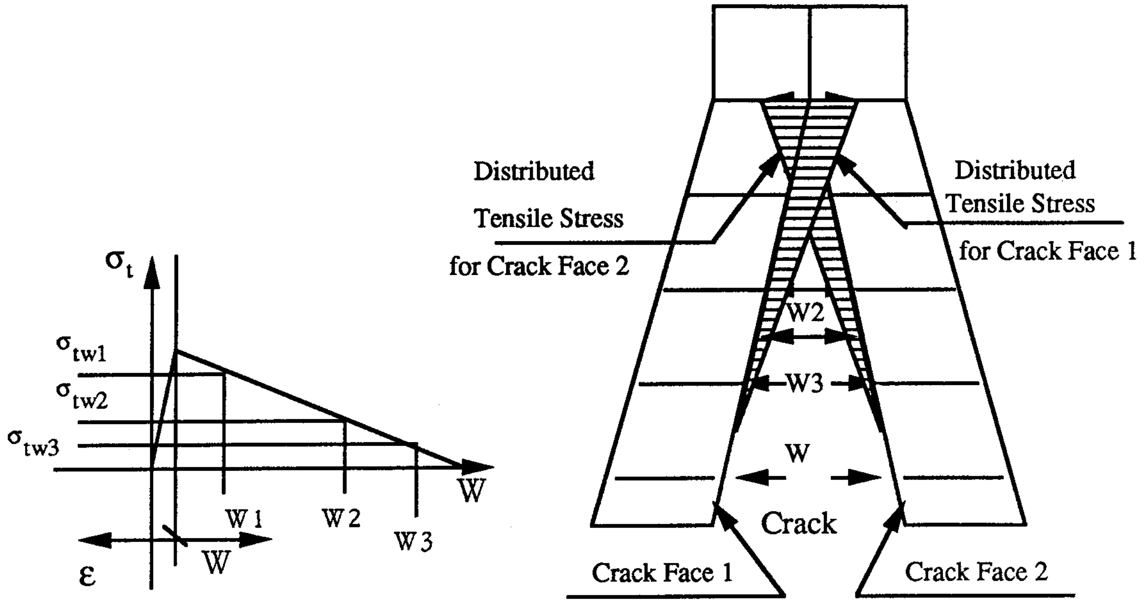

(a) Relation Between Normal Tensile Stresses and Crack Width

(b) Corresponding Distributed Tensile Stress at Crack Faces

Fig. 5.5 Application of Surface Traction on Crack Faces

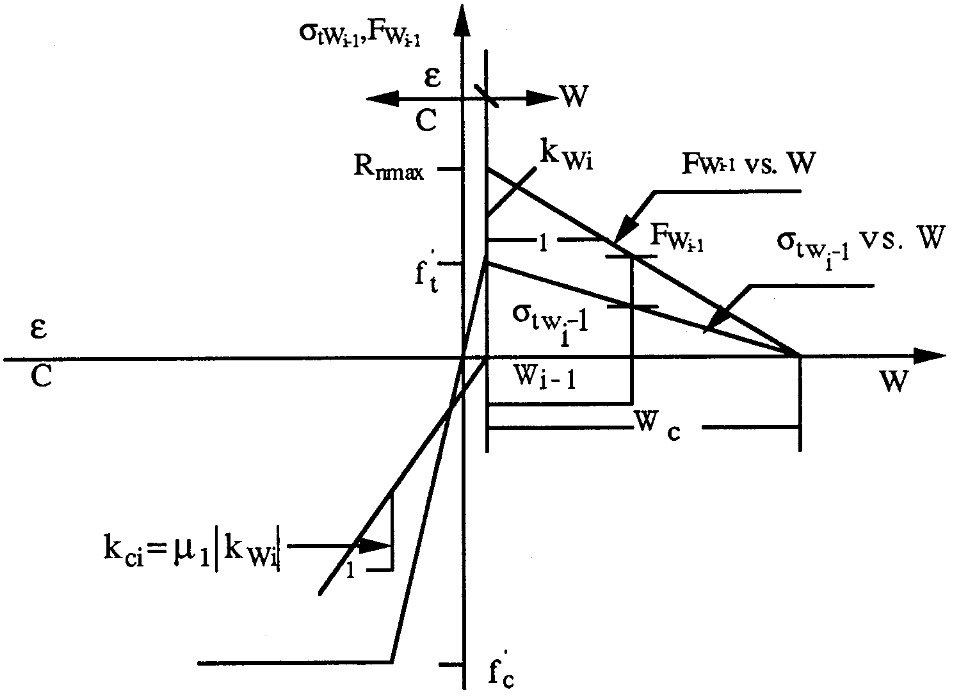

Fig. 5.6: Curves for Equivalent Nodal Forces

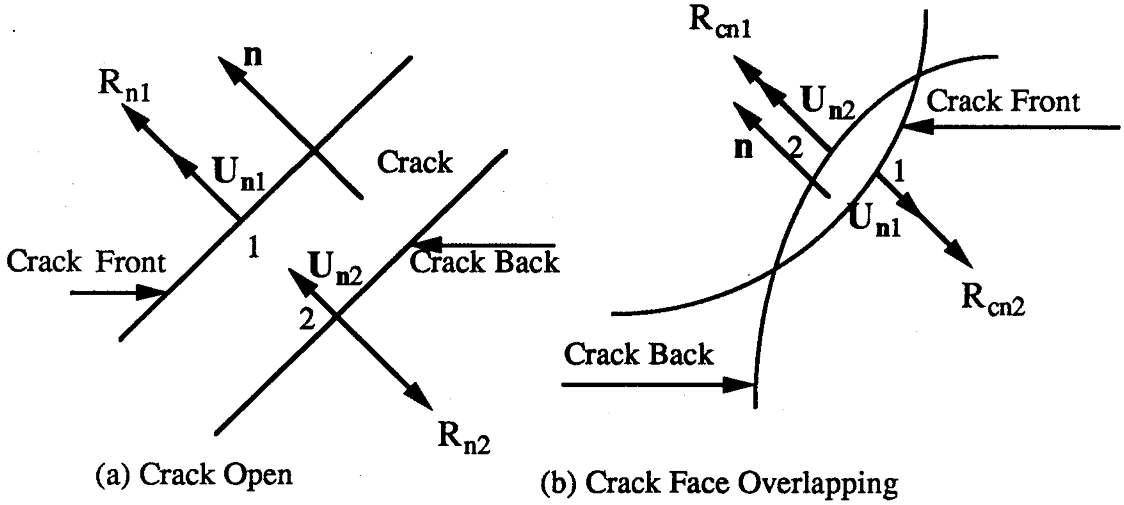

Fig. 5.7 **Orientations of Nodal Forces in Cases of (a) Crack Opening and (b) Crack Face Overlapping**

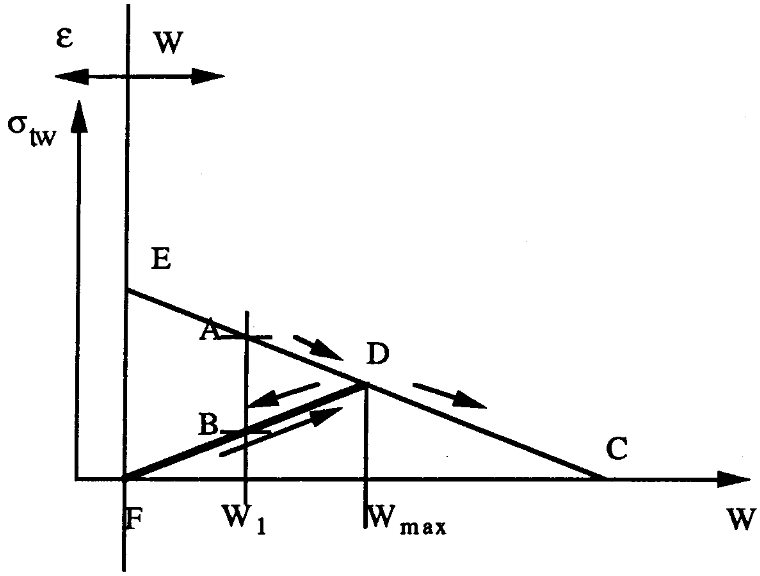

Fig. 5.8 Normal Tensile Stress for Decreasing Crack Width

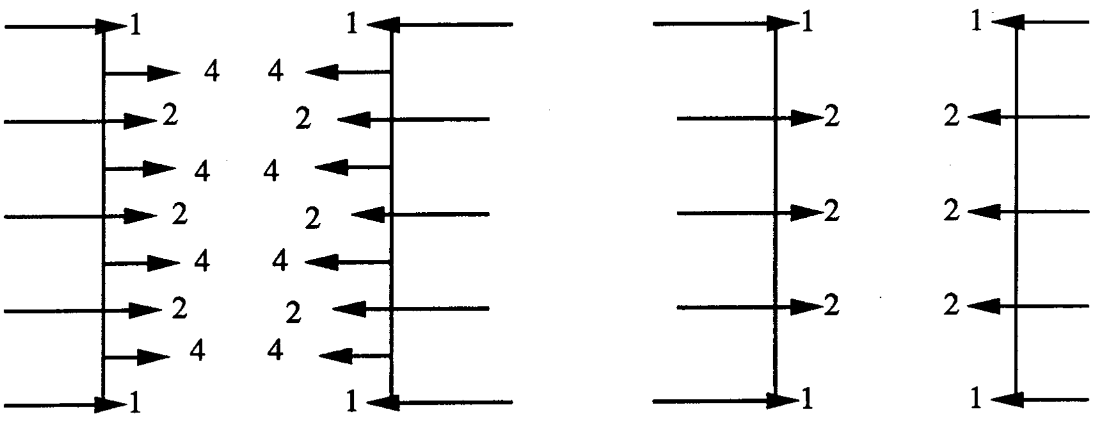

(a) Equal Sized Quadratic Elements

(b) Equal Sizes Linear Elements

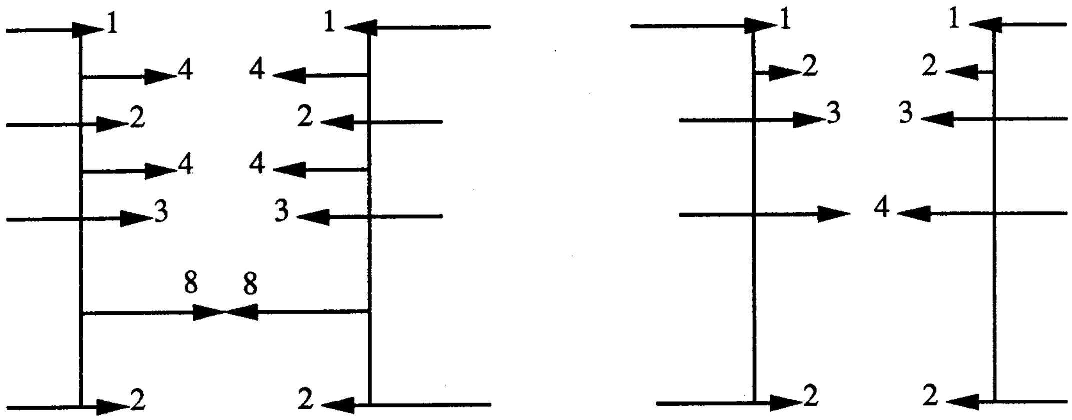

(c) Unequal Sized Quadratic Elements

(d) Unequal Sized Linear Elements

Fig. 5.9 Nodal Forces for Uniformly Opened Crack Faces

CHAPTER 6

SOLUTION STRATEGY

6.1 Introduction

The finite element model for distributed discrete cracking has been described from Chapter 3 to Chapter 5. The related solution strategy, is discussed in this chapter.

Equation (5.3.3.1) of Sect. 5.3.3.1 can be rewritten as:

$$\mathbf{K}_i^t \Delta \mathrm{U}_i = \Delta\lambda_i \mathbf{F} + \mathbf{Q}_{i-1} \qquad (6.1.1)$$

where i is an iteration number, t is a load step number, and $\Delta\lambda_i$ is the increment of the load factor during the iteration. The vector of unbalanced force $\mathbf{Q}_{i-1}$ is expressed as

$$\mathbf{Q}_{i-1} = \lambda_{i-1}^t \mathbf{F} - \mathbf{R}_{i-1}^t \qquad (6.1.2)$$

where λ_{i-1}^t is the total load factor at the end of iteration i-1.

If n is the number of displacement degrees of freedom for the structure, Eq. (6.1.1) contains n+1 unknowns because of the presence of $\Delta\lambda_i$. Consequently, an additional scalar equation is introduced. This may usually be written in the form:

$$h(\Delta\lambda, \Delta\mathbf{U}) = 0 \qquad (6.1.3)$$

A common approach to solve Eq.(6.1.1) with constraint Eq.(6.1.3) is to decompose $\Delta\mathrm{U}_i$ according to the following expression (Batoz and Dhatt,1979):

$$\Delta\mathbf{U}_i = \Delta\lambda_i \Delta\mathbf{U}_i^{I} + \Delta\mathbf{U}_i^{II} \qquad (6.1.4)$$

where $\Delta\mathbf{U}_i^{I}$ and $\Delta\mathbf{U}_i^{II}$ can be solved from the following equations:

$$\mathbf{K}_i^t \Delta\mathbf{U}_i^{I} = \mathbf{F} \qquad (6.1.5a)$$

and

$$\mathbf{K}_i^t \Delta\mathbf{U}_i^{II} = \mathbf{Q}_{i-1}. \qquad (6.1.5b)$$

In this study three different methods were used to formulate the constraint equation. These are:

Method 1 - The norm of the set of accumulated displacements for a load step, $\delta\mathrm{U}_i$, defined in (6.2.1.2), is constrained to a prescribed value;

Method 2 - The norm of the crack widths, W_i, is constrained to a prescribed value;

Method 3 - The increment of work done by the external forces is constrained to be equal to the strain energy absorbed in the solid elements plus that dissipated in the cracks.

Because constraint equations for Methods 1 and 2 are closely related, they are discussed together in Sect. 6.2. The constraint equation for Method 3 is discussed in Sect. 6.3.

6.2 Constraint Equations Based on Displacement or Crack Width

6.2.1 Displacement Control

One widely used form of Eq. (6.1.3) as proposed by Crisfield (1981), is

$$(\delta U_i)^T(\delta U_i) = (\Delta \ell)^2 \qquad (6.2.1.1)$$

where $\Delta \ell$ is a specified arc-length. This procedure is designated as the 'cylindrical arc-length' method by Bellini and Chulya (1987).

The accumulated displacements of the current load step are given by

$$\delta \mathbf{U}_i = \mathbf{U}^t_{i-1} - \mathbf{U}^{t-1} + \Delta\lambda_i \Delta \mathbf{U}^I_i + \Delta \mathbf{U}^{II}_i \qquad (6.2.1.2)$$

in which $\mathbf{U}^t_{i-1}$ are the total displacements at the end of the previous iteration, and $\mathbf{U}^{t-1}$, the total displacements at the end of the previous load step.

Substituting Eq.(6.2.1.2) into Eq.(6.2.1.1) and carrying out the multiplication, Eq.(6.2.1.1) is

$$(\Delta\lambda_i)^2(\Delta \mathbf{U}^I_i)^T(\Delta \mathbf{U}^I_i)+2\Delta\lambda_i(\Delta \mathbf{U}^I_i)^T(\mathbf{E}_{i-1})+(\mathbf{E}_{i-1})^T(\mathbf{E}_{i-1})-(\Delta \ell)^2=0$$

(6.2.1.3a)

where $\mathbf{E}_{i-1} = \mathbf{U}^t_{i-1} - \mathbf{U}^{t-1} + \Delta \mathbf{U}^{II}_i$. (6.2.1.3b)

The two roots for Eq.(6.2.1.3) are

$$\Delta\lambda_{i1,2} = \frac{-b \pm \sqrt{b^2-4ac}}{2a}$$

in which a, b and c denote the following expressions:

$a = (\Delta \mathbf{U}_i^I)^T(\Delta \mathbf{U}_i^I)$

$b = 2(\Delta \mathbf{U}_i^I)^T(\mathbf{E}_{i-1})$

$c = (\mathbf{E}_{i-1})^T(\mathbf{E}_{i-1}) - (\Delta \ell)^2$.

The rules for selecting $\Delta\lambda_i$ from the two roots of Eq.(6.2.1.3), again following Crisfield (1981), are:

1) If the roots are imaginary, reset $\Delta \ell$ and restart the current iteration;

2) If the roots are real and different, experience has shown that the root which gives the largest algebraic value of d should be selected as $\Delta\lambda_i$, where d is defined as

$d = (\delta\mathbf{U}_i)^T(\delta\mathbf{U}_{i-1})$ for $i > 1$;

$d = (\mathbf{U}^{t-1}/\lambda^{t-1})^T\delta\mathbf{U}_1$ for $t > 1$ and $i = 1$ where λ^{t-1} is the total load factor at the end of previous load step ;

$d = (\mathbf{U}_e)^T\delta\mathbf{U}_1$ for $i=1$ and $t=1$ where $\mathbf{U}_e$ is an estimation of elastic displacement vector under the external reference load.

The displacement vector $\delta\mathbf{U}_i$ in Eq.(6.2.1.1) usually includes all nodal displacements. However a set of selected nodal displacements, such as the displacements at the loading points, may be used to form the vectors.

6.2.2 Crack Width Control

As pointed out by de Borst (1988), constraint equations like Eq. (6.2.1.1) in which displacement vector $\delta\mathbf{U}_i$ includes all nodal displacements,

> "have been employed successfully within the realm of geometrically nonlinear problems, where snapping and buckling of thin shells can be traced quite elegantly. Nevertheless, for materially nonlinear problems the method sometimes fails, which may be explained by considering that for materially nonlinear problems, failure or bifurcation modes are often highly localized. Hence, only a few nodes contribute to the norm of displacement increments, and failure is not sensed accurately by such a global norm."

He also suggested that when δU_i "contains only a limited number of degrees of freedom" it is more suitable to use the term "indirect displacement control" instead of "arc-length".

However, determination of the selected degrees of freedom to be included in the constraint equation is not always an easy task. In the initial loading stage, the displacements at the points of load application are often selected as control displacements. As the nonlinearity becomes more apparent, slow convergence or divergence often reflects failure of the displacement control associated with loading positions. In this case experience in this study has shown that it is usually advantageous to switch to crack width control.

The crack width control approach uses the split nodal numbers and computes a norm for the corresponding crack widths. If the nonlinearity is crack-dominated, the constraint equation based on crack width, may provide a rational way to trace the load path. The constraint equation, Eq. (6.1.3), based on crack width is

$$(\mathbf{W}_i)^T(\mathbf{W}_i) = (\Delta \ell)^2 \qquad (6.2.2.1)$$

where $\mathbf{W}_i$ is the crack width vector which includes all the crack widths at split nodes, W_i, as defined by Eq.(5.2.1.2.a), and $\Delta \ell$ represents a specified constraint on crack width, instead of on displacement.

In Eq.(6.2.2.1), because W_i, by its definition, is the relative displacement of a pair of split nodes, only the nodal displacements at crack faces are included in the equation. The procedure for obtaining $\Delta\lambda_i$ from Eq.(6.2.2.1) is exactly the same as that for displacement control, with the $\mathbf{U}$'s denoting displacements being replaced by $\mathbf{W}$'s denoting crack width.

6.3 Constraint Equation Based on Fracture Energy

6.3.1 Introduction

6.3.1.1 Fracture Energy Criterion

The basic criterion for fracture mechanics, the fracture energy criterion or 'the Griffith energy criterion', states that

> "crack propagation will occur if the energy released upon crack growth is sufficient to provide all the energy that is required for crack growth." (Broek, 1986)

An example of a concrete prism with a steel bar inserted in the center, which illustrates this criterion is shown in Figs. 6.1 and 6.2. The following derivations assume that the material remains linearly elastic.

For Case 1, shown in Fig.6.1, the end of the prism is uniformly pulled to a displacement Δu, where the crack initiates, and is held at that displacement as the crack propagates. The configuration just before cracking, designated as A, is shown in Fig.6.1a, and the configuration after cracking, designated as B, is shown in Fig. 6.1b. Because the end of the prism is kept fixed during cracking, the work done by the external force, denoted as $\Delta\mathcal{W}$, is zero. On the load vs. displacement curve shown in Fig.6.1c, point A represents configuration A with its strain energy given by the area of triangle 0-A-C, while point B represents configuration B with its stain energy given by the area of triangle 0-B-C. Then the area of triangle 0-A-B gives the release of strain energy during cracking. If the external force drops from P_u in configuration A to P_c in configuration B, the change of strain energy is

$$\Delta\mathcal{U} = \Delta u(P_c-P_u)/2 \qquad (6.3.1.1)$$

where the sign of $\Delta\mathcal{U}$ is negative because $P_c < P_u$, which indicates release of strain energy.

The energy required for crack growth, $\Delta\mathcal{W}_c$, is

$$\Delta\mathcal{W}_c=\int_{A_c}\int_{W}\sigma_{tw}dWdA_c \qquad (6.3.1.2)$$

where A_c is the area of the crack surface (i.e. cross section of the concrete prism which forms the transverse crack), W is the crack width defined by Eq.(5.2.1.2a) and σ_{tw} is the normal tensile stress on the crack faces, defined in Sect. 5.2.2.

According to the fracture energy criterion, the following equation should be satisfied if crack propagation occurs:

$$\Delta\mathcal{W}_c \le -\Delta\mathcal{U}\,. \qquad (6.3.1.3)$$

Eq.(6.3.1.3) can be rearranged as

$$\Delta\mathcal{W}_c + \Delta\mathcal{U} \le 0. \qquad (6.3.1.4)$$

In Case 2 shown in Fig. 6.2, the end of the prism is uniformly pulled to a displacement Δu where the crack initiates. If the load is now kept constant the end of the prism is pulled further during cracking until a total displacement Δ_c is reached. Since the external force is kept constant, $P_u = P_c = P$, in the process.

As shown in Fig. 6.2c, the work done by the external force during the process is

$$\Delta \mathcal{W} = P(\Delta_c-\Delta_u), \tag{6.3.1.5}$$

and the change of the strain energy is

$$\Delta \mathcal{U} = P\Delta_c/2 - P\Delta_u/2 = P(\Delta_c-\Delta_u)/2. \tag{6.3.1.6}$$

The energy supplied for cracking is

$$\Delta \mathcal{W} -\Delta \mathcal{U} = P(\Delta_c-\Delta_u) - P(\Delta_c-\Delta_u)/2 = P(\Delta_c-\Delta_u)/2 \tag{6.3.1.7}$$

which is the area of the triangle 0-A-B.

If the crack propagation shown in Fig. 6.2c occurs, the value of $\Delta \mathcal{W} -\Delta \mathcal{U}$ should at least equal the energy required for crack growth. That is

$$\Delta \mathcal{W} -\Delta \mathcal{U} \geq \Delta \mathcal{W}_c \tag{6.3.1.8}$$

or

$$\Delta \mathcal{W}_c+\Delta \mathcal{U} \leq \Delta \mathcal{W}. \tag{6.3.1.9}$$

Comparing Eq.(6.3.1.4) and Eq.(6.3.1.9), we note that 6.3.1.4 is a special case of 6.3.1.9 for $\Delta \mathcal{W} =0$, and Eq.(6.3.1.9) is, therefore, assumed to be valid for general cases of cracking.

6.3.1.2 Fracture Energy as a Constraint for Solution Control

The general condition for propagation of distributed (or multiple) cracking is controlled by the energy balance associated with incremental crack extension, which may be stated in a form similar to (6.3.1.9) as:

a) No crack extension (Crack pattern stable)

$$\Delta \mathcal{W}_c > \Delta \mathcal{W} - \Delta \mathcal{U} \tag{6.3.1.10a}$$

b) Energy Balance

$$\Delta \mathcal{W}_c = \Delta \mathcal{W} - \Delta \mathcal{U} \tag{6.3.1.10b}$$

c) Crack propagation (Crack pattern unstable)

$$\Delta \mathcal{W}_c < \Delta \mathcal{W} - \Delta \mathcal{U} \tag{6.3.1.10c}$$

in which $\Delta\mathcal{W}_c$ is the sum of the energy required to form the crack growth in the structure, and $\Delta\mathcal{W} - \Delta\mathcal{U}$ is the total energy available to propagate this growth.

Condition (6.3.1.10a) indicates the energy available for distributed crack propagation, is less than that required for it. This is defined as a stable distributed crack pattern. This definition of stability is based on the whole structure.

Condition (6.3.1.10c) indicates the energy available, is more than that required to propagate the distributed crack pattern. This is defined as unstable crack propagation. The instability is defined on the basis of the whole structure, though one crack may be locally stable. Under condition (6.3.1.10c), distributed cracks propagate in a dynamic manner because the excess energy $\Delta\mathcal{W} - \Delta\mathcal{U} - \Delta\mathcal{W}_c$ is transferred into kinetic energy. Because the eqilibrium equation for nonlinear finite element analysis, Eq. 6.1.1, is based on static considerations, excessive unbalanced force Q_{i-1} arises as unstable crack propagation occurs.

The approach proposed in this study as unstable distributed crack propagation occurs, is to replace constraint equation (6.1.3) with the energy balance requirement of Eq. (6.3.1.10b). Then the load increment factor $\Delta\lambda_i$ is determined so as to eliminate the excess energy $\Delta\mathcal{W} - \Delta\mathcal{U} - \Delta\mathcal{W}_c$ associated with a displacement increment. As a result, Eq. (6.1.1) is appropriate again for the eqilibrium configuration and the excessive Q_{i-1} can be reduced.

The load convergence ratio, $\eta = \| Q_{i-1} \| / \| \lambda_{i-1} F \|$, where the symbol $\| \ \|$ represents the norm of the vector, is used as a criteria for switching from displacement control to fracture energy control. If the value of η is smaller than a specified η_s, displacement control is used; otherwise, fracture energy control is used. The η_s is problem dependent. In this study, it ranges from 40% to 80%.

The formulation for application of the energy constraint equation, for control of the iterative solution for distributed cracking of a structure, is described in Sect. 6.3.2.

6.3.2 Formulation of the Constraint Equation

6.3.2.1 Incremental Work of Applied Force

The increment work done by the external forces at iteration i, $\Delta \mathcal{W}_i$, is

$$\Delta \mathcal{W}_i = (\lambda^t_{i-1}\mathbf{F})^T \Delta \mathbf{U}_i + (\Delta\lambda_i \mathbf{F})^T \Delta \mathbf{U}_i/2 \qquad (6.3.2.1)$$

6.3.2.2 Assemblage of Equilibrating Force $\mathbf{R}^t_{i-1}$

As described in Sect. 5.3.3, the vector of equilibrating forces $\mathbf{R}^t_{i-1}$ in Eq.(6.1.1) is assembled from three vectors:

$$\mathbf{R}^t_{i-1} = \mathbf{R}^t_{i-1_e} + \mathbf{R}^t_{i-1_{oc}} + \mathbf{R}^t_{i-1_c} \qquad (6.3.2.2)$$

where $\mathbf{R}^t_{i-1_e}$ are the equivalent nodal forces required to equilibrate the internal stress of the solid elements; $\mathbf{R}^t_{i-1_c}$ are the nodal forces to which link elements are subject when the associated cracks are open, with components equal to the R_n's defined in Sect. 5.3.3.2; and $\mathbf{R}^t_{i-1_{oc}}$ are the nodal forces to which link elements are subject when the cracks are overlapped, with components equal to the R_{cn}'s defined in Sect. 5.4 .

For an unsplit node, the associated components of both the second and the third terms on the right hand side of Eq.(6.3.2.2) do not exist and are set to zero. For a split node, the associated component of either the second term or the third term on the right hand side does exist, because the crack faces at the split node must be in one of the two possible crack situations: crack faces are either open or overlapped.

6.3.2.3 Incremental Strain Energy Absorption

The strain energy increment at iteration i, $\Delta \mathcal{U}_i$, is the sum of strain energy absorbed by solid elements and link elements subject to compression caused by crack face overlapping:

$$\Delta \mathcal{U}_i = (\mathbf{R}^t_{i-1_e} + \mathbf{R}^t_{i-1_{oc}})\Delta \mathbf{U}_i + (\Delta\mathbf{R}^t_{i_e} + \Delta\mathbf{R}^t_{i_{oc}})\Delta \mathbf{U}_i/2 \qquad (6.3.2.3a)$$

where

$$\Delta\mathbf{R}^t_{i_e} = \mathbf{R}^t_{i_e} - \mathbf{R}^t_{i-1_e} \qquad (6.3.2.3b)$$

and

$$\Delta \mathbf{R}^{t}_{i_{oc}}=\mathbf{R}^{t}_{i_{oc}}-\mathbf{R}^{t}_{i-1_{oc}}. \qquad (6.3.2.3c)$$

Neglecting the terms of second order, namely, $(\Delta \mathbf{R}^{t}_{i_e}+\Delta \mathbf{R}^{t}_{i_{oc}})\Delta U_i/2$, Eq.(6.3.2.3a) reduces to

$$\Delta \mathcal{U}_i=(\mathbf{R}^{t}_{i-1_e}+\mathbf{R}^{t}_{i-1_{oc}})\Delta U_i \qquad (6.3.2.4)$$

6.3.2.4 Incremental Energy Absorption in Cracks

The increment of energy required for crack growth at iteration i, $\Delta \mathcal{W}_{ci}$, is

$$\Delta \mathcal{W}_{ci}=\sum_{1}^{n}\int_{L}\int_{W_i}^{W_i+\Delta W_i}(\sigma_{tw_{i-1}}+\Delta\sigma_{tw_i})dW_i h dL \qquad (6.3.2.5)$$

where n is the total number of split nodes and other terms have been defined in Chapter 5.

The three distributed quantities, W_i, $\sigma_{tw_{i-1}}$ and $\Delta\sigma_{tw_i}$, can be represented by the quantities at the nodes j along edge **L**, namely, $W_{i,j}$, $\sigma_{tw_{i-1},j}$ and $\Delta\sigma_{tw_i,j}$, and the shape function of the nodes, N_j, as

$$dW_i=\sum_j N_j dW_{i,j};$$
$$\sigma_{tw_{i-1}}=\sum_j N_j\sigma_{tw_{i-1},j}; \qquad (6.3.2.6)$$
$$\Delta\sigma_{tw_i}=\sum_j N_j\Delta\sigma_{tw_i,j}$$

where j indicates the local nodal number on edge **L**.

If the term of second order in Eq.(6.3.2.5), $\Delta\sigma_{tw_i}dw_i$, is neglected, the energy required for crack growth along edge **L** is

$$\Delta \mathcal{W}_{ci}=\int_{L}\int_{W_i}^{W_i+\Delta W_i}\sigma_{tw_{i-1}}dW_i h dL \qquad (6.3.2.7)$$

$$=\int_L [S_a S_b S_c] \begin{Bmatrix} N_a \\ N_b \\ N_c \end{Bmatrix} [\, N_a \quad N_b \quad N_c \,] \begin{Bmatrix} \Delta W_a \\ \Delta W_b \\ \Delta W_c \end{Bmatrix} h dL$$

(6.3.2.8)

where symbols Sa, Sb, Sc, Na, Nb, Nc were defined in Eq.(5.3.2.1). According to Eq.(5.3.2.1), Eq.(6.3.2.8) can be expressed by equivalent nodal forces F_a, F_b and F_c which are also defined in Eq.(5.3.2.1), as

$$\Delta \mathcal{W}_{ci} = [F_a F_b F_c] \begin{Bmatrix} \Delta W_a \\ \Delta W_b \\ \Delta W_c \end{Bmatrix} = \sum_j F_j \Delta W_j \qquad (6.3.2.9)$$

where the summation over j, is for j=a,b,c.

Eq.(6.3.2.9) indicates that the energy absorbed at node 'a' is $\Delta \mathcal{W}_{ca} = F_a \Delta W_a$. Substituting Eq.(5.2.1.2.a) for W into Eq.(6.3.2.9), and considering the forces, R_{n1} and R_{n2} (defined in Sect. 5.3.3.2), which a link elements is subject to, equal to F_a and $-F_a$ respectively, $\Delta \mathcal{W}_{ca}$ can be expressed as:

$$\Delta \mathcal{W}_{ca} = R_{1x}\Delta U_{1x} + R_{1y}\Delta U_{1y} + R_{2x}\Delta U_{2x} + R_{2y}\Delta U_{2y}.$$

(6.3.2.10)

The quantities R_{1x}, R_{1y}, R_{2x} and R_{2y} are the components of $\mathbf{R}^t_{i-1_c}$, and the energy required for crack growth at every pair of split nodes is evaluated and summed together to get $\Delta \mathcal{W}_{ci}$. So $\Delta \mathcal{W}_{ci}$ can be expressed as:

$$\Delta \mathcal{W}_{ci} = \mathbf{R}^t_{i-1_c} \Delta U_i. \qquad (6.3.2.11)$$

6.3.2.5 Incremental Energy Balance

Substituting Eq.(6.3.2.1) for $\Delta \mathcal{W}$, Eq.(6.3.2.4) for $\Delta \mathcal{U}$ and Eq.(6.3.2.11) for $\Delta \mathcal{W}_c$ into Eq.(6.3.1.9), the following equation is obtained:

$$(\lambda^t_{i-1}\mathbf{F})^T \Delta \mathbf{U}_i + (\Delta\lambda_i \mathbf{F})^T \Delta \mathbf{U}_i / 2 = (\, \mathbf{R}^t_{i-1_e} + \mathbf{R}^t_{i-1_{oc}} + \mathbf{R}^t_{i-1_c}) \Delta \mathbf{U}_i.$$

(6.3.2.12)

Substituting Eq.(6.3.2.2) into Eq.(6.3.2.12) and rearranging the terms yields

$$(\lambda^t_{i-1}\mathbf{F})^T\Delta\mathbf{U}_i + (\Delta\lambda_i\mathbf{F})^T\Delta\mathbf{U}_i/2 - \mathbf{R}^t_{i-1}\Delta\mathbf{U}_i = 0. \qquad (6.3.2.13)$$

Using the expression given by Eq.(6.1.2), Eq.(6.3.2.13) can be further simplified to

$$\mathbf{Q}_{i-1}{}^T\Delta\mathbf{U}_i+(\Delta\lambda_i\mathbf{F})^T\Delta\mathbf{U}_i/2 = 0. \qquad (6.3.2.14)$$

Substituting Eq.(6.1.4) into Eq. (6.3.2.14), the following quadratic equation for unknown $\Delta\lambda_i$ is obtained:

$$\mathbf{Q}_{i-1}{}^T(\Delta\lambda_i\Delta\mathbf{U}^{I}_{i}+\Delta\mathbf{U}^{II}_{i})+(\Delta\lambda_i\mathbf{F})^T(\Delta\lambda_i\Delta\mathbf{U}^{I}_{i}+\Delta\mathbf{U}^{II}_{i})/2 = 0$$

or

$$\left(\frac{\mathbf{F}^T\Delta\mathbf{U}^{I}_{i}}{2}\right)(\Delta\lambda_i)^2+\left(\mathbf{Q}_{i-1}{}^T\Delta\mathbf{U}^{I}_{i}+\frac{\mathbf{F}^T\Delta\mathbf{U}^{II}_{i}}{2}\right)\Delta\lambda_i+\mathbf{Q}_{i-1}{}^T\Delta\mathbf{U}^{II}_{i} = 0$$

(6.3.2.15)

Different solution situations of Eq.(6.3.2.15) are illustrated in Fig. 6.3. Parabola 'A' corresponds to the situation where both roots of $\Delta\lambda_i$ are imaginary. This corresponds to a situation where a load path which leads to a stable crack in terms of the fracture energy criterion cannot be found. Differentiation of Eq.(6.3.2.15) with respect to $\Delta\lambda_i$ leads to

$$\mathbf{Q}_{i-1}{}^T\Delta\mathbf{U}^{I}_{i}+\mathbf{F}^T\Delta\mathbf{U}^{II}_{i}/2+\Delta\lambda_i\mathbf{F}^T\Delta\mathbf{U}^{I}_{i} = 0$$

from which

$$\Delta\lambda_i = -(\mathbf{Q}_{i-1}{}^T\Delta\mathbf{U}^{I}_{i}+\mathbf{F}^T\Delta\mathbf{U}^{II}_{i}/2)/\mathbf{F}^T\Delta\mathbf{U}^{I}_{i}. \qquad (6.3.2.16)$$

The $\Delta\lambda_i$ given by Eq.(6.3.2.16) corresponds the minimum of function $f(\Delta\mathbf{U}_i, \Delta\lambda_i)=\Delta w - \Delta u - \Delta w_c$ as represented by point m on parabola A in Fig.6.3.

When the two roots of $\Delta\lambda_i$ are real and different, the selection rule in the cylindrical arc-length method, described in Sect. 6.2.1, is used.

If the unbalanced nodal force at iteration i-1, $\mathbf{Q}_{i-1}$, is a zero vector, so is $\Delta\mathbf{U}^{II}_{i}$ (Eq.(6.1.5.b)). Then Eq.(6.3.2.16) gives zero value of $\Delta\lambda_i$. This means that when the structure is in the linear stage, or nonlinearity is not dominant, the constraint based on the fracture energy criterion cannot provide a proper magnitude for the load increment factor $\Delta\lambda_i$. Therefore the efficiency of iteration is low. On the other hand, displacement control can give a large load increment factor $\Delta\lambda_i$, if a large $\Delta \ell$ in Eq.(6.2.1.1) is specified.

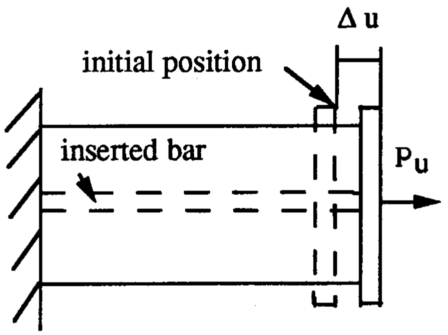

Fig. 6.1a Configuration A:
just before cracking

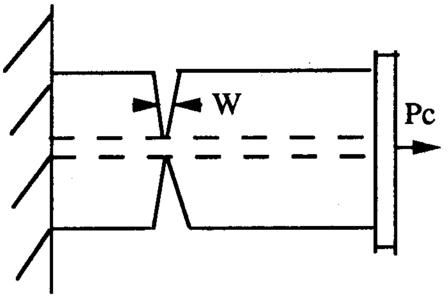

Fig. 6.1b Configuration B:
after cracking

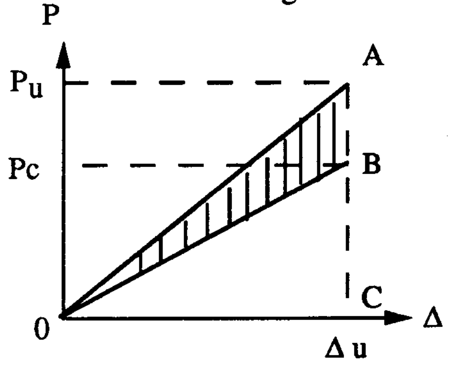

Fig. 6.1c Load-displacement
response

Fig. 6.1 Strain Energy Release for Cracking under Zero Elongation

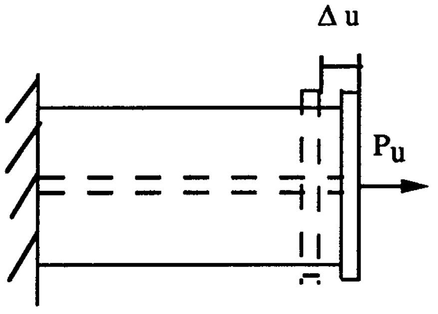

Fig. 6.2a Configuration A:
just before cracking

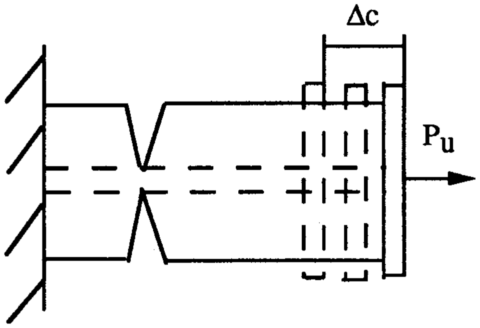

Fig. 6.2b Configuration B:
after cracking

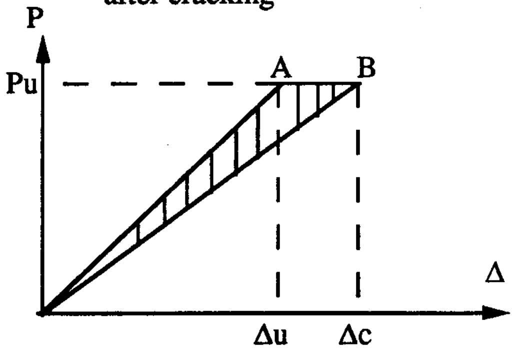

Fig. 6.2c Load-displacement
response

Fig. 6.2 Strain Energy Absorption for Cracking under Constant Load

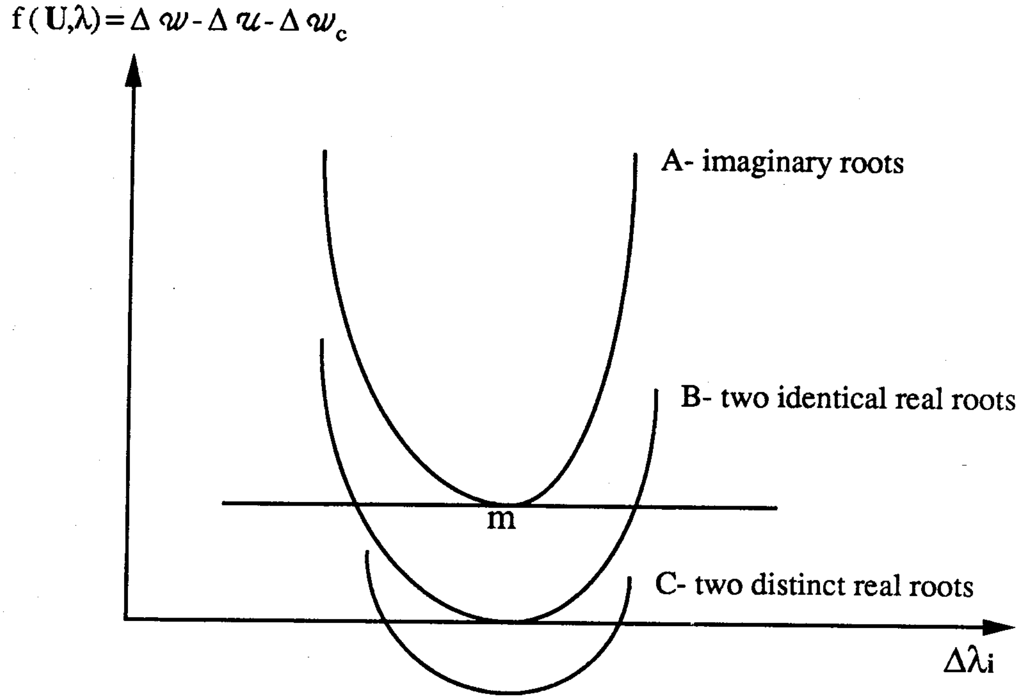

Fig. 6.3: Solution Control Situations

CHAPTER 7

APPLICATIONS

7.1 Introduction

In this chapter, four examples of application for the approaches described in Chapters 3 to 6 are presented. The brief descriptions of these examples and what they are intended to accomplish are as follows.

The first example is a concrete prism under uniform tension. A transverse crack of uniform width is assumed to occur as the cracking strength is reached. The uniform tension applied at the ends of the prism is controlled to balance the traction across the crack when either the crack width or end displacement is specified. This example is used to verify the performance for basic automatic operations of discrete concrete cracking, such as nodal splitting, addition of traction to cracked faces, and control of the load increment according to the constraints of displacement or crack width.

The second example is a simplification of three-point bending of a notched beam. A single crack initiated from the bottom of the middle span and propagating vertically is traced. The correspondence obtained between the concentrated load level and displacement at the point of loading is compared with the result from the previous study of Hillerborg (1985).

The third and fourth examples, which form the main contents of this chapter, deal with "tension-pull" problems.

In the third example, two tests conducted by Goto (1971), are numerically simulated through their whole loading history using the proposed modeling approach. The lengths of the specimens correspond to the maximum and minimum crack spacings as defined for the tests. The modeling approach includes representation of discrete concrete cracking, explicit modeling of lugs of deformed bars, compressive concrete yielding and longitudinal cracking. The solution strategy combines the displacement control and fracture energy control. Bond stresses at individual lugs are extracted from the analyses at every iteration, and their history can be traced. By comparison of test and analytical results, the influences of some important factors are investigated.

The test conducted by Watstein and Mathey (1959) is simulated in the fourth example, following the same procedure as is used for the third example.

7.2 A Concrete Prism under Uniform Tension

7.2.1 Introduction

Tests (Evans and Marathe, 1968; Petersson, 1981; Gopalaratnam and Shah, 1985) were carried out to investigate the behavior of a concrete prism subject to uniform tension. In these tests, the relative displacements between two faces of a localized crack were measured, and a softening relation between the average of the relative displacements and the associated stress levels was found (Fig. 2.1). The simplified forms of this softening relation, as described in Sect. 5.2.2, were adopted in this study.

To verify the implementation of the relation in Sect. 5.2.2, a numerical simulation for the concrete prism subject to uniform tension was carried out. The concrete prism fixed at one end and pulled by uniform traction at another end, shown in Fig. 7.1a, was modelled with two elements as shown in Fig. 7.1b. Because the concrete prism was assumed symmetrical about line A-A shown in Fig. 7.1a, only the half under line A-A was modelled.

In the tests (Gopalaratnam and Shah, 1985) a crack occurred at the location where a notch was preset. Similarly in the finite element simulation, only the boundary between elements 1 and 2, line 7-8-11 shown in Fig. 7.1b, was allowed to split. The two material properties which are the most important for the analysis, the modulus of elasticity E and the tensile strength f_t', were assumed to be E = 2,600,000 psi and f_t' = 200 psi. The linear softening relation between crack width and tensile stress at crack faces described in Sect. 5.2.2 was used with the ultimate crack width W_C assumed to be 0.00126 in.. The height of the prism, H, and its thickness h, are H = 2 in. and h = 1 in. respectively.

Two different aspect ratios, H/L = 1 and H/L = 1/12, were used. For both cases, the two constraint methods described in Sect. 6.2.1 and 6.2.2, namely, the accumulated load step displacement increment at a point of loading (cylindrical formulation, Crisfield, 1981) and total crack width, were applied.

The first of these methods is denoted as ALSDI (accumulated load step displacement increment) and the second as TCW (total crack width).

When the tensile strength f_t' was reached, elements 1 and 2 were separated along their common boundary, line 7-8-11. Exhaustive nodal splitting numbers were assigned to these nodes as described in Chapter 3 and 4. The configuration for post-cracking is shown in Fig. 7.1c. The link elements connecting related split nodes to represent the post-cracking softening relation are not shown in the diagram.

7.2.2 Theoretical Analyses

In tracing the load path, the tensile stress in the solid elements vs. the associated displacement at Node 14 was plotted. The displacement, d, at Node 14 can be expressed as:

$$d=d_e+d_w \tag{7.1.1a}$$

in which d_e is the elastic component, given by

$$d_e=\frac{\sigma_{tw}L}{E}, \tag{7.1.1b}$$

and d_w is the component due to crack propagation.

Before crack initiation

$$d_w=0, \tag{7.1.1c}$$

and after crack initiation

$$d_w=(1-\frac{\sigma_{tw}}{f_t'})W_c. \tag{7.1.1d}$$

Before crack initiation, only the elastic displacement component, d_e, exists. When the tensile stress reaches f_t', d_e reaches its maximum value of

$$d_{em}=\frac{f_t'}{E}L, \qquad (7.1.1e)$$

at which point the crack initiates. Then the load, the tensile stress, σ_{tw}, and the elastic displacement, d_e, drop but the displacement component due to crack propagation, d_w, increases. When the load decreases to zero, the elastic displacement component, d_e, vanishes, and d_w reaches the ultimate crack width W_c. Because both components are linear in the post-cracking range, the total displacement is also linear, and its slope can be determined completely by two points on the stress-displacement curve. These two known points are d_{em} associated with maximum tensile stress f_t', and W_c associated with zero tensile stress.

Equating Eq. 7.1.1e to W_c indicates that when the length L is smaller than the critical length

$$L_c=\frac{E}{W_c}f_t', \qquad (7.1.1f)$$

the displacement at the point of loading, d, increases as the load drops. When L is larger than L_c, d decreases as load drops. This indicates that a snap back occurs for large L. For the values cited for the example problem of this section, L_c is 22.68 in. which gives a critical aspect ratio of H/L=1/11.34. Consequently, the values of H/L selected for the numerical tests straddle the critical length for snap-back behavior.

7.2.3 Finite Element Analyses

For an aspect ratio H/L=1, which is a 'stumpy' prism, the computing results for ALSDI and TCW constraints are given in Fig. 7.2 and Fig. 7.3 respectively. It is seen that both approaches reach good agreement with the theoretical solution for this simple problem. In the TCW approach, the crack initiated at a tensile stress of 210 psi instead of f_t' = 200 psi because crack width control can only take effect after crack initiation. Before that the tensile stress was increased by an increment equivalent to the specified reference load, which was 70 psi for this example.

The results for the case of an aspect ratio H/L =1/12, a 'slender' prism which exceeds the critical length, are presented in Fig. 7.4 for ALSDI constraint and in Fig. 7.5 for TCW constraint. The ALSDI constraint failed to follow the snap back behavior. The TCW constraint can trace the load path of post-cracking with satisfactory accuracy.

7.2.4 Discussion

The superiority of TCW over ALSDI in following the load path of the snap back, which occurred in the case of the 'slender' prism, may be explained as follows. The TCW constraint controls width of cracks which are localized and are not directly related to the size of structure. Because the crack widths for the 'stumpy' prism and the 'slender' prism in this example are the same if the applied loads are the same, the TCW is not sensitive to the effects caused by the size of the structure, such as snap back. On the other hand, the displacement at the point of loading, which may snap back as cracks initiate, is the variable which is controlled in the ALSDI. Therefore, for the cases of a single crack TCW may be more favorable than ALSDI. However, for cases of multiple cracks, uncertainty occurs for the application of TCW because there may be many combinations of individual crack widths whose sum equals the specified value of total crack width.

7.3 Three-Point Bending of a Notched Concrete Beam

The numerical example shown in Fig. 7.6 was first used by Hillerborg (1985) to demonstrate the numerical methods to simulate softening and fracture of concrete. A notch is preset at the bottom of the middle span, and only an upward vertical discrete crack (or 'fictitious' crack as Hillerborg put it) initiated from the notch, is allowed to propagate. In the approach, the tensile strength f_t' is assumed to be reached at the current crack tip. Then for every step as the crack tip extends, the corresponding load is calculated by iteration (Petersson, P.-E., 1981).

The approach of Chapters 3, 4, 5 and 6 was applied to this example. As illustrated in Fig. 7.7 the finite element model was for only half of the beam, because of symmetry about the center of the span.

The procedure for automatic nodal splitting to simulate crack propagation, described in Chapters 3 and 4, was used to predict the crack growth. Both the constraint of displacement at the point where the concentrated force F was applied and the constraint of total crack width, as described in Chapter 6, were used separately to control the load increment ΔF. To be consistent with the analysis carried out by Hillerborg (1985) and Petersson (1981), the linear relation between crack width and tensile stress, as shown in Fig. 5.2, was used for the behavior of the crack faces and a linear elastic strain-stress relation was used in the solid elements.

Because the analytical results from the displacement control and the crack width control are quite close, only those from crack width control are plotted in Fig. 7.8. The abscissa represents the displacement of the point at which the concentrated force F was applied. The analytical result from Hillerborg (1985) and Petersson (1981) is also plotted in the figure. Good agreement between the two sets of results was obtained.

7.4 Numerical Simulation of Cracks Formed in "Tension-Pull" Tests

7.4.1 Introduction

A numbers of "tension-pull" tests in which a single reinforcing bar surrounded by a concentric prism is pulled at its two protruding ends have been carried out (Watstein and Mathey, 1959; Broms, 1965; Goto, 1971; Nilson, 1971; Mirza and Houde, 1979). The cross section of the prisms can be square or round as shown in Fig. 7.9. The focus of these tests varies. Some of the variables documented are: crack pattern, crack spacing, crack width, relative displacements between bar and concrete, and the relation between these entities and the steel stress levels, or the differential of the steel stress along the bar.

The interest in the investigation of the tension-pull specimen is caused mainly by the assumption that it can serve as a "simplified model of the situation which occurs on the tension side of a reinforced concrete beam" or "a portion of a steel reinforced diaphragm under tension"(Ingraffea and Saouma, 1985).

Tests show that the behavior of tension-pull specimens reinforced by deformed bars is quite different from that of specimens reinforced by plain bars (Watstein and Mathey, 1959). The effect of the deformations, or lugs, on the surface of the bar may be investigated by means of numerical simulations of tension-pull tests. In these numerical simulations, the lugs should be explicitly included in the finite element model. The "micromechanics of bond slip" (Ingraffea and Saouma, 1985) between deformed bar and surrounding concrete may be clarified by comparing results of test and finite element analyses. The following sections present some results of such numerical simulations.

7.4.2 The Finite Element Model

Because a cylindrical specimen is symmetrical to the central plane A as shown in Fig. 7.10a, only half of it needs to be considered. To model this three-dimensional axisymmetric problem in the domain of two dimensional finite element analysis, axisymmetric elements were used. As a result, only one quarter of the cross sectional plane which coincides with the axis of the cylinder is meshed, as shown in Fig. 7.10b.

Regular triangular elements with two angles of 45^o and one angle of 90^o were used for concrete. Such an arrangement produces regular distributed nodes from which eight edges emanate. This means that at these nodes eight possible crack orientations are provided to simulate concrete cracking initiated by the principal stress on the element boundaries, with an orientation error less than 22.5^o. As a result, cracks of zigzag shape are produced and their smoothed versions are assumed to represent the real crack paths.

A typical lug on the surface of a reinforcing bar is shown in Fig. 7.11a. The shape of cross section of the lug is an isosceles trapezoid. The finite element model simplifies the trapezoid into a triangle by merging the two tips of the trapezoid into one as shown in Figs. 7.11b.

The discontinuous linear relation between crack width and tensile stress described in Sect. 5.5(Fig. 5.4) was used to model the cracking behavior of crack faces. Displacement constraint at the point of loading was combined with the constraint based on the fracture energy criterion to control the loading increments.

As the compressive strength of concrete or the yield strength of the steel is reached, plastic yielding is initiated.

Since the two-dimensional axisymmetric element cannot simulate discrete longitudinal splitting, this kind of cracking was simulated by the smeared approach. The approach can be described as follows. When the circumferential stress reaches the concrete tensile strength at a point, a longitudinal splitting crack is considered to occur at this point, and the crack width is smeared over the circumference which intercepts the mesh plane at the point. The post-cracking tensile stress which crosses the longitudinal crack faces is set to zero, as shown in Fig. 7.12. Thereafter the post-cracking stiffness calculated at the point should be consistent with plane stress conditions rather than axisymmetric conditions.

The dashed line in Fig. 7.11b represents an element boundary on which a high tensile strength has been specified in order to inhibit cracking because, in the judgement of the investigator (Sect. 2.3.2), it is not considered to be a possible crack path.

7.4.3 Description of the Tests by Goto (1971)

In his tests, Goto assumed "the spacing L of lateral cracks, after cracking stabilizes", "roughly follows the following rule:

$$L_{min} \leq L \leq L_{max} \qquad L_{max} = 2\,L_{min}"$$

in which L_{min} and L_{max} represent maximum crack spacing and minimum crack spacing, respectively.

Tests were conducted on two different setups as shown in Table 7.1. In the first setup, one specimen has a 19 mm (3/4 in.) bar encased in 100 mm square of concrete while the other has a 32 mm bar encased in 120 mm square. The lengths of the specimens were four times the assumed maximum crack spacing, which was assumed to be 250 mm for the first setup. Cracks were initiated by prefabricating notches in the specimens at the discrete crack spacings. The bars were axially loaded in tension, and internal cracks were dyed and examined by cutting the specimens along the bars(see Fig. 7.22).

In the second setup, three specimens were axially loaded in tension. They had the same cross section, consisting of a 19 mm bar encased in 120 mm square of concrete, but different lengths equal to: the maximum crack spacing, which is assumed to be 300 mm; the minimum crack spacing (150 mm); and, the intermediate crack spacing (200 mm). The elongation of the perimeter of a 60 mm square on the end faces of these prisms (see Fig. 7.13a) was measured as steel stress levels increased. In the following, the first of these specimens (L=300 mm) will be referred to as Case 1, and the second (L=150 mm) as Case 2 (see Table 7.1).

Because the method of defining the maximum crack spacing is not mentioned in the documentation of Goto's tests (note that the minimum crack spacing is assumed to be the half of the maximum crack spacing), the generally accepted approach as described by Watstein and Mathey (1959) is assumed applicable. The approach is described for "tension-pull" specimens which "simulate a portion of a beam between two successive cracks". The maximum crack spacing was determined by trial to be the maximum length of specimens which would not develop transverse cracks during testing (Watstein and Mathey, 1959).

7.4.4 Numerical Simulation of Goto's Case 1

7.4.4.1 Parameter Inputs

The specimen having length equal to the maximum crack spacing (i.e.- Case 1, for which L=300 mm) in the second setup of Goto's tests was simulated as follows. For the purpose of modeling, the 120 mm square cross section was transferred to an area-equivalent circular one with radius equal to 135.4 mm as shown in Fig. 7.13a. Then the two-dimensional axisymmetric finite element can be applied to this model. The compressive strength, $f_c^{'}$, used in the analysis was 29 MPa (4,200 psi) according to Goto(1971). The modulus of elasticity E for concrete and steel were assumed to be 24,822 MPa (3.6×10^6 psi) and 199,955 MPa (2.9×10^7) psi, respectively. The tensile strength for concrete crack initiation was assumed to be 3.4475 MPa (500 psi) which is about $0.623\sqrt{f_c^{'}}$ ($7.5\sqrt{f_c^{'}}$) according to Lutz and Gergely (1967).

Because the "specimens were tested in a moist condition to avoid any shrinkage complication" (Goto,1971), the adhesive strength of the concrete-steel interface, denoted as $f_{cs}^{'}$, was estimated by assuming that the adhesion is of the "saturated surface dry" category whose strength ranges from 150 to 300 psi (Lutz and Gergely, 1967; Hsu and Slate, 1963). The $f_{cs}^{'}$ used in the analysis described in this Section is 1.724 MPa (250 psi), which was selected by optimal fit of Goto's Case 1 tests from four numerical simulations ($f_{cs}^{'}$=180, 215, 230 and 250 psi). The ratios μ_1 for overlapping cracks defined in Sect. 5.4 was assumed to be 20.

Switching from displacement constraint at the point of loading, to the fracture energy criterion constraint, was carried out when the specified load convergency factor η_s defined in Sect. 6.3.2 was exceeded. The η_s used in the analysis is 60%.

The 60 mm square on the end face of the test specimen, along whose perimeter the elongation was measured, was transferred to an area-equivalent circle with radius equal 67.7 mm in the analytical model, as shown in Fig. 7.13a. The elongation of this circle calculated from analysis is considered equivalent to that of the square measured from the test.

7.4.4.2 Illustrations of Analytical Results

The measured elongation of the perimeter of the square and the calculated elongation of the perimeter the circle are plotted in Fig. 7.13b.

The crack distributions, stress distributions and enlarged deformed meshes associated with the 8 data points on the curve for the analytical results shown in Fig. 7.13b are presented, in ascending order of steel stress levels ranging from 68.8 to 294.1 MPa (9.6 ksi to 41.2 ksi), in Figs. 7.14 to 7.21 respectively. The crack paths, shown in Figs. 7.14a to 7.21a, are drawn by lines of three different weights: light, medium and heavy. These represent closed cracks or structural boundaries, open cracks with width less than W_c, and open cracks with width greater than W_c, respectively. Because of discontinuous relation for tensile stress vs. crack width (Fig. 5.4) is used, the W_c is about four time of that for linear relation.

Some observations of the crack propagation obtained from this analysis are summarized in the following Sects. 7.4.4.3 to 7.4.4.6.

7.4.4.3 Progression of the Most Prominent Cracks

Cracks initiate from the back face of lugs and may extend to the outer surface. Though cracks nucleate at the back face of every lug, propagation is quite uneven. As the tensile load increased, some cracks located several lug spaces further inside the specimen than the current most prominent crack (i.e. - the crack with the greatest crack propagation radius from the center of the bar or the greatest crack width), propagated rapidly and emerged as the most prominent. These cases happened in such transitions as those from the crack configuration shown in Fig. 7.17 to that shown in Fig. 7.18, and from that shown in Fig. 7.18 to that shown in Fig. 7.19.

When a new most prominent crack emerged, some of the previous cracks decreased their crack width (crack unloading) or even closed as indicated by comparisons among Fig. 7.17a, 7.18a and 7.19a. After the emergence of the crack pattern shown first in Fig. 7.19a, no new cracks emerged, and the most prominent crack became so dominant that nearly all the previous cracks closed. Even the adhesion between concrete and steel on the front faces of the lugs which were located in front of the dominant crack was damaged due to tension. These cracks at the front face of lugs soon closed due to compression which developed immediately after the crack pattern stabilized.

The shaded areas in Fig. 7.19a to 7.21a represent the parts of concrete which are enclosed by cracks and have no node (or only one node) connected to other parts of concrete. This separation indicates that the concrete in the shaded areas disconnects from the remainder of the specimen.

The domination of the current most prominent cracks is shown by the evolution of the deformed meshes from Fig. 7.14b to Fig. 7.21b. For the purpose of illustration the nodal displacements were enlarged 80 times before they were added to their associated undeformed nodal positions. The part of the steel-concrete interface which is positioned in front of the current most prominent crack separates, and the concrete lifts up from the bar, with the highest gap found at the exit of the bar from the concrete.

Unfortunately, Goto did not longitudinally cut the specimens in the second setup to examine the crack patterns. Therefore, crack pattern comparison between tests and their associated simulations described in this Section cannot be made. However, Goto did cut the specimens in the first setup, and the dye crack pattern in the cross sections are shown in Fig. 7.22. The halves on which the reinforcing bars are not attached show that at some crack spacings black dye penetrating through the concrete-steel interface from the lateral cracks to a considerable extent. This may be explained by lift-up of the concrete interface from the steel.

The current most prominent crack and the open cracks positioned behind it can be recognized by the distinct crack faces in these 'b' figures. But the concrete cracks positioned in front of the current most prominent cracks cannot be recognized, even though they are still marked as open cracks by lines of medium thickness in the 'a' figures. Due to the enlargement of displacements by 80 times, a false impression is given that the surfaces initially cemented to the front face of the lugs lift up and move back from the bar so much that they clear the associated lugs. In fact, these concrete surfaces still contact the associated front faces of the lugs in the form of closed cracks. Compressive bond forces are exerted on these faces by the overlap springs described in Sect. 5.4.

7.4.4.4 Longitudinal Splitting Cracks

Goto observed the formation of longitudinal cracks on sides of the specimens at steel stress levels around 155 MPa. In the present numerical simulation, the longitudinal cracks were modelled by the smeared approach described in Sect. 7.4.2. The extent of longitudinal cracking at the eight steel stress levels are illustrated in Figs. 7.14c to 7.21c respectively. In these figures, the small longitudinal dashes indicate that longitudinal cracks are present at these locations. As shown in Fig. 7.17c, the longitudinal cracks have reached the sides of the specimen at the associated steel stress level of 165 MPa. This is consistent with the test. The configurations shown in Fig. 7.17c to 7.19c indicate rapid propagation of longitudinal cracks.

In contrast, the predicted steel stress increased only 20 MPa from Fig. 7.17c to Fig. 7.18c. This causes the deviation of the analytical results from the test result as shown in Fig. 7.13b. This delay of the increase of steel stress during the rapid propagation of the longitudinal crack may be explained by the inability of the two-dimensional approach adopted in this study to simulate discrete circumferential cracking which is typically a three dimensional effect. This argument is supported by comparison of Figs. 7.19c to 7.21c, in which propagation of longitudinal splitting cracks slowed, and the curve obtained from the finite element analysis again approaches the one obtained from the test, as shown in Fig. 7.13b.

The stress distributions at the eight steel stress levels in the parent plane of the cylinder are shown in Figs. 7.14d to 7.21d. This technique is not very informative for the type of problem considered and parts (d) have been included primarily for completeness and to show the consistency of these stress distributions with parts (a) to (c).

Comparison of the crack distributions shown in Figs. 7.14a to 7.21a to their associated distributions of longitudinal splitting crack shown in Figs. 7.14c to 7.21c, indicates that 'the most prominent crack' appears to remain close to the front of deepest penetration of the longitudinal splitting cracks.

7.4.4.5 Compressive Yielding of Concrete on the Front Faces of Lugs

In the approach adopted by the study, the option of compressive yielding of concrete is included. The locations at which the compressive yield strength is reached and plastic yielding takes effect are marked in Fig. 7.14c to 7.21c by small dashes oriented in the direction perpendicular to the axis of reinforcing bar. As shown, compressive yielding of concrete occurs on the front slope of lugs which are in the vicinity of the most prominent cracks.

For the conditions, as shown in Fig. 7.14c, 7.17c and 7.18c respectively, compressive yielding of concrete occurs at the front faces of the lugs from whose back faces the cracks initiate. For the last crack, as shown in Fig. 7.19c to 7.21c, the concrete located behind the crack yields.

As the most prominent crack progresses, the concrete yielding vanishes at the previous crack location, and new yielding occurs at the current location. In this sense, progressions of the most prominent cracks, longitudinal cracks and concrete yielding at the front faces of lugs are synchronized.

7.4.4.6 Illustrations of Bond Stresses and Bond Slips

On steel-concrete interfaces, as shown in Fig. 7.10 and 7.11, bond forces (or stresses) exist. At the locations where the reinforcement and concrete are in contact, the bond forces applied to the reinforcement have the same magnitudes as those applied to the concrete, but have opposite directions.

If the nodal forces which are integrated from the stresses in the solid elements of the reinforcement are assembled for the nodes which are located on the interface, these assembled nodal forces represent the bond forces applied to the reinforcement by the concrete.

The interface presented in the finite element model of Fig. 10 is divided into 8 intervals of length as shown in Fig. 7.23, each equal to 16.76 mm (0.66 in.) as shown in Fig. 7.11b. Every interval is centered by a lug, and these are numbered from No.1 to No.8 in a sequence starting from the symmetry plane A-A, as shown in Fig. 7.23. (The two half lugs with their associated half intervals in the finite element mesh, one at the line of symmetry and another at the exit of steel from concrete, are not counted).

For every interval, the component of bond forces in the longitudinal direction is summed up to obtain the total bond force in this direction. This force may be divided by the nominal area of the surface of the reinforcement (nominal diameter of the bar $\times \pi \times$ length of the interval) to obtain the interval averaged longitudinal bond stress, denoted as σ_{IALB}.

The σ_{IALB}'s in a interval at 10 ascending steel stress levels are plotted in Fig. 7.24a on one of the 8 curves which represent σ_{IALB}'s versus steel stresses in intervals No.1 to No. 8, respectively. If the 10 steel stress levels associated the 10 data points on the curves are denoted as Level 1 to 10 in ascending order of magnitude (with Level 1 representing the initial zero stressed state), the 8 steel stress levels shown in Fig. 7.14 to 7.21 correspond to Levels 3 to 10, respectively.

The eight σ_{IALB}'s associated with the same steel stress level in the eight intervals are averaged to obtain the specimen averaged longitudinal bond stress denoted as σ_{SALB}. The σ_{SALB}'s are plotted versus the associated steel stress levels in Fig. 7.24b.

Following the same procedure, radial components of bond forces are processed. The interval averaged radial bond stresses, denoted as σ_{IARB}, are plotted versus steel stress levels in Fig. 7.25a. The specimen averaged radial bond stress, denoted as σ_{SARB}, are plotted versus the steel stress levels in Fig. 7.25b.

In any interval, the displacements of the nodes at the steel-concrete interface, U_x's and U_y's, are averaged separately in terms of material types, that is, one pair of interval averaged displacements (longitudinal and radial) for steel reinforcement, U_{IALS} and U_{IARS}, and another pair of averaged displacements for surrounding concrete, U_{IALC} and U_{IARC}. The difference between the averaged displacements of steel and concrete in longitudinal (or radial) direction is the average slip in this direction,

$$s_{IALB} = U_{IALS} - U_{IALC} \qquad (7.4.1a)$$

$$(\text{or } s_{IARB} = U_{IARS} - U_{IARC}) \qquad (7.4.1b)$$

in which s_{IALB} (or s_{IARB}) denotes interval averaged longitudinal (or radial) slip.

The s_{IALB}'s (or s_{IARB}'s) versus associated steel stresses are plotted in Fig. 7.26a (or 7.27a) on one of 8 curves corresponding to the 8 intervals. The specimen averaged longitudinal (or radial) slip, denoted as s_{SALB} (or s_{SARB}), is plotted versus associated steel stress levels in Fig. 7.26b (or 7.27b).

7.4.4.7 Progressive Deterioration of Bond

As shown in Fig. 7.24a, the σ_{IALB}'s have negative signs indicating that they are opposite to the direction of applied external load. Except for the σ_{IALB}'s in the interval No. 2, the σ_{IALB}'s decreased after a certain steel stress level was reached. The steel stress level for which this peak bond stress was produced in the different intervals is given in Table 7.2. The correspondences indicate a trend of a higher level number for a interval positioned further inside the specimen. This trend, in turn, indicates bond deterioration begins at the outer edge of the specimen and progresses inward as steel stress increases.

The crack distributions at different steel stress levels have been shown in Fig. 7.14 to 7.21. An examination of these indicates that the emergence of a new most prominent crack causes the concrete surface surrounding the bar located immediately in front of the crack to lift and separate from the bar surface. Comparing these crack distributions with their associated data points of bond stresses on the curves in Fig. 7.24a, indicates that the bond between the concrete and the steel is reduced as the concrete lifts up.

For the cylindrical interfaces located between two consecutive lugs (the faces of the two lugs are not included), there is complete loss of bond as the concrete lifts up from the bar on the interface. On the front faces of lugs, the adhesion is destroyed as the concrete lifts up from the bar, but increased longitudinal movement of bar occurs keeping concrete and steel in contact on the faces. Compressive bond forces can still be delivered through the contact, as illustrated in Fig. 7.28a.

As contact on the front face of a lug is lost, loss of bond occurs as shown in Fig. 7.28b. Loss of contact on the front face of a lug occurs as the the following condition is met

$$|s_{RB}|\times\cos\gamma \geq |s_{LB}|\times\sin\gamma \qquad (7.4.2)$$

in which $|s_{LB}|$ and $|s_{RB}|$ represent the absolute values of longitudinal slip and radial slip respectively, and γ represents the angle of inclination of the front face of the lug to the axis of the bar. When the last most prominent crack emerged and the longitudinal splitting crack propagated rapidly, the bond stresses in the intervals located in front of the crack were almost all lost due to the surge in $|s_{RB}|$.

7.4.4.8 Local Variations of Bond

As shown in Fig. 7.24a, the maximums of σ_{IALB}'s obtained in the different intervals range from 2.758 to 8.62 MPa (400 to 1,250 psi). The maximum of σ_{SALB} is about 4.0 MPa (580 psi) as shown in Fig. 7.24b. This maximum occurred at the steel stress level of 160 MPa (22ksi), just before the emergence of the last most prominent crack.

It is noticed in Fig. 7.24a that the σ_{IALB}'s averaged in intervals No.7 and No.5, in which the first two most prominent cracks initiated, have considerably lower magnitudes than the σ_{IALB}'s averaged on the adjacent intervals (interval No.8, No.6 and No.4). It is also noticed that the lower σ_{IALB}'s in the intervals No.7 and No.5 are associated with higher s_{IALB}'s than the one's in the intervals No.8 and No.6, as shown in Fig. 7.29.

The lower σ_{IALB}'s and higher s_{IALB}'s in the vicinities of these two most prominent cracks may be explained as follows. As the prominent cracks initiate from the back faces of the lugs located in these two intervals and propagate to the outer surface, the cylindrical concrete interfaces between these lugs and the next lugs inside the specimen are split and lift up from the steel interface. Therefore the longitudinal bond stresses are reduced, and the longitudinal slips are considerably increased.

As shown in Fig. 7.25a, most of the σ_{IARB}'s obtained at different intervals are negative. This indicates that the radial bond stresses applied to the bar are compressive.

In contrast to the case of σ_{IALB}'s in the vicinities of the first two prominent cracks, σ_{IARB}'s in intervals No.7 and No.5, have higher magnitudes in compression than σ_{IARB}'s in the adjacent intervals, No.8. No.6 and No.4. The σ_{IARB}'s in these three intervals have quite flat low magnitudes in compression and transient high magnitudes in tension during by the emergence of the last prominent crack.

The σ_{IALB}'s in interval No.2 in which the last prominent crack is located, increased monotonically to the second highest magnitude among the 8 intervals, as shown in Fig. 7.24a. Part of the adhesion of the interface behind this crack, as shown in Fig.7.21a, is still sound at high steel stress levels. This portion of undamaged adhesion behind the crack may contribute to the high σ_{IARB}'s in the interval.

7.4.5 Numerical Simulation of Goto's Case 2

7.4.5.1 Comparison of Results of Test and Analyses

By removing the elements on the right half of the mesh for Case 1 (L=300 mm) shown in Fig. 7.11, the remainder of the mesh can be used as the finite element mesh to simulate the "pull-tension" specimen having length equal to the minimum crack spacing (150 mm), designated as Case 2 in Sect. 7.4.3. The input parameters for the analysis are the same as that used for the analysis of Case 1 except for one of them. That is the strength for tension in the circumferential (hoop) direction, denoted as f'_{th}, which was set equal to 1.3 times f'_t instead of f'_t. This value was determined by trial in order to obtain an optimal fit of the test result. Similar to the procedure for Case 1, the elongations of the perimeters in the end face (Fig. 7.13a), one from the test and another from analysis, are plotted against the steel stresses in Fig. 7.30a. In addition to the plotting of the curves for Case 2, the curves for Case 1, plotted in Fig. 7.13b, are reproduced in Fig. 7.30b to give a comparison of the magnitudes of the elongations for the two cases. It is seen that the ratio of the perimeter elongations for Case 1 and Case 2, which is approximately 6, is considerably larger than the ratio of the lengths of the two specimen, which is 2.

The crack and stress distributions at two steel stress levels, 225.8 MPa and 347.2 MPa, are presented in Fig. 7.31 and 7.32 respectively. It is seen that the longitudinal splitting cracks only reach three quarters of the specimen's radius at the steel stress level higher than 300 MPa. This is contrary to the result of the analysis for Case 1 in which longitudinal splitting cracks reached the side of the specimen for all steel stresses higher than 150 MPa. The difference in the two specimens is also noted in Goto's tests. In the document of the test, it states that

> "the closer the specimen length is to the maximum crack spacing, the more probable is the development of longitudinal cracks. Where the primary crack spacing is close to the minimum, longitudinal cracks are seldom seen at a steel stress less than 42 ksi (3,000 kg/cm^2)".

In Fig. 7.33, comparison of 3 analytical results characterized by 3 different magnitudes of f'_{th} ($f'_{th}= f'_t$, $1.2f'_t$ and $1.3f'_t$, respectively) are presented. It is seen that f'_{th} greater than f'_t must be selected in order to obtain a good fit to Goto's Case 2 tests.

7.4.5.2 Bond Stresses and Bond Slips

The prominent crack located at the plane of symmetry of the specimen, A-A (Fig. 7.10), propagates slowly but steadily upwards as shown in Fig. 7.32, but it does not reach the outer surface at the high steel stress level of 347.2 MPa. The σ_{IALB} in the vicinity of the crack, represented by interval No.1 as designated in Sect. 7.4.4.6 and Fig. 7.23, changes sign at the steel stress level of about 300 MPa as shown in Fig. 7.34a. The σ_{IARB} in this interval also has a deep drop at this steel stress level as shown in Fig. 7.35a. The curve obtained from Goto's test plotted in Fig. 7.30a shows the elongation of the perimeter on the end face becomes flat at the steel stress level of about 300 MPa. This may be explained by the propagation of the prominent crack located on the plane of symmetry.

Comparisons between the corresponding specimen averaged quantities obtained in Case 2 and Case 1 are presented in the following. The maximum σ_{SALB} in Case 1 is about 4.0 MPa (580 psi) obtained at steel stress of 160 MPa (at which the longitudinal splitting cracks reached the side of specimen and began rapid propagation), as shown in Fig. 7.24b. The maximum σ_{SALB} in Case 2 is about 4.82 MPa (700 psi) obtained at steel stress of approximately 220 MPa, as shown in Fig. 7.34b. The maximum σ_{SARB} in Case 1 is about 1.58 MPa (230 psi) obtained at steel stress of 160 MPa as shown in Fig. 7. 25b, and the maximum σ_{SARB} in Case 2 is also about 160 MPa (230 psi) obtained at steel stress of 300 MPa as shown in Fig. 7.35b.

The maximum s_{SALB} in Case 1 is about 0.0609 mm (0.0024 in.) as shown in Fig. 7.26b, and the maximum s_{SALB} in Case 2 is about 0.0304 mm (0.0012 in.) as shown in Fig. 7.36b. So the ratio of these two maximums of s_{SALB} is 2 which is equal to the ratio of the lengths of the specimens. For Case 1, the s_{SALB} is only about 0.00635 mm (0.00025 in.) at the steel stress level of 160 MPa, and after that it increases rapidly to 0.0609 mm (0.0024 in.) at the steel stress level of 300 MPa. On the other hand, the s_{SALB} in Case 2 increases nearly linearly in the whole range of steel stress levels. The maximum s_{SARB} in Case 1 is about 0.0355 mm (0.0014 in.) as shown in Fig. 7.27b while the s_{SARB} in Case 2 is only about 0.00762 mm.(0.0003 in.) as shown in Fig. 7.37b. The ratio of these two maximums is about 4.6 which is considerably larger than the ratio of the lengths of the specimens.

7.4.6 Numerical Simulation of the Test Conducted by Watstein and Mathey

7.4.6.1 Outlines of the Test and the Finite Element Modeling

In the tests conducted by Watstein and Mathey (1959), 6 inch square prisms, 8 in. long, with a centrally embedded reinforcing bar, were tested by applying a tensile force to the ends of the reinforcing bar. The length of specimen was selected by trial to be the the maximum length "which would not develop a transverse crack during the test" (Watstein and Mathey, 1959). The measurements included "the over-all extension of concrete at a point 3/8 in. from the surface of the bar, the extension of the embedded length of the bar, and the strain distribution on the sides of the specimens". Bars of different diameters were used, but only the specimens reinforced by the bar with diameter 7/8 in. were recorded with all three measurements mentioned.

The finite element model was formed by the same procedure as used in the simulation of Goto's test shown in Fig. 7.10. A axisymmetric cylinder, with 3.38 in. radius for the equivalent circular cross section to the 6×6 square of the tested specimens, was modelled on a quarter of the parent plane as an axisymmetric prism by axisymmetric 2-D elements. The lug detail was dimensioned in the same way as the model for Goto's test shown in Fig. 7.11.

The material properties were the same as used in the simulation of Case 2 of Goto's test except for the compressive strength of concrete and yield strength of reinforcement, which are 4,140 psi and 104 ksi respectively, according to the test data.

Because the specimens "were all moist cured until test" (Watstein and Mathey, 1959), the adhesive strength for the concrete-steel interface, f'_{cs}, was assumed to be in the range of 150 to 300 psi (Lutz and Gergely, 1967; Hsu and Slate, 1963) and set to be 180 psi, which was selected as the best fit of the tests from two simulations (f'_{cs} = 180 and 250 psi).

7.4.6.2 Extension of Concrete Adjacent to the Bar

The extension of concrete was measured at the point 0.375 in. from the face of the bar as shown in Fig. 7.38a. The curve denoted by 'finite element' in Fig. 7.39 represents the extensions of concrete from finite element simulation versus steel stress levels. In comparison with the curve from the test, which is shown in the same figure, the analytical result presents good agreement.

7.4.6.3 Extension for Embedded Bars

The measurement of the extension for embedded bars as shown in Fig. 7.38b was presented in the form of the ratio E_g/E_f in which E_g is the "effective" modulus of the embedded bar defined as "the ratio of applied stress to average strain in the embedded length" (Watstein and Mathey, 1959), and E_f is the modulus of free bar. The comparison between the analytical result and the test result is given in Fig. 7.40. The curve for analytical results shows a horizontal shift from the curve for the test, but the shapes of two curves exhibit similar characteristics. The experimental result is significantly stiffer than the analytical result for low steel stresses.

7.4.6.4 Distribution of Strain on the Surface of Specimens

The strains on the outer surface of the specimens were measured in the tests at the locations shown in Fig. 7.38c. The test result shows that the strain at the midpoint is slightly tensile (10-25 $\times 10^{-6}$) up to a steel stress of 60 ksi as shown in Fig. 7.41. Above this value of stress, the strain at the midpoint of the concrete became a compressive one.

The analytical result also shows this reversal of midpoint strain, as shown in Fig. 7.41. The analytical crack distributions which occurred before and after the reversal are presented in Fig. 7.42 and 7.43 respectively. The steel stress levels associated with these two cracking states are 32 ksi and 43 ksi respectively. Comparison of these two crack distributions indicates three changes occurred: (1) the longitudinal splitting crack reached and propagated along the outer surface; (2) the concrete separated from the front face of the lug located in interval No.5 and lifted up; and, (3) the crack located in interval No.1 propagated upward and other two cracks located in intervals No.2 and No. 4 became wider in width. The reversal of strain at the midpoint may be caused by combinations of these changes.

The crack distribution associated with steel stress level equal to 75 ksi is presented in Fig. 7.44. It is seen that the crack located in interval No. 1 has apparent growth in the vertical direction after the reversal of the strain at the midpoint, while the two cracks in the intervals No.2 and 4 have no development in crack length.

The comparison between different simulations in which only the tensile strength in the circumferential direction, f'_{th}, is varied as shown in Fig. 7.45. This indicates that the greater the f'_{th} specified, the greater the steel stress level required to produce the reversal of the strain at the midpoint.

7.4.6.5 Bond Stresses and Bond Slips

The four interval averaged quantities of bond, namely, the σ_{IALB}'s, σ_{IARB}'s, s_{IALB}'s and s_{IARB}'s, are plotted against steel stress levels in Fig. 7.46a to 7.49a, respectively, for the Watstein and Mathey tests. The four specimen averaged quantities, σ_{SALB}, σ_{SARB}, s_{SALB} and s_{SARB}, are plotted against steel stress level in Fig. 7.46b to 7.49b, respectively.

The σ_{IALB} in interval No.1 changes sign at about 27 ksi of steel stress level. The steel-concrete interface behind the most prominent crack located in the center of this interval is completely destroyed at early loading stage. This is evidenced in Fig. 7.42a, 7.43a and 7.44a where the part of the interface behind the crack is marked as an open crack. On the other hand, part of the interface in front of the crack is still sound at high steel stress levels due to the compressive radial bond stress, and this portion of undamaged adhesion is assumed to deliver the longitudinal bond stress, and it is unmarked in these Figs., i.e.- retains sound adhesion. In Fig. 7.48a the s_{IALB} in interval No.1 has a greater magnitude than the s_{IALB} in interval No.2 due to the complete damage of adhesion behind the crack.

The σ_{IALB} in interval No.5 reduces to zero due to the lifting up of concrete from the front face of the lug in the interval associated with the reversal of strain at midpoint as described in Sect. 7.4.6.4. The σ_{IALB} in interval No.4 keeps a nearly constant value of about 700 psi through the whole loading history (0-80 ksi) as shown in Fig. 7.46a.

The σ_{IALB} in interval No.3 developed the maximum value of about 2,100 psi for the specimen and then drops quickly to 600 psi. This is associated with the reversal of strain at midpoint as described in Sect. 7.4.6.4. It then gradually reduces to zero due to the complete loss of contact in the front face of the lug in interval No.3. On the other hand, the σ_{IALB} in interval No.2 has a big jump as the deep drop of the σ_{IALB} in interval No.3 occurs, and keeps increasing until the final loading stage.

Comparison of Fig. 7.42b, 7.43b and 7.44b indicates that contact on the front face of the lug in interval No. 3 is greatly reduced while the contact on the front face of interval No. 4 remains nearly unchanged. This is in contrast to the configurations which occurred in the analyses of Case 1 for Goto's tests, in which the loss of contact in the front face of lugs progresses in proportion to the positions of lugs. That is, the closer to the protruding end of the steel the lug is, the earlier the loss of contact on the front face of the lug occurs.

The maximums of specimen averaged quantities are as follows. The maximum of σ_{SALB}, 780 psi, occurred at about a steel stress of 27 ksi, after which the σ_{IALB} in interval No.1 begins to change sign. At the same steel stress level, the maximum of σ_{IARB}, which is about 265 psi, is reached. The maximum of σ_{SALB} of Watstein and Mathey tests is 30% greater than Case 1 and about 11% greater than Case 2 of Goto's tests. The maximum of σ_{IARB} is about 15% greater than both Case 1 and 2. This increase may be related to the increase of concrete cover in Watstein and Mathey test in which the area of cross section is 36 in.^{2} while that in Goto's test is only 22.3 in.^{2}. The maximum of s_{SALB} is about 0.0008 in. which is about 1/3 of that (0.0024 in.) obtained from the analysis of Case 1 of Goto's test. The maximum of s_{SARB} is 0.00065 in. which is about 1/2 of that (0.0012 in.) obtained from Case 1 of Goto's test. These decreases in s_{SALB} and s_{SARB} also may be explained by the increase of concrete cover in Watstein and Mathey test.

7.4.7 Discussion on Bond Stress-Bond Slip Relationships

7.4.7.1 Nilson and Tanner's Test Arrangements

In Nilson and Tanner's tests (1971), bond-slip in "tension-pull" specimens, shown in Fig. 7.50, was investigated. The steel strains were measured by electric strain gages which were placed in milled grooves inside the reinforcing bars as shown in Fig. 7.51. The concrete strains were measured from the concrete strain gages embedded in the vicinities of and parallel to the bars as shown in Fig. 7.50. The bar size is No. 8.

The unknown bond slip at a location b, S_b, is determined by integration of the strains in the reinforcing bar and concrete

$$S_b = S_a + \int_a^b \varepsilon_s - \int_a^b \varepsilon_c \qquad (7.4.3)$$

in which S_a is the known slip at location a, ε_s is the steel strain and ε_c is the concrete strain. In the tests, the slips at the center of the specimens, are assumed to be zero, and were used as known slips.

The bond stress at any point was calculated using the slope of the steel strain curve at that point. This was done by using the formula:

$$dT = u \cdot \Sigma_0 \cdot dx$$

in which, the bond stress, u, is

$$u = (dT/dx)/ \Sigma_0. \qquad (7.4.4)$$

This equation is evaluated using the relations

$$dT/dx = (d\varepsilon_s/dx) \cdot E \cdot A$$

and

$\Sigma_0 = \pi D$

in which $d\varepsilon_s/dx$ is the slope of steel strain curve, E is Young's Modulus, A is the area of the bar and D is the diameter of the bar.

7.4.7.2 Nilson and Tanner's Test Results

The specimens tested were categorized into two groups, II-A and II-B. The concrete compressive strength for the specimens in group II-A was about 3,500 psi. It is recorded in the documentation of the tests that "since these specimen developed lateral cracks near the center, it was impossible to measure the slip at the higher bond stresses developed after the cracking".

The results of two specimens in group II-A, named II-A-1 and II-A-3, are shown in Figs. 7.52 and 7.53. The two specimens are identical except for the positions at which the concrete strain gages were placed. In the II-A-1 specimen, concrete strain gages are placed at 1/2 to 1 in. from the bar surface, while in the II-A-3 specimen, they are placed at 1/4 to 1/2 in. from the bar surface. It is shown in Fig. 7.52 and 7.53 that at the same bond stress 200 psi, the slip for II-A-1 is about 350 microinches, while that for II-A-3 is about 150 microinches. As a result, the slope of the curve for II-A-1 is considerably flatter than that for II-A-3. Therefore, the documentation of the tests states that it "indicated in turn, a large strain gradient in the concrete, and thus the necessity to keep the concrete strain gages as close to the reinforcing bar as possible" (Tanner, 1971).

The concrete compressive strengths for the specimens in group II-B varies from 4,000 to 4,500 psi. All the concrete strain gages placed in the specimens of this group were located 1/4 to 1/2 in. from the bar surfaces. Lateral cracking did not occur, but "there was extensive cracking longitudinally along the reinforcing bar propagating from the ends toward the center of specimens" (Tanner,1971). The test results for three specimen of this group, II-B-1, II-B-2 and II-B-3, are given in Fig. 7.54 to 7.56. From these curves it is shown that "as the center of the specimen is approached, the maximum bond stresses increase" (Tanner, 1971).

7.4.7.3 Comparison with the Results of this Study

The σ_{IALB}'s and s_{IALB}'s, obtained in the finite element simulation of Case 1 of Goto's tests, are shown in Fig. 7.24 and 7.26 respectively. The σ_{IALB}'s and s_{IALB}'s in intervals No.7 and No.8 are averaged to represent the bond stress and bond slip at the point which joins the two intervals and is located 1 in. from the loaded end. Similarly, averages of σ_{IALB}'s and s_{IALB}'s in intervals No.5 and No.6 give the bond stress and bond slip at a point located 2.3 in. from the the loaded end. The bond stress and bond slip at the point located 3.7 in. from the loaded end are obtained from the averages of σ_{IALB}'s and s_{IALB}'s in interval No. 3 and No.4. The curves for bond stress- bond slip relationships at these three points are plotted in Fig. 7.57.

By comparison of the curves for the simulation of Goto's Case 1 shown in Fig. 7.57 to the curves for group II-B of Nilson and Tanner's tests shown in Figs. 7.54-7.56, it is seen that they share the common feature, that "as the center of the specimen is approached, the maximum bond stresses increase" (Tanner, 1971).

The progressive deterioration of bond in Case 1 of Goto's tests, described in Sect. 7.4.4.7 is due to the progressive lift-up along the concrete-steel interface caused by the progression of the most prominent cracks, longitudinal splitting cracks and compressive concrete yielding at the front faces of lugs as described in Sect. 7.4.4.3-7.4.4.5.

Because extensive longitudinal cracking was recorded for group II-B of Nilson and Tanner's tests, it is natural to infer that the mechanism of progressive deterioration of bond existing in the simulation of Goto's Case 1 may explain the phenomena where local maximum bond stress increases from the loaded end to the center, as occurred in Nilson and Tanner's tests. It seems that this mechanism of progressive bond deterioration dominates for the general cases where longitudinal cracking dominates.

The differences between the curves shown in Fig. 7.57 to the curves shown in Figs. 7.54-7.56 are also obvious. In the simulation of Goto's Case 1, the magnitudes of bond slips at which local maximum bond stresses are obtained are much smaller, and the values of local maximum bond stresses are higher, than in group II-B of Nilson and Tanner's tests. In addition, the bond stress at zero bond slip is not zero in the simulation of Goto's Case 1.

The differences can be attributed to the different geometries of the specimens used in the two tests: a No. 8 bar embedded in a 18 in.× 6 in.×6 in. prism for Nilson and Tanner's test and a No. 6 bar embedded in a 12 in.× 4.7 in.×4.7 in. prism for Goto's tests.

These differences can also be attributed to the locations where the bond slips are evaluated. The specimens II-A-1 and II-A-3 of Nilson and Tanner's tests have shown that moving the measuring positions from 1/2-1 in. to 1/4-1/2 in. reduces the slips by about 350/150= 2.3 times. Because the bond-slip in the simulation of Goto's Case 1 is evaluated at the interface of concrete and steel, that is, at a zero distance from the bar, much smaller slips than that in the II-B group of Nilson and Tanner's tests are anticipated, and at zero slip the bond stresses are not zero due to the adhesion.

7.4.8 Effect of the Parameter η_s

The effect of parameter η_s defined in Sect. 6.3.1.2, is shown by giving it a value which is so big that the switch from displacement control to fracture energy control does not occur. Two results of elongation of the perimeters in the end faces in simulations of Goto's Case 1 are plotted in Fig. 7.58. The only difference between them is that one is with fracture energy control and the other is without. It is seen that after the rapid propagation of longitudinal cracking, the one with fracture energy control approaches the test result, but the one without the control deviates from the test results substantially.

For those displacement control points which deviate substantially from the energy control points in Fig. 7.58, the ratio of the unbalanced force norm to the applied force norm is greater than 0.6. Thus these points may be considered to have 'not satisfied' a 'reasonable' force convergence criterion. On the other hand, the satisfaction of force convergence criterion is much more difficult to achieve than for displacement criterion. The entire field of convergence criterion appears to be lacking a rational treatment and is awaiting a disciplined analysis to provide reliable guidelines for practical solutions.

The displacement measure used in Fig. 7.58 is particularly sensitive to the convergence criteria. The longitudinal displacements of the loading point for the same solution, which are shown in Fig. 7.59, are less sensitive.

Table 7.1: Specimens of Goto's Tests

Setup	First Setup		Second Setup	
Case			Case 1	Case 2
Length	1,000 mm	1,000 mm	300 mm	150 mm
Maximum Crack Spacing	250 mm	250 mm	300 mm	300 mm
Bar Diameter	19 mm	32 mm	19 mm	19 mm
Cross Section	100mm ×100mm	120mm×120mm	120mm× 120mm	120mm× 120mm
Documented Measurements	None		Elongation of perimeters on the end faces	
Oberservations of Dye Internal Cracks	Longitudinal splitting cross sections show Dye Cracks		None	

Table 7.2: Steel Stress Levels associated with Interval Maximum σ_{IALB} 's

Interval No.	1	2	3	4	5	6	7	8
Steel Stress level No.	8	10	7	7	6 - 7	6	2	4

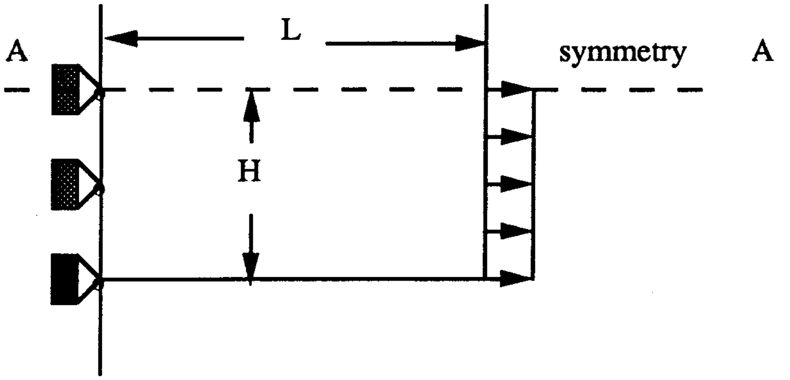

a) Concrete Prism Subject to Uniform Tension

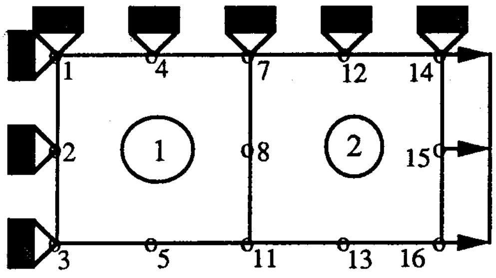

b) Finite Element Modelling

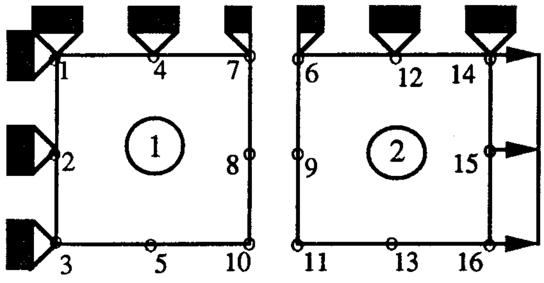

c) Configuration for Post-cracking

Figure 7.1: Simulation of Concrete Prism Subject to Uniform Tension

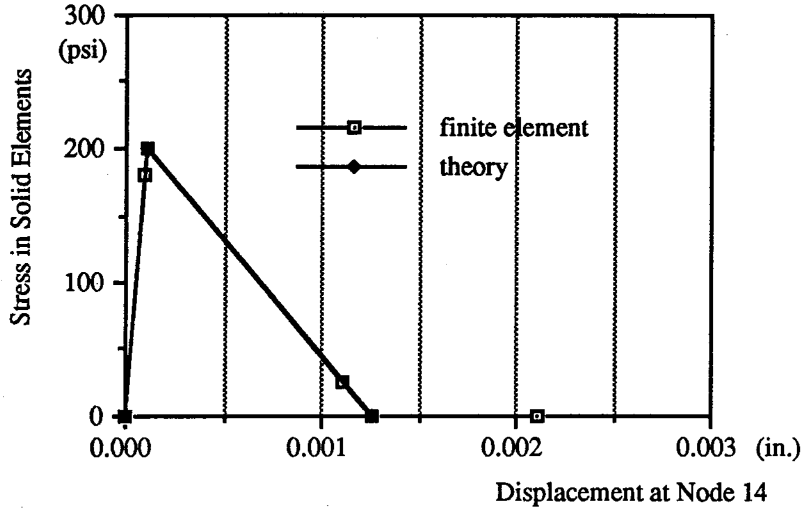

Fig. 7.2: Solution for H/L=1 and ALSDI Constraint

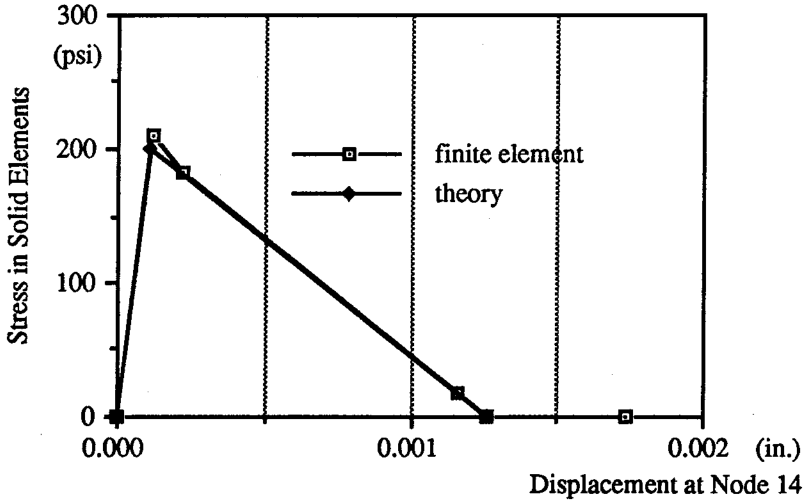

Fig. 7.3: Solution for H/L=1 and TCW Constraint

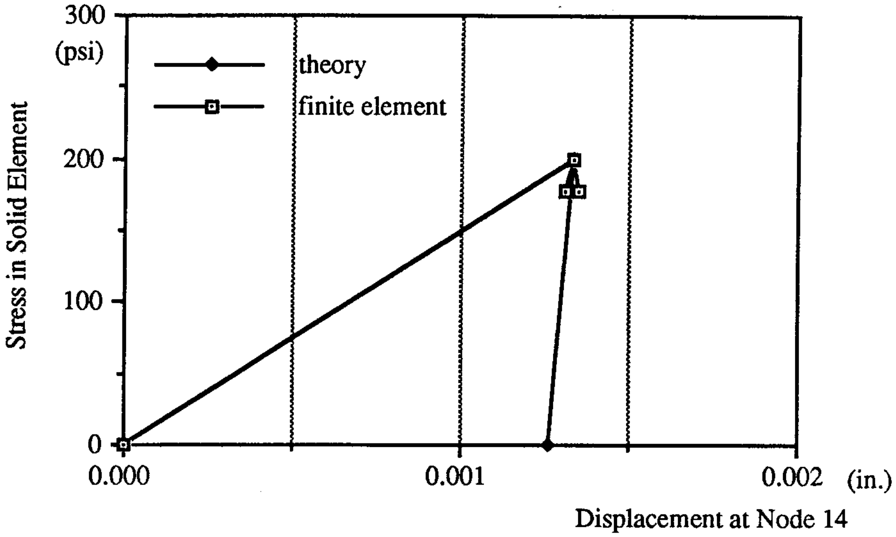

Fig. 7.4: Solution for H/L=1/12 and ALSDI Constraint

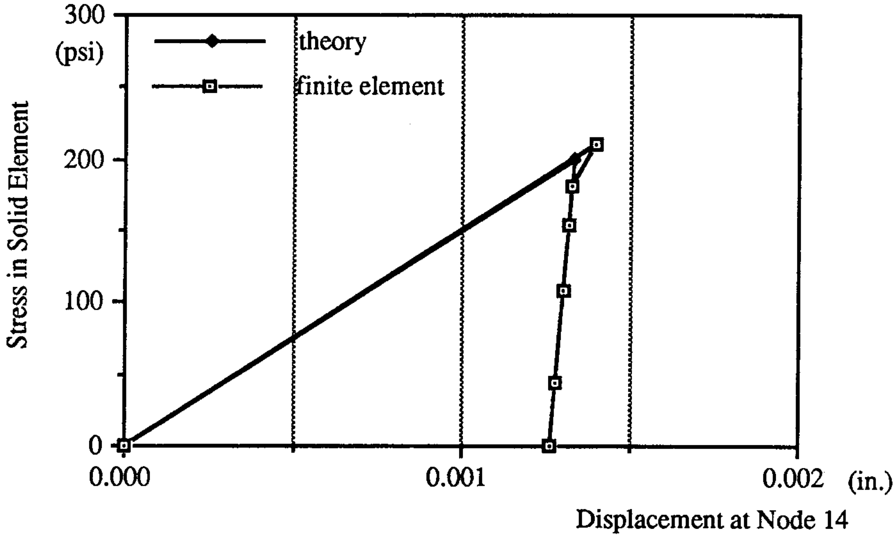

Fig. 7.5: Solution for H/L=1/12 and TCW Constraint

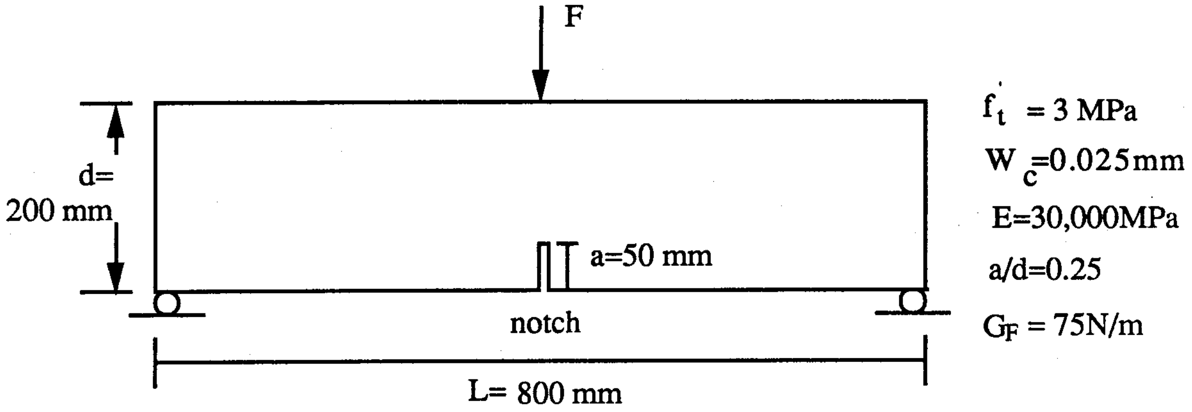

Figure 7.6: Three-Point Bending of Notched Concrete Beam

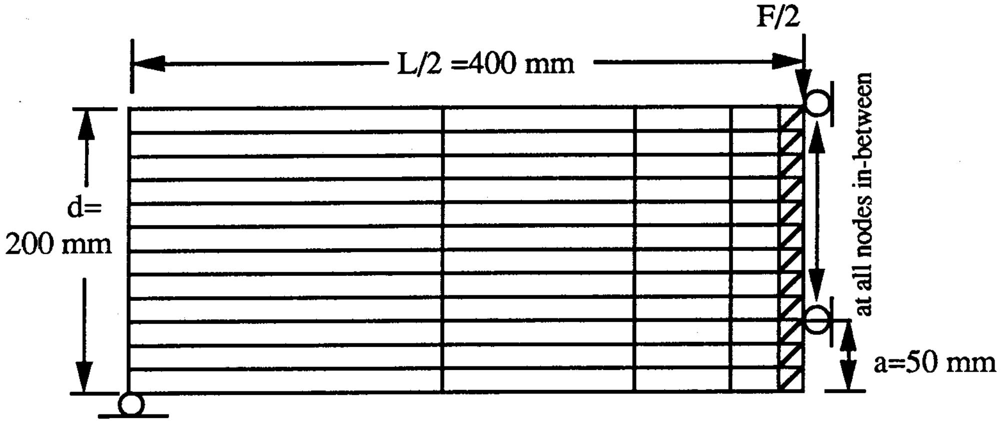

Figure 7.7: Finite Element Model for Notched Concrete Beam

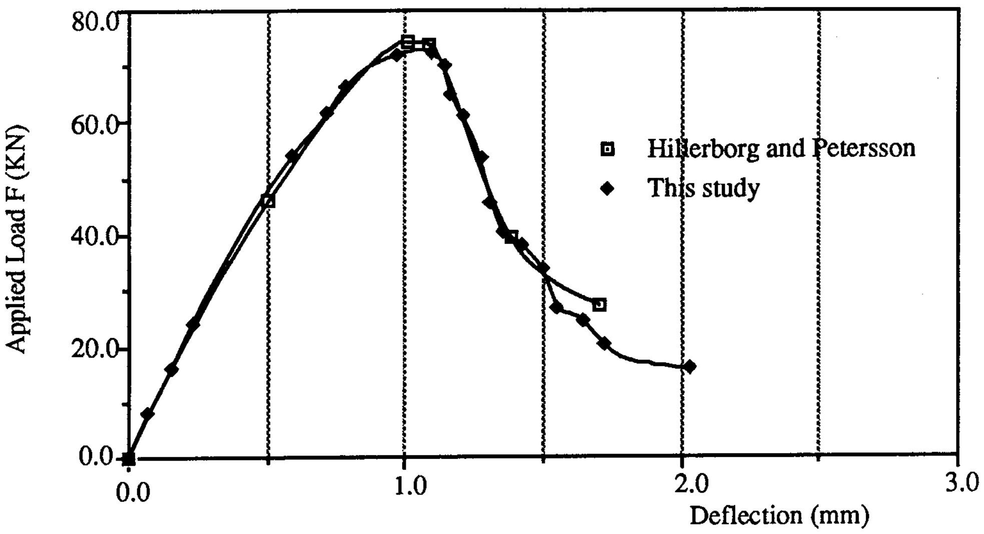

Fig. 7.8: Load vs. Deflection for Notched Concrete Beam

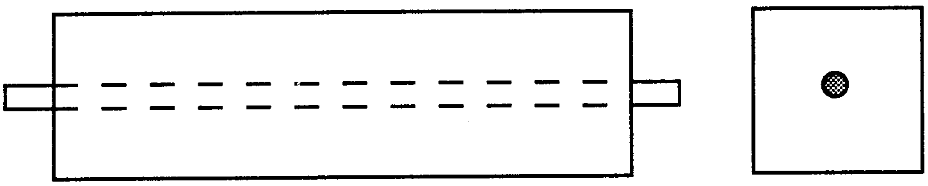

a) Bar Encased in a Squared Concrete Prism

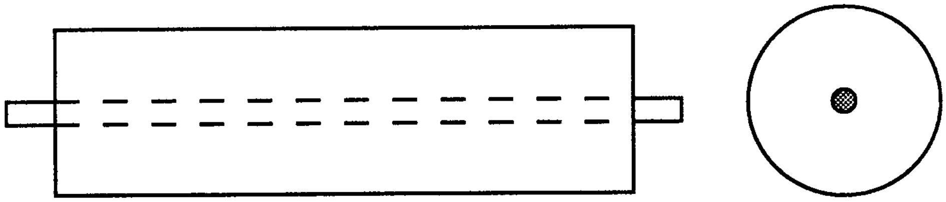

b) Bar Encased in a Rounded Concrete Prism

Fig. 7.9: Deformed Reinforcing Bar in a Concrete Prism

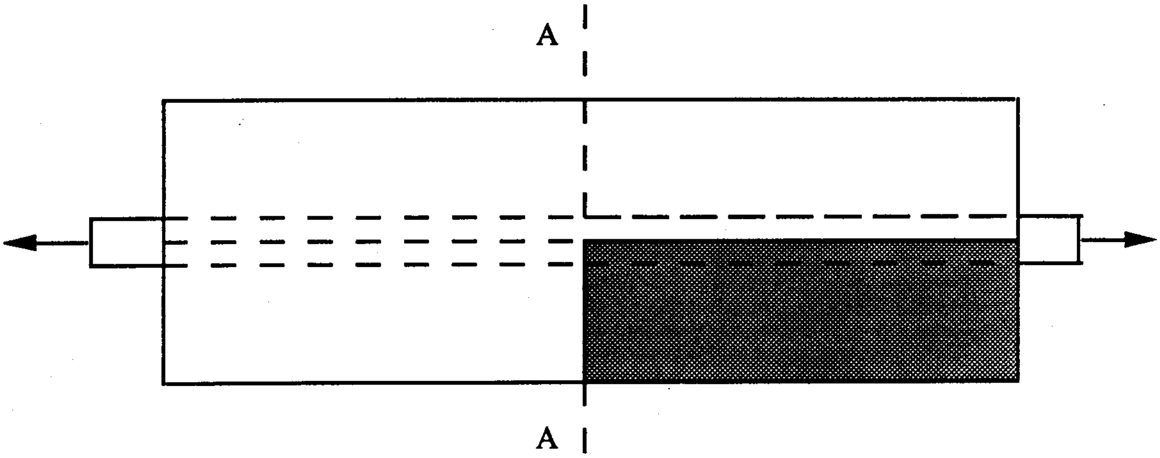

a) Due to Symmetry to Central Plane A-A and Axisymmetry, only One Quarter of the Parent Plane was Modelled

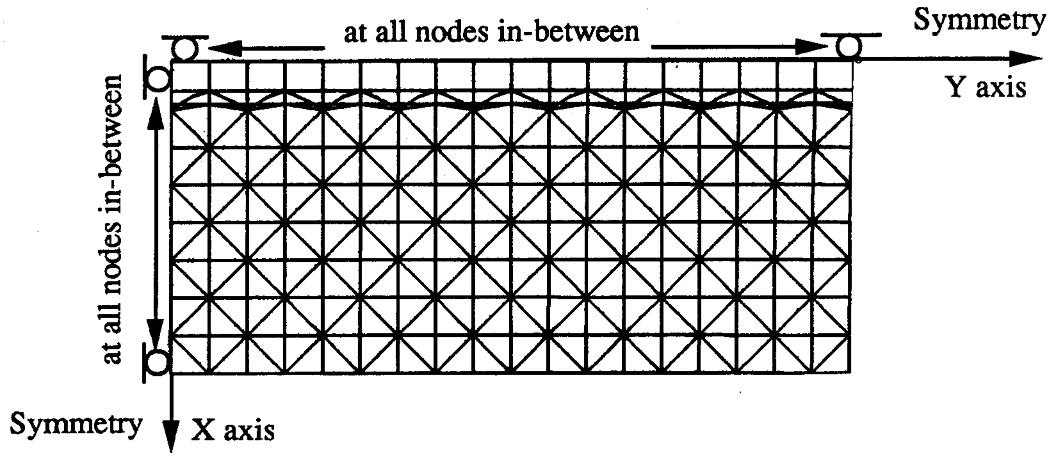

b) Finite Element Mesh

Figure 7.10: Mesh for Axisymmetrical "Tension-Pull" Specimens

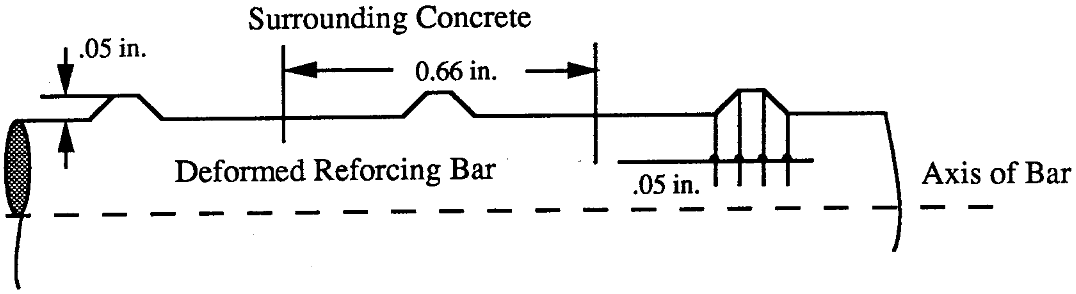

a) Profile of the Deformed Reinforcing Bar

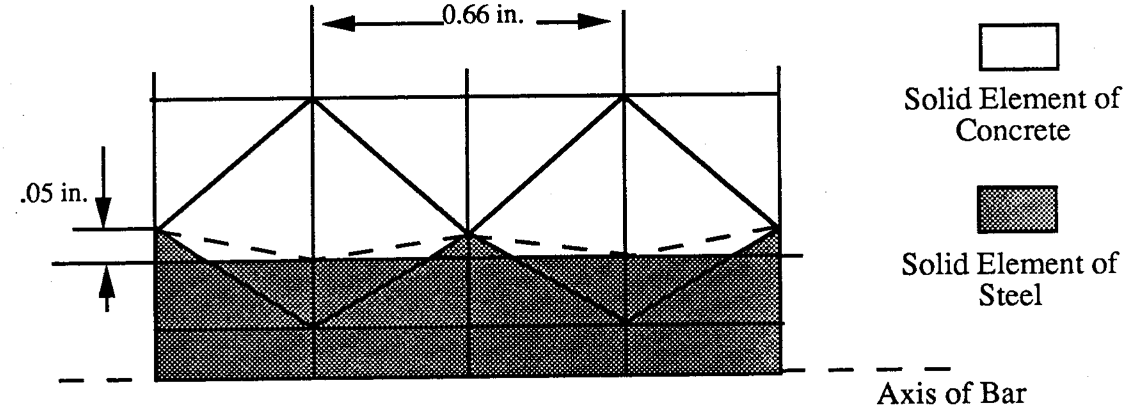

b) Finite Element Model for Deformed Reforcing Bar

Fig. 7.11: Modeling of Deformed Reforcing Bar

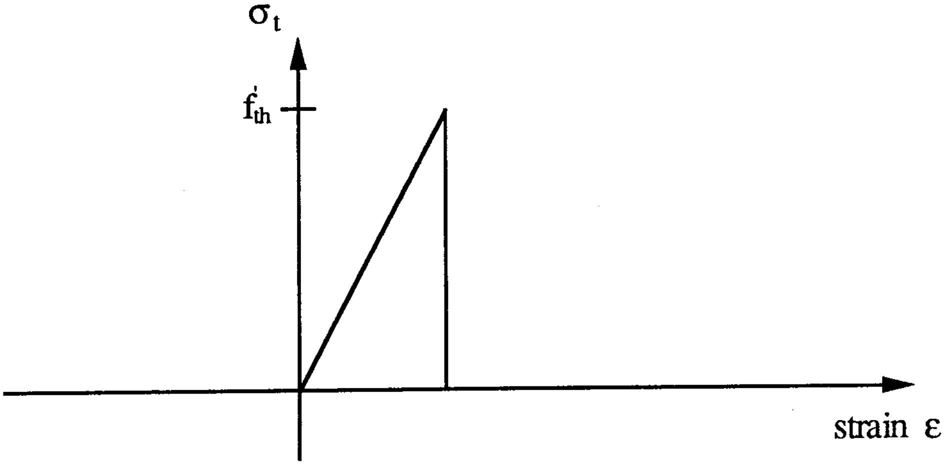

Fig. 7.12: Tensile Stress-Strain in the Circumferential Direction

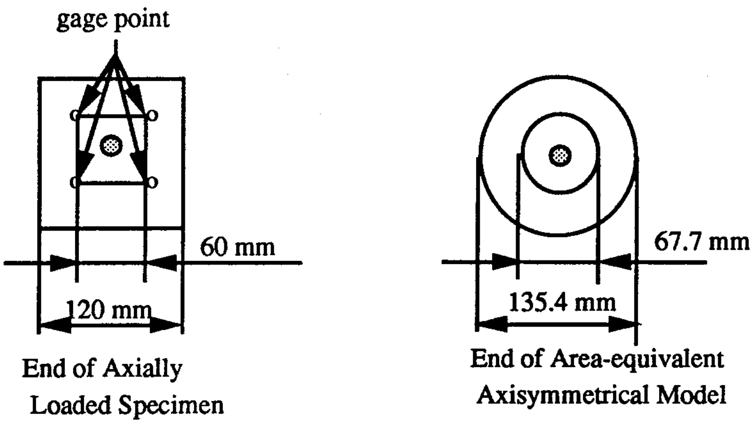

a) End face of the Axially Loaded specimen and the
Area-equivalent Axisymmetrical Model

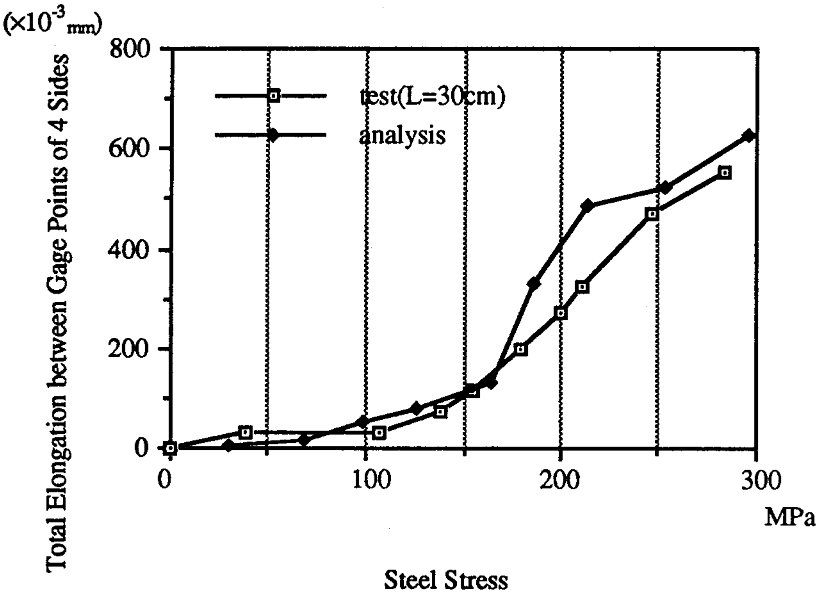

b) Comparison between Test Result and Finite Element Analysis
(Case 1, L=300 mm)

Fig. 7.13: Stress of Reinforcing vs. Perimeter Elongation

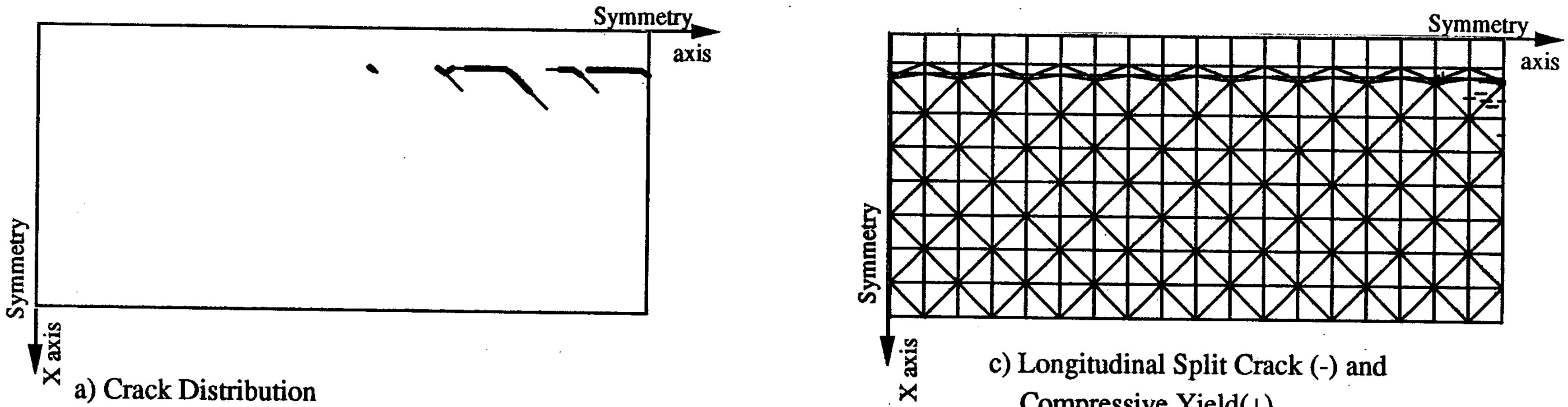

a) Crack Distribution

c) Longitudinal Split Crack (-) and
Compressive Yield(|)

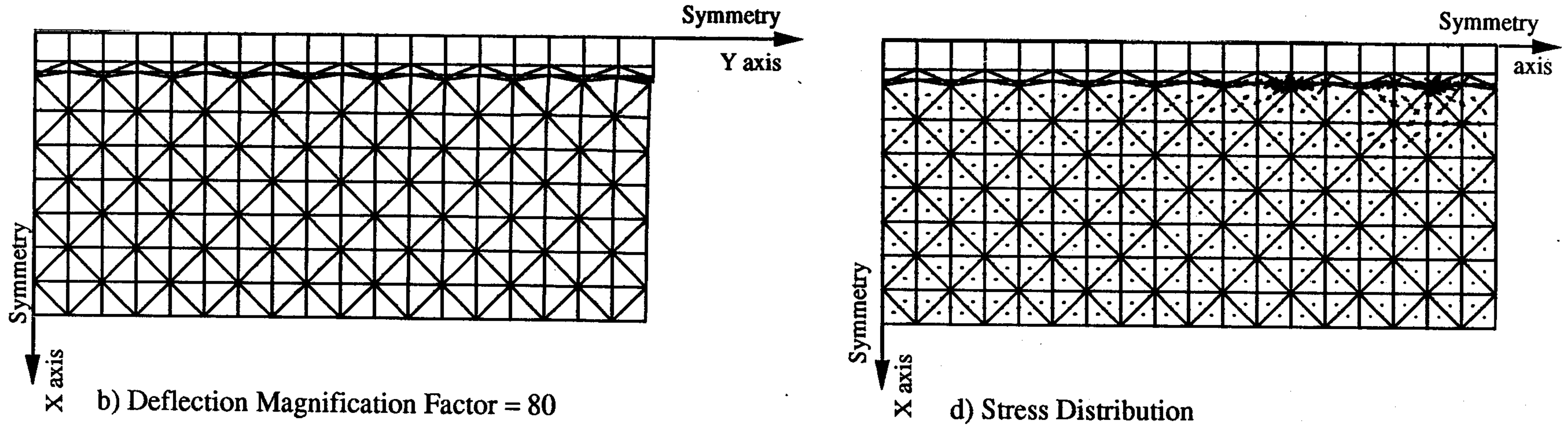

b) Deflection Magnification Factor = 80

d) Stress Distribution

Figure 7.14: Solution for Case 1: Steel Stress Level = 68.8 MPa

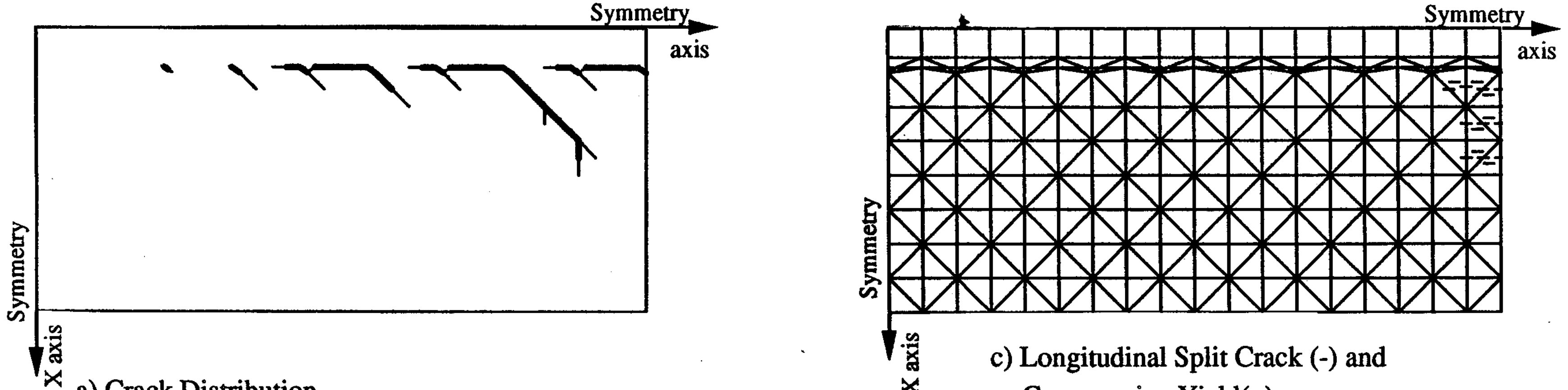

a) Crack Distribution

c) Longitudinal Split Crack (-) and Compressive Yield(|)

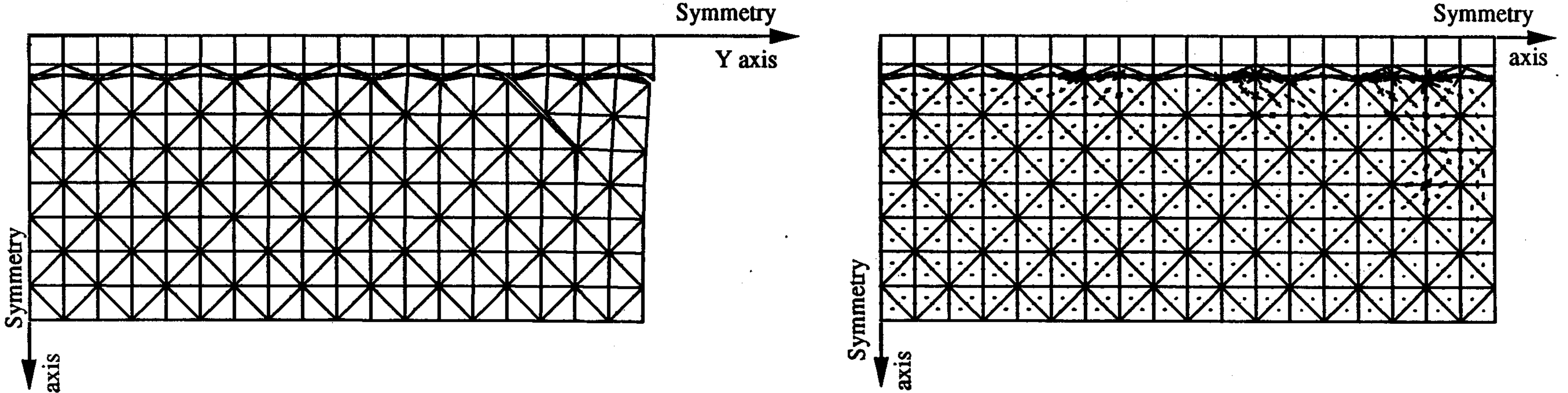

b) Deflection Magnification Factor = 80

d) Stress Distribution

── incipient crack, closed crack or boundaries of structure

━━ open crack and crack width ≤ W_c

▬▬ open crack and crack width ≥ W_c

Figure 7.15: Solution for Case 1: Steel Stress Level = 98.8 MPa

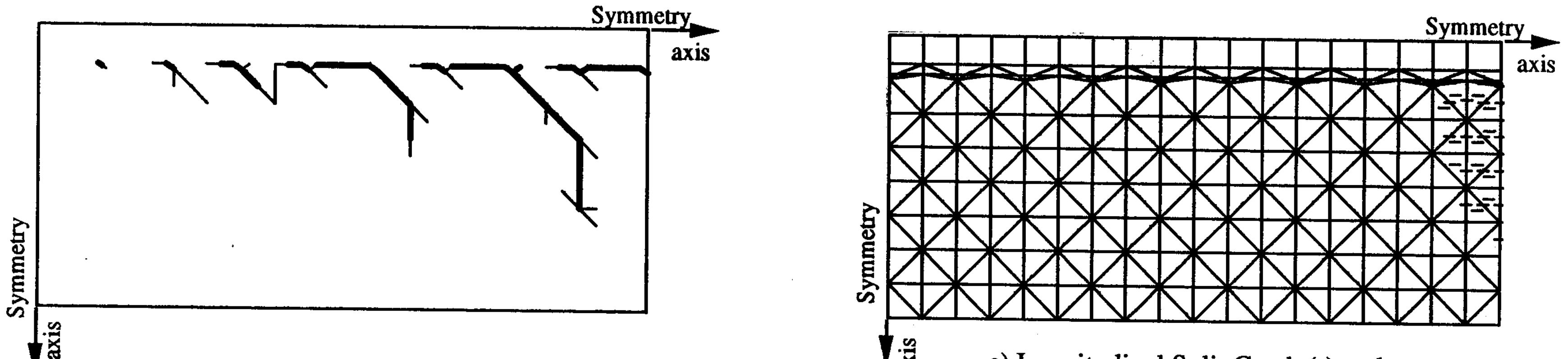

a) Crack Distribution

c) Longitudinal Split Crack (-) and Compressive Yield(ı)

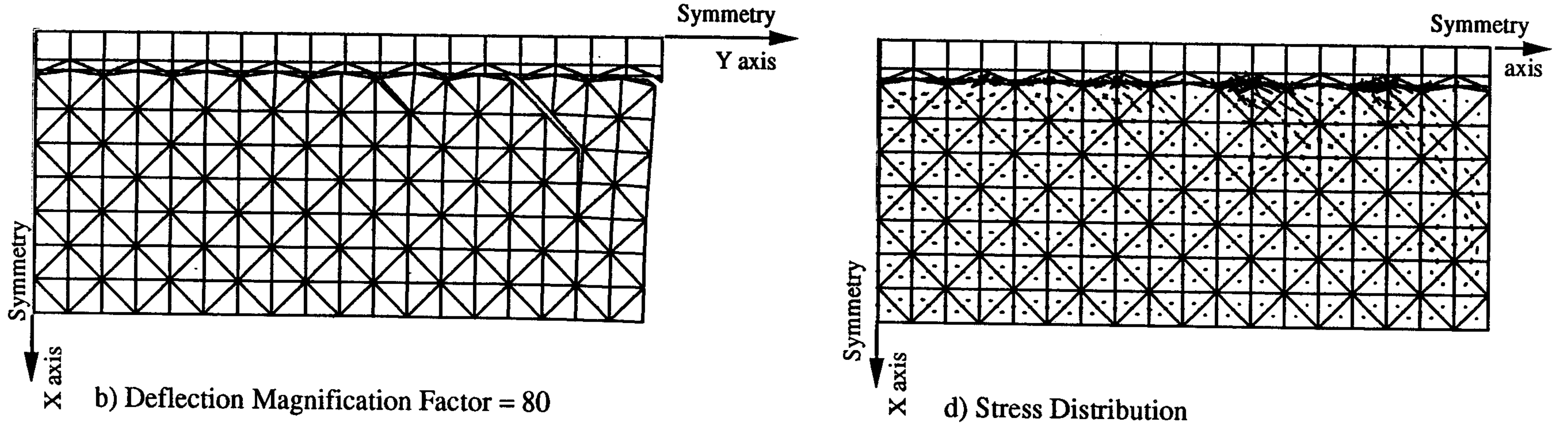

b) Deflection Magnification Factor = 80

d) Stress Distribution

incipient crack, closed crack or boundaries of structure

open crack and crack width ≤ W_c

open crack and crack width ≥ W_c

Figure 7.16: Solution for Case 1: Steel Stress Level =125.8 MPa

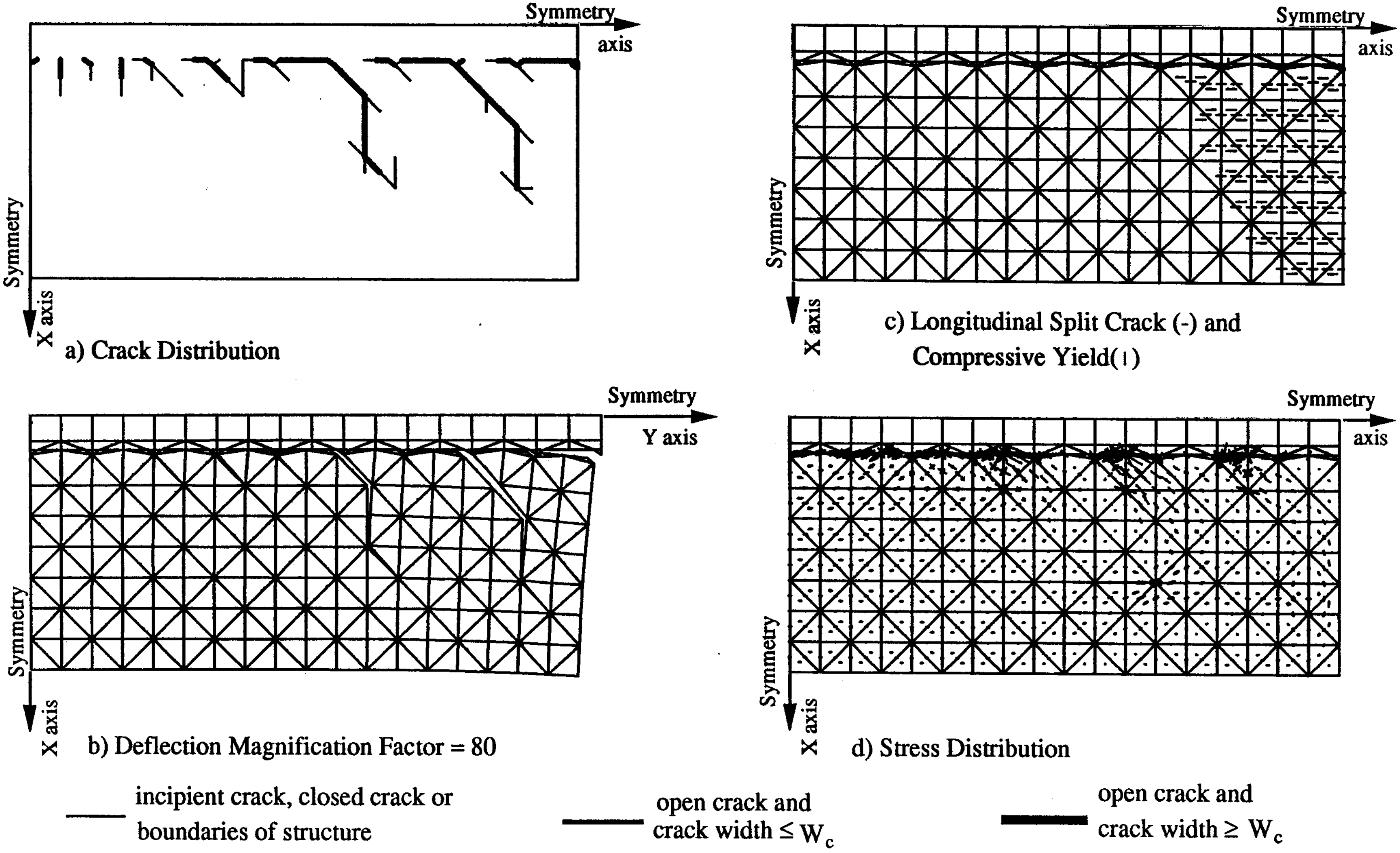

a) Crack Distribution

c) Longitudinal Split Crack (-) and Compressive Yield(|)

b) Deflection Magnification Factor = 80

d) Stress Distribution

Figure 7.17: Solution for Case 1: Steel Stress Level =165 MPa

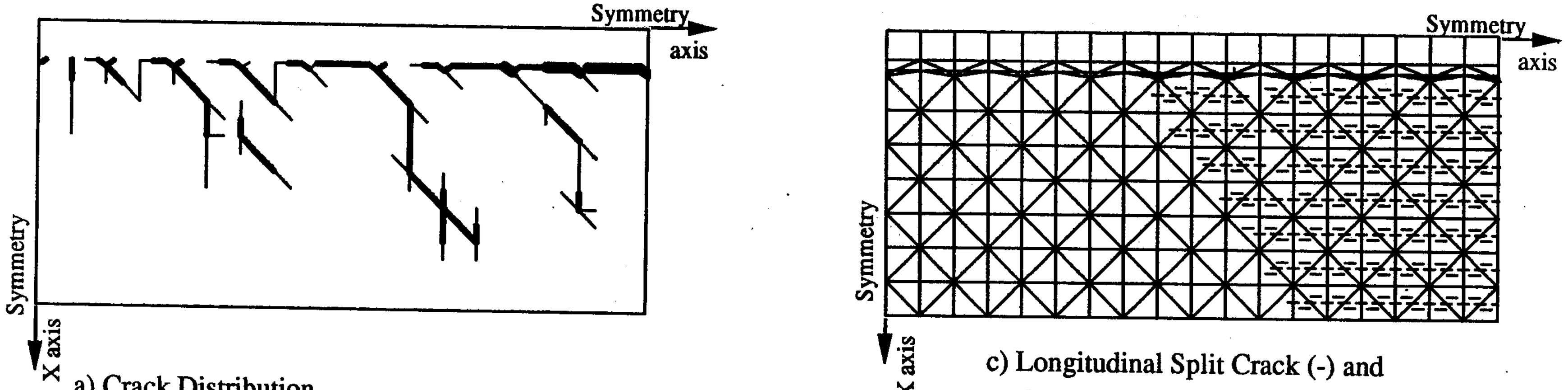

a) Crack Distribution

c) Longitudinal Split Crack (-) and Compressive Yield(|)

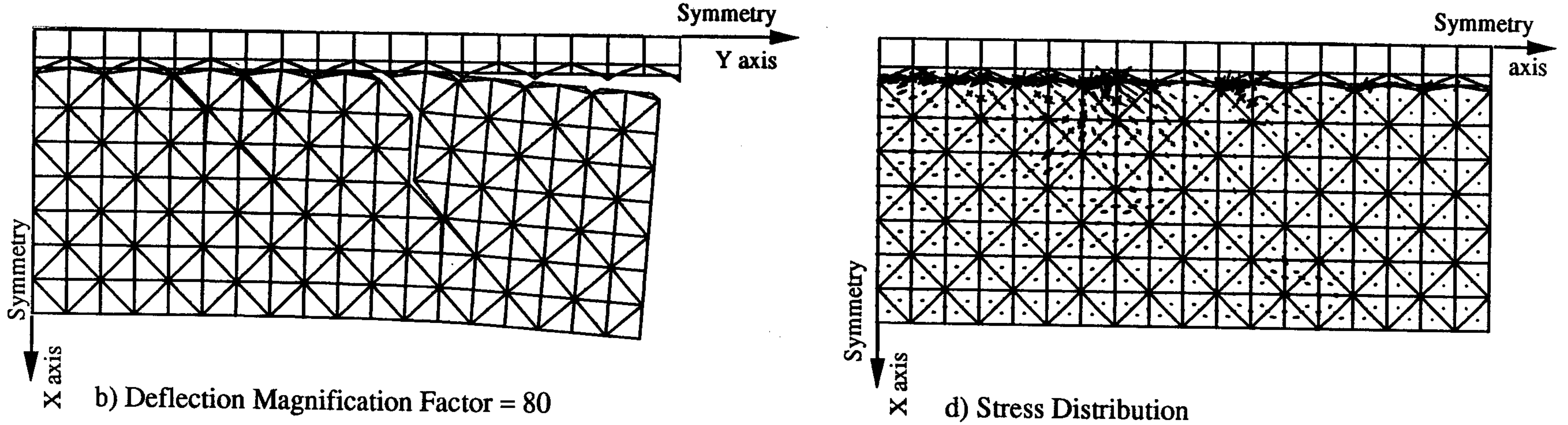

b) Deflection Magnification Factor = 80

d) Stress Distribution

— incipient crack, closed crack or boundaries of structure

— open crack and crack width ≤ W_c

▬ open crack and crack width ≥ W_c

Figure 7.18: Solution for Case 1: Steel Stress Level =185.3 MPa

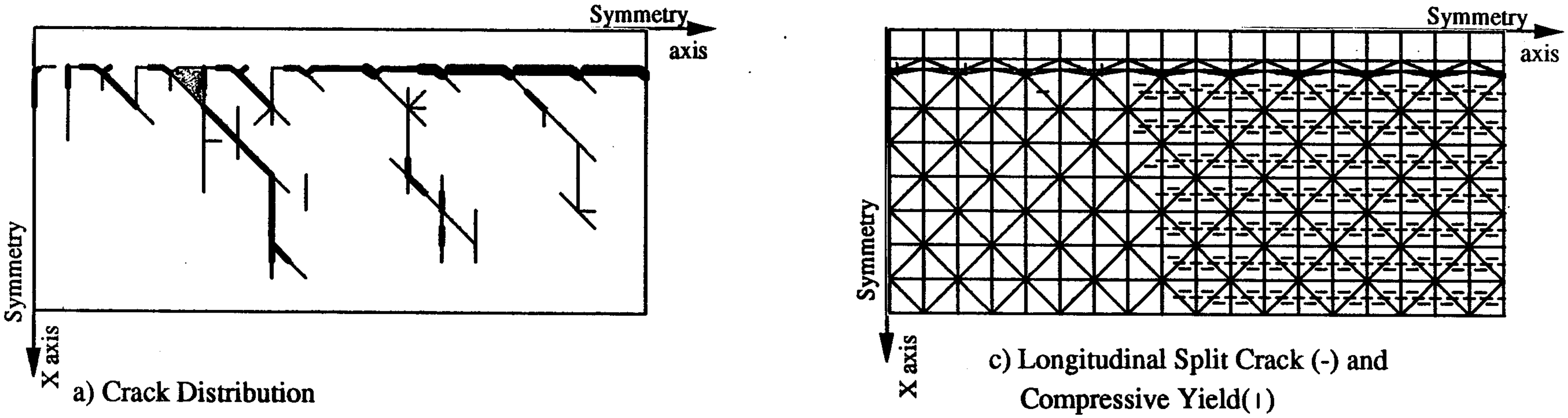

a) Crack Distribution

c) Longitudinal Split Crack (-) and Compressive Yield(I)

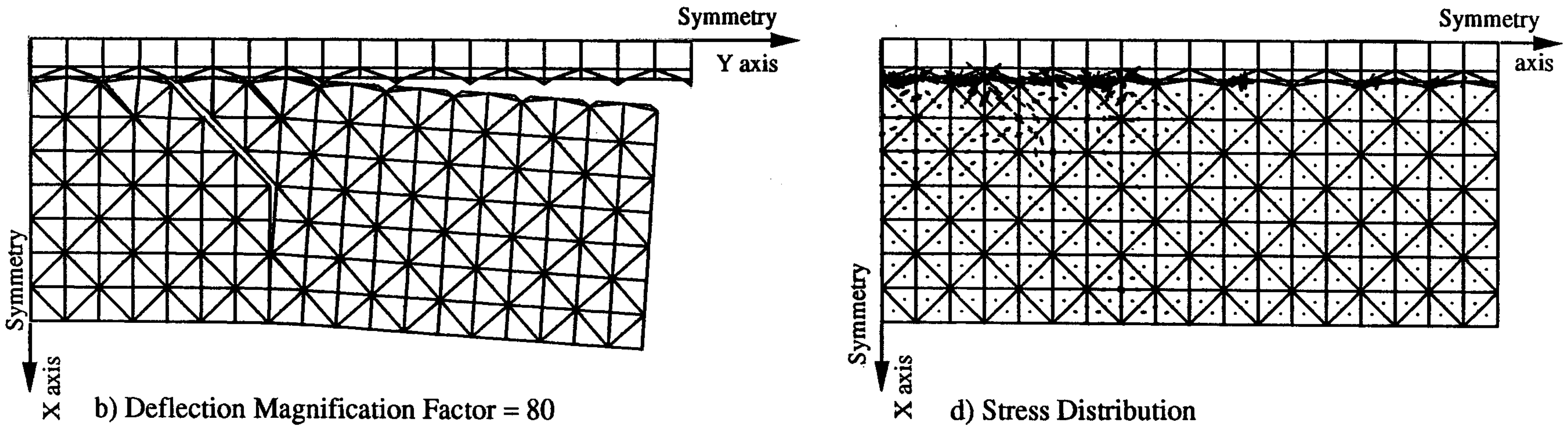

b) Deflection Magnification Factor = 80

d) Stress Distribution

— incipient crack, closed crack or boundaries of structure

— open crack and crack width ≤ W_c

— open crack and crack width ≥ W_c

Figure 7.19: Solution for Case 1: Steel Stress Level =211.9 MPa

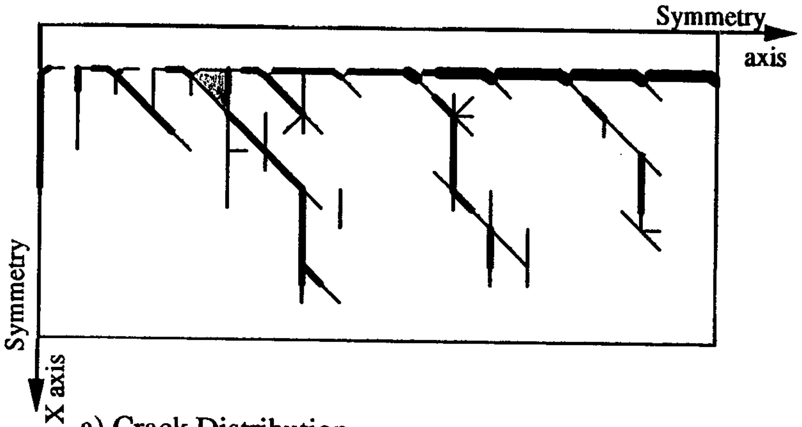

a) Crack Distribution

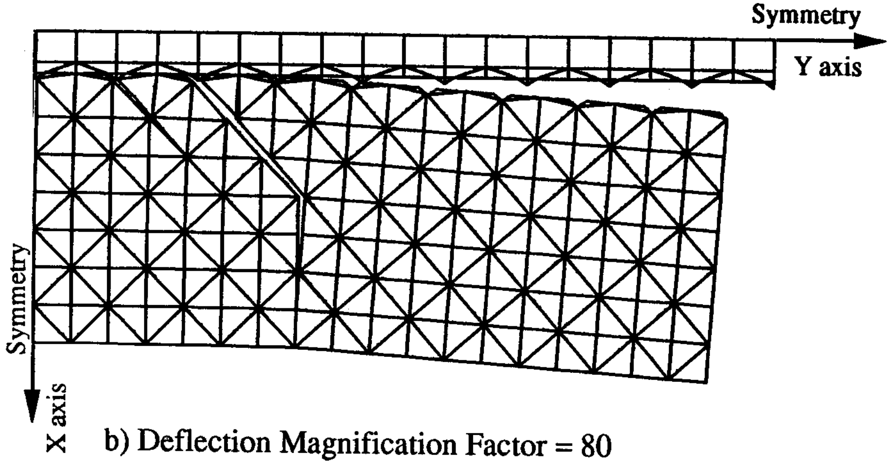

b) Deflection Magnification Factor = 80

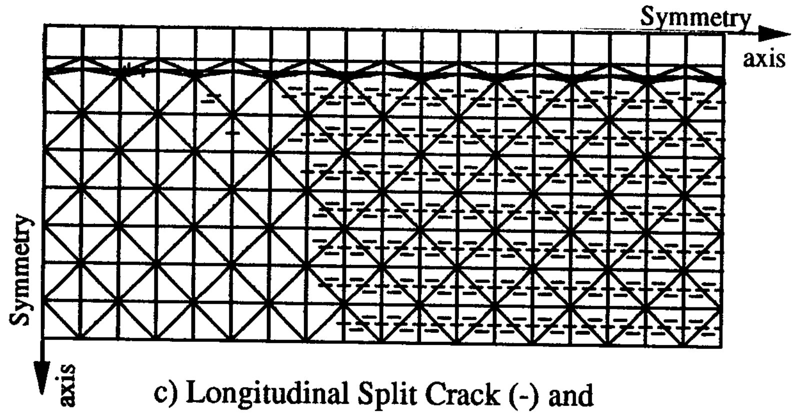

c) Longitudinal Split Crack (-) and Compressive Yield(ı)

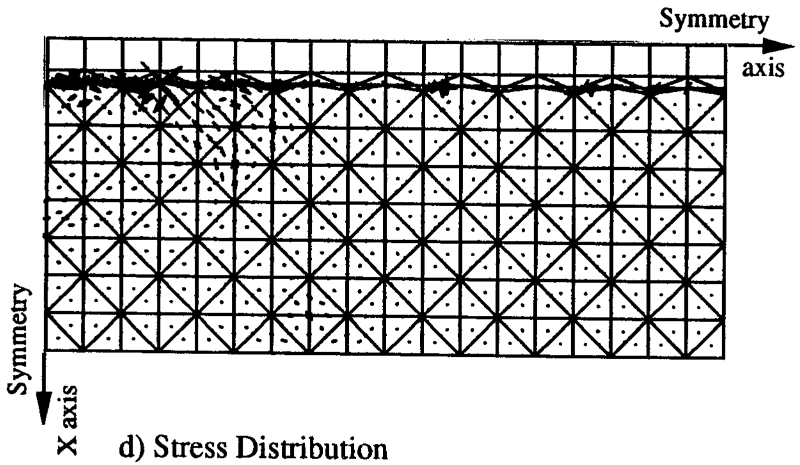

d) Stress Distribution

— incipient crack, closed crack or boundaries of structure

— open crack and crack width ≤ W_c

▬ open crack and crack width ≥ W_c

Figure 7.20: Solution for Case 1: Steel Stress Level =251.2 MPa

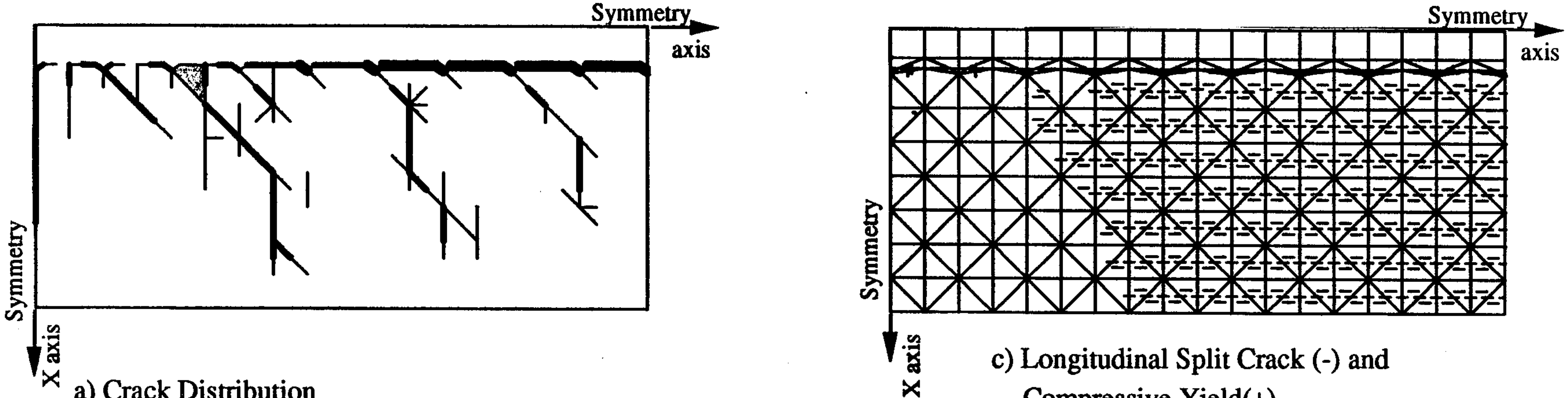

a) Crack Distribution

c) Longitudinal Split Crack (-) and Compressive Yield(|)

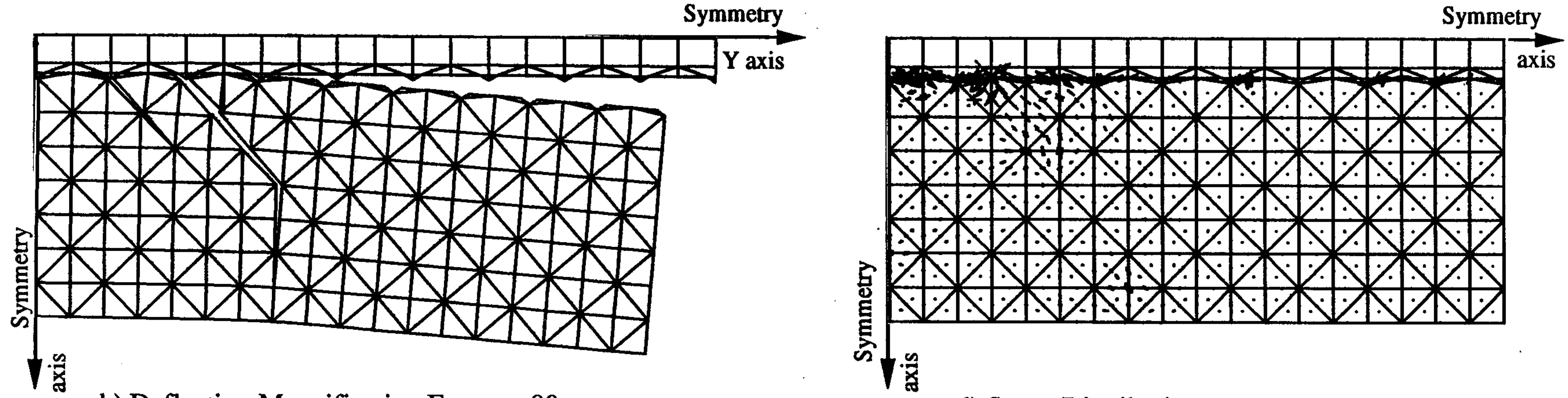

b) Deflection Magnification Factor = 80

d) Stress Distribution

— incipient crack, closed crack or boundaries of structure

— open crack and crack width ≤ W_c

▬ open crack and crack width ≥ W_c

Figure 7.21: Solution for Case 1: Steel Stress Level =294.1 MPa

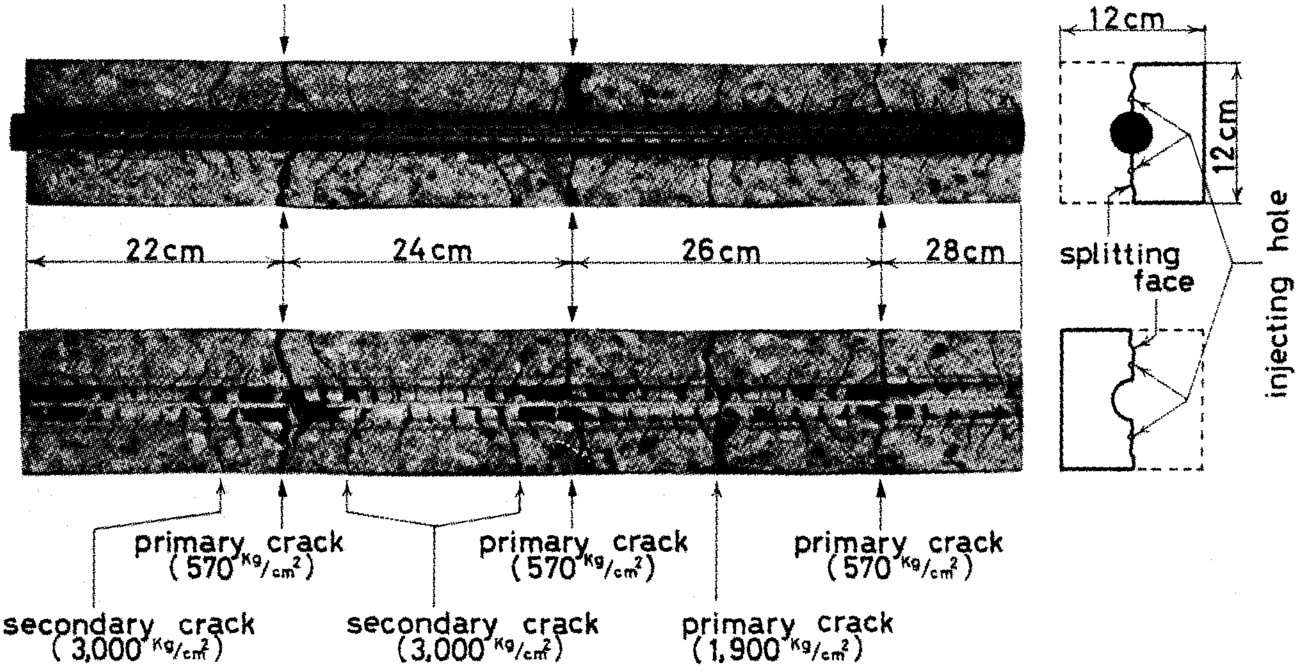

a) Prism with 32 mm Bar and 12cm × 12 cm Square

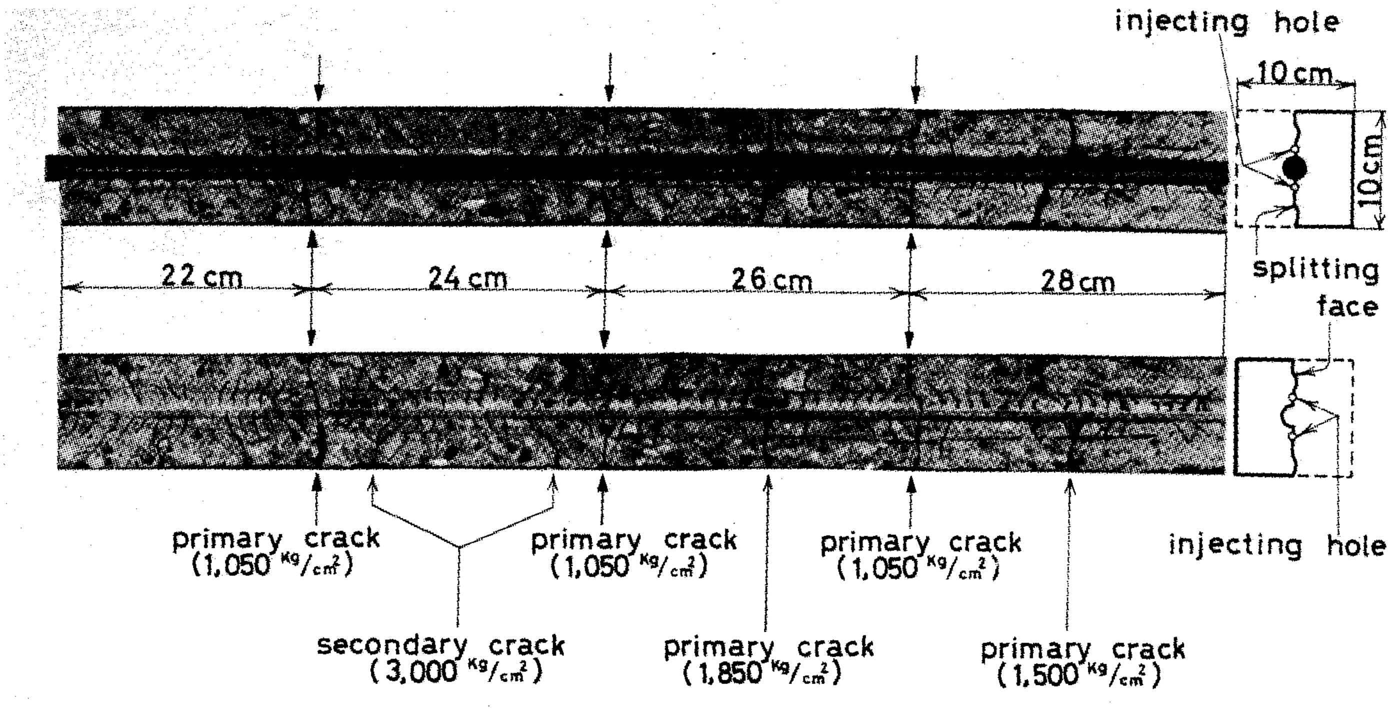

b) Prism with .75 in. Bar and 10cm × 10 cm Square

Notation: ↓↑ Location of Notch

( ) Values in Parentheses indicate Steel Stress at Formation of Cracks

Fig. 7.22: Longitudinal Splitting Faces and Cross Sections: First Setup (Permission of ACI Journal)

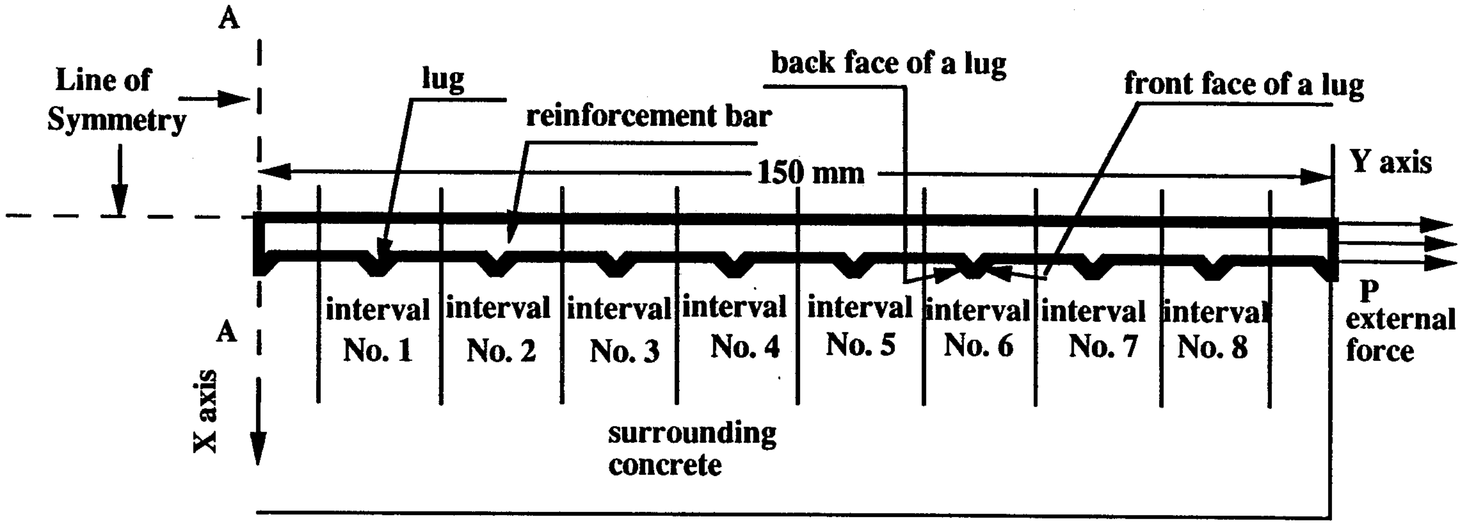

Figure 7.23: Definition of Intervals along the Reinforcing Bar

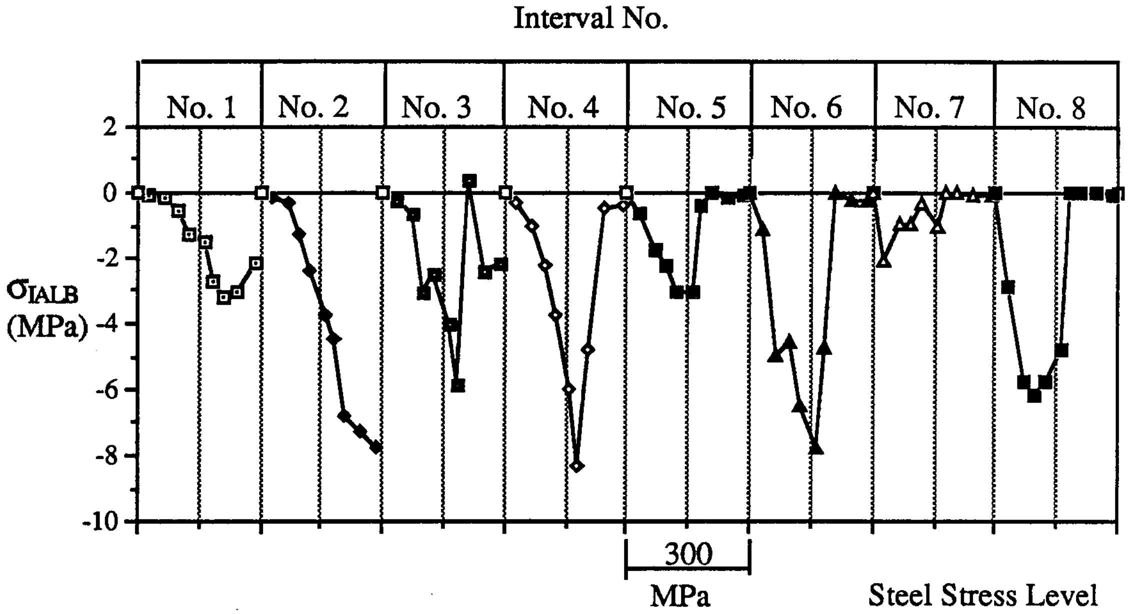

a) Interval Averaged Longitudinal Bond Stress σ_{IALB}

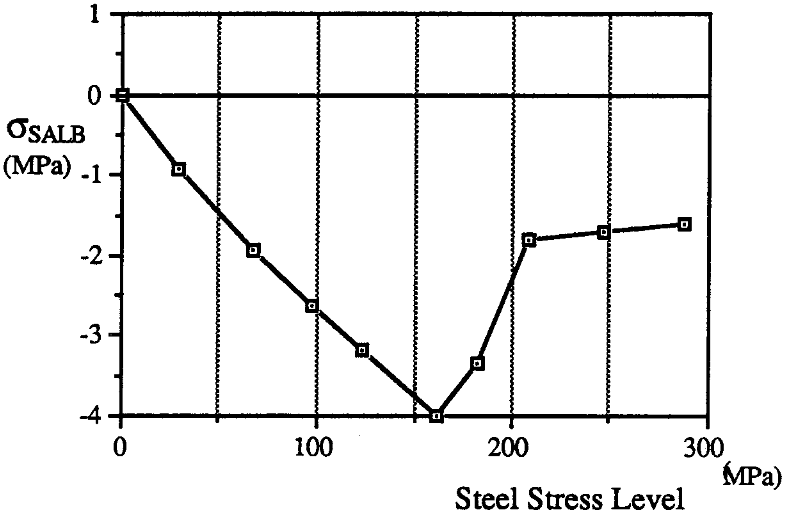

b) Specimen Averaged Longitudinal Bond Stress σ_{SALB}

Figure 7.24: Bond Stresses in Longitudinal Direction: Case 1

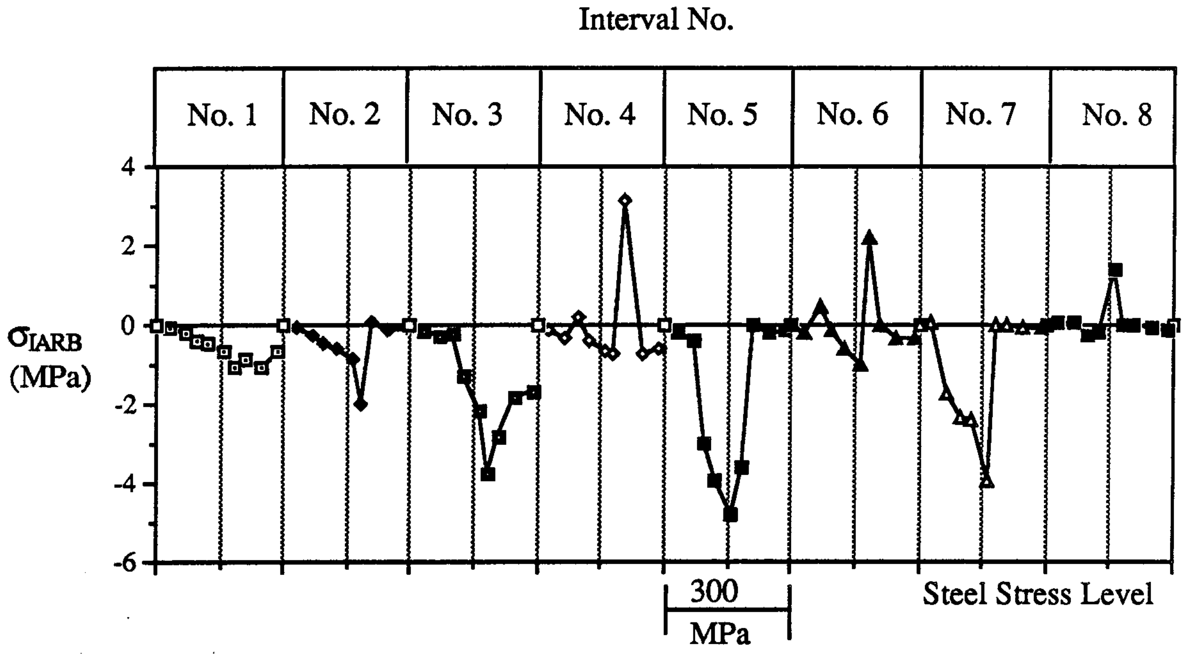

a) Interval Averaged Radial Bond Stress σ_{IARB}

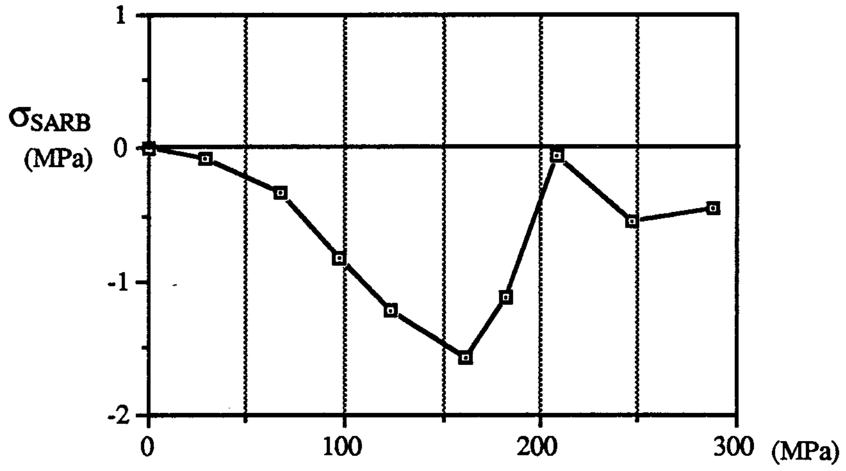

b) Specimen Averaged Radial Bond Stress σ_{SARB}

Figure 7.25: Bond Stresses in Radial Direction: Case 1

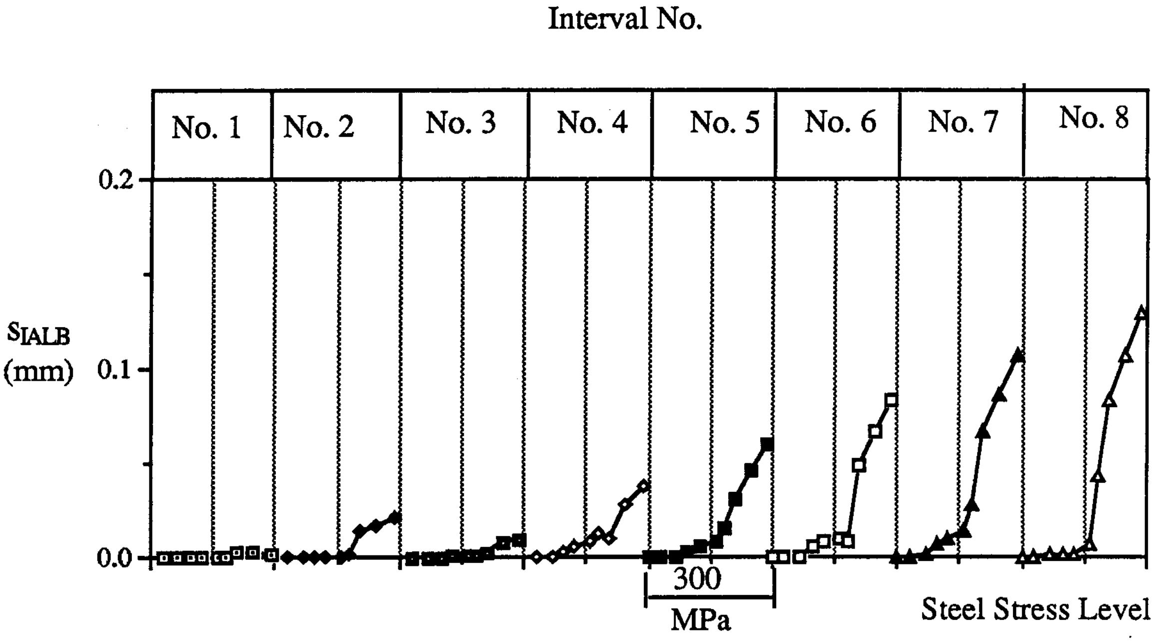

a) Interval Averaged Longitudinal Bond Slip SIALB

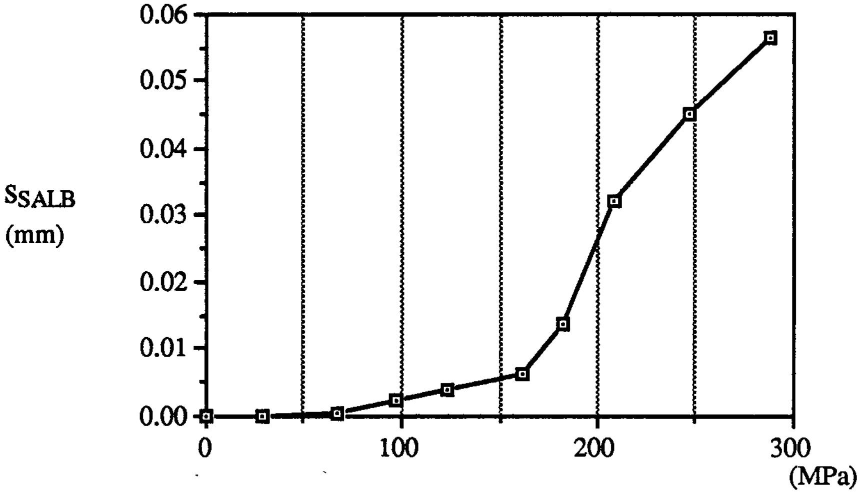

b) Specimen Averaged Longitudinal Bond Slip SSALB

Figure 7.26: Bond Slips in Longitudinal Direction: Case 1

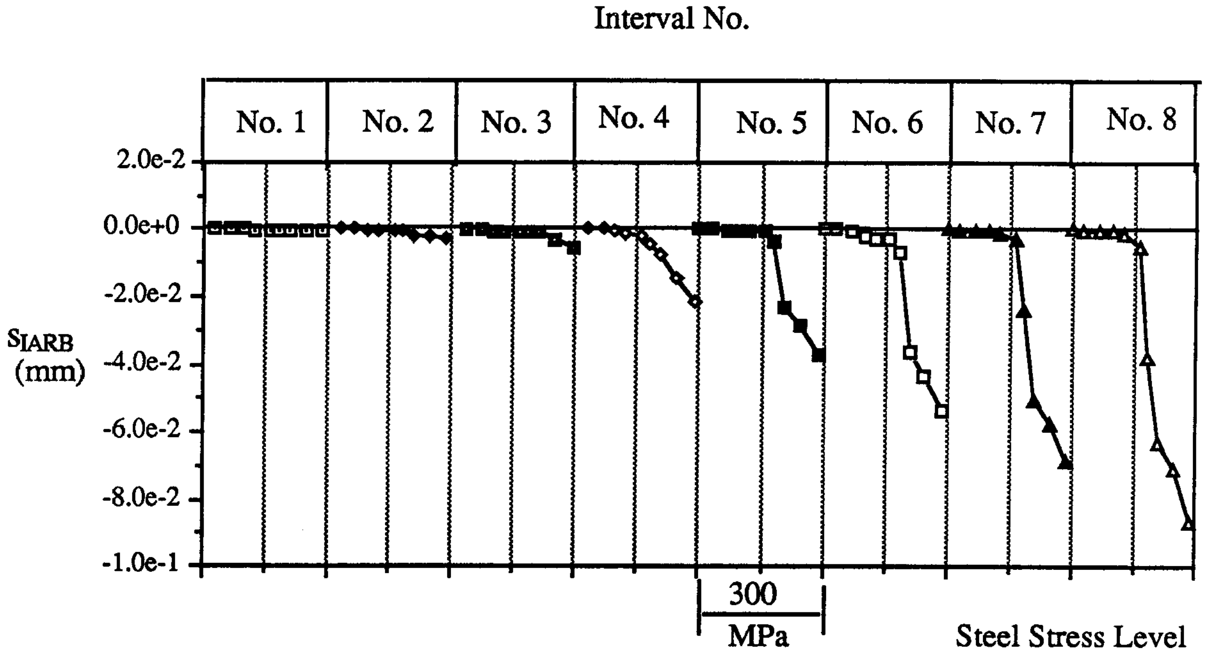

a) Interval Averaged Radial Bond Slip S_{IARB}

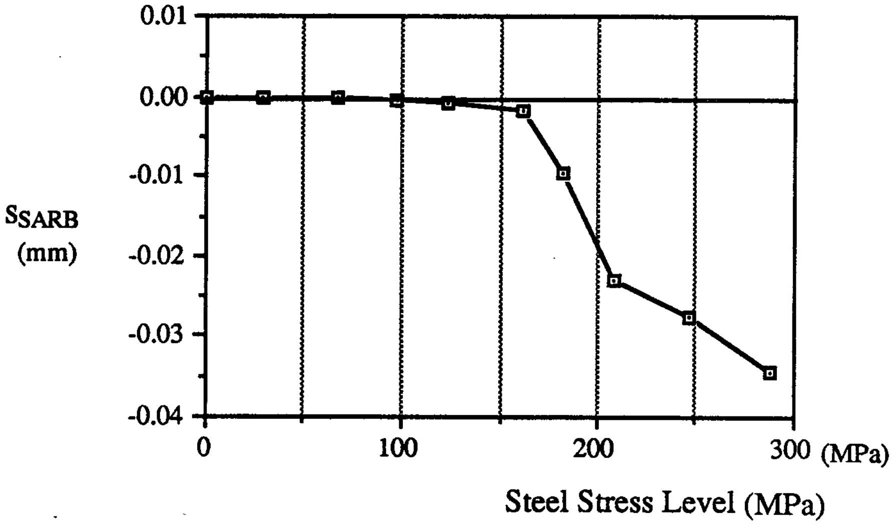

b) Specimen Averaged Radial Bond Slip S_{SARB}

Figure 7.27: Bond Slips in Radial Direction: Case 1

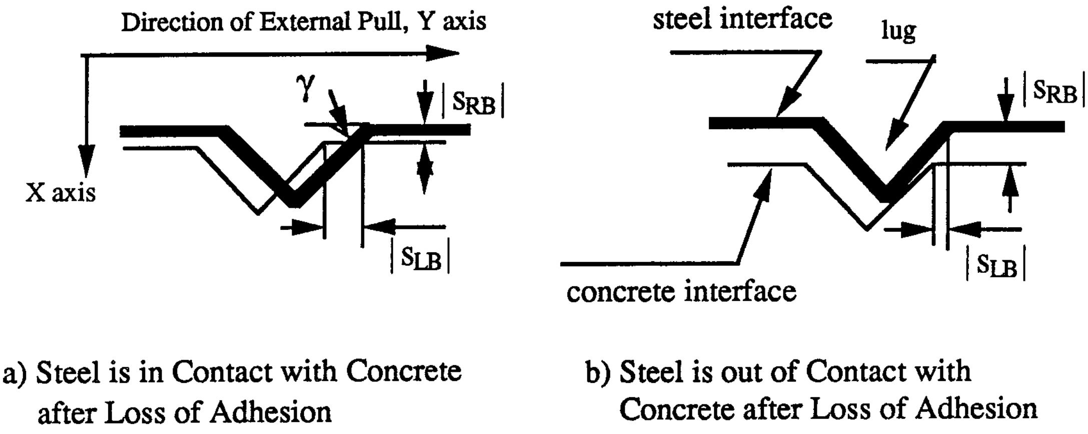

a) Steel is in Contact with Concrete after Loss of Adhesion

b) Steel is out of Contact with Concrete after Loss of Adhesion

Figure 7.28 : Contact on the Front Face of a Lug after Loss of Adhesion

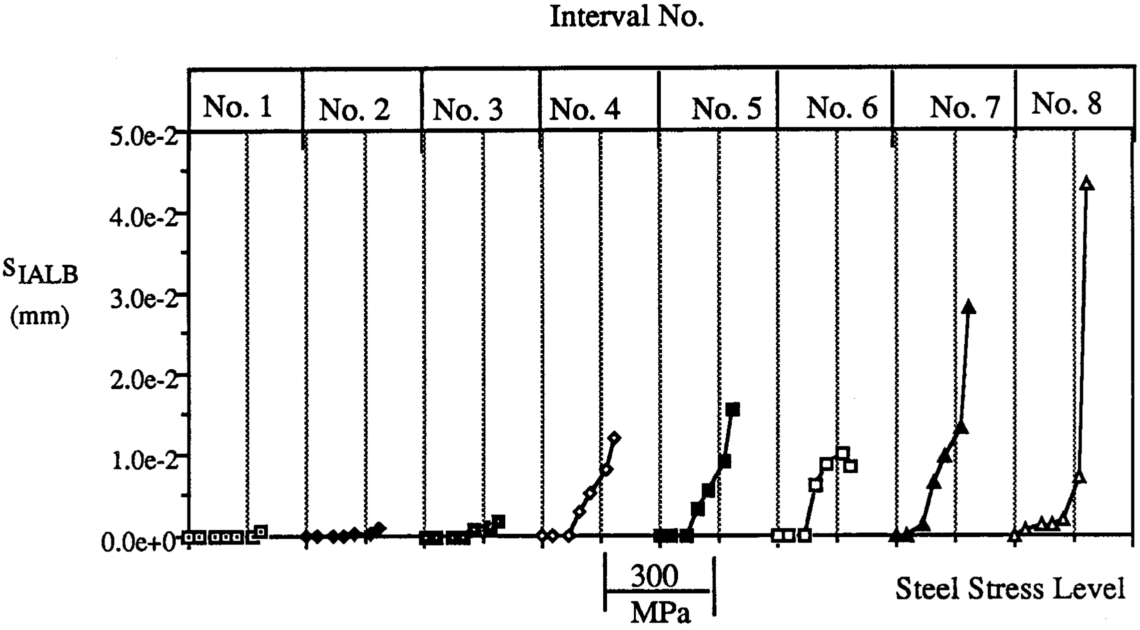

Figure 7.29: Interval Averaged Longitudinal Bond Slips: s_{IALB}

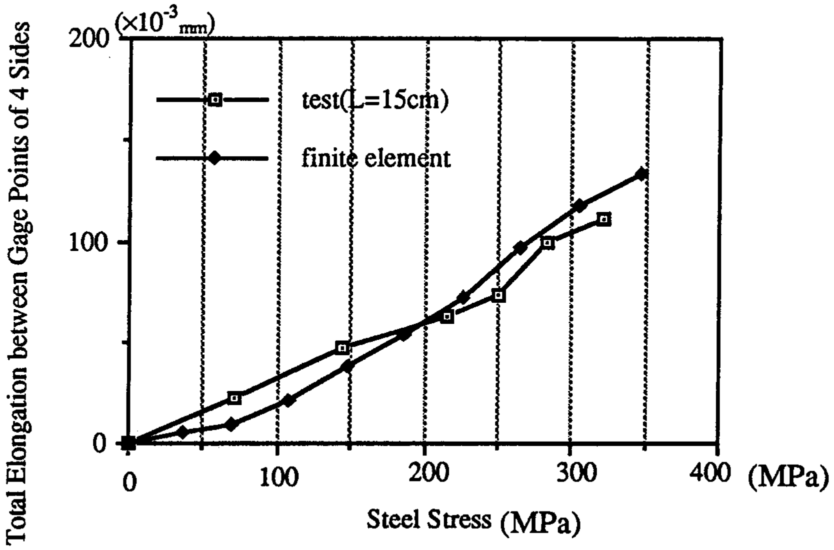

a) Comparison between Test and Analytical Results (Case 2)

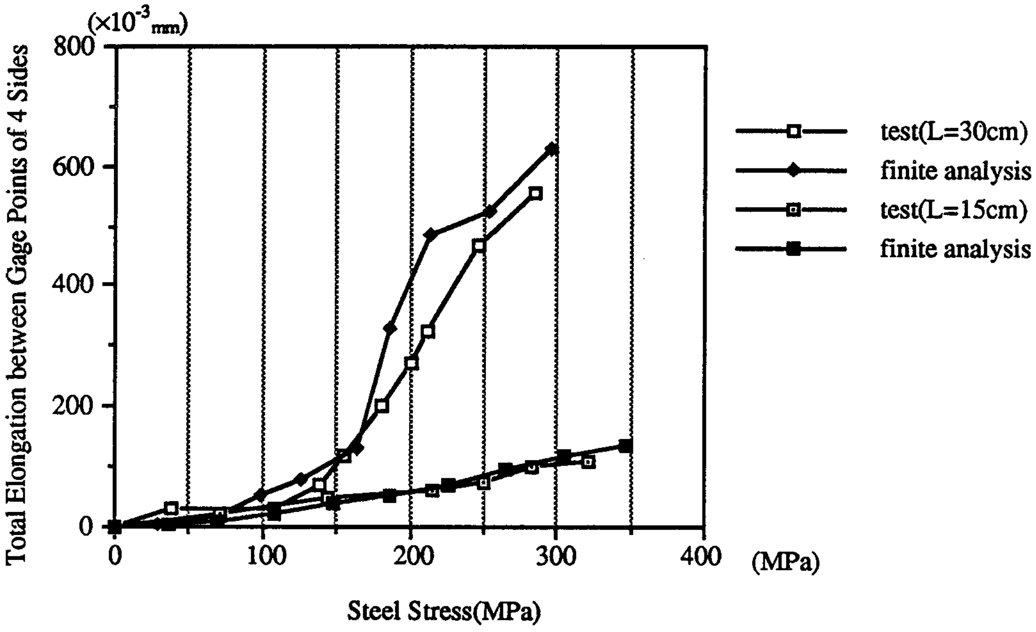

b) Comparison between Test and Analytical Results (Case 1 and 2)

Figure 7.30: Perimeter Elongations in the End Faces for Cases 1 and 2

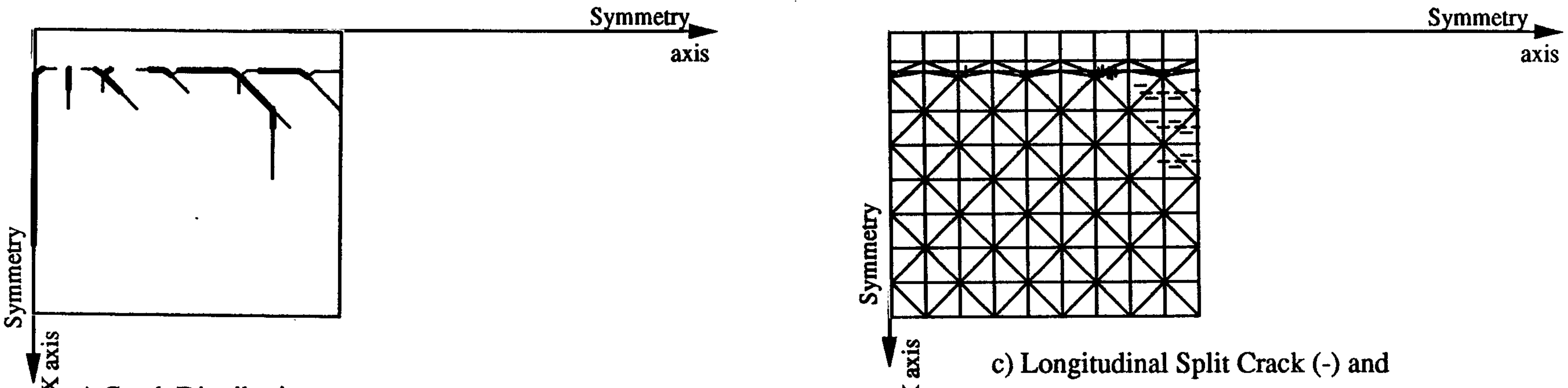

a) Crack Distribution

c) Longitudinal Split Crack (-) and Compressive Yield(|)

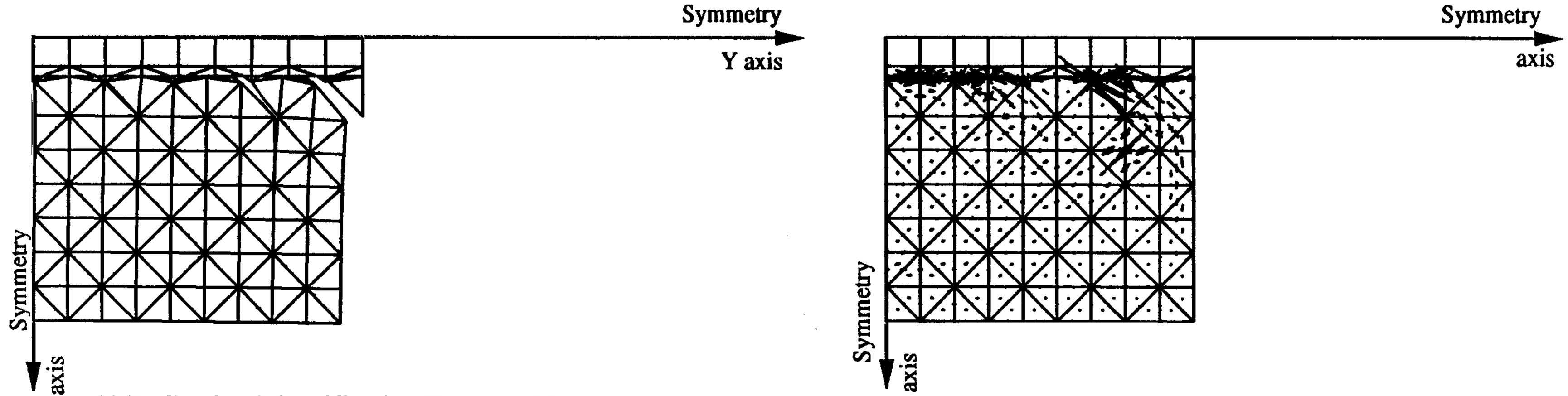

b) Deflection Magnification Factor = 80

d) Stress Distribution

— incipient crack, closed crack or boundaries of structure

— open crack and crack width ≤ W_c

▬ open crack and crack width ≥ W_c

Figure 7.31: Solution for Case 2: Steel Stress Level =225.8 MPa

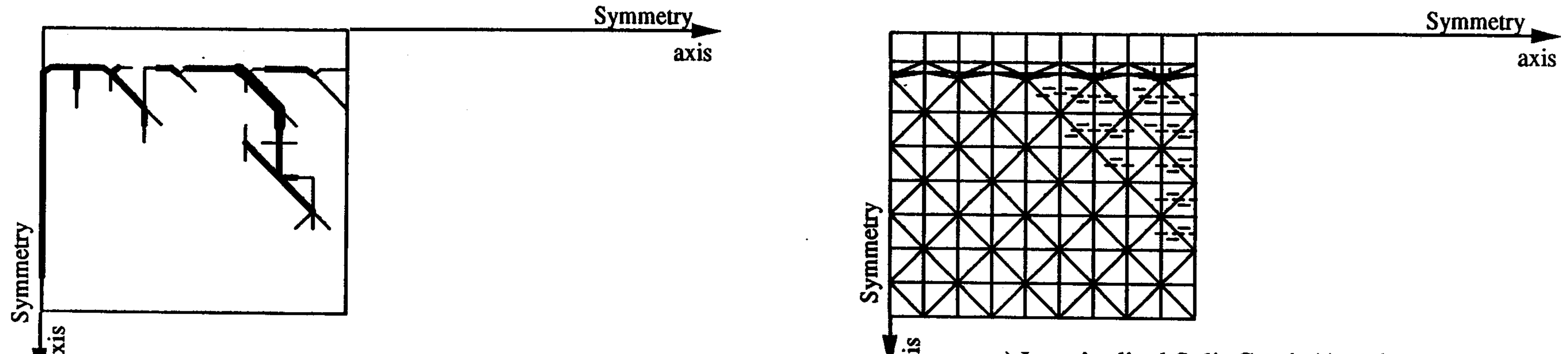

a) Crack Distribution

c) Longitudinal Split Crack (-) and Compressive Yield(ı)

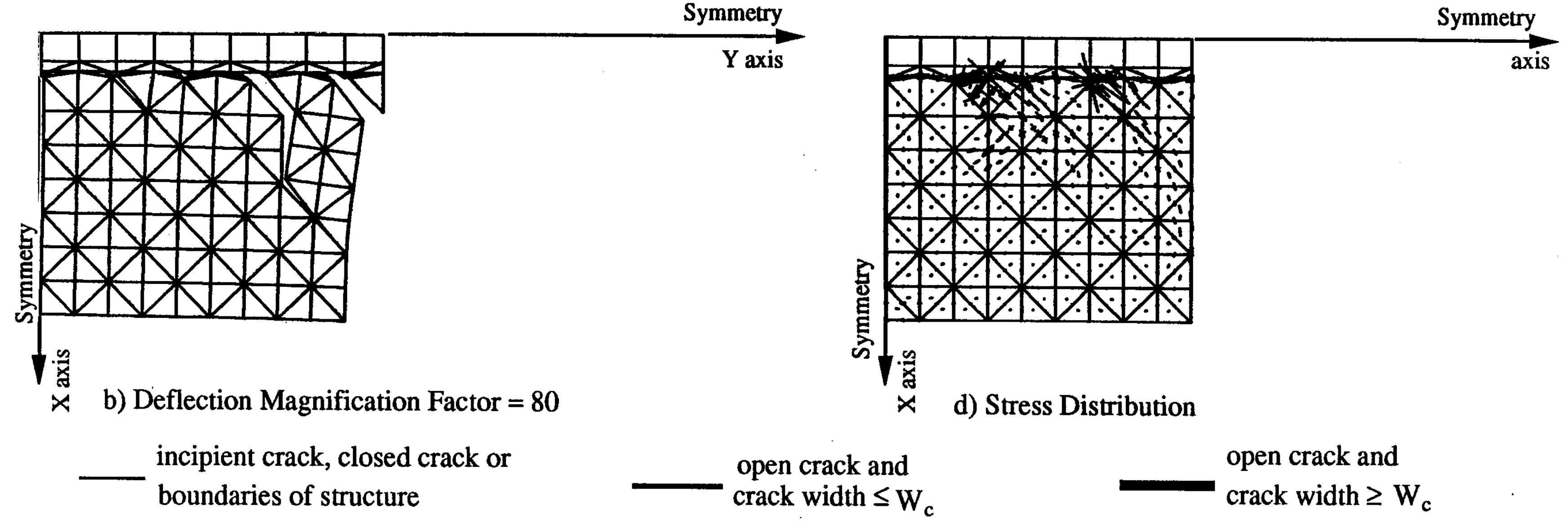

b) Deflection Magnification Factor = 80

d) Stress Distribution

— incipient crack, closed crack or boundaries of structure

━ open crack and crack width ≤ W_c

▬ open crack and crack width ≥ W_c

Figure 7.32: Solution for Case 2: Steel Stress Level =347.1 MPa

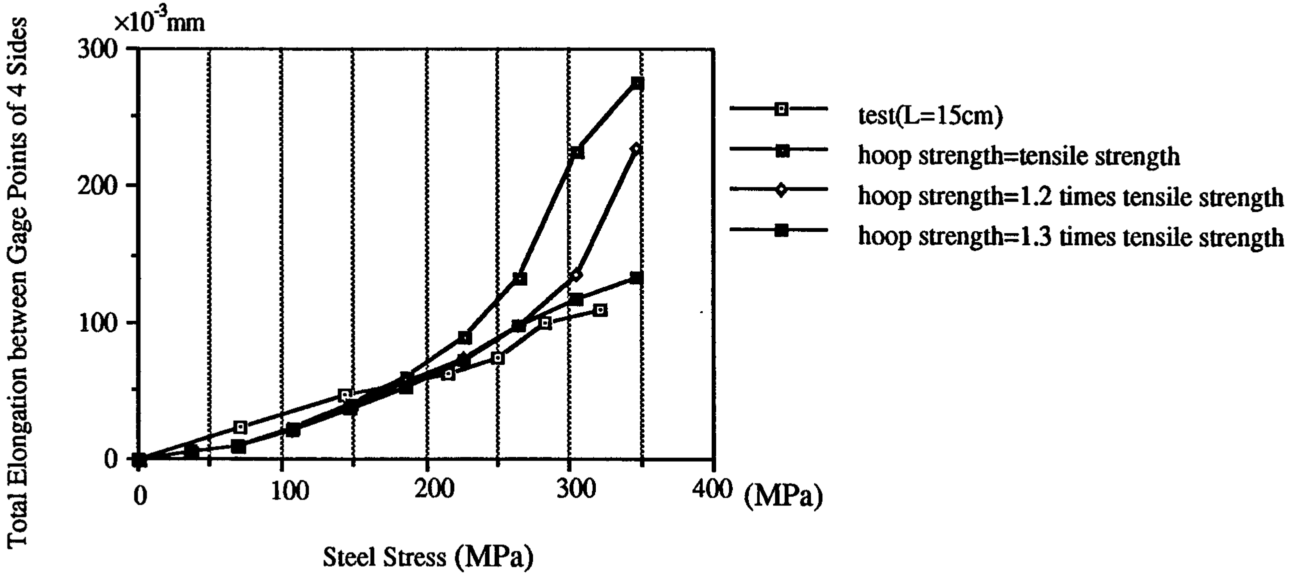

Figure 7.33: Comparison of Analyses with different f'_{th} : Case 2

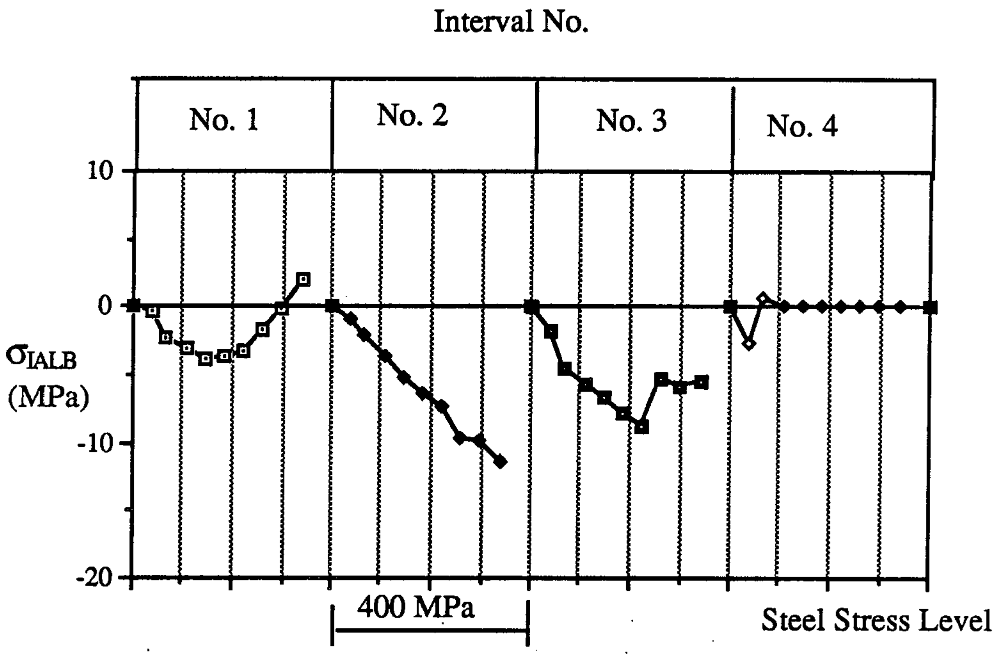

a) Interval Averaged Longitudinal Bond Stress σ_{IALB}

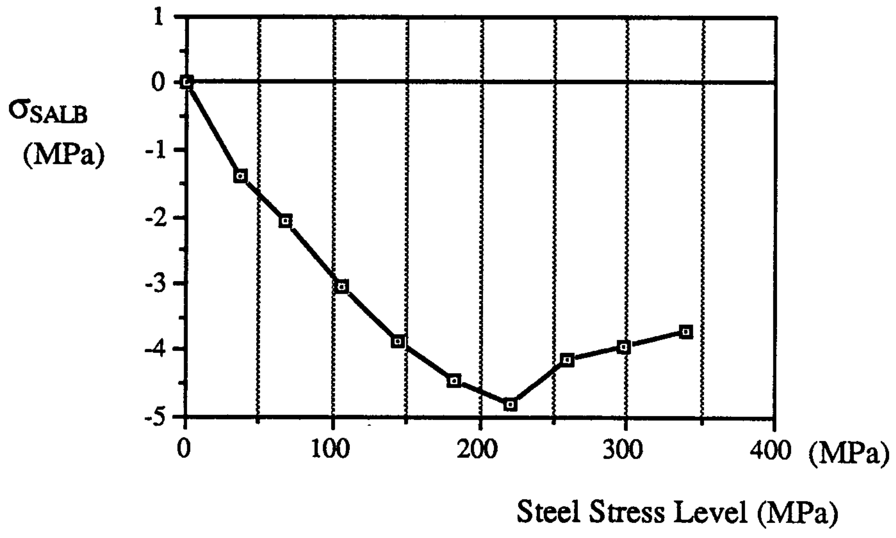

b) Specimen Averaged Longitudinal Bond Stress σ_{SALB}

Figure 7.34: Bond Stresses in Longitudinal Direction: Case 2

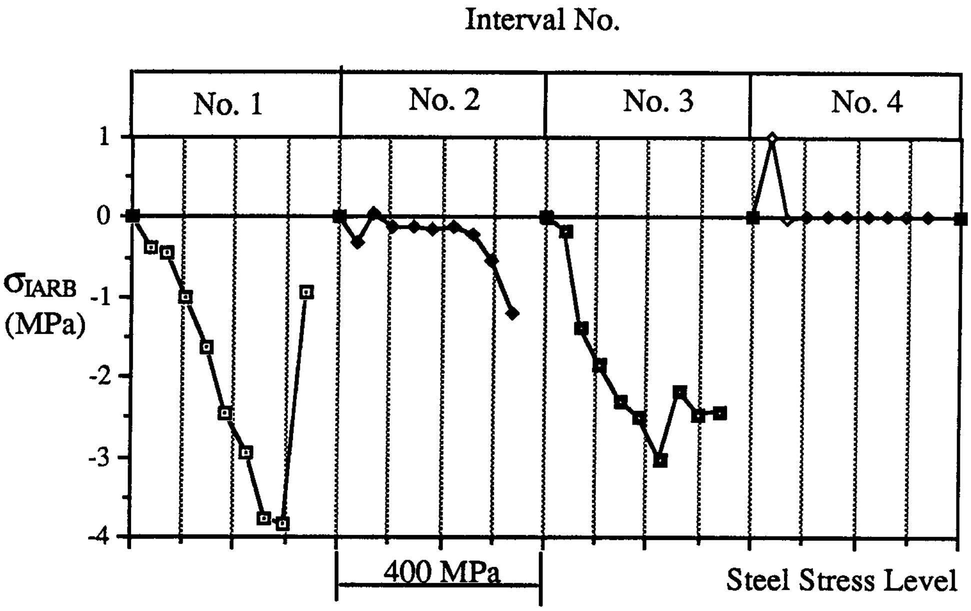

a) Interval Averaged Radial Bond Stress σ_{IARB}

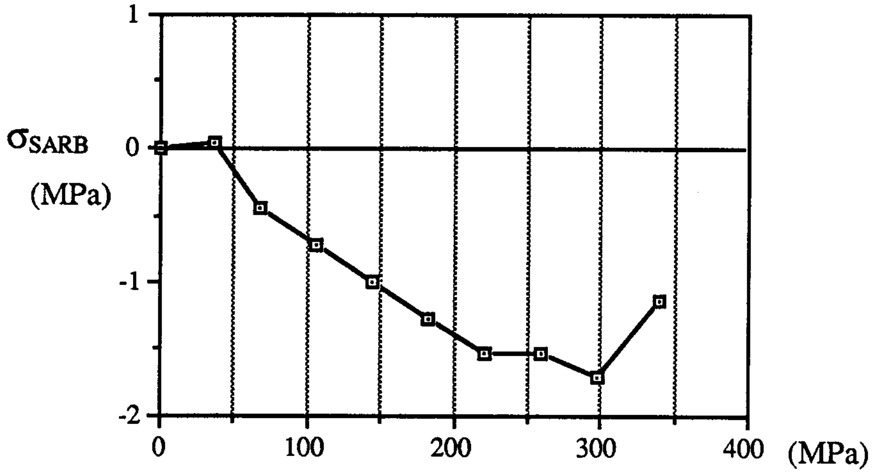

b) Specimen Averaged Radial Bond Stress σ_{SARB}

Figure 7.35: Bond Stresses in Radial Direction: Case 2

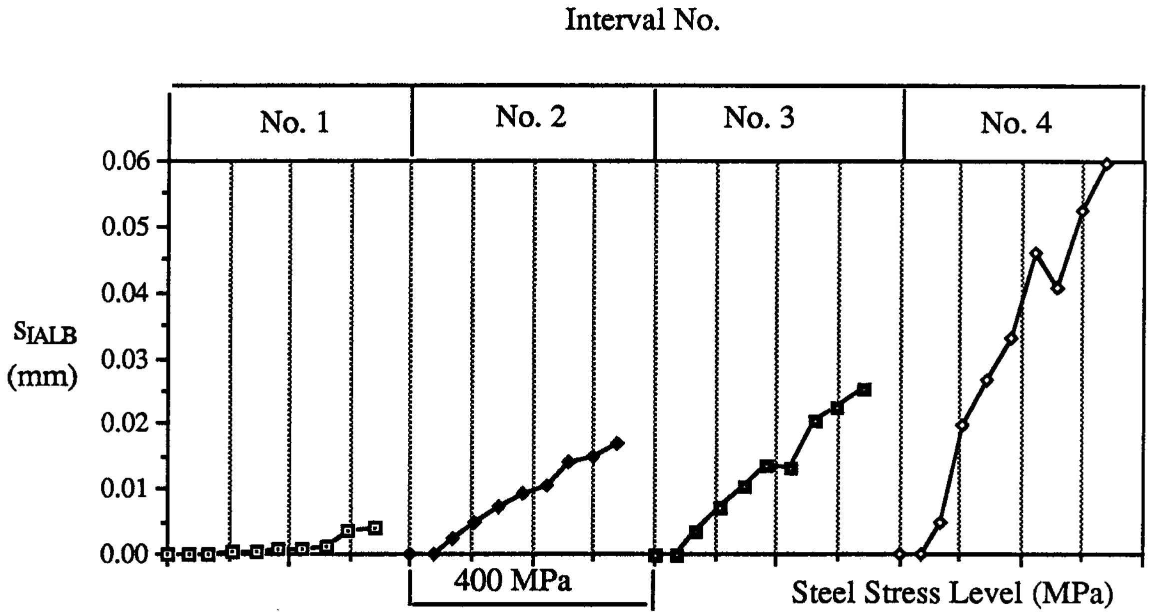

a) Interval Averaged Longitudinal Bond Slip s_{IALB}

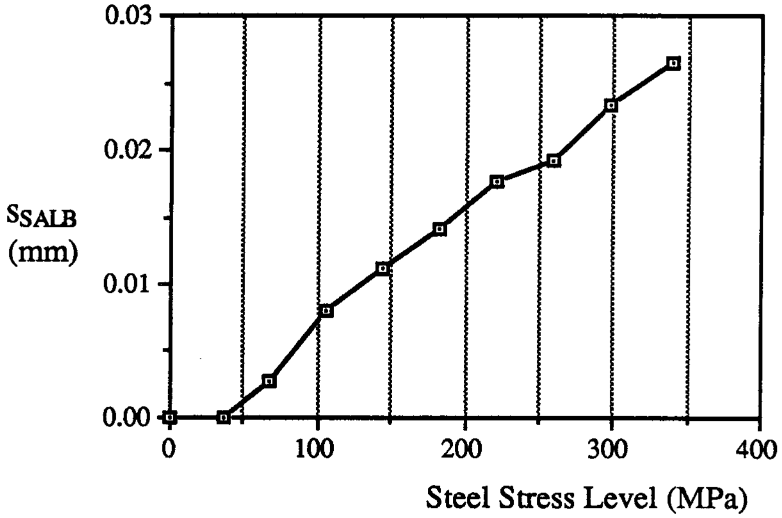

b) Specimen Averaged Longitudinal Bond Slip s_{SALB}

Figure 7.36: Bond Slips in Longitudinal Direction: Case 2

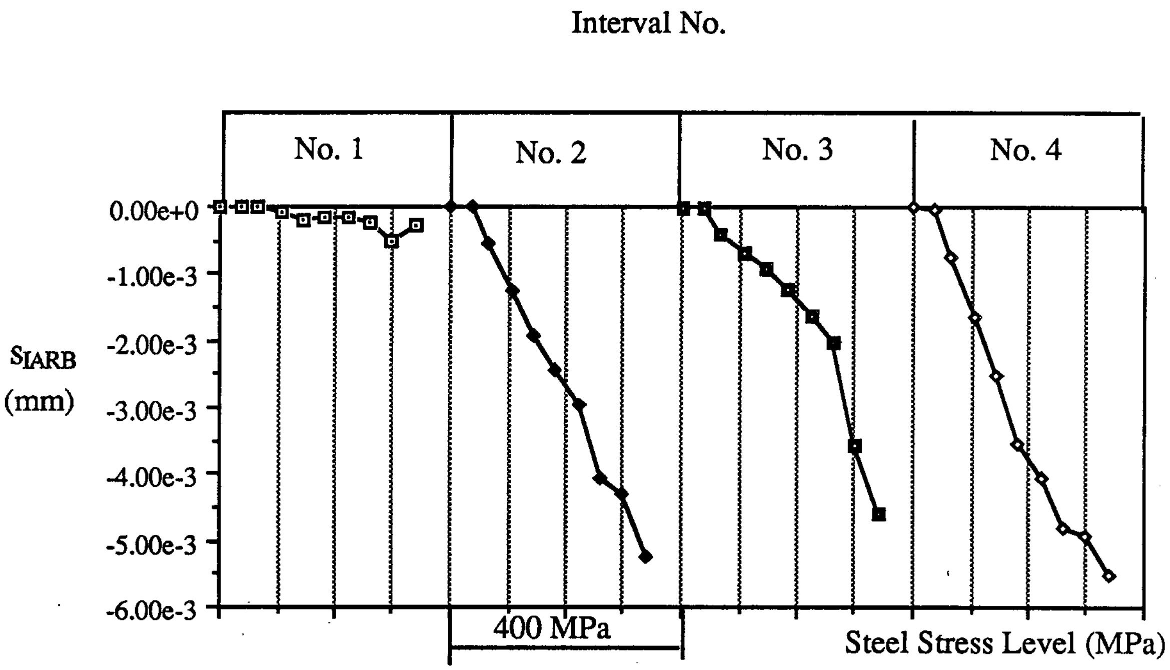

a) Interval Averaged Radial Bond Slip S_{IARB}

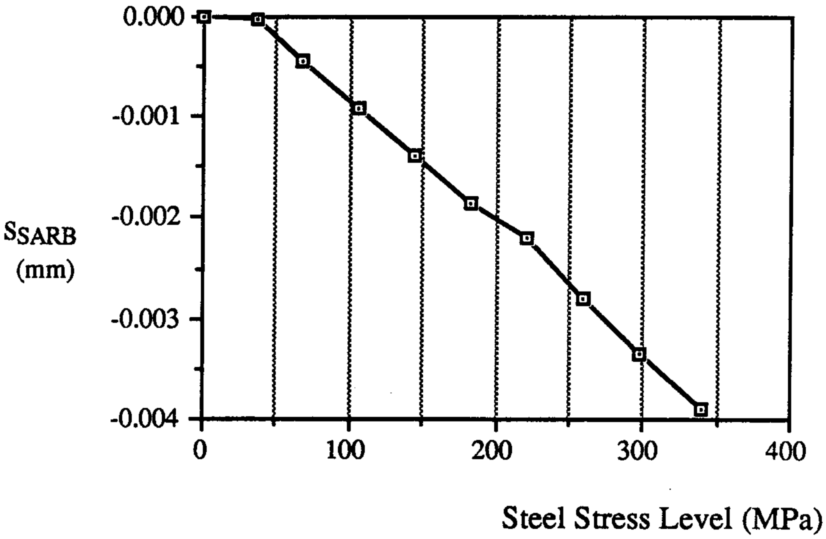

b) Specimen Averaged Radial Bond Slip S_{SARB}

Figure 7.37: Bond Slips in Radial Direction: Case 2

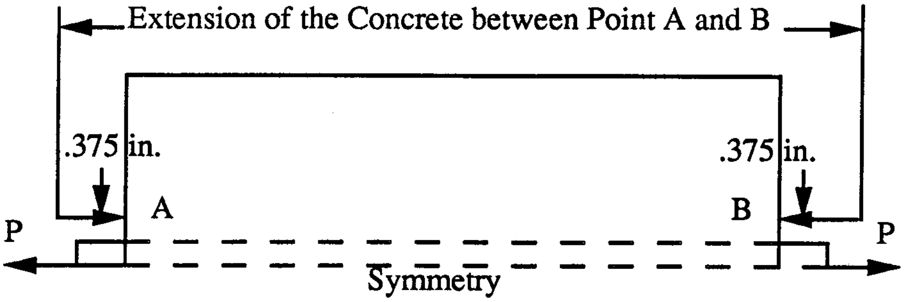

a) Location of Measurement for Extension of Concrete

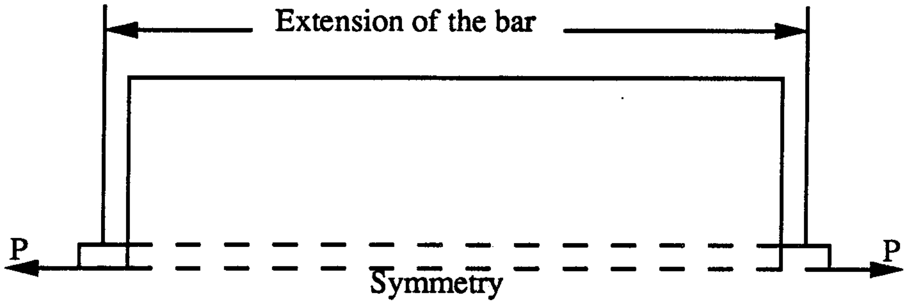

b) Location of Measurement for Extension of the Bar

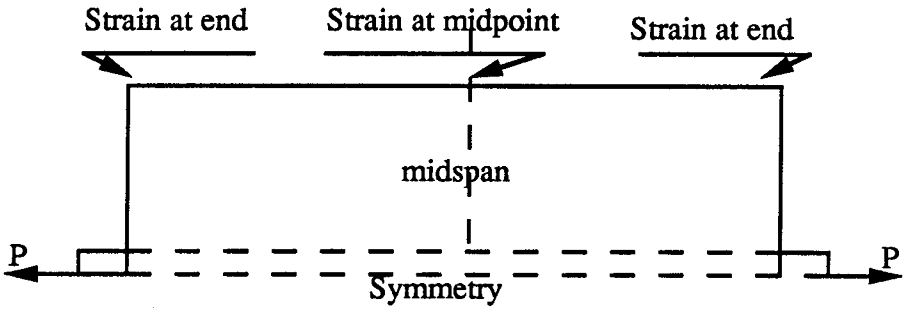

a) Location of Measurement for Strains on the Outer Surfaces

Figure 7.38: Locations of Measurements for Watstein and Mathey (1959)

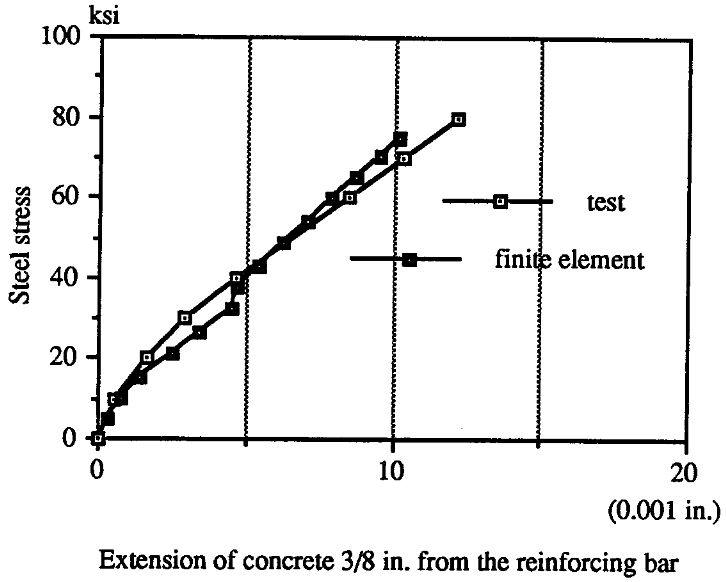

Figure 7.39: Comparisons of Concrete Extensions: Watstein & Mathey Tests

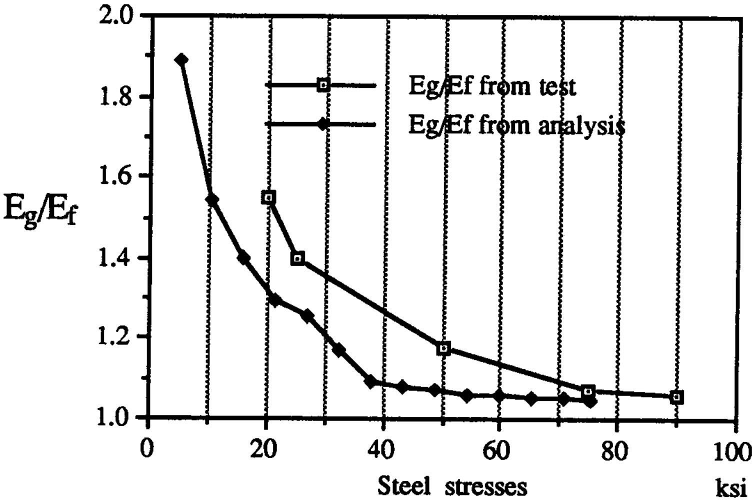

Figure 7.40: Comparisons of Effective Modulus: Watstein & Mathey Tests

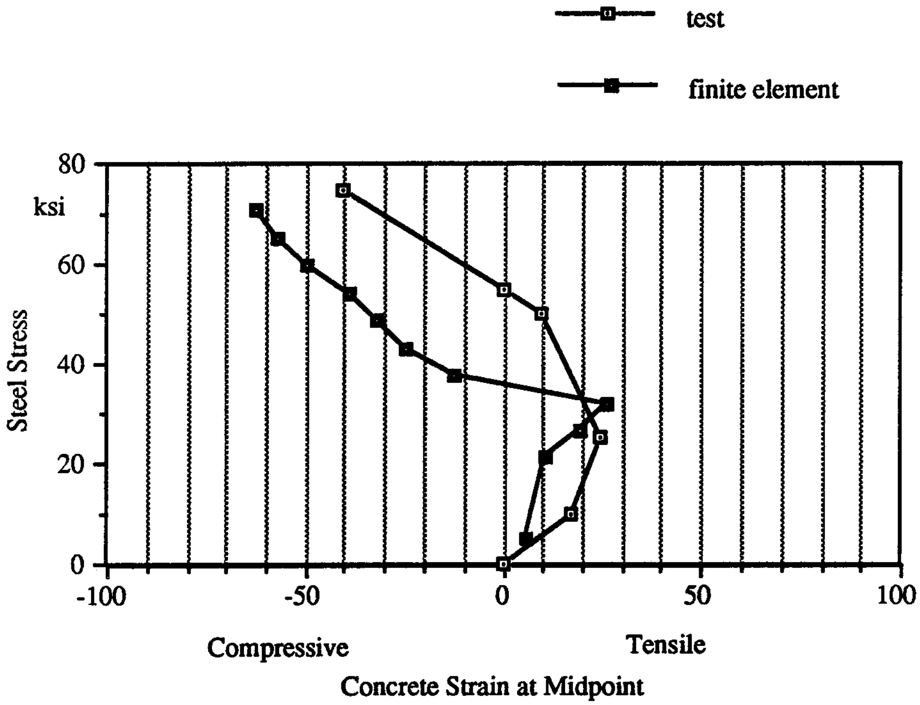

Figure 7.41: Comparisons of Concrete Strain at Midpoint: Watstein & Mathey Tests

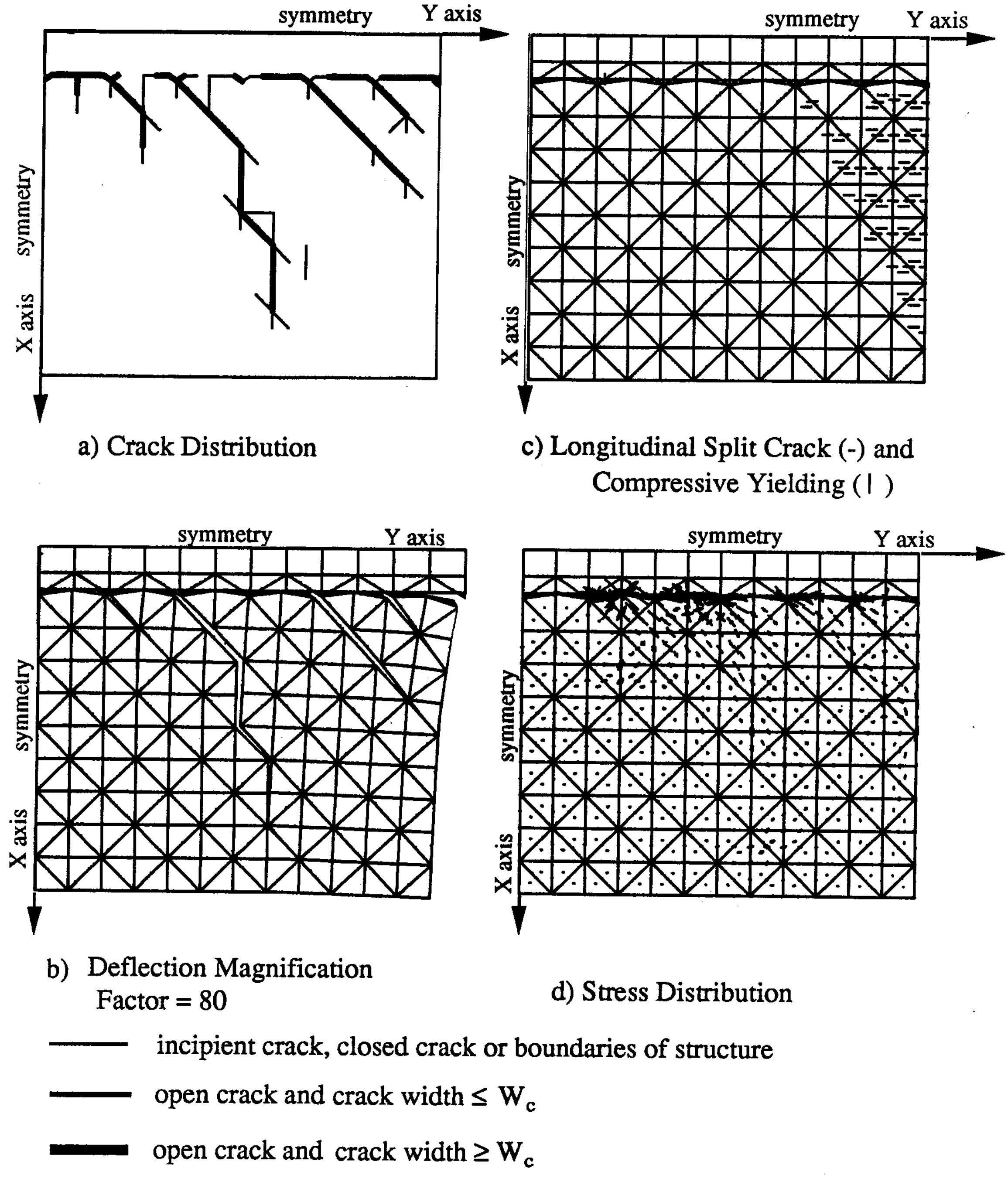

a) Crack Distribution

c) Longitudinal Split Crack (-) and Compressive Yielding (|)

b) Deflection Magnification Factor = 80

d) Stress Distribution

Figure 7.42: Solution for Watstein & Mathey Tests: Steel Stress Level = 32.36 ksi

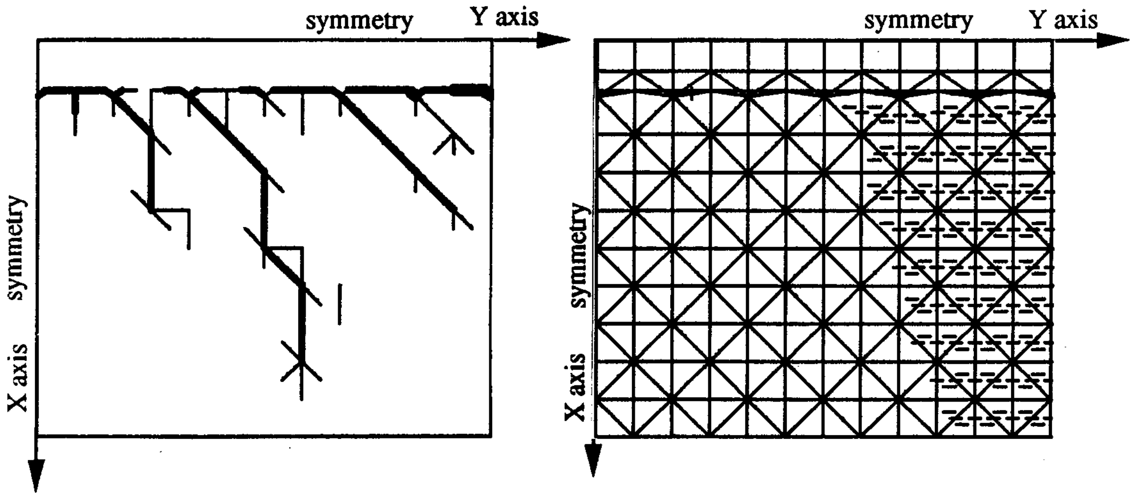

a) Crack Distribution

c) Longitudinal Split Crack (-) and Compressive Yielding (|)

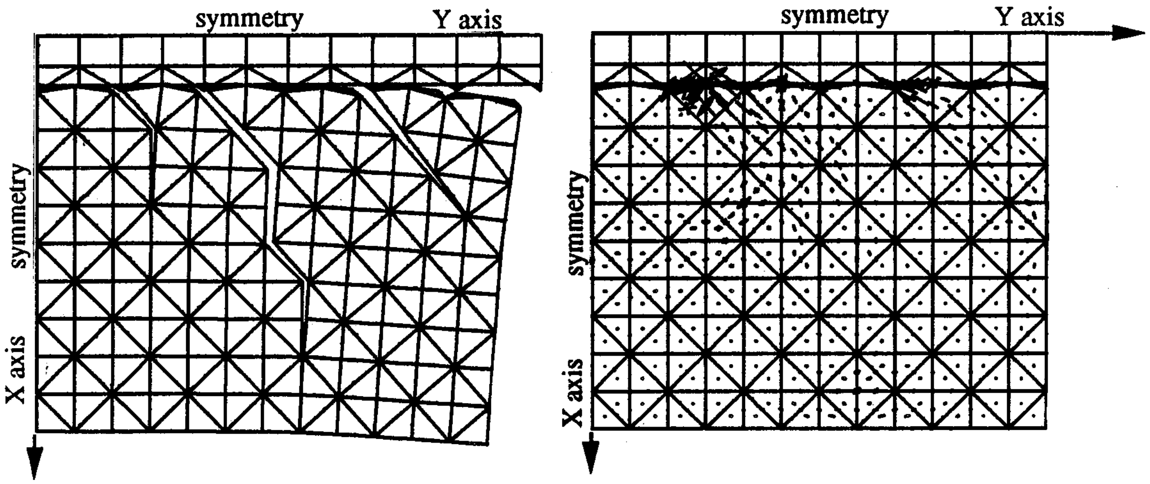

b) Deflection Magnification Factor = 80

d) Stress Distribution

— incipient crack, closed crack or boundaries of structure

— open crack and crack width ≤ W_c

▬ open crack and crack width ≥ W_c

Figure 7.43: Solution for Watstein & Mathey Tests: Steel Stress Level = 43.35 ksi

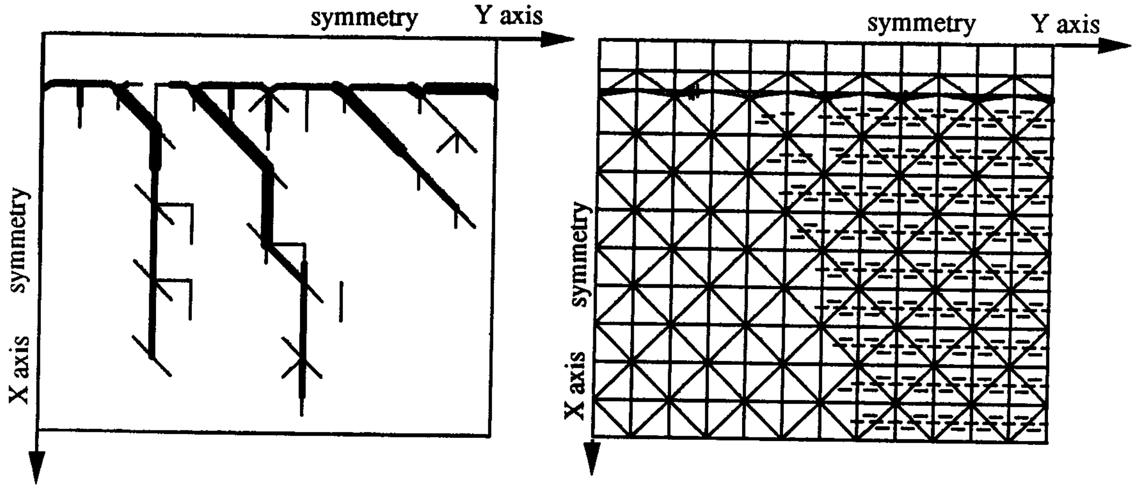

a) Crack Distribution

c) Longitudinal Split Crack (-) and Compressive Yielding (|)

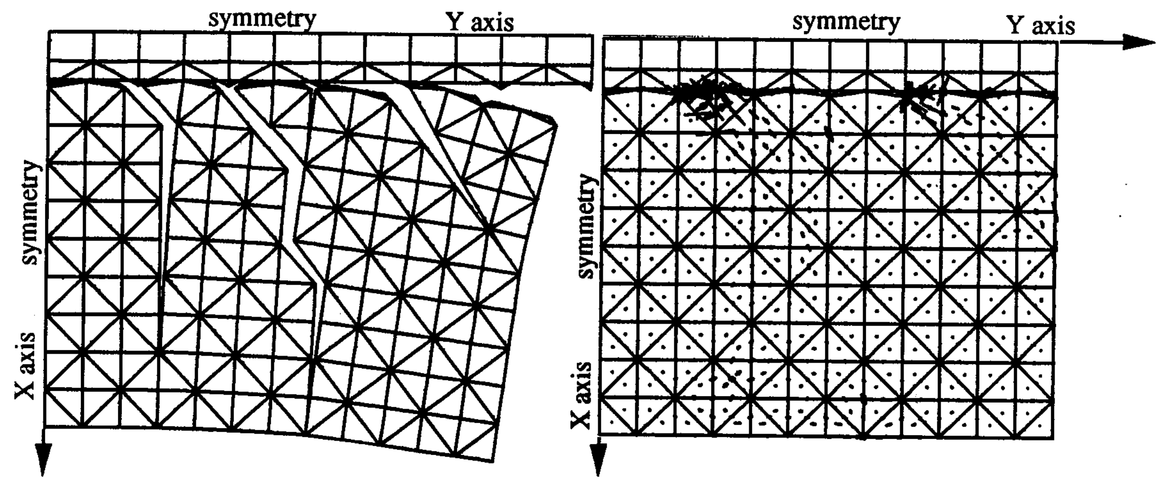

b) Deflection Magnification Factor = 80

d) Stress Distribution

— incipient crack, closed crack or boundaries of structure

━ open crack and crack width ≤ W_c

▬ open crack and crack width ≥ W_c

Figure 7.44: Solution for Watstein & Mathey Tests: Steel Stress Level = 75.35 ksi

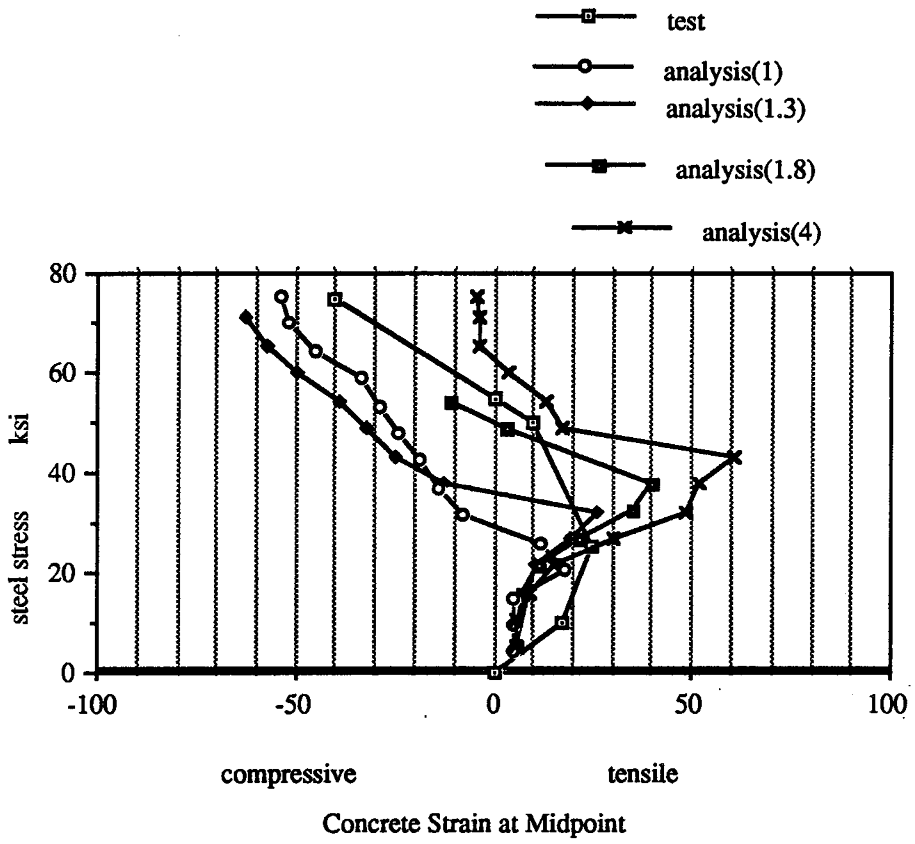

Fig. 7.45: Comparisons of Concrete Strain at Midpoint with Different Ratios of f'_{th} to f'_t :Watstein and Mathey Tests (ratio=1.0, 1.3, 1.8 and 4.0)

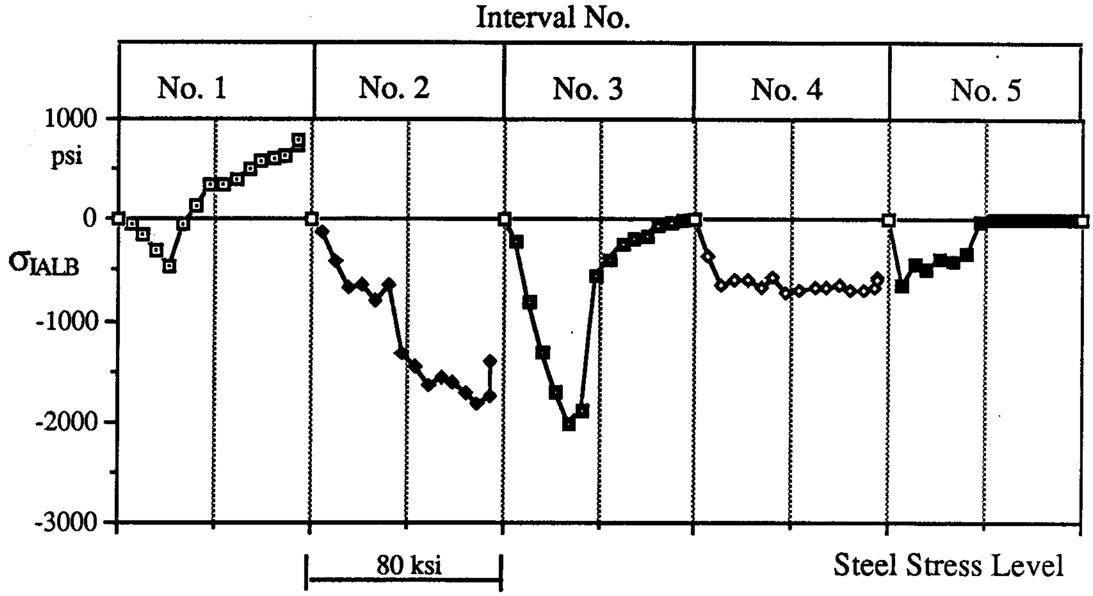

a) Interval Averaged Longitudinal Bond Stress σ_{IALB}

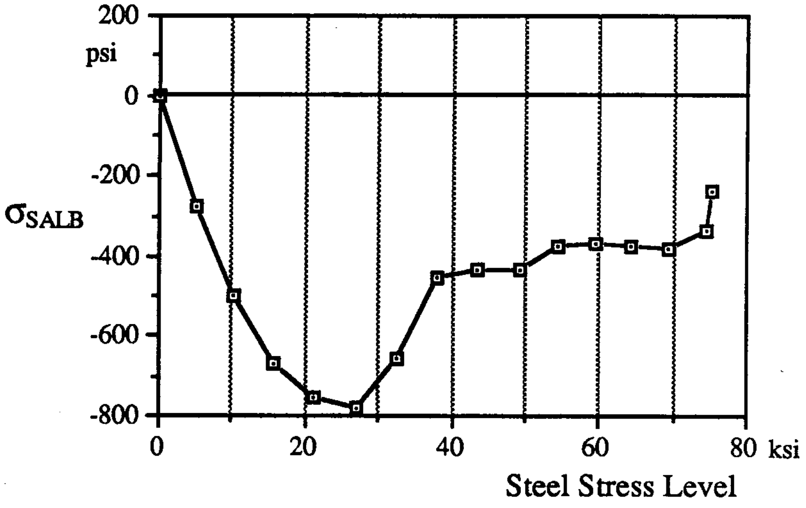

b) Specimen Averaged Longitudinal Bond Stress σ_{SALB}

Figure 7.46: Bond Stresses in Longitudinal Direction: Watstein & Mathey Tests

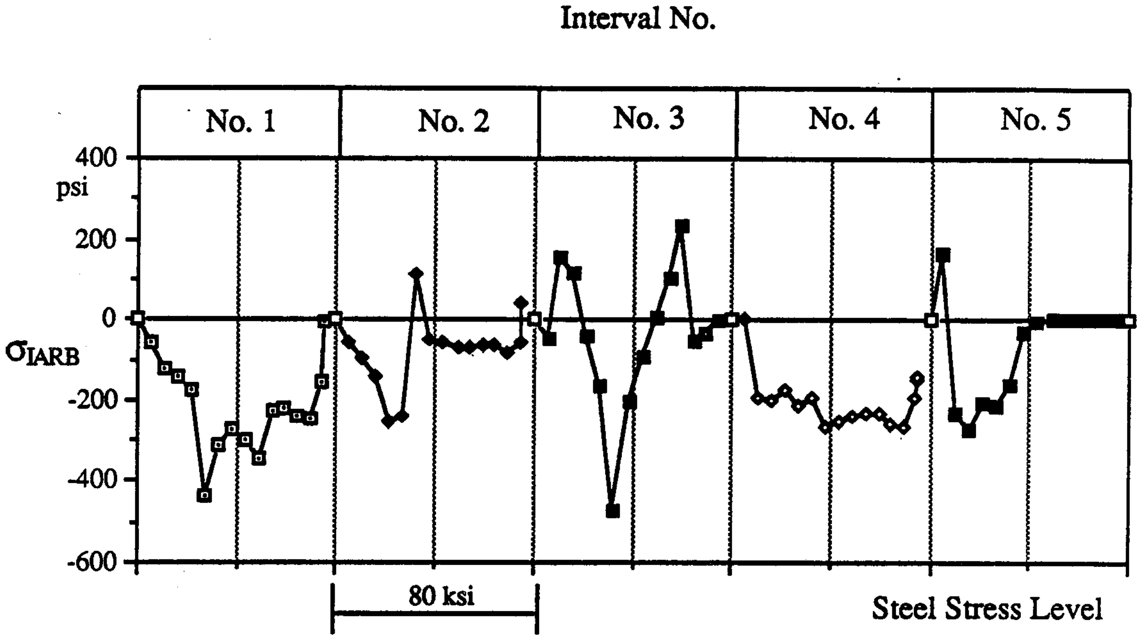

a) Interval Averaged Radial Bond Stress σ_{IARB}

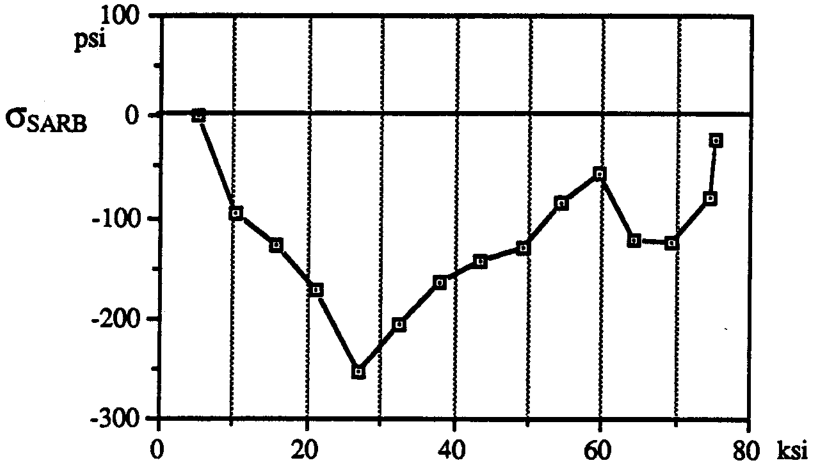

b) Specimen Averaged Radial Bond Stress σ_{SARB}

Figure 7.47: Bond Stresses in Radial Direction : Watstein & Mathey Tests

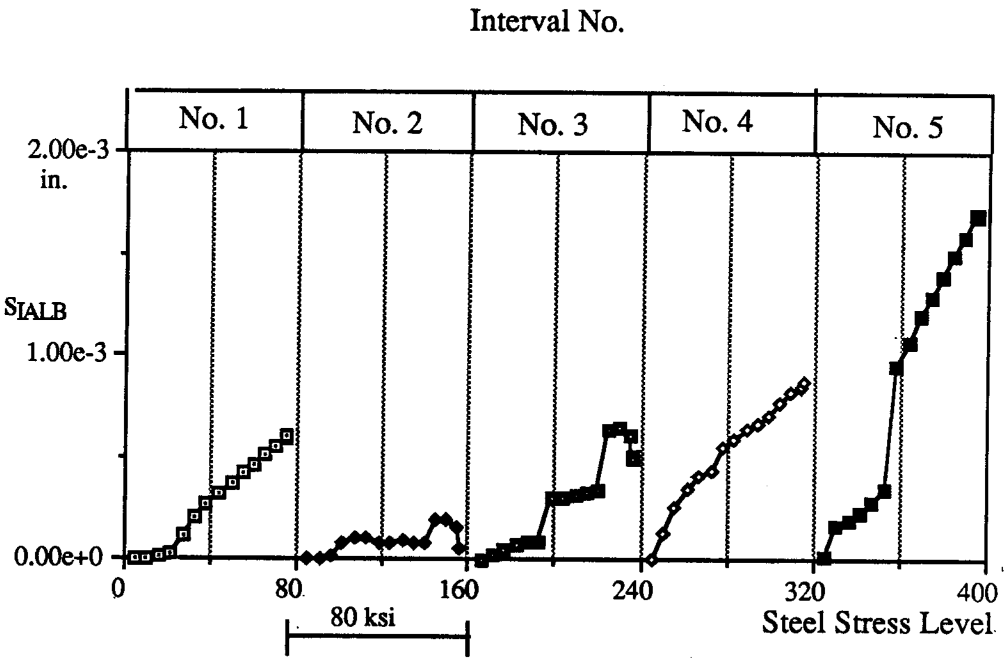

a) Interval Averaged Longitudinal Bond Slips S_{IALB}

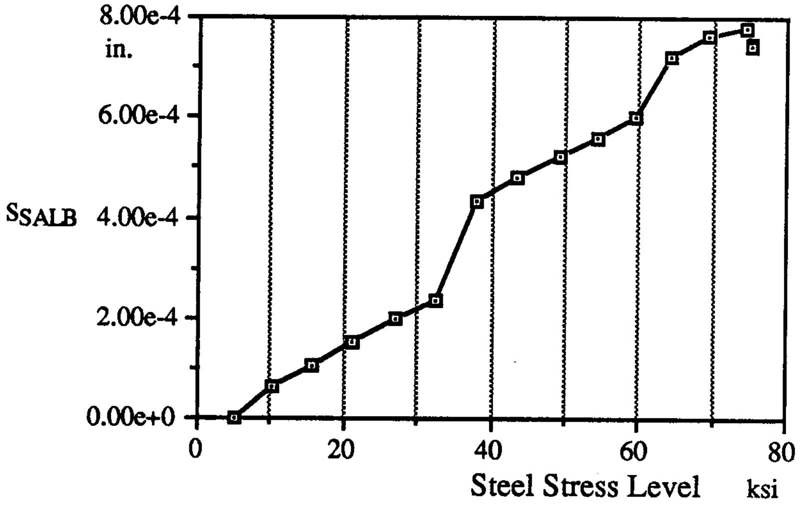

b) Specimen Averaged Longitudinal Bond Stress S_{SALB}

Figure 7.48: Bond Slips in Longitudinal Direction: Watstein & Mathey Tests

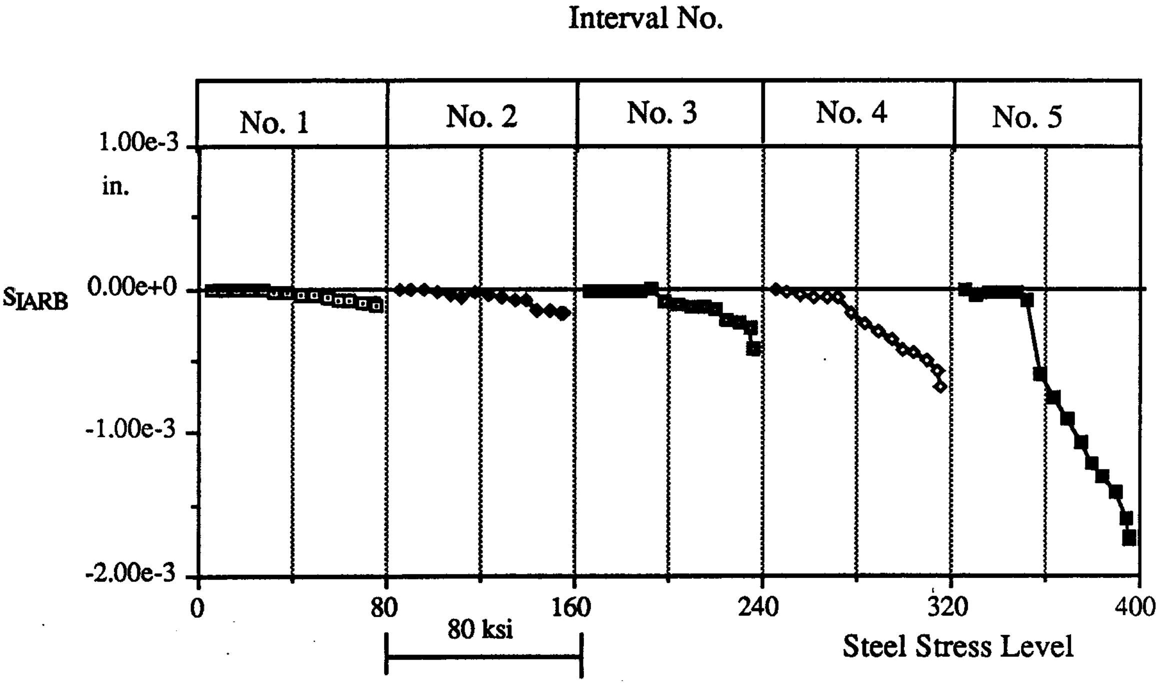

a) Interval Averaged Radial Bond Slips S_{IARB}

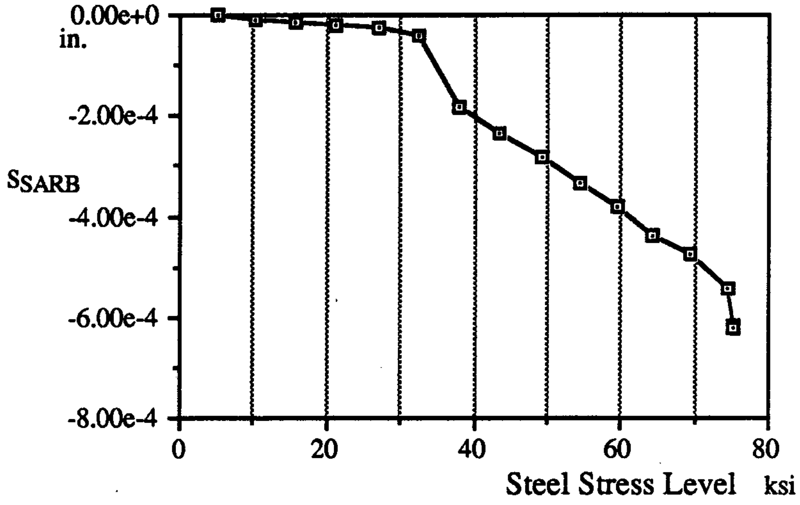

b) Specimen Averaged Radial Bond Stress S_{SARB}

Figure 7.49: Bond Slips in Radial Direction:

Watstein & Mathey Tests

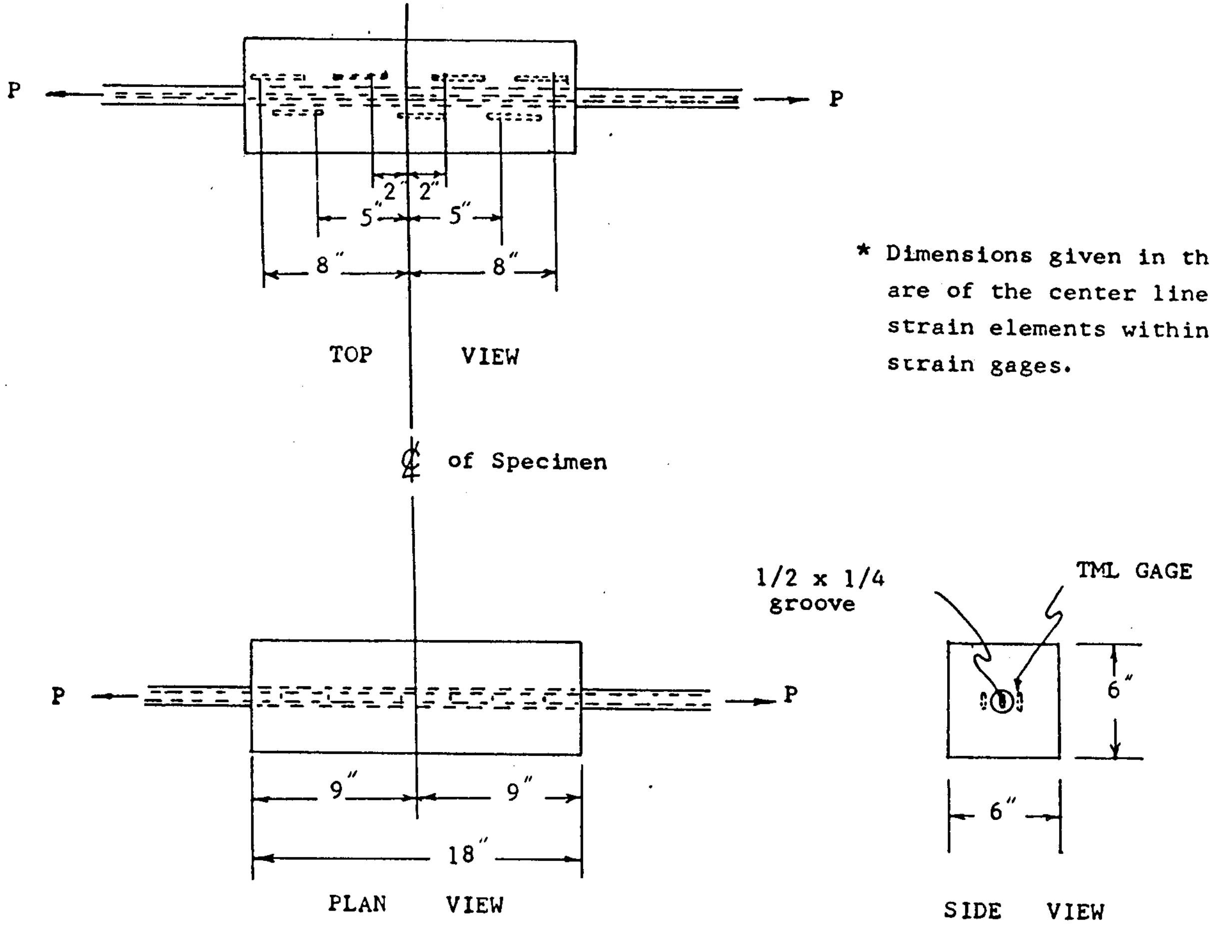

* Dimensions given in the top view are of the center lines of the strain elements within the concrete strain gages.

Fig. 7.50: Specimen for Test Series II (Adapted from Tanner, 1971)

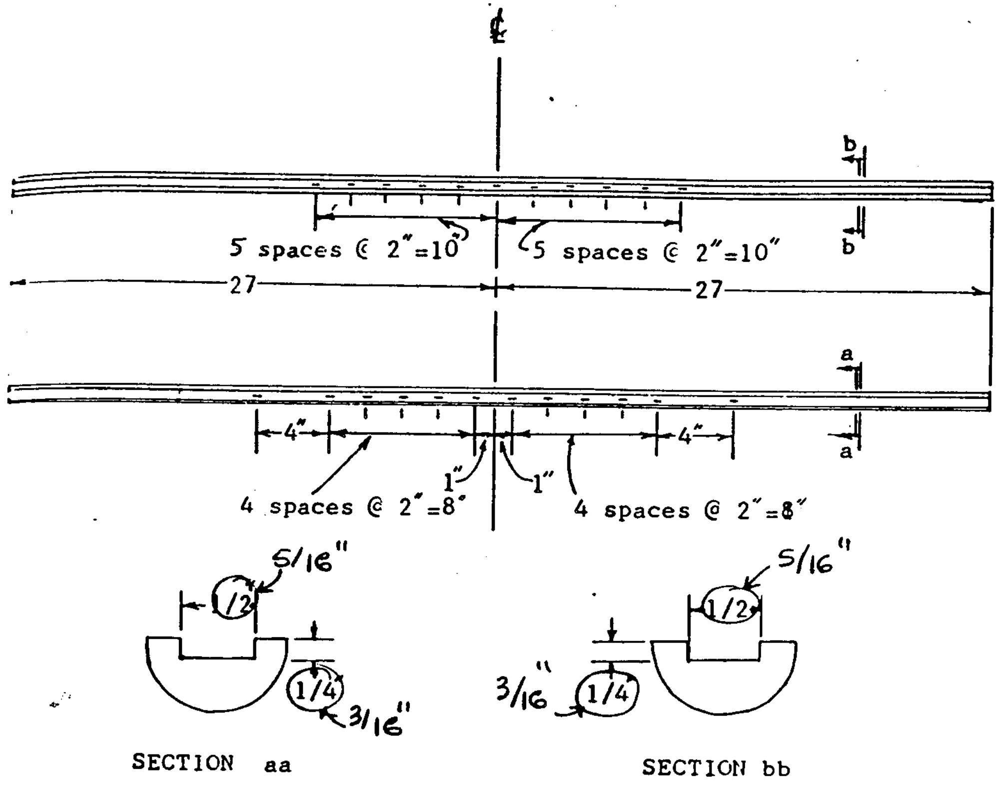

Fig. 7.51: Strain Gauge Placement in Grooved Reinforcing (Adapted from Tanner, 1971)

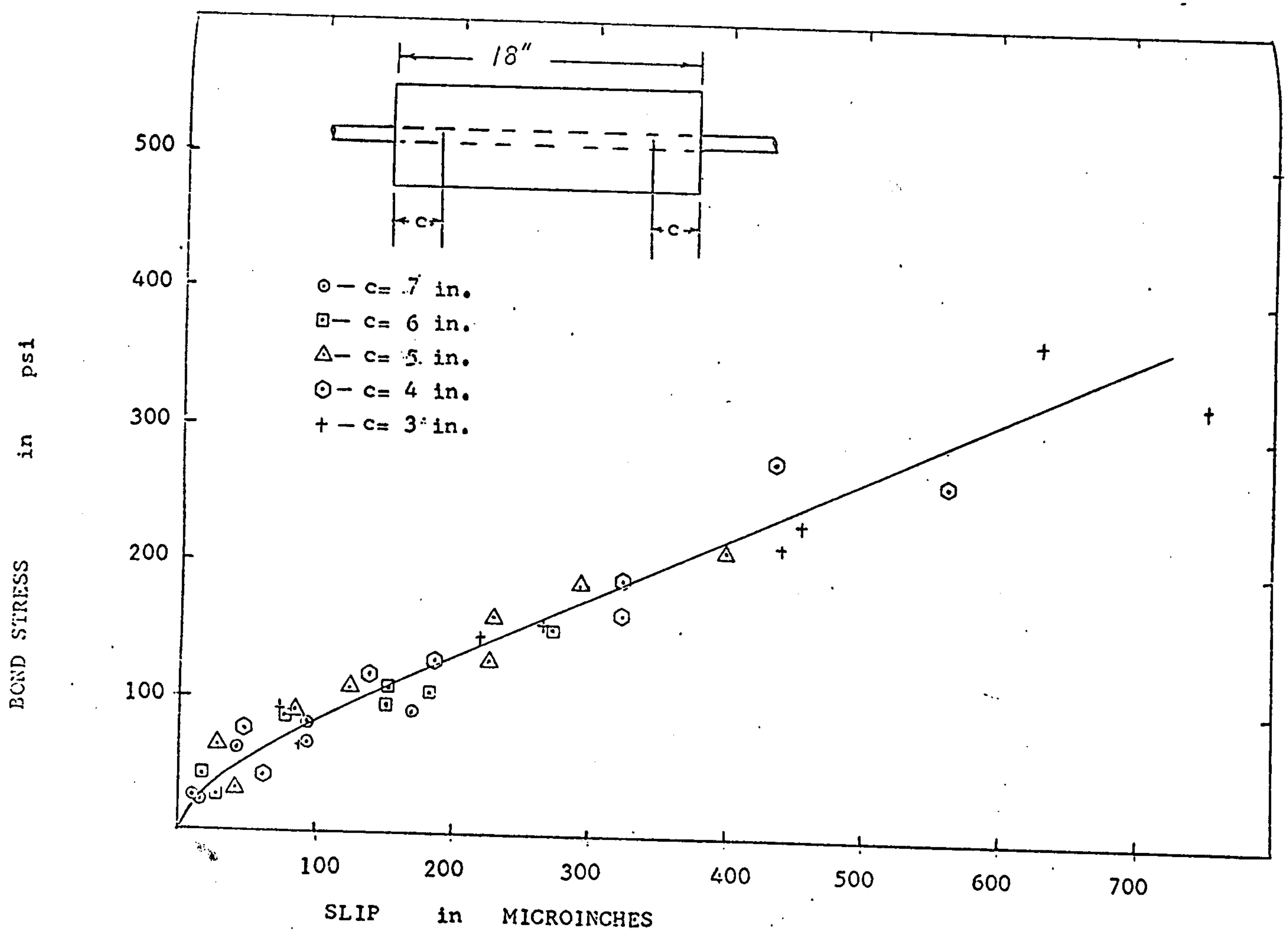

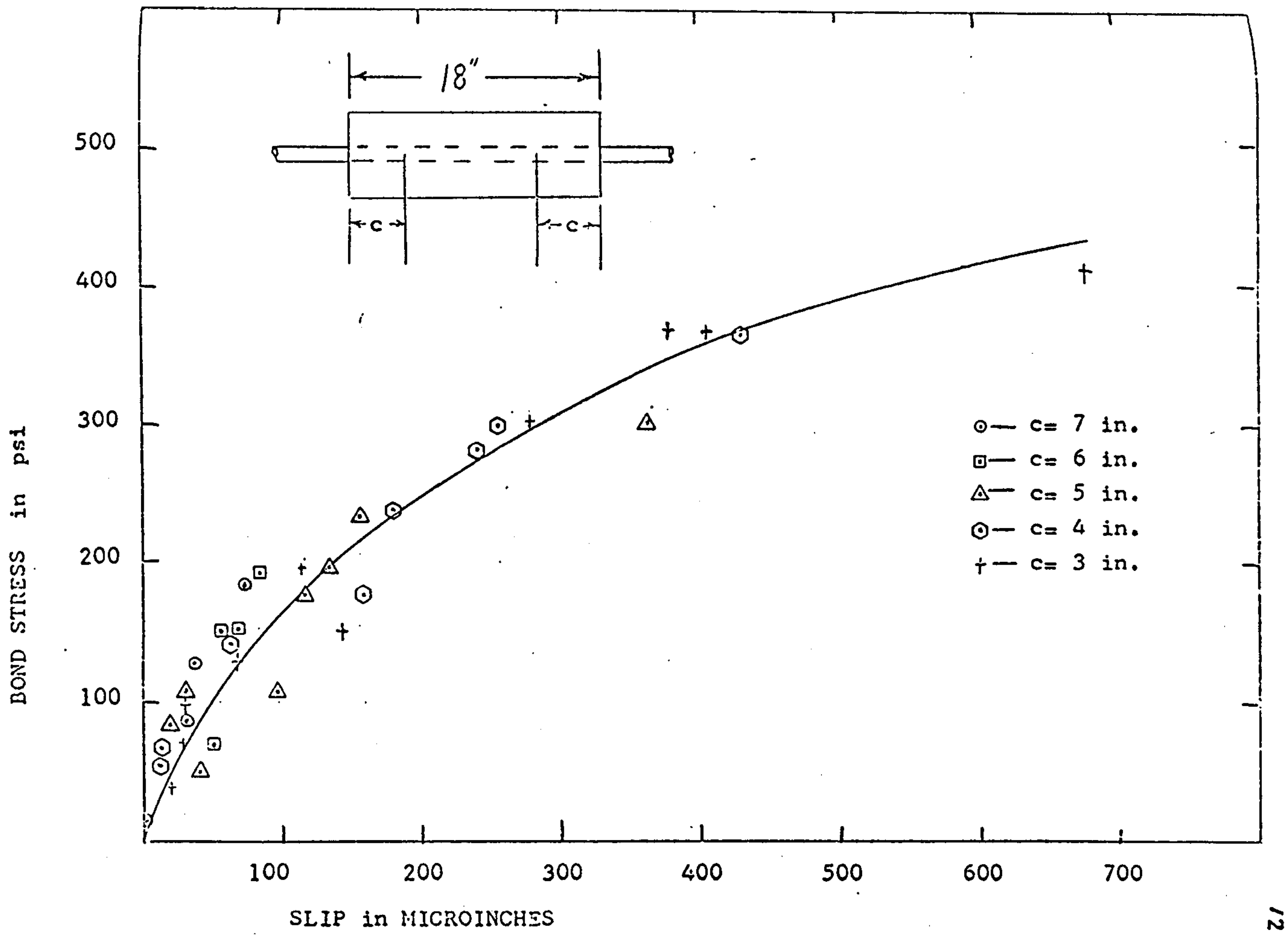

Fig. 7.53: Bond Stress vs. Slip for Test II-A-3 (Adapted from Tanner, 1971)

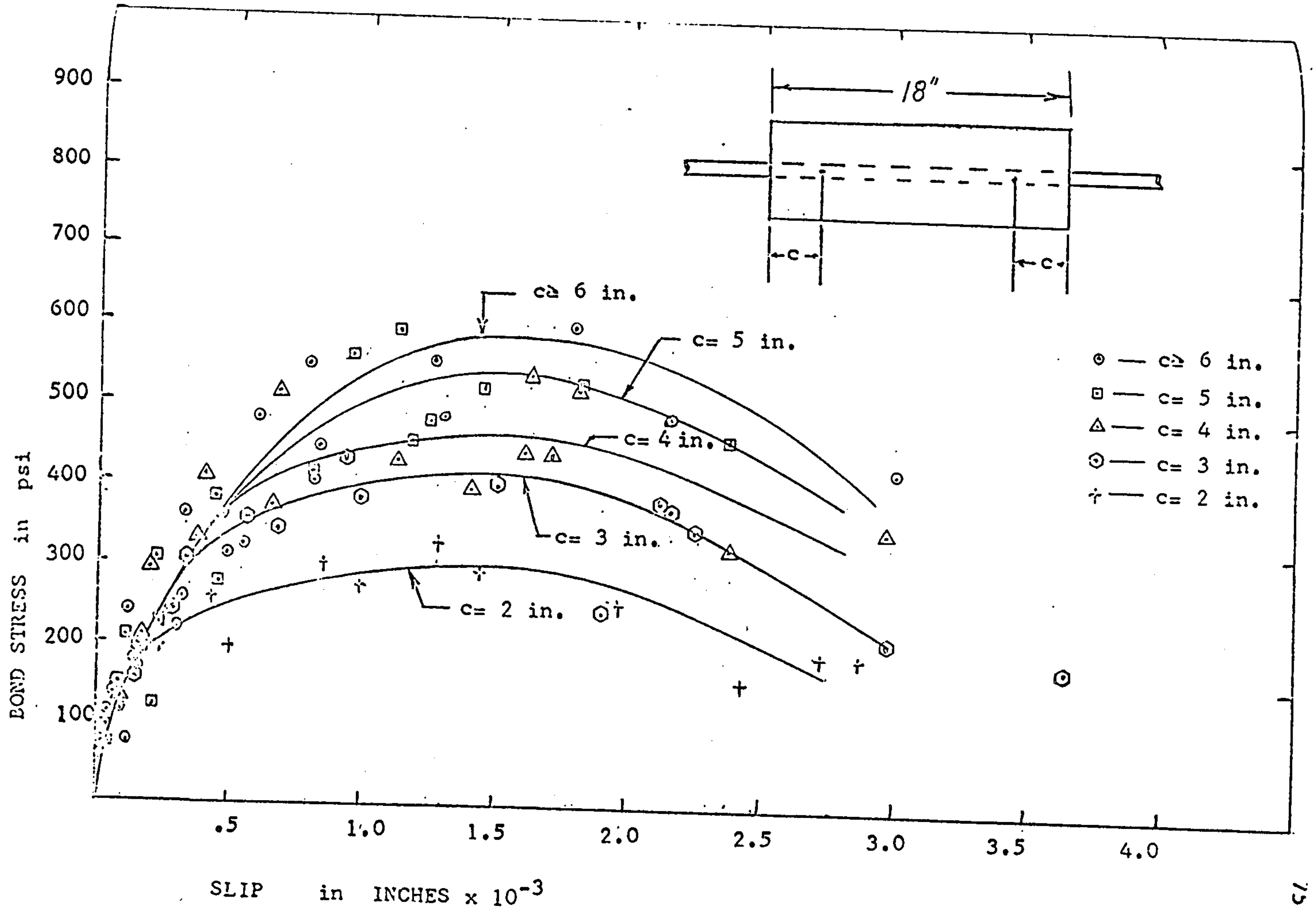

Fig. 7.54: Bond Stress vs. Slip for Test II-B-1 (Adapted from Tanner, 1971)

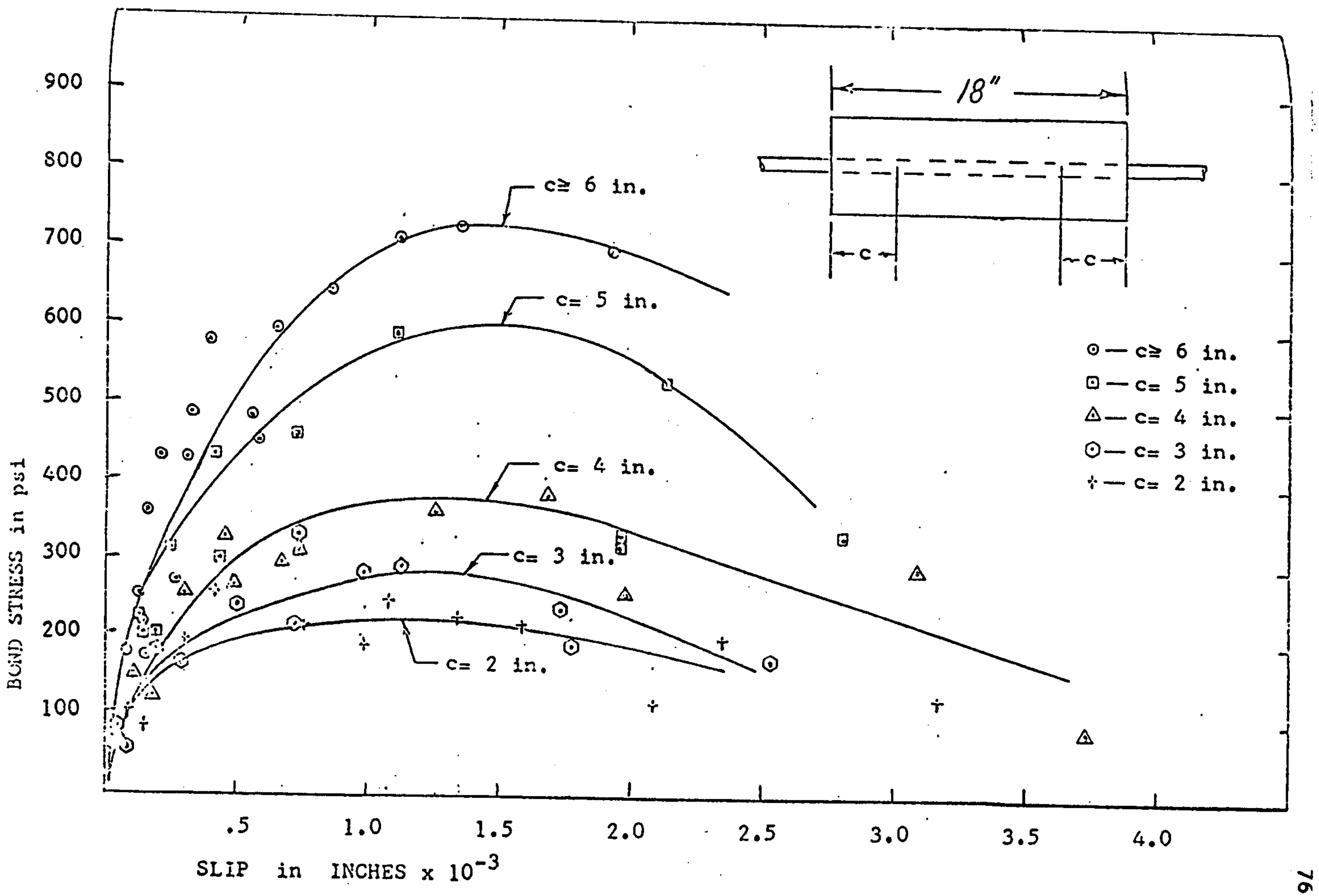

Fig. 7.55: Bond Stress vs. Slip for Test II-B-2 (Adapted from Tanner, 1971)

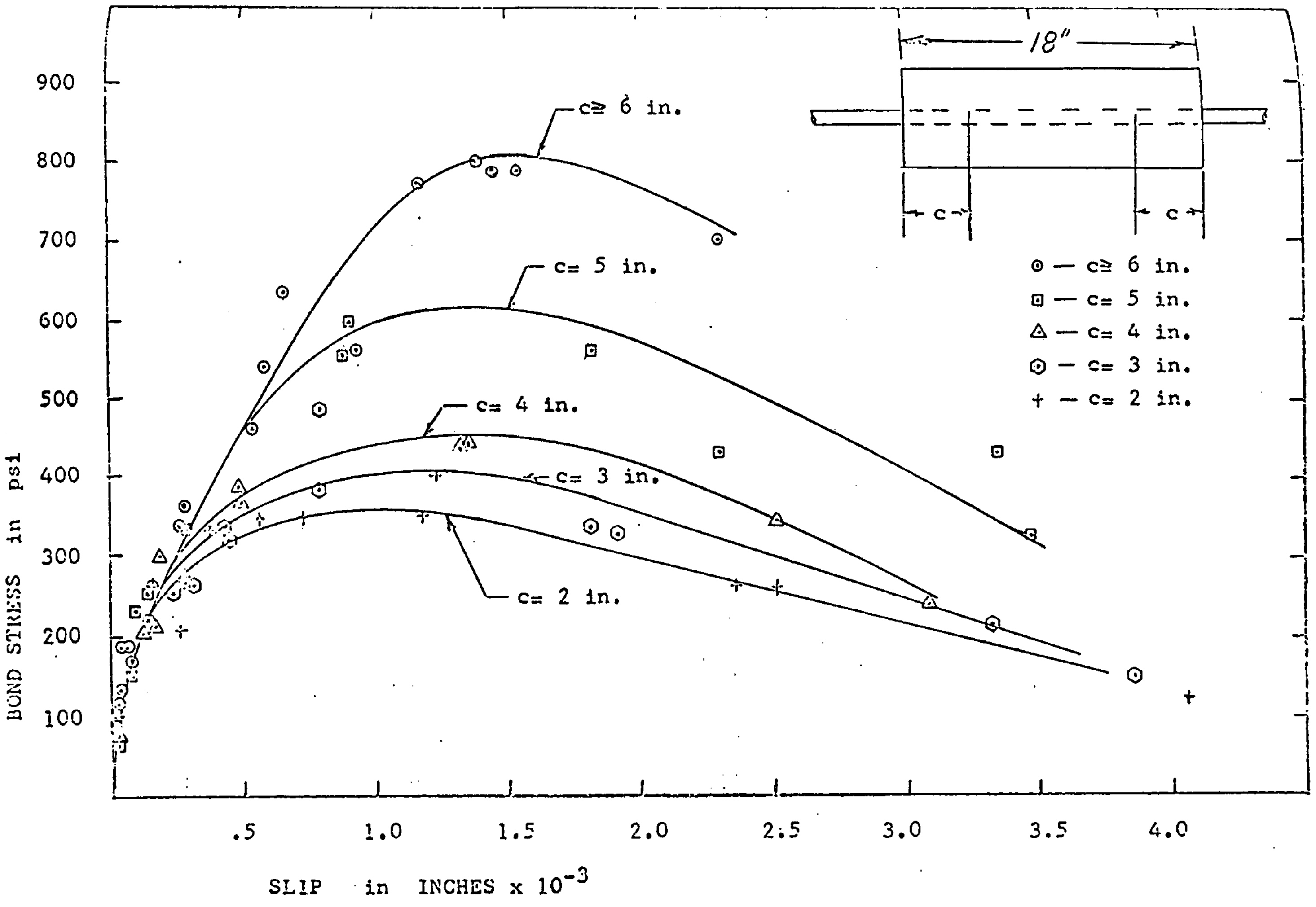

Fig. 7.56: Bond Stress vs. Slip for Test II-B-3 (Adapted from Tanner,1971)

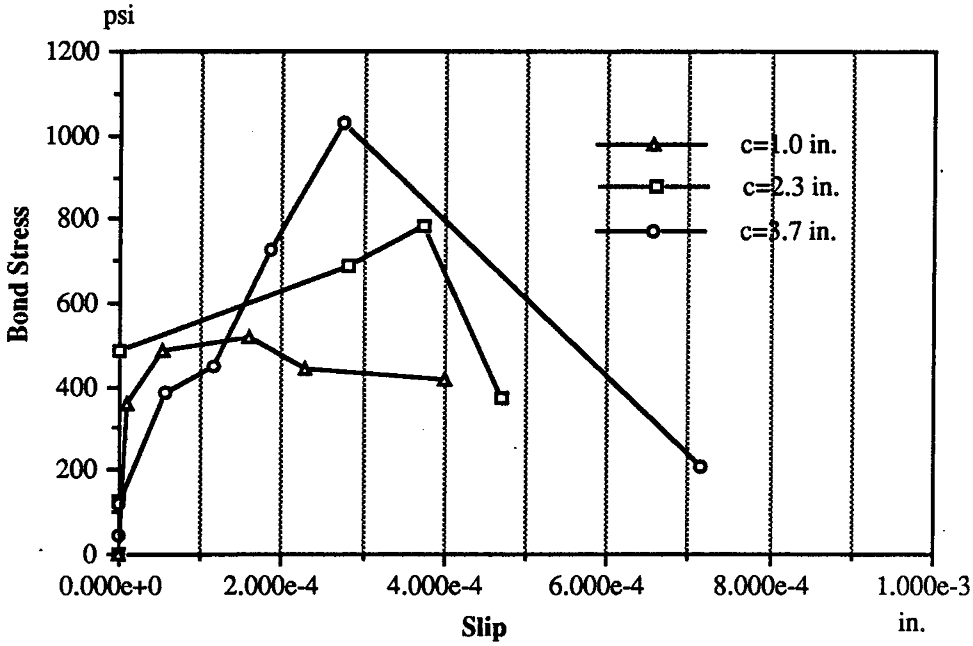

Fig. 7.57: Bond Stress vs. Bond Slip from Simulation of Goto's Case 1

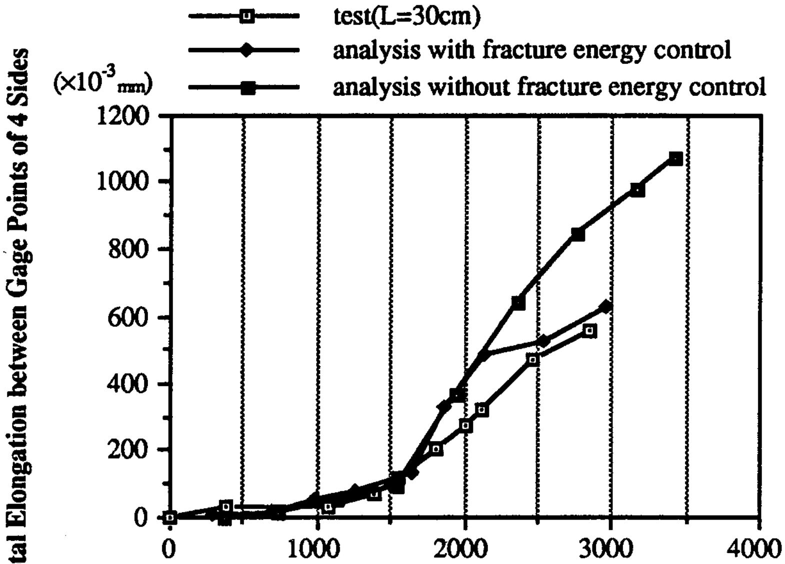

Fig. 7.58: Comparisons of Simulations of Goto's Case 1 for Energy Control

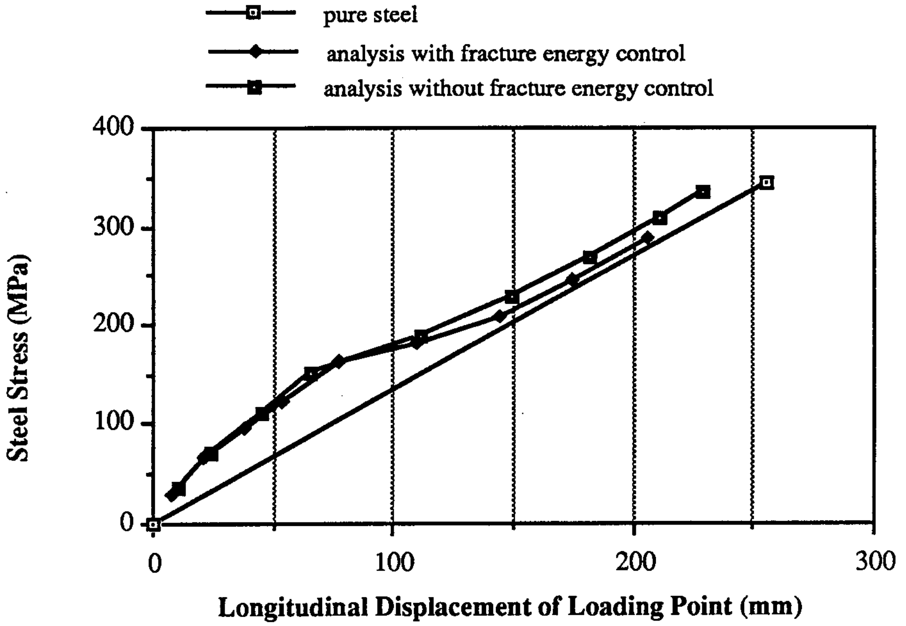

Figure 7.59: Longitudinal Displacement at the Loading Point vs. Steel Stress

CHAPTER 8

SUMMARY AND CONCLUSIONS

8.1 Summary

In this study, a systematic and automated approach for the finite element analyses of distributed discrete concrete cracking, has been developed. As the first step of the approach, a topological data structure, or data base, is built from the input data for the finite element mesh in the 'data preparation phase'.

This vertex-based data structure represents explicitly all the adjacency relations included in the input finite element mesh. Possible crack patterns of the mesh are exhaustively represented in the data structure by the technique of "exhaustive nodal splitting", developed herein.

Crack initiation and propagation can be simulated by activating or deactivating the associated "nodal splitting numbers". This process is carried out by referencing and modifying the topological data base.

Link elements of the continuous type are used to represent crack face behaviors. The softening response of cracked concrete associated with the tensile fracture energy forms the basis for the constitutive relation at the crack faces.

A fracture energy criterion is introduced to the solution strategy which controls the load increment to stabilize crack propagation.

To represent longitudinal splitting cracking, which is typical of three-dimensional behavior, by a two-dimensional axisymmetrical finite element model, a smeared crack model is applied in the circumferential direction when cracks in that direction are initiated.

A Von Mises plastic model has been used to reflect the concrete compressive yielding.

The approach developed has been applied to: (1) the solution of a concrete prism under uniform tension; (2) the problem of three-point bending of a notched concrete beam; (3) the numerical simulation of the "tension-pull" tests conducted by Goto (1971); (4) the numerical simulation of the "tension-pull" tests conducted by Watstein and Mathey (1959).

The finite element simulation of a concrete prism in direct tension reproduces the basic behavior of post-cracking softening in the form of a discrete crack representation.

The analysis of a notched concrete beam under three-point bending demonstrated that the approach adopted in this study is capable of producing results consistent with the well established previous study (Hillerborg, 1985).

The finite element simulations of "tension-pull" tests explicitly model the lugs on the reinforcement surface as solid elements. A number of aspects of the behavior of "tension-pull" members which have been recorded in experimental tests, have been compared with the results of these finite element simulations.

Discrete cracking, longitudinal splitting cracking, interface behavior and local crushing are identified in these simulations. Progressions of these mechanisms at different stages during the loading history are clearly represented in the simulation processes. The correlations of the mechanisms have been discussed.

Bond stresses and bond slips were evaluated along the concrete-steel interface. The variables of bond were averaged at intervals referenced to lugs on the surface of the reinforcing bars along the length of the "tension-pull" specimens. The influence of cracking on the response of different variables at different loading stages for different tests, has been discussed.

8.2 Conclusions

8.2.1 General

1. The major conclusion from this study is that the finite element method with discrete crack representation can be used to closely simulate not only the global behavior of reinforced concrete members, such as load deflection behavior, crack pattern, failure load and failure mode, but also detailed local behavior at particular stages during the loading history, such as patterns of dominant crack progression and patterns of bond deterioration progression, which may determine and explain a variety of global behaviors.

2. In order to obtain satisfactory simulations it is necessary to include approaches to simulate major sources of nonlinearity of reinforced concrete. This appears to require: (i) a robust and efficient topological data base and a dynamic bookkeeping scheme for the stiffness matrix in order to automate simulation of discrete tensile crack initiation and propagation; (ii) constitutive relationships for link elements based on the softening response of cracked concrete associated with the tensile fracture energy, in order to simulate discrete crack face behavior such as crack widening, crack unloading and crack closure; (iii) a solution strategy of fracture energy control for simulating transition of crack instability; and (iv) a plastic material model for simulating compressive yielding and crushing of concrete.

8.2.2 Conclusions from the Simulation of "Tension-Pull" Tests

3. Agreement with reasonable accuracy of global behavior for "tension-pull" members has been obtained between the finite element simulations and tests. The global behavior compared includes the elongation along the circumferential direction, on the end faces of the specimens for the maximum and minimum crack spacings of Goto's tests (1971); and, the extension of concrete located close to the bar, the effective modulus of elasticity of the embedded bar, and the concrete strain at the midpoint, in the tests conducted by Watstein and Mathey (1959).

To obtain agreements with reasonable accuracy between finite element simulations and the tests, input parameters for numerical analyses must be properly defined. If some of them are not available in the documents of tests, they should be selected in the practical range of the parameters by optimal fit of the test results. Most important among these parameters are the tensile strength of concrete, f_t', the compressive yield strength of concrete, f_c', the tensile strength of concrete for crack initiation in the circumferential direction, f_{th}' and the tensile strength of adhesion between concrete and steel, f_{sc}'.

4. Finite element simulations of the "tension-pull" tests indicate that longitudinal split cracking has an important influence on the bond effect between concrete and reinforcement. Therefore, a model which simulates

this cracking, such as the circumferential smeared crack model adopted in this study, is necessary for the analyses of local bond effects.

5. Finite element simulations of Goto's "tension-pull" tests indicate that tensile strength for crack initiation in the circumferential direction, f'_{th}, should be given a greater value for a smaller crack spacing. When the f'_{th} for maximum crack spacing was set to be equal to f'_t, and the f'_{th} for minimum crack spacing was set to be 1.3 times f'_t, good agreement was obtained for global behavior in simulating Goto's tests.

6. Finite element simulations of Goto's "tension-pull" tests reveal that the pattern of dominant crack progression for 'maximum' crack spacing is different from that for 'minimum' crack spacing.

7. For Goto's maximum crack spacing, the concrete-steel adhesion and contact at the front faces (and back faces) of lugs were lost progressively from the protruding end of reinforcement to the center of crack spacing due to the progressive lifting up of the concrete from the interface bar surface as the 'dominant' crack, the front of the longitudinal splitting cracks, and the local compressive yielding of concrete synchronously relocate toward the center of the crack spacing.

8. For Goto's minimum crack spacing, the progressive loss of contact at the front faces of lugs does not occur. Instead, the contact between concrete and steel at the front face of a lug located close to the protruding end of the reinforcement remains until the final failure, while the contact at the front faces of lugs which are located behind this lug is lost earlier. As a result, dragging forces applied by the lugs which are in contact with surrounding concrete, lead the vertical concrete cracks located at, or close to, the center of the crack spacing to grow slowly and steadily. Final failure at high steel stress levels appears to involve complete unbonding along the concrete-steel interface and cracking to the exterior concrete surface at the center of the specimen.

9. The different patterns of dominant crack progression explain why the ratio of elongations in the circumferential direction in the end faces of maximum and minimum crack spacings of Goto's tests, which is 6, is much greater than the ratio of the crack spacings, which is 2.

10. Finite element simulations of the Watstein and Mathey "tension-pull" tests indicate that the reverse of the strain at the midpoint is caused by the three synchronously occurring factors, namely: propagation of

longitudinal splitting cracks reaching the outer surface of the specimen; lifting of concrete from the interface at the lugs near the protruding end of reinforcement; and, propagation of the vertical discrete cracks located close to the center of the specimen.

11. Modeling lugs of reinforcement as solid elements provides realistic evaluation of bond stresses which are characteristic of deformed bars. The modeling provides evaluation of bond slip at the interface of concrete and steel, rather than at a distance away from the interface.

12. In general, low longitudinal bond stresses and high longitudinal bond slips exist at the concrete-steel interface just behind dominant cracks. On the other hand, high radial bond stresses exist at the front faces of the lugs where these dominant cracks are located, because of the compressions which are applied on the front faces. This produces tension and tensile cracking in the circumferential direction. High longitudinal bond stresses occur on the interface where the concrete-steel adhesion is not damaged, but radial bond stresses at these locations are usually low.

13. The pattern of dominant crack progression determines the associated pattern of progression of bond deterioration. Different typical behavior patterns were observed.

For Goto's maximum crack spacing, the specimen averaged bond slip has a sudden increase, and the specimen averaged bond stress has a sudden decrease, as the last dominant crack emerges. This change is associated with the propagation of the longitudinal splitting crack.

For Goto's minimum crack spacing, the specimen averaged bond slips increase linearly through the whole loading history as the steel stresses increase. The specimen averaged bond stresses begin to decrease at high steel stress levels, as the local bond stresses at the the center of the crack spacing change sign due to the adjacent vertical crack propagating toward the outer surface.

If Goto's maximum and minimum crack spacings are considered as two opposite extremes for the patterns of progression of bond deterioration, the tests conducted by Watstein and Mathey exhibit a pattern which is between the two extremes. That is, the effect of longitudinal splitting causes it to have some characteristics of Goto's maximum crack spacing, and the dominant crack progression causes it to have some characteristics of Goto's minimum crack spacing.

8.2.3 Other Conclusions

14. Finite element simulation of a concrete prism under uniform tension indicates that for the analyses of a single discrete crack, the crack width control approach can successfully deal with the "snap back" problem, while the displacement control approach fails.

15. Analysis of results of the tests of plain concrete in direct tension (Gopalaratnam and Shah, 1985) suggests that the ultimate crack width defined by linear tension softening of concrete (or mortar), $W_c = 2G_F/\sigma_p$, is a more invariant measure of the tension softening relationship than the other parameters, such as σ_p, the peak tensile stress, or G_F, the fracture energy density.

8.3 Final Perspectives

In spite of the significant effort devoted to the distributed discrete cracking analysis discussed in this work there are many aspects of this type of analysis which have been only partially explored, or remain unexplored. Further exploration of some of these aspects could contribute substantially to our understanding of both the analytical technique, and the mechanisms of behavior in the response of concrete structures.

In this respect one could, for instance, single out the influence of mesh design, the configuration of the reinforcement, the effects of including interface shear behavior across cracks, the nature of the tensile cracking relationship across steel-concrete interfaces, and the effectiveness of truss elements for modeling web reinforcement in concrete beams.

It is important to recognize, however, that there is a great scarcity of reliable test data against which the analyst can calibrate his model and verify the mechanisms of progressive failure that his models predict. It appears that modern feed-back controls, such as those used by Gopalaratnam and Shah (1985), now make it feasible to design experiments and accumulate data on important mechanisms which would be necessary for a proper modeling and verification of some of the factors identified in the previous paragraph. Thus, well-conceived projects in the future should probably involve experiments appropriate to the phenomena that they are attempting to represent.

At the same time the work presented herein suggests that, because of the importance of longitudinal splitting, attempts to model tensile-pull behavior cannot now be properly undertaken with two dimensional models. Yet, to develop a general three dimensional splitting model would be very complex. (See, for instance, Martha, 1989). In addition, as shown in Chapter 7, bond behavior in tension-pull specimens depends on transverse crack spacing. A general purpose program should be capable of predicting the response which leads to the establishment of primary cracks and growth of secondary cracks until a stable crack pattern has been established. If the spacing between cracks reduces, the direction of the forces on some of the lugs of the bar, which play a major part in the force transfer mechanism, may reverse, thus leading to diagonal cracks at the opposite orientation to those that first formed. Consequently, the loading history can become complex. Also, the control of the numerical solution associated with propagation of a secondary crack into a primary crack may not be accomplished in a simple manner.

The current state of development, as reflected by this work, has avoided these problems by selecting specimen dimensions in a manner similar to Goto (1971).

If one now returns to the discussion of Chapter 1, involving the relations postulated between the 'micro-' and 'meso-' level models, it is apparent that the need for implementation of micro-level analysis to determine properties for meso-level analysis, has not been significantly reduced by this work. It is hoped that the exhaustive nodal splitting scheme developed herein will provide a valuable facility to attack this problem but it is apparent that much development work remains to be done.

REFERENCES

Balakrishnan, S. and Murray, D. W (1986), Finite element prediction of reinforced concrete behavior, Structural Engineering Report No. 138, Department of Civil Engineering, University of Alberta, Edmonton, Alta.

Bathe, K. J. and Dvorkin E. N. (1983), On the Automatic Solution of Nonlinear Finite Element Equations, Computer & Structures, Vol. 17, No. 5-6, pp. 871-879.

Bellini, P. X. and Chulya, A. (1987), An Improved Automatic Incremental Algorithm for the Efficient Solution of Nonlinear Finite Element Equations, Computers & Structures, Vol 26, No. 1/2, pp. 99-110.

Batoz, J. L. and Dhatt, G. (1979), Incremental displacement algorithm for nonlinear problems, Int. J. Numer. Meth. Engng 14, pp. 1262-1267.

Broms, B. B. (1965), Technique for Investigation of Internal Cracks in Reinforced Concrete Members, ACI Journal, Vol. 62, No. 1, January, pp.35-44.

Broms, B. B. (1965), Crack Width and Crack Spacing in Reinforced Concrete Members, ACI Journal, Proceedings, V. 62, No. 10, Oct., pp. 1237-1256.

Broms, B. B. and Lutz, L. A. (1965), Effects of Arrangement of Reinforcement on Crack Width and Spacing of Reinforced Concrete Members, ACI Journal, Proceedings, V. 62, No. 11, Nov., pp. 1395-1410.

Broek, D. (1986), *Elementary Engineering Fracture Mechanics*, 4th revised edition, Martinus Nijhoff Publishers, The Hague, Boston, pp. 18 and pp. 103.

Catalano, D. and Ingreffea, A.R. (1982), Concrete Fracture: A Linear Elastic Fracture Mechanics Approach, Department of Structural Engineering Report 82-1, School of Civil and Environmental Engineering, Cornell University, Ithaca, NY.

Cedolin,L., Darwin, D., Ingraffea, A.R., Pecknold, E.A. and Schnobrich, W.C. (1982), Chapter 4 Concrete Cracking, Finite Element

Analysis of Reinforced Concrete, Published by the American Society of Civil Engineers, pp. 204.

Cedolin, L., Dei Poli, S., and Iori, L. (1983), Experimental Determination of the Fracture Process Zone in Concrete, Cement and Concrete Research, Vol. 13, pp. 577-567.

Cedolin, L., Dei Poli, S., and Iori, L. (1983), Experimental Determination of the Stress-Strain Curve and Fracture Zone for Concrete in Tension, Proc., Int. Conf. on Constitutive Laws for Engineering Materials, ed. by C. Desai, University of Arizona, Tucson.

Chen, W. F. (1982), *Plasticity in Reinforced Concrete,* McGraw-Hill, Inc., pp. 240-242.

Crisfield, M. A. (1981), A Fast Incremental/Iterative Solution Procedure that Handles Snap-through, Comput. Struct. 13, pp. 55-62.

De Borst, R. (1988), Bifurcations in Finite Element Models with a Non-associated Flow Law, International Journal for Numerical and Analytical Methods in Geomechanics, Vol. 12.

Dugdale, D. S., Yielding of Steel Sheet Containing Slits, J. Mech. Phys. Sol. 8, pp. 100-108.

Erdogan, F. and Sih, G.C. (1963), On the Crack Tension in Plates Under Plane Loading and Transverse Shear, ASME Journal of Basic Engineering, Vol., 85, pp. 519-527.

Evans, R.H. and Marathe, M.S. (1968), Microcracking and Stress-Strain Curves for Concrete in Tension, Matẽriaux et Constructions, Vol. 1, No. 1, pp. 61-64.

Gerstle, W., Ingraffea, A.R. and Gergely, P. (1982), The Fracture Mechanics of Bond in Reinforced Concrete, Department of Structural Engineering Report 82-7, School of Civil and Environmental Engineering, Cornell University, Ithaca, NY, pp.144.

Goodman, R. E., Taylor, R. L. and Brekke, T. L. (1968), A Model for the Mechanics of Jointed Rock, Journal of the Solid Mechanics and Foundations Division, Proceedings of ASCE, May, pp. 637-659.

Gopalaratnam, V.S. and Shah S.P. (1985), Softening Response of Plain Concrete in Direct Tension, Journal of the American Concrete Institute, No 3, Vol. 82, pp. 310-323.

Goto, Y. (1971), Cracks Formed in Concrete Around Deformed Tension Bars, ACI journal, Vol. 68, No. 4, April, pp. 244-251.

Hillerborg, A. (1985), Numerical Method to Simulate Softening and Fracture of Concrete, Fracture mechanics of Concrete: Structural Application and Numerical Calculation, edited by G.C. Sih and A. Ditommaso, Martinus Nijhoff Publishers, Dordrecht, pp. 144.

Hognestad, E. (1962), High Strength Bars as Concrete Reinforcement. 2-Control of Flexural Cracking, Journal, PCA Research and Development Laboratories, V. 5, No.1, Jan., pp. 46-62.

Houde, J. (1973), Study of Force-Displacement Relationships for the Finite Element Analysis of Reinforced Concrete, Report No. 73-2, Dept. of Civil Engineering and Applied Mechanics, McGill University, Montreal, December.

Hsu, T. C., and Slate, F.O. (1963), Tensile Bond Strength Between Coarse Aggregate and Cement Paste or Mortar, ACI JOURNAL, Proceedings V. 60, No. 4, Apr., pp. 465-496.

Ingraffea, A.R., and Saouma, V. (1985), Numerical Modeling of Discrete Crack Propagation in Reinforced and Plain Concrete, Fracture Mechanics of Concrete: Structural Application and Numerical Calculation, edited by G.C. Sih and A. Ditommaso, Martinus Nijhoff Publishers, Dordrecht, pp. 171-225.

Irons, B.M. (1970), A Frontal Solution Program for Finite Element Analysis, Int. J. Numerical Methods in Engineering, Vol. 2, pp. 119-130.

Kåre Hellan (1984), *Introduction to Fracture Mechanics*, McGraw-Hill, Inc., pp. 1.

Khouzam, M. (1977), A Finite Element Investigation of Reinforced Concrete Beams, M.Eng. Thesis, McGill University, Montreal, Canada, October.

Mains, R. M. (1951), Measurement of the Distribution of Tensile and Bond Stresses Along Reinforcing Bars, ACI Journal, Proceedings V. 48, No. 2, Nov., pp. 225-252.

Mäntylä, M. (1988), An Introduction to Solid Modeling, Computer Science Press, Rockville, Mayland.

Martha, L. F. and Ingraffea, A. R. (1989), Topological and Geometrical Modeling Approach to Numerical Discretization and Arbitrary Fracture Simulation in Three-Dimensions, Department of Structural Engineering Report 89-9, School of Civil and Environmental Engineering, Cornell University, Ithaca, NY, August.

Mindess, S. and Diamond, S. (1980), A Preliminary SEM Study of Crack Propagation in Mortar, Cement and Concrete Research, Vol 10., pp 509-519.

Mirza, M.S. and Houde J. (1979), Study of Bond Stress-Slip Relationships in Reinforced Concrete, ACI journal, Proceedings, Vol. 76, No. 1, January, pp. 19-46.

Ngo, D. and Scordelis, A.C. (1967), Finite Element Analysis of Reinforced Concrete Beams, Journal of the American Concrete Institute,Vol. 64, No. 14, pp. 152-163.

Ngo, D., Scordelis, A.C., and Franklin, H.A. (1970), Finite Element Study of Reinforced Concrete Beams with Diagonal Tension Cracks, UC-SESM Report No. 70-19, University of California at Berkeley December.

Ngo, D. (1975), A Network-Topological Approach for the Finite Element Analysis of Progressive Crack Growth in Concrete Members, Ph. D. Dissertation, Division of Structural Engineering and Structural Mechanics, University of California, Berkeley, UC-SESM 75-6.

Nilson, A. H. (1968), Finite Element Analysis of Reinforced Concrete, Ph. D. Thesis, University of California at Berkeley.

Nilson, A. H. (1968), Non-Linear Analysis of Reinforced Concrete by the Finite Element Method, ACI Journal, Vol. 65, No. 9, Sept., pp. 757-766.

Nilson, A.H. (1971), Bond Stress-Slip Relations in Reinforced Concrete, Report 345, School of Civil and Environmental Engineering, Cornell University, Ithaca, December.

Nilson, A.H. (1972), Internal Measurement of Bond Slip, ACI Journal, Vol. 69, No. 7, July, pp.439-441.

Petersson, P.-E. (1981), Crack Growth and Development of Fracture Zones in Plain Concrete and Similar Materials, Report TVBM-1006, University of Lund, Sweden.

Petersson, P.-E. (1980), Fracture Energy of Concrete: Method of Determination, Cement and Concrete Research, Vol.10, pp.78-89.

Rashid Y.R. (1968), Analysis of Prestressed Concrete Pressure Vessels, Nuclear Engng. and Design, Vol. 7, No.4, pp. 334-344.

Rots, J.G., Blaauwendradd, J. (1989), Crack Models for Concrete: Discrete or Smeared? Fixed, Multi-Directional or Rotating?, HERON, Vol. 34. No.1.

Shih, C.F., de Lorenzi, H.G., and German, M.D. (1967), Crack Extension Modeling with Singular Quadratic Isoparametric Elements, International Journal of Fracture, Vol 12, pp. 647-651.

Sih, G.C. (1974), Strain-Energy-Density Factor Applied to Mixed Mode Crack Problem, International Journal of Fracture, Vol. 10. pp. 305-321.

Taylor, M. A. and Broms, B. B. (1964), Shear Bond Strength Between Coarse Aggregate and Cement Paste or Mortar, ACI Journal, Proceedings V. 61, No. 8, Aug. pp. 939-958.

Tanner, J.A. (1971), An Experimental Determination of Bond Slip in Reinforced Concrete, M.S. Thesis, Cornell University, Ithaca, N.Y., November.

Watstein, P. and Mathey, R.G. (1959), Width of Cracks in Concrete at the Surface of Reinforcing Steel Evaluated by Means of Tensile Bond Specimens, ACI Journal, Vol. 56, No. 1, July, pp. 47-56.

Wawrzynek, P. A. and Ingraffea, A. R (1986), Interactive Finite Element Analysis of Fracture Processes: An Integrated Approach, Theor. Appl. Frac. Mech. Nov.

Wawrzynek, P. A. and Ingraffea, A. R (1987), An Edge-Based Data Structure for Two-Dimensional Finite Element Analysis, Engng. with Comput., 3, pp. 13-20.

Weiler, K. (1986), Topological Structures for Geometric Modeling, Ph.D Dissertation, Rensselaer Polytechnic Institute, Troy, NY.

Wittmann, F. H. (1983), Chapter 2: Structure of Concrete with Respect to Crack Formation, Fracture Mechanics of Concrete, edited by Folker H. Wittmann, Elsevier Science Publishers, B. V., pp. 43-74.

Zienkiewicz, O. C. (1971), *The Finite Element Method in Engineering Science*, 2nd edition, McGraw-Hill, London, pp. 151.

APPENDIX A

RECOGNITION AND TREATMENT OF MECHNISMS

A.1 Introduction

A structure becomes a "mechanism" if there exists a displacement pattern for it for which it does not absorb energy. Such a structure is unstable and it is not possible to determine an unique set of displacements from the solution of the equilibrium equations.

In discrete cracking two-dimensional finite element analysis, a group of elements representing a block of a structure forms a mechanism if it does not have any nodes, or only has one node, connecting it to the "main block". This 'main block' is a group of elements for which a set of supports ensuring its stability are defined on its boundary. Fig. A.1 shows some examples of mechanisms.

The two elements in Fig. A.1a under uniform tension may separate along their common boundary, as shown in Fig. A.1b. As support S is on the boundary of element No. 1, element No. 1 is a main block. Since element No. 2 has no nodes connecting to the main block, it becomes free to move and therefore is a mechanism.

A second example of a mechanism is shown in Figs. A.1c and d. In Fig. A.1.c, point S at the symmetry line of a "tension-pull" concrete bar with a steel bar embedded along its center, is the support sufficient to define a main block. Fig. A.1d shows that elements B and C, located at the exit of the steel from the concrete may become mechanisms because inclined cracks in the concrete, may develop, and the adhesive bond between the steel face and concrete be destroyed.

Fig. A.1d also shows the tensile stress trajectories which indicate tensile stress distributed along vertical edges of elements in columns E and F of Fig. A.1c. As the cracking load P_c is reached the stresses on both vertical edges of these elements may exceed the tensile strength and cracks may be introduced on both sides, as shown in Fig. A.1e. Then each of the element columns E and F is separated from a main block.

A fourth type of mechanism is shown in Fig. A.1.g where element No.2 has only one node connected to the main block.

These mechanisms cause numerical difficulties. They cause zero or negative diagonal values for some equations in the mechanism blocks during Gaussian elimination and, normally, the solution is terminated because it is no longer unique.

Adoption of coarse element meshes sometimes eliminates these difficulties. But coarse meshes reduce accuracy, and in the case of the discrete crack approach, greatly reduce the capability to predict distributed discrete cracking behavior.

A.2 Mechanism Recognition and Treatment

The procedure of mechanism recognition and treatment is illustrated by the example shown in Fig. A.2. For the purpose of illustrating recognition of a mechanism, an artificial crack pattern is introduced, without supporting engineering calculations, as shown in Fig. A.2.b. Note that, because of the cracking, the unsplit nodes in the mesh of Fig. A.2a have multiple numbers in the configuration of Fig. A.2b. However, no 'gaps' have been used in the nodal numbers of Fig. A.2b, as would occur in exhaustive enumeration, since such gaps do not influence the procedure described in the following.

A.2.1 Step 1: Formation of Node-Element Incidence Array KEMT

As described in Sect. 3.6.2, a node-element incident array KEMT is formed in which KEMT (I,1) gives the number of elements incident to node I, and from KEMT(I,2) to KEMT(I,KEMT(I,1)+1), give the element numbers. The array KEMT for the example in Fig. A.2b is shown in Table A.1.

A.2.2 Step 2: Formation of Element-Element Incidence Array KEMT3

From array KEMT, build the element-element incidence array KEMT3(I,J,K) where I represents the element number, J represent the sequential order of elements incident to element I and K ranges from 1 to 2. In KEMT3 (I,J,1), the incidental element number is given, and in KEMT3(I,J,2) the number of nodes of this incidental element common to element I is given. For a quadratic displacement element, a maximum of 3 nodes can be shared by two elements, so the maximum of KEMT3(I,J,2) is 3. Table A.2 gives KEMT3 for the example.

The process of producing KEMT3 from KEMT is illustrated for node 35 of the example. After node 34 is processed, node 35 is processed as follows. From Table A.1, node 35 has 3 elements incident to it: 7, 8 and 9. These 3 element numbers produce 3 pairs of connected elements: 7 and 8, 8 and 9 and 7 and 9. For the first pair, 7 and 8, the elements incident to element 7 are stored in KEMT3(7,K,J) shown in Table A.2 under I=7, and KEMT3(7,2,1)=8 already exists. Because node 35 adds another incidental node, so KEMT3(7,2,2) is changed from 2 to 3. Similarly KEMT3(8,2,2) is increased from 2 to 3. Pair 8 and 9 repeats the same routine as for pair 7 and 8. Pair 7 and 9 adds KEMT3(7,3,1)=9, KEMT3(7,3,2)=1, KEMT3(9,3,1)=7 and KEMT3(9,3,2)=1 to KEMT3.

A.2.3 Step 3: Recognizing Distinct Blocks in the Cracked Configuration

A 'distinct' block is defined as a group of elements for which any element of the group must be incident to at lease one other element in the group by at least 2 nodes. As the example in Fig. A.2b is concerned, elements 1, 2 and 3 belong to the same block, but element 15 and 16 do not belong to the same block. According to this rule, the example is composed of 4 distinct blocks marked by the numbers in the rectangular boxes shown in Fig. A.2c.

Two arrays, the one-dimensional array MEM, and the two-dimensional array MEM1(L,M), with L ranging from 1 to 2, are used to identify these blocks. The example of Fig. A.2 is again used and all operations are shown in Table A.3 where they are numbers.

Before operation No. 1, arrays MEM and MEM1 are set to zero. In operation No.1, the number of the first element, namely, 1, is stored in MEM1(1,1) and MEM(2). Referring to array KEMT3 of Table A.2 under I=1, element 2 and 8 are found incident to element 1 by at least two nodes (that is, KEMT3(1,1,2)=2 and KEMT3(1,3,2)=3), and these for 2 and 8 are stored in MEM1(2,1) and MEM1(2,2), and also in MEM(3) and MEM(4).

In operation No. 2, all numbers in the second row of MEM1(L,M) (L=2) are copied to first row of MEM1(L,M), and then the second row of

MEM1(L,M) is set to zero. Referring now to array KEMT3, under I=2,8, elements 1, 3, 7 and 9 are found incident to elements 2 and 8 by at least 2 nodes, but because element 1 has already been stored in MEM(1,1), only 3, 7 and 9 are stored in second row of MEM1 and also in MEM.

Operations No. 3 to No.5 repeat the same routine as for operation No.1. At operation No. 6, all elements listed in the first row of MEM1 do not have any two or three nodes incidental elements which are not already in array MEM. This indicates the exhaustive search for elements in the first distinct block is completed. Then a zero is added behind the last nonzero number in MEM to mark this completion. Since element 1 was the start of this chain of operations for completing the first distinct block, sequential element number starting at 2 are checked for existence in array MEM, until the first element number which is not in MEM, that is, element 13, is found.

Operations Nos. 7 and 8 are similar to operations No. 1 to 6 and add another distinct block of only two elements (13 and 14). Operation No. 9 indicates element 15 is a one element block. Operations Nos. 10 and 11 give another two element Block (16 and 17). Table A.4 shows the final result of array MEM in which the 4 distinct blocks are separated by zeros.

A.2.4 Step 4: Finding Common Nodes between Distinct Blocks

An array KEMT4 is built to record the total number of elements incident to a node and also inside a specified block. Recall that in array KEMT (Table A.1), KEMT(I,1) is the total number of elements which are incident to a node. But these are not limited to any particular block. Array KEMT4 for the first distinct block in the example of Fig. A.2b is listed in Table A.4. It is seen that KEMT4(40)=1, because only one element in the block is incident to it. But in Table A.1, KEMT4(40,1) equals 3 which differ from KEMT4(40) and therefore indicates that node 40 is a common node between the first block and other blocks. For the first block, another node, node 62, also is a common node as shown in Fig. A.2c. Common nodes for every distinct block are shown in Table A.5.

A.2.5 Step 5: Determination of Main Block and Mechanism Blocks

As described in Sect. A.1, a main block is the block on whose boundary support conditions are defined. In the example in Fig. A.2, the first distinct block is the main block. In this study, a block which has at least 2 common nodes with a main block is also defined as a part of main block. So the 4th block which has 2 common nodes with the main block, namely, nodes 40 and 62, is also included in the main block. The second and third distinct blocks become mechanism blocks because the former has no connection to the main block while the second is connected to main block by only one node, which is a hinged connection.

A.2.6 Treatment of Mechanism Blocks

To prevent numerical problems caused by block mechanisms, the following measures are taken:

(a) A flag is set for elements in a block mechanism, so that these elements will not be brought into the stiffness matrix formulation.

(b) For all nodes in mechanism blocks, except common nodes with main block, the equation numbers in the array of degrees of freedom (ID array) are set to zero, so they become inactive nodes. For the example of Fig. A.2, the common node of block 3 with the main block is node 37, all other node is block 3 (47, 48, 57, 58 and 59 as shown in Fig. A.2b) are set to be inactive. All nodes in block 2 are also set to be inactive.

(c) Set all the nodal forces at the crack faces between the main block and the mechanism blocks to zero. The results of these measures are that the mechanism blocks are removed from the structure as shown in Fig. A.2d.

Table A.1 Nodal-Element Incidence Array KEMT for Fig. A.2

I	KEMT (I,1)	KEMT(I,2), -,	I	KEMT(I,1)	KEMT(I,2), -,
1	2	1, 2	32	2	13, 14
2	1	2	33	1	7
3	3	2, 3, 4	34	1	14
4	1	4	35	3	7, 8, 9
5	3	4, 5, 6	36	1	14
6	1	6	37	1	15
7	1	6	38	1	16
8	1	1	39	1	9
9	2	1,2	40	3	9, 16, 17
10	2	2, 3	41	3	10, 11, 18
11	2	3, 4	42	2	11, 18
12	2	4, 5	43	3	11, 12, 18
13	2	5, 6	44	1	13
14	1	6	45	2	13, 14
15	3	1, 7, 8	46	1	14
16	2	1, 8	47	1	15
17	3	1, 8, 9	48	1	15
18	3	2, 3, 10	49	1	16
19	2	3, 10	50	2	16, 17
20	6	3, 4, 5, 10, 11, 12	51	1	17
21	2	5, 12	52	1	18
22	3	5, 6, 12	53	1	18
23	1	7	54	1	13
24	2	7, 8	55	1	13
25	2	8, 9	56	2	13, 14
26	1	9	57	1	15
27	1	10	58	1	15
28	2	10, 11	59	1	15
29	2	11, 12	60	2	16, 17
30	1	12	61	1	17
31	1	7	62	2	17, 18

**Table A.2: Element- Element Incidence Array KEMT3(I,J,K)
for Fig. A.2**

I =	K=	J=1	J=2	J=3	J=4	J=5	J=6	J=7
1	1	2	7	8	9			
	2	2	1	3	1			
2	1	1	3	4	10			
	2	2	3	1	1			
3	1	2	4	10	5	11	12	
	2	3	3	3	1	1	1	
4	1	3	10	11	5	6	12	2
	2	3	1	1	3	1	1	1
5	1	3	4	6	10	11	12	
	2	1	3	3	1	1	3	
6	1	4	5	12				
	2	1	3	1				
7	1	1	8	9				
	2	1	3	1				
8	1	1	7	9				
	2	3	3	3				
9	1	1	8	7	16	17		
	2	1	3	1	1	1		
10	1	2	3	4	5	11	12	18
	2	1	3	1	1	3	1	1
11	1	3	4	5	10	12	18	
	2	1	1	1	3	3	3	
12	1	3	4	5	6	10	11	18
	2	1	1	3	1	1	3	1
13	1	14						
	2	3						
14	1	13						
	2	3						
15	1	16						
	2	1						
16	1	15	9	17				
	2	1	1	3				
17	1	16	9					
	2	3	1					
18	1	10	11	12	17			
	2	1	3	1	1			

Table A.3: Operations for Identifying Distinct Blocks

Operation No.	MEM1(1,M), M=1,2,3,... MEM1(2,M), M=1,2,3,...	MEM(N), N=1,2,3,...	Comment
1	1	0, 1, 2, 8	
	2, 8		
2	2, 8	0, 1, 2, 8, 3, 7, 9	
	3, 7, 9		
3	3, 7, 9	0, 1, 2, 8, 3, 7, 9, 4, 10	
	4, 10		
4	4, 10	0, 1, 2, 8, 3, 7, 9, 4, 10, 5, 11	
	5, 11		
5	5, 11	0, 1, 2, 8, 3, 7, 9, 4, 10, 5, 11, 6, 12, 18	
	6, 12, 18		
6	6, 12, 18	0, 1, 2, 8, 3, 7, 9, 4, 10, 5, 11, 6, 12, 18	first block
	0		complete
7	13	0, 1, 2, 8, 3, 7, 9, 4, 10, 5, 11, 6, 12, 18,	
	14	0, 13, 14	second block
8	14	0, 1, 2, 8, 3, 7, 9, 4, 10, 5, 11, 6, 12, 18,	complete
	0	0, 13, 14	
9	15	0, 1, 2, 8, 3, 7, 9, 4, 10, 5, 11, 6, 12, 18,	third block
	0	0, 13, 14, 0, 15	complete
10	16	0, 1, 2, 8, 3, 7, 9, 4, 10, 5, 11, 6, 12, 18,	
	17	0, 13, 14, 0, 15, 0, 16, 17	
11	17	0, 1, 2, 8, 3, 7, 9, 4, 10, 5, 11, 6, 12, 18,	fourth block
	0	0, 13, 14, 0, 15, 0, 16, 17	complete

Table A.4: Nodal-Element Incidence Array KEMT4 for the First Block in Fig. A.2

I	KEMT4 (I,1)	KEMT4 (I,2), -,	I	KEMT4 (I,1)	KEMT4 (I,2), -,
1	2	1, 2	32	2	13, 14
2	1	2	33	1	7
3	3	2, 3, 4	34	1	14
4	1	4	35	3	7, 8, 9
5	3	4, 5, 6	36	1	14
6	1	6	37	1	15
7	1	6	38	1	16
8	1	1	39	1	9
9	2	1,2	40	1	9
10	2	2, 3	41	3	10, 11, 18
11	2	3, 4	42	2	11, 18
12	2	4, 5	43	3	11, 12, 18
13	2	5, 6	44		
14	1	6	45		
15	3	1, 7, 8	46		
16	2	1, 8	47		
17	3	1, 8, 9	48		
18	3	2, 3, 10	49		
19	2	3, 10	50		
20	6	3, 4, 5, 10, 11, 12	51		
21	2	5, 12	52	1	18
22	3	5, 6, 12	53	1	18
23	1	7	54		
24	2	7, 8	55		
25	2	8, 9	56		
26	1	9	57		
27	1	10	58		
28	2	10, 11	59		
29	2	11, 12	60		
30	1	12	61		
31	1	7	62	1	18

Table A.5: Array MEM(I), the Blocks and Common Nodes for the Example in Fig. A.2

I	1	2	3	4	5	6	7	8	9	10	11	12	13	14	15	16	17	18	19	20	21	22	23
MEM(I)	0	1	2	8	3	7	9	4	10	5	11	6	12	18	0	13	14	0	15	0	16	17	0
Distinct Block No.	▨	$\boxed{1}$													▨	$\boxed{2}$		▨	$\boxed{3}$	▨	$\boxed{4}$		▨
Common Nodes	▨	40, 62													▨	None		▨	37	▨	37, 40, 62		▨

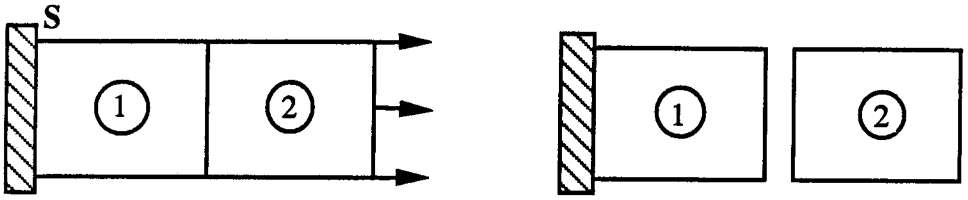

a) Model for concrete prism in uniform tension

b) Crack pattern

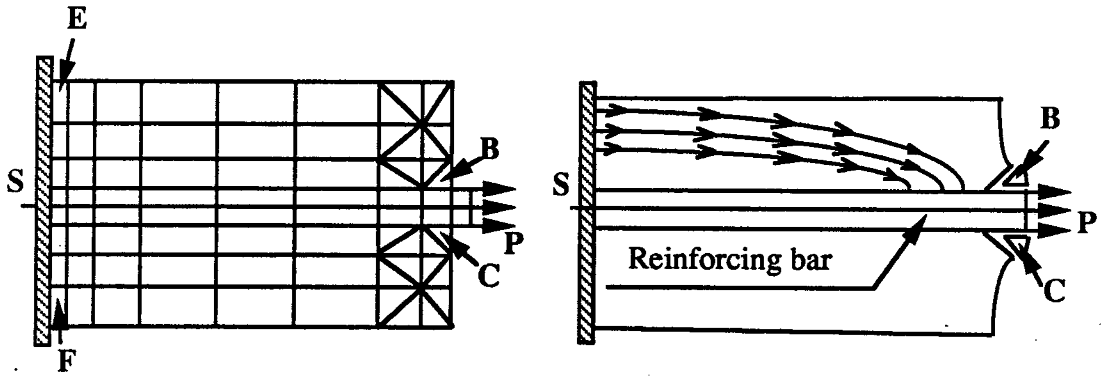

c) Model for "Tension-pull" bar

d) Concrete elements **B** and **C** separated from main block

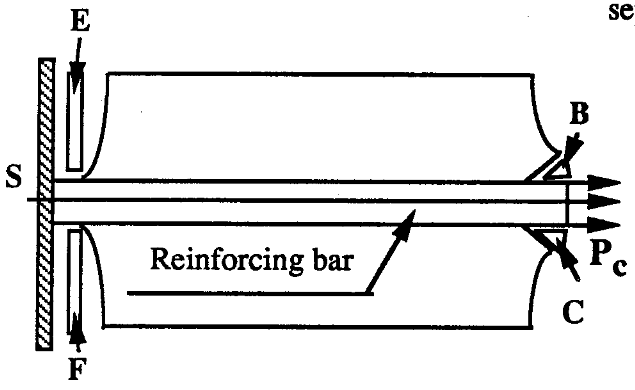

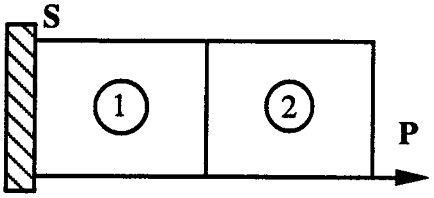

f) Model for concrete prism in eccentric tension

e) Columns of concrete element **E** and **F** separated from main block

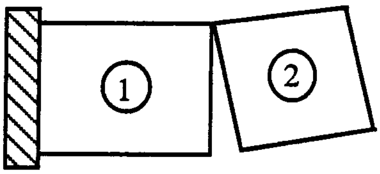

g) Crack pattern: hinge connection

Fig. A. 1: Examples of Mechanisms in Finite Element Analyses of Discrete Cracking

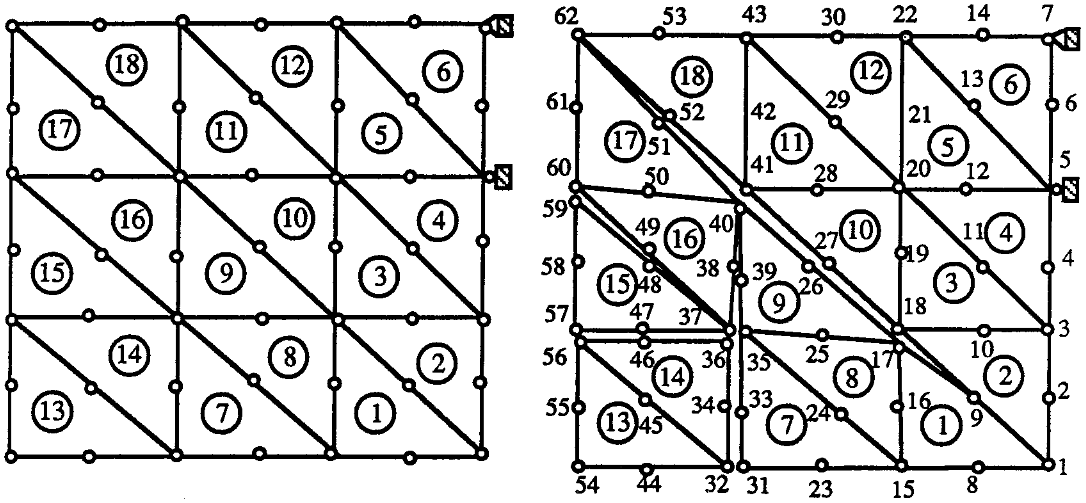

a) Element mesh for uncracked state

b) Element mesh for cracked state

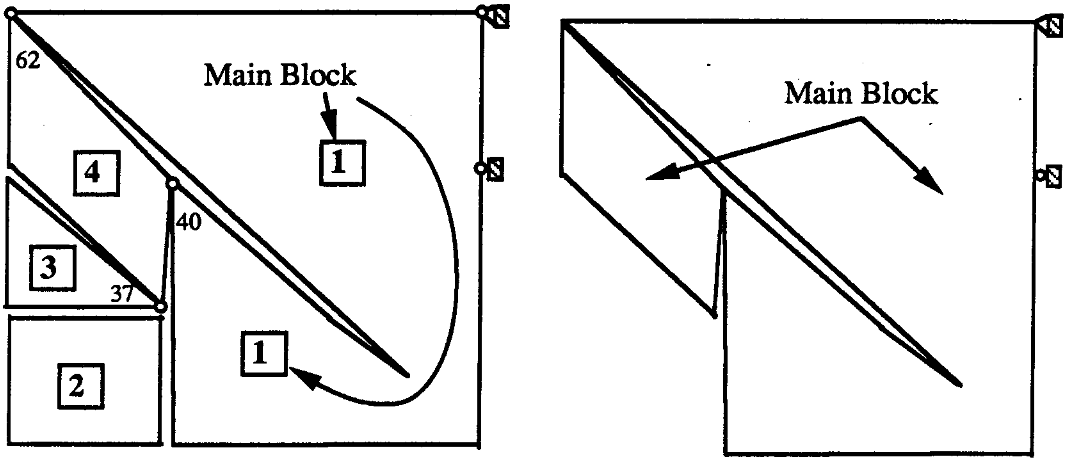

c) Distinct blocks and common nodes

d) Result structure

Fig. A.2: Example for Recognition and Treatment of Mechanisms

RECENT STRUCTURAL ENGINEERING REPORTS

Department of Civil Engineering
University of Alberta

151. *Behaviour and Ultimate Strength of Partial Joint Penetration Groove Welds* by D.P. Gagnon and D.J.L. Kennedy, July 1987.

152. *KBES for Design of Reinforced Concrete Columns* by A. Bezzina and S.H. Simmonds, July 1987.

153. *Compressive Behavior of Gusset Plate Connections* by S.Z. Hu and J.J. Cheng, July 1987.

154. *Development of Structural Steel Design Standards* by P.J. Marek and D.J.L. Kennedy, October 1987.

155. *Behaviour of Bolted Joints of Corrugated Steel Plates* by R.W.S. Lee and D.J.L. Kennedy, January 1988.

156. *Masonry Veneer Wall Systems* by W.M. McGinley, J. Warwaruk, J. Longworth and M. Hatzinikolas, January 1988.

157. *Stability of Concrete Plates* by A.O. Aghayere and J.G. MacGregor, February 1988.

158. *The Flexural Creep Behaviour of OSB Stressed Skin Panels* by P.C.K. Wong, L. Bach and J.J. Cheng, April 1988.

159. *Ultimate Strength of Eccentrically Loaded Fillet Welded Connections* by D.F. Lesik and D.J.L. Kennedy, May 1988.

160. *Fatigue Strength of Coped Steel Beams* by M.C.H. Yam and J.J. Cheng, June 1988.

161. *Analysis of Concrete Panels* by B. Massicotte, A.E. Elwi and J.G. MacGregor, July 1988.

162. *Behavior and Design of Reinforced Concrete Ice-Resisting Walls* by R.M. Ellis and J.G. MacGregor, November 1988.

163. *An Analysis of the Performance of Welded Wide Flange Columns* by D.E. Chernenko and D.J.L. Kennedy, December 1988.

164. *Nonlinear Dynamic Analysis of Caisson-Type Offshore Structures* by I.R. Soudy and T.M. Hrudey, March 1989.

165. *NORCO - A Program for Nonlinear Finite Element Analysis of Reinforced Concrete Structures - Users' Manual* by S. Balakrishnan, A.E. Elwi and D.W. Murray, April 1989.

166. *An Eigenvector-Based Strategy for Analysis of Inelastic Structures* by J. Napoleao, Fo., A.E. Elwi and D.W. Murray, May 1990.

167. *Elastic-Plastic and Creep Analysis of Casings for Thermal Wells* by S.P. Wen and D.W. Murray, May, 1990.

168. *Erection Analysis of Cable-Stayed Bridges* by Z. Behin and D.W. Murray, September 1990.

169. *Behavior of Shear Connected Cavity Walls* by P.K. Papinkolas, M. Hatzinikolas and J. Warwaruk, September 1990

170. *Inelastic Transverse Shear Capacity of Large Fabricated Steel Tubes,* by K.H. Obaia, A.E. Elwi and G.L. Kulak, April 1991.

171. *Fatigue of Drill Pipe* by G.Y. Grondin and G.L. Kulak, April 1991.

172. *The Effective Modulus of Elasticity of Concrete in Tension* by Atif F. Shaker and D.J. Laurie Kennedy, April 1991.

173. *Slenderness Effects in Eccentrically Loaded Masonry Walls* by Muqtadir, Mohammad A., Warwaruk, J. and Hatzinikolas, M.A., June 1991.

174. *Bond Model For Strength of Slab-Column Joints* by Scott D.B. Alexander and Sidney H. Simmonds, June 1991.

175. *Modelling and Design of Unbraced Reinforced Concrete Frames* by Yehia K. Elezaby and Sidney H. Simmonds, February 1992.

176. *Strength and Stability of Reinforced Concrete Plates Under Combined Inplane and Lateral Loads* by Mashhour G. Ghoneim and James G. MacGregor, February 1992.

177. *A Field of Fastener Tension in High-Strength Bolts* by G.L. Kulak and K. H Obaia, April 1992.

178. *Flexural Behaviour of Concrete-Filled Hollow Structural Sections* by Yue Qing Lu and D.J. Laurie Kennedy, April 1992.